



AFRL-OSR-VA-TR-2013-0499

**DEVELOPMENT OF ELASTO-ACOUSTIC INTEGRAL EQUATION
BASED SOLVER TO ASSESS/SIMULATE SOUND CONDUCTING
MECHANISMS IN HUMAN HEAD**

MAREK BLESZYNSKI

MONOPOLE RESEARCH

**09/09/2013
Final Report**

DISTRIBUTION A: Distribution approved for public release.

**AIR FORCE RESEARCH LABORATORY
AF OFFICE OF SCIENTIFIC RESEARCH (AFOSR)/RSL
ARLINGTON, VIRGINIA 22203
AIR FORCE MATERIEL COMMAND**

REPORT DOCUMENTATION PAGE

Form Approved
OMB NO. 0704-0188

Public Reporting burden for this collection of information is estimated to average 1 hour per response, including the time for reviewing instructions, searching existing data sources, gathering and maintaining the data needed, and completing and reviewing the collection of information. Send comment regarding this burden estimate or any other aspect of this collection of information, including suggestions for reducing this burden, to Washington Headquarters Services, Directorate for information Operations and Reports, 1215 Jefferson Davis Highway, Suite 1204, Arlington, VA 22202-4302, and to the Office of Management and Budget, Paperwork Reduction Project (0704-0188,) Washington, DC 20503.

1. AGENCY USE ONLY (Leave Blank)		2. REPORT DATE 31 May, 2013		3. REPORT TYPE AND DATES COVERED Final report 01 June, 2009 - 31 May, 2013	
4. TITLE AND SUBTITLE Development of Elasto-Acoustic Integral Equation Based Solver to Assess/Simulate Sound Conducting Mechanisms in Human Head				5. FUNDING NUMBERS Contract No: FA9550-09-1-0419	
6. AUTHOR(S) Elizabeth Bleszynski, Marek Bleszynski and Thomas Jaroszewicz					
7. PERFORMING ORGANIZATION NAME(S) AND ADDRESS(ES) Monopole Research 739 Calle Sequoia Thousand Oaks, CA 91360				8. PERFORMING ORGANIZATION REPORT NUMBER MON-14-14	
9. SPONSORING / MONITORING AGENCY NAME(S) AND ADDRESS(ES) Air Force Office of Scientific Research 875 N. Randolph Street, RM 3112 Arlington, VA 22203				10. SPONSORING / MONITORING AGENCY REPORT NUMBER not known	
11. SUPPLEMENTARY NOTES The views, opinions and/or findings contained in this report are those of the author(s) and should not be construed as an official Department of the Air Force position, policy or decision, unless so designated by other documentation.					
12 a. DISTRIBUTION / AVAILABILITY STATEMENT Approved for public release, distribution is unlimited.				12 b. DISTRIBUTION CODE	
13. ABSTRACT (Maximum 200 words) The project objectives were (a) to construct an accurate and efficient numerical simulation tool capable of handling a variety of aspects of wave propagation and the resulting energy flow in a human head subject to an incident acoustic wave propagating in the surrounding air; and (b) to develop understanding of mechanisms of energy transfer to the inner ear/cochlea region and quantitatively estimate the amounts of energy due to various sound-wave conduction paths. The problem is rather unique in that it involves very small amounts of energy transferred from air to a dense inhomogeneous object: such small energy flows are relevant only because of the exceedingly high sensitivity of the animal hearing apparatus. Therefore, in order to be able to achieve an adequate accuracy in the solutions for the pressure and its derivative, we have chosen to base our analysis on surface integral formulations for multi-region topologies with individual piecewise homogeneous sub-regions. A generalization of this approach to problems involving collection of piecewise homogeneous and inhomogeneous material regions was formulated. We constructed a detailed model of human head geometry which contains essential features needed to study energy transfer to the cochlea region. Since details of the geometry appear to be critical in controlling the energy flow to the cochlea region, a significant fraction of the effort was devoted to the construction of an anatomically faithful geometry model. The model was subsequently used in numerical simulation providing insight into the energy flow to the cochlea region through air and bone conduction paths. The main findings of our analysis were: (i) The distributions of pressure and velocity fields depend in very different ways on the object geometry, hence the behavior of the resulting energy flux may be highly nontrivial and difficult to predict without an actual computation. (ii) The resonances associated with the outer ear canals emanate energy to the surrounding tissues and provide an important contribution to the energy flux reaching the inner ear by means of non-airborne sound transmission. (iii) The overall magnitude of the energy flux inside the model is primarily controlled by the outer model surface and is fairly independent of the skull. (iv) The skull, however, affects the local distribution of the flux, possibly through reflections from the interfaces between the bone and the soft tissue. Such effects may be important in a more detailed analysis of the interaction of the pressure waves with the cochlea. Comparison of the results for models with and without outer ear canals (with the latter model representing effects of "perfect ear-plugs") shows that at relatively high frequencies (the wavelength smaller than 15 cm) a large part of the non-air-borne energy transfer to the inner ear is due to the resonant behavior of the wave in the outer ear canals. This contribution to the energy flux can be significantly reduced by blocking the ear canals. However, as the frequency decreases, the contribution of the energy penetrating through the surfaces of the head and the skull becomes dominant; and this energy-transfer mechanism can only be suppressed by protecting the entire surface of the head. Extension of the integral equation solver employing the first and second kind elastodynamics integral equation formulation for complex multi-domain geometries consisting of subregions characterized by different Lamé parameters was constructed which will constitute the basis for designing noise protection devices.					
14. SUBJECT TERMS computational acoustics and elastodynamics , integral equation formulation, matrix compression, large scale numerical simulations, bone conducted sound, noise protection devices				15. NUMBER OF PAGES 1 + 118	
				16. PRICE CODE not known	
17. SECURITY CLASSIFICATION OR REPORT UNCLASSIFIED	18. SECURITY CLASSIFICATION ON THIS PAGE UNCLASSIFIED	19. SECURITY CLASSIFICATION OF ABSTRACT UNCLASSIFIED	20. LIMITATION OF ABSTRACT UNCLASSIFIED		

1 Significance of the Problem

It has been long recognized that airborne sound transmission in the human auditory system (through the ear canal to the middle ear and to the inner ear) is not the only physical mechanism responsible for hearing. The other mechanisms (generally termed “bone conduction”, although not only the bone may be involved) include vibrations of the ear canal walls, direct mechanical excitation of the ossicular system and of the cochlea through bone and soft tissue vibrations, excitation of the middle ear by waves passing through the nose cavity, and similar phenomena. While those mechanisms may be beneficial in the context of hearing aids, in the noisy environment they constitute a significant risk, which may be difficult to mitigate by means of protective devices, typically designed to reduce the airborne energy transfer. Numerical simulation of energy transfer processes may be, therefore, of significant value in understanding the risks and preventing them by an appropriate design of protective devices, especially considering the fact that many relevant physical quantities are difficult and sometimes impossible to measure experimentally (particularly in vivo), and physiological measurements (such as hearing thresholds) may be biased by individual subjective perception differences.

2 Project Objectives

The objectives of this project were:

- to develop a formulation capable of describing energy flow in a human head subject to an incident acoustic wave propagating in the surrounding air, and construct a corresponding accurate, error controlled, and efficient numerical simulation tool,

and, using the developed simulation tool,

- to investigate and assess quantitatively various mechanisms of energy transfer to the inner ear due to various sound-wave conduction paths.

3 Overview of the approach

The present project consisted of three main parts:

- development of a fast surface integral equation solver with FFT-based matrix compression,
- development of an anatomically faithful geometry model
 - containing all essential anatomical elements needed to study energy transfer to the cochlea region, and
 - fulfilling all the requirements ensuring its usability in numerical simulations.
- analysis employing the developed geometry and the new solver which had as a goal providing information on energy flow to the inner ear area.

A very unique and non-trivial algorithmic challenge of constructing an accurate and efficient solution procedure for the problem of a human body/human head surrounded by air and exposed to the incoming acoustic wave is the high contrast nature of the problem. Due to the large (of the order of 10^3) density ratio of human versus air tissues there is a large impedance mismatch at the air-human body interface and only a small fraction of the incoming energy is transferred into the body interior. As the result, a very high accuracy in evaluating pressure and velocity fields at the air-human body interface is required in order to reliably compute the corresponding fields inside the human interior and, in particular, in the inner ear.

In our previous analysis [1, 2] we developed a novel, *two-stage approach* based on a *volumetric* integral equation formulation for objects of inhomogeneous material properties. That enhanced approach required introducing *surface* distributions of the pressure and velocity fields associated with the external high-contrast interfaces.

However, in the course of subsequent work, cases of slow convergence which lead to a reduced accuracy (e.g., for geometries containing internal high-contrast interfaces) were encountered/identified.

Therefore a part of our current effort was devoted to the development of a full surface integral equation formulation for a problem involving multiple piecewise-homogeneous material regions characterized by high-contrast interfaces. The constructed solver incorporates non-lossy, error controlled, FFT-based matrix compression which, due to its $N \log N$ (where N is the number of unknowns) memory and complexity performance, allows handling large anatomically realistic models without compromising the accuracy. Using the developed solver we achieved numerically reliable results when describing wave propagation in multi-region topologies with individual piecewise homogeneous sub-regions.

The developed approach/solver constitutes a significant addition with respect to both our previous formulation, as well as to other competitive methods. It also establishes the basis towards a combined surface-volume formulation which,

- would integrate the developed volumetric and surface integral equation solvers, and,
- would be particularly applicable to topologies consisting of adjacent, high complexity, strongly inhomogeneous, but relatively low contrast regions (e.g., bone, brain, ligament tissues) embedded in regions approximately homogeneous but characterized by high-contrast (e.g. skin tissue exposed to air).

Development of such a formulation we have already initiated and to pursue its continuation would be of significant interest and value.

Another ingredient critical in numerical simulations is a proper surface representation of the geometry of interest. Therefore significant fraction of the effort was devoted to the construction of a geometry model which would be anatomically faithful, would contain all the relevant components controlling the energy flow through the human head and, at the same time, would meet the stringent requirements of numerical simulations. Principal components of the developed human head model include:

- the outer surface of the skin surrounding the skull and containing
 - the outer ear represented by its exterior surface,

- the surface of the auditory canal,
- the tympanic membrane modeled as a finite-thickness surface,
- the skull including the temporal bone and boundaries of the inner ear cavity:
 - the cochlea with oval and round windows,
 - the vestibule,
 - the semi-circular canals.
- the middle ear cavity, consisting of the system of ossicles and supporting structures,

The third main part of our effort comprised extensive numerical analysis employing the developed formulation and the geometry. The main results can be summarized as follows:

- Distributions of pressure and velocity fields depend in a very nontrivial way on the object geometry, hence the behavior of the resulting *energy flux into the inner ear may be difficult to predict without realistic simulations.*
- Resonances associated with the outer ear canal emanate energy to the surrounding tissues and provide an important contribution to the energy flux reaching the inner ear by means of non-airborne sound transmission.

Comparison of the results for various head geometries shows that at relatively high frequencies (above about 2 kHz, corresponding the wavelengths $\lesssim 15$ cm) a large part of the non-air-borne energy transfer to the inner ear is due to the resonant behavior of the wave in the outer ear canals. This contribution to the energy flux can be significantly reduced by means of ear-plugs. However, as the frequency decreases, the contribution of the energy penetrating through the surfaces of the head and the skull becomes dominant; and this energy-transfer mechanism can only be suppressed by protecting the entire surface of the head.

- The skull affects the local energy flux distribution to the inner ear, possibly through reflections from the interfaces between the bone and the soft tissue.

The continuation/completion of the above described approach may constitute a solid basis for investigations of the effectiveness of air- and bone-conduction noise-protection devices, as well as the effectiveness of various hearing-enhancement aids.

4 Publications

- (1) "Formulation and applications of an integral-equation approach for solving scattering problems involving an object consisting of a set of piecewise homogeneous material regions"

J. Acoust. Soc. Am. Volume 130, Issue 4, pp. 2435-2435 (2011); Elizabeth Bleszynski, Marek Bleszynski, and Thomas Jaroszewicz

- (2) "Numerical simulation of acoustic wave interaction with inhomogeneous elastic bodies containing homogeneous inclusions"
J. Acoust. Soc. Am. Volume 129, Issue 4, pp. 2382-2382 (2011); Elizabeth Bleszynski, Marek Bleszynski, and Thomas Jaroszewicz
- (3) "Formulation and selected applications of a regularized elastodynamics integral equation approach to large scale scattering problems involving inhomogeneous objects" J. Acoust. Soc. Am. Volume 131, Issue 4, pp. 3510-3510 (2012); Elizabeth Bleszynski, Marek Bleszynski, and Thomas Jaroszewicz
- (4) "Reduction of Volume Integrals to Nonsingular Surface Integrals for Matrix Elements of Tensor and Vector Green Functions of Maxwell Equations"
IEEE Transactions on Antennas and Propagation, vol. 61, No. 7, July 2013; Elizabeth Bleszynski, Marek Bleszynski, and Thomas Jaroszewicz
- (5) "Integral-equation solver for investigation of acoustic energy flow in the human head"
(to be submitted to JASA); Elizabeth Bleszynski, Marek Bleszynski, and Thomas Jaroszewicz
- (6) "Formulation and Applications of the First and the Second Kind Elastodynamics Integral Equations "
(to be submitted to JASA); Elizabeth Bleszynski, Marek Bleszynski, and Thomas Jaroszewicz

5 Summary of the results

We briefly summarize here the areas of our work and our main results:

5.1 Development of integral-equation formulation and solution algorithm

- We assessed merits of various forms of integral equations employing different volumetric and surface representations in their ability to model problems of our interest: propagation of an elasto-acoustic wave through the human head.
- We selected and constructed formulations based on first and second kind surface integral equations for geometries composed of multiple, homogeneous regions:

- in acoustics, the problem is formulated for two unknown scalar fields,

$$p(\mathbf{r}) \quad \text{and} \quad q(\mathbf{r}) \equiv \frac{1}{\rho(\mathbf{r})} \frac{\partial p(\mathbf{r})}{\partial n(\mathbf{r})} ,$$

where p is the pressure on an interface, ρ the medium density, and \mathbf{n} the normal to the interface,

- in elastodynamics, for two unknown vector fields,

$$\mathbf{u}(\mathbf{r}) \quad \text{and} \quad \mathbf{t}(\mathbf{r}) ,$$

i.e., for the displacement and traction on the interfaces.

- An important element of the formulation enabling its efficient implementation was the reduction, by means of suitable integration by parts, of singular terms appearing in matrix elements arising in surface integral equations to weakly singular integrals. The paper describing the approach has been submitted and accepted for publication (see Ref. []).
- We developed a parallel solver based on the selected formulation. The solver uses an FFT-based error-controlled matrix compression which
 - is suitable to problems involving highly sub-wavelength discretization (such as the middle and inner ear cavity problem),
 - is characterized by $N \log N$ memory and complexity performance (where N is the number of unknowns), and hence allows handling large anatomically realistic models without compromising the accuracy.
- We initiated development of a combined surface-volume formulation suitable for geometries consisting of adjacent, high complexity, strongly inhomogeneous, but relatively low contrast regions (e.g., bone, brain, ligament tissues) embedded in or adjacent to regions approximately homogeneous but characterized by high-contrast (e.g. skin tissue exposed to air, lining of nasal cavity, etc.). As the first step we developed discretization methods for equations coupling surface and volume variables on interfaces and in inhomogeneous domains.

Completion of this approach may lead to the state of the art numerical simulation tool capable of accurate determination of acoustic energy transfer and its deposition in geometrically very intricate and most vulnerable regions of a human head.

5.2 Geometry construction

- Availability of a high quality geometry model of a human head is of critical importance in obtaining reliable results. By a high quality model we understand:
 - a model anatomically faithful, with the proper choice of relevant organs/tissues and, at the same time,
 - a model with geometry discretization complying with the strict requirements of the numerical tool.

Therefore, geometry construction constituted a very intense part of the project. Our geometry model has been built by using several publicly available sources and required considerable work in matching the components. In its present form it contains essential features needed to study energy flow/transfer to the human head and to the cochlea region.

- The principal components of our human head model are:
 - the outer surface of the skin surrounding the skull and containing

- the outer ear represented by its exterior surface,
 - the surface of the auditory canal, and
 - the tympanic membrane modeled as a finite-thickness surface,
 - the skull, described by surfaces of the bones and containing
 - the required boundaries of the middle ear cavity,
 - the boundaries of the inner ear cavity (the cochlea, the vestibule, and the semi-circular canals),
 - the middle ear cavity, consisting of the system of ossicles and supporting structures,
- We stress that there are several imperative requirement in constructing a geometry representation suitable for numerical simulations which make it a tedious and time consuming process. They include:
- nearly uniform discretization with local variations reproducing small geometry details,
 - good quality (aspect ratio) triangular mesh,
 - closed surfaces with no intersecting or overlapping patches and,
 - grid connectivity on joints between patches.

Below we show some representative examples of the head geometry used in our simulations.

Please zoom the pdf file when you are viewing the figures below to see better the geometry details and the mesh quality.



Figure 1: The discretized skin geometry.

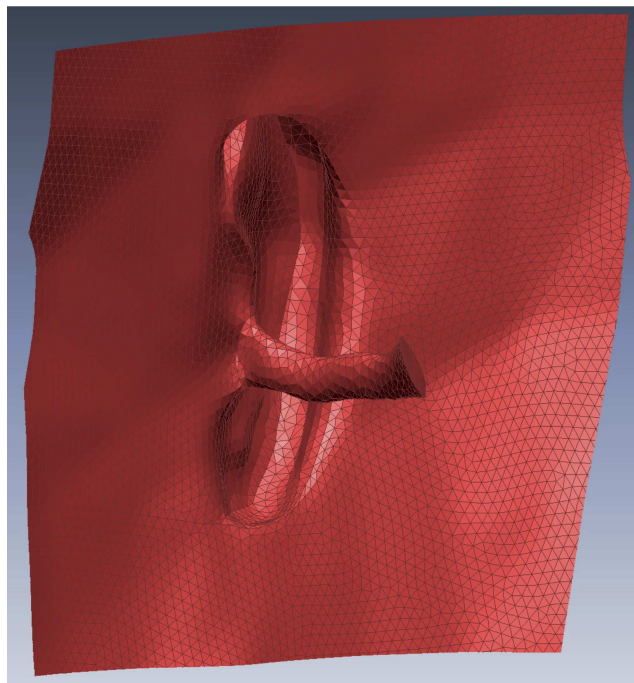


Figure 2: A detail of the discretized skin geometry viewed from the inside - the outer meatus.

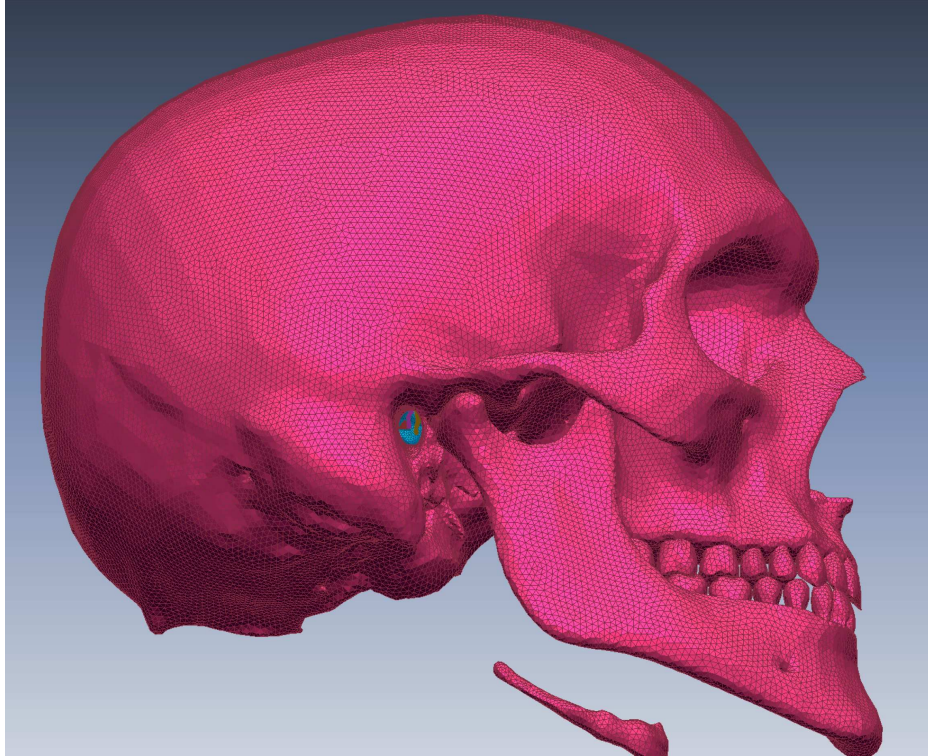


Figure 3: A view of the skull geometry modeled as a closed surface with the ear canal and the ossicles in the middle ear cavity (the eardrum was removed for a better view).

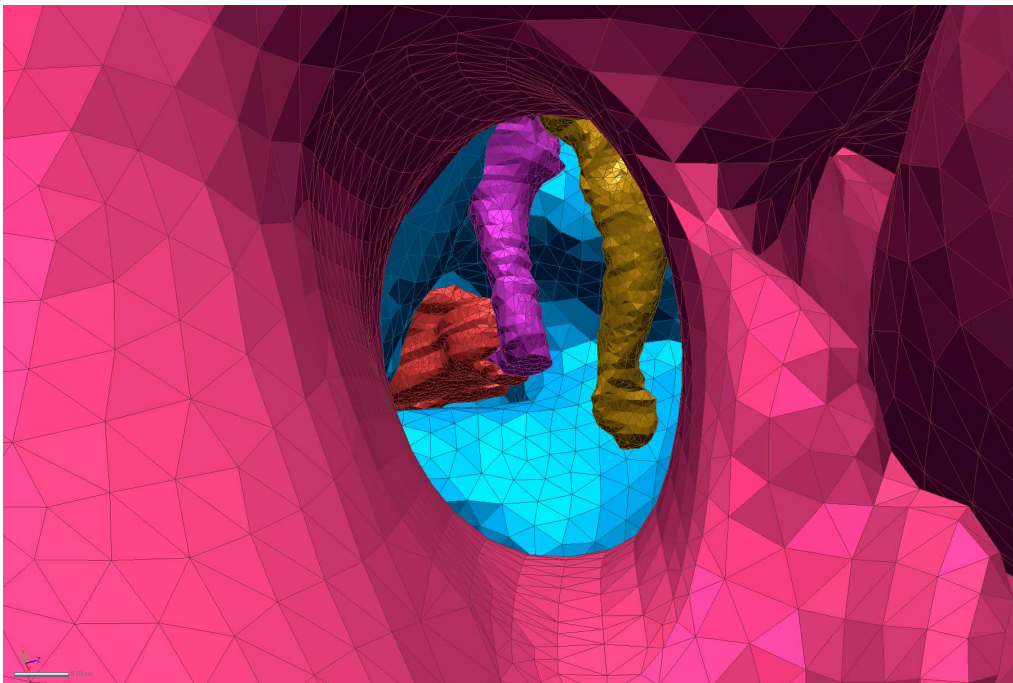


Figure 4: A close view at the outer ear canal, the middle ear cavity and the ossicles (the eardrum was removed for a better view).

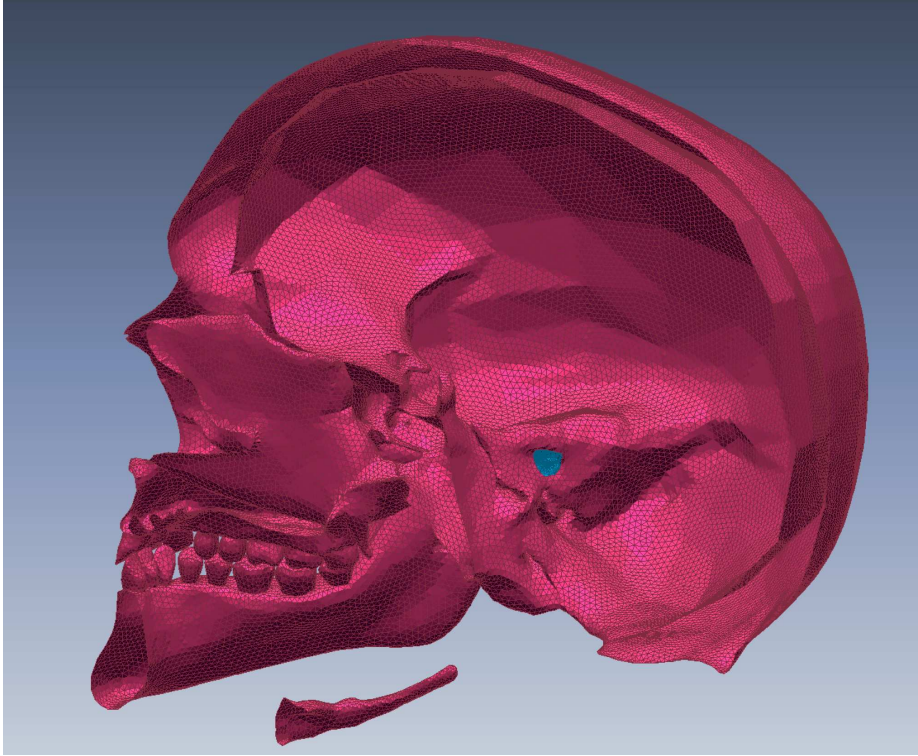


Figure 5: A view of the skull geometry modeled as a closed surface from the inside - note the temporal bone and the inner meatus.

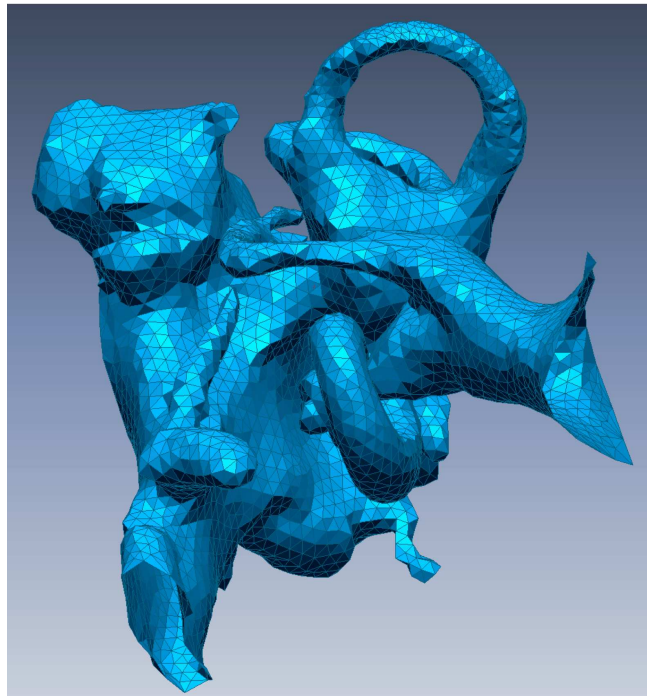


Figure 6: A detail of the skull surface: the inner meatus, cochlea, semicircular canals, the middle ear cavity). The triangulation used for this particular component of the geometry resulted in about 280,000 unknowns.

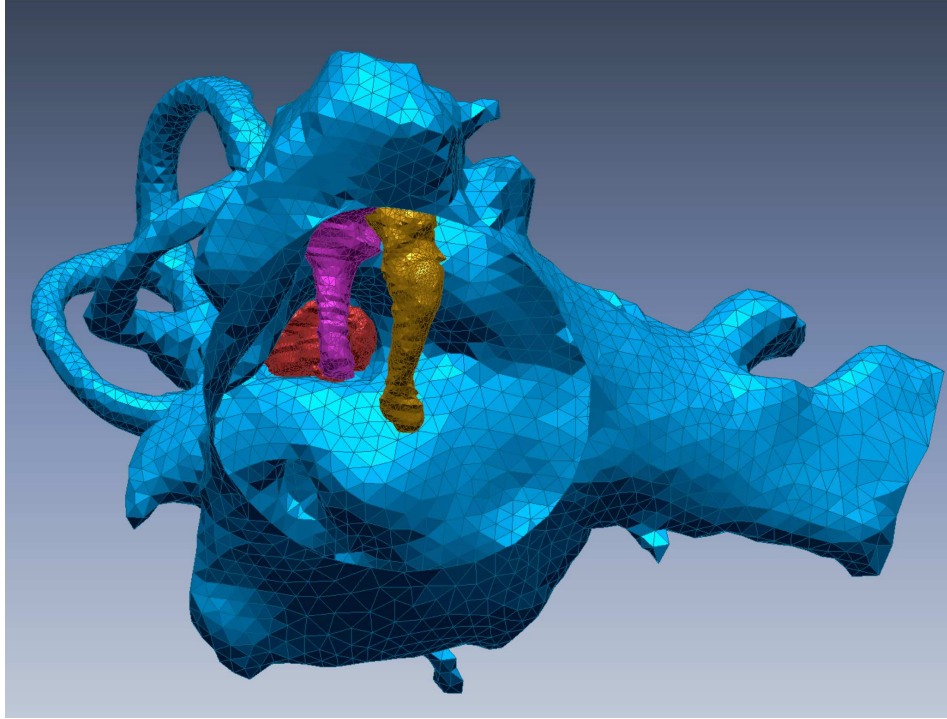


Figure 7: Another detail of the skull surface: the middle ear cavity with the attic, the semi-circular canals, and the ossicles (with the eardrum removed for a better view).

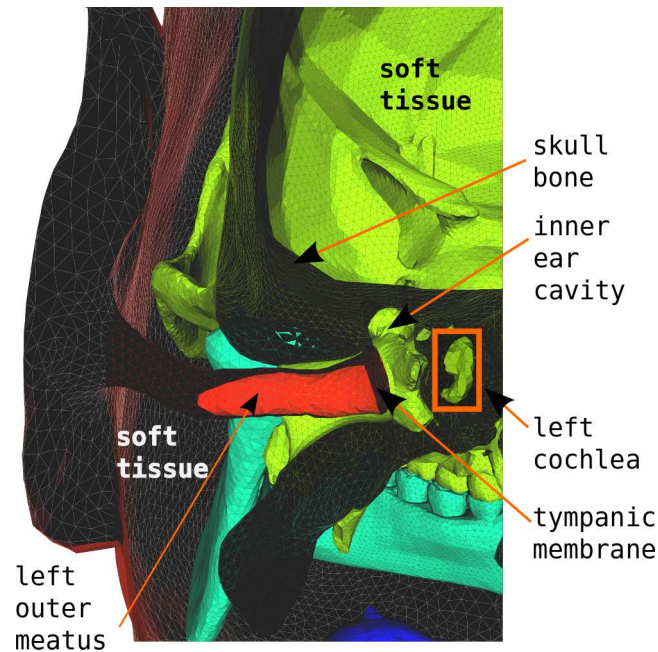


Figure 8: A part of the discretized head geometry model in the vicinity of the left ear, shown as a coronal section seen from the back. The dark surfaces visible in the cross-section are interior sides of the boundaries of the bone and the outer boundary of the head (the skin). The space between the skin and skull, and the interior of the skull are filled with soft tissue. Since the clipping plane intersects the outer ear canal, its interior is partly exposed.

- Although the degree of detail and complexity of our model allows us to carry out reasonably realistic numerical simulations, it would be beneficial to further enhance the geometry model by including, in particular, such additional elements as
 - the nasal cavity,
 - the brain tissue, the latter characterized by nontrivial elasto-viscous properties.

Such components should be carefully and in as much as possible complete manner taken into account, as they may play a significant role in controlling the distribution of the energy flow into the inner ear and therefore further improve fidelity of the simulations.

An important and very valuable aspect of the created geometry is that, due to its perfect connectivity, the shapes and sizes of individual organs can be locally deformed (rescaled) leading to different head geometry realizations. Hence, sensitivity of the energy flow and energy flux distribution on the geometrical details of the human head can be studied.

5.3 Numerical simulations and assessment of the relative importance of the bone conduction mechanism

5.3.1 Overview

As we mentioned in the Introduction, the acoustic and elastic wave propagation problems we are investigating involve penetration of waves from a low-density medium (air) to the interior of an object consisting of high-density tissues.

This category of problems have been relatively little explored in the past, either theoretically or in applications. Most of the theoretical work concentrated on essentially single-region problems involving hard- or soft-surface or impedance boundary conditions, while the transmission boundary problems have been receiving much less attention. Similarly, typical applications were either (1) dealing with much lower contrasts than in our case (for instance, in marine applications, rock- or metal-to-water density ratios not exceeding about 10, compared to our ratios ≥ 1000), or (2) considering wave sources embedded in the dense medium rather than in the surrounding air, as is the case in seismic or vibration mechanics problems.

In view of this status of the current research, our problem required a considerable effort to develop an insight into the mechanisms of wave penetration through high-contrast interfaces and its propagation in the dense medium. In particular, our extensive numerical simulations allowed us to establish a general picture of energy flow inside the human head model and identify the main mechanisms controlling its distribution (including reflection from and transmission through high contrast interfaces, as well as resonances in air cavities); we were also able to obtain *quantitative* estimates of the amount of energy (relative to the incident energy flux density) reaching the inner ear by means of bone- and soft-tissue conduction. We stress here that, although the overall level of the energy flux entering the cochlear cavity is relatively insensitive to the geometry and material parameters variations, its detailed distribution and even orientation *do* depend on the geometry in a nontrivial way and would have been impossible to predict without the actual computations.

The main results of the simulations are presented below. Additional results are contained in the attached draft of a paper (Appendix B).

5.3.2 Energy flux as a measure of the tissue conduction effects

As a quantitative measure of the amount of bone-conducted acoustic energy reaching the inner ear we compute the integral of the *absolute value* of the average energy flux density F over the surface S of the cochlear cavity,

$$\Phi_S := \frac{1}{|S|} \int_S d^2r |F(\mathbf{r})|, \quad F(\mathbf{r}) := \frac{\rho_0}{k_0 \rho(\mathbf{r})} \text{Im} \{ p(\mathbf{r}) \partial_n p^*(\mathbf{r}) \}, \quad (5.1)$$

where $|S|$ is the area of the surface.

5.3.3 Bone-conducted energy flow into inner ear in the presence and absence of the external ear canal

We present here results for the energy flow distribution in two models, both including the full skull and middle/inner ear cavity, but differing in the presence or absence of the outer ear canal. The latter model can be considered a realization of a *perfect ear-plug*, with which the outer auditory canal is effectively closed.

In both models we assume typical approximate values of the relative densities and the refractive indices, $\rho/\rho_0 = 1000$ and $n = 0.2$ for the soft tissues, and $\rho/\rho_0 = 2000$ and $n = 0.4$ for the bone. The model is being subject to a pressure plane wave of unit amplitude, incident from the left side of the head. In most of the examples we carried out computations in a wide range of wavelengths, from $\lambda = 3$ cm (about 10 kHz) to $\lambda = 80$ cm (about 400 Hz); $\lambda = 2\pi/k_0$ is always the wavelengths in the air.

We note that in these simulations we *excluded* the impedance-matching mechanism of the middle ear; hence, the entire energy arriving at the inner ear has propagated exclusively through the bone and other tissues, and *not* through the air-conduction pathway.

Distribution of the energy flux in the temporal bone area for $\lambda = 5$ cm is visualized in Fig. 9(a). The flux density has large values on the walls of the outer ear canal and the energy evidently emanates from there to the surrounding tissues. In fact, by comparing this distribution with that for the alternative model we find that the presence of the outer ear canal increases the energy flux through the inner ear by about a factor of 10.

An interesting feature is that in different parts of the canal the energy flows from the air into the tissue or in the opposite direction. Moreover, we found that the energy flow *changes direction* several times with the changing wavelength in the considered range. Such a behavior is characteristic of a standing acoustic wave being formed in the ear canal [3].

A more systematic and quantitative comparison of the models is provided in Fig. 9(b) which shows the average relative energy flux through the cochlea (Eq. (5.1)) as a function of the wavelength of the incident wave. At larger wavelengths the presence of the outer auditory canal increases the energy flux by about a factor of two. At smaller wavelengths the effect is larger and exhibits a resonant behavior, manifesting itself by the two peaks at $\lambda \approx 5$ cm and $\lambda \approx 15$ cm.

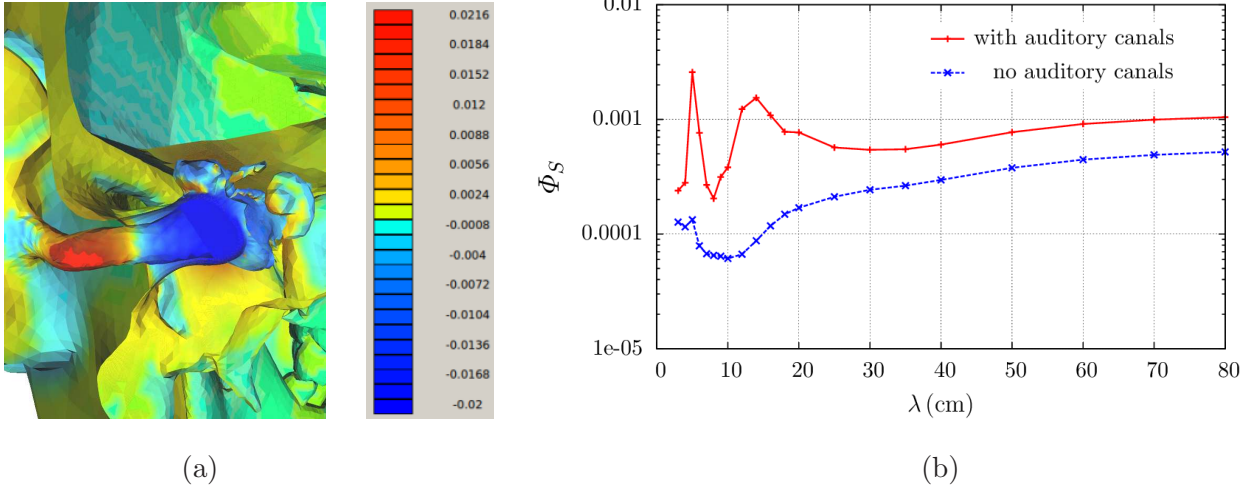


Figure 9: (a) Distribution of the energy flux density on the material interfaces in the vicinity of the left temporal bone, for $\lambda = 5$ cm. Positive (red) and negative (blue) flux indicates energy flowing into and out of the bone. (b) The average energy flux density through the surface of the cochlear cavity (relative to the incident wave flux density), as a function of the wavelength, for the model with the skull and soft tissues.

5.3.4 The role of acoustic bone conduction vs. soft tissue conduction

In order to assess the significance of bone conduction vs. soft-tissue conduction, we also computed the amount of energy flowing through the cochlea in a model of the human head filled entirely with a *homogeneous* material, *without* the skull structure. In this comparison we considered, as before, two models of the outer head surface: without outer ear canals (i.e., with “perfect ear-plugs”) and with ear canals.

We first consider the model *without* the outer ear canals, in which the entire head is filled with the soft tissue ($\rho/\rho_0 = 1000$, $n = 0.2$). We solve the transmission problems with the outer head surface (the “skin”) and a part of the middle- and inner-ear ear cavity, including the cochlear cavity. The presence of the latter surface does not affect the solution itself, but allows us to compute the average energy flux

$$\Phi_S := \frac{1}{|S|} \int_S d^2r |F(\mathbf{r})|, \quad F(\mathbf{r}) := \frac{\rho_0}{k_0 \rho(\mathbf{r})} \text{Im} \{ p(\mathbf{r}) \partial_n p^*(\mathbf{r}) \}, \quad (5.2)$$

through the same part S of the cochlea cavity surface as used before. (Fig. 10).

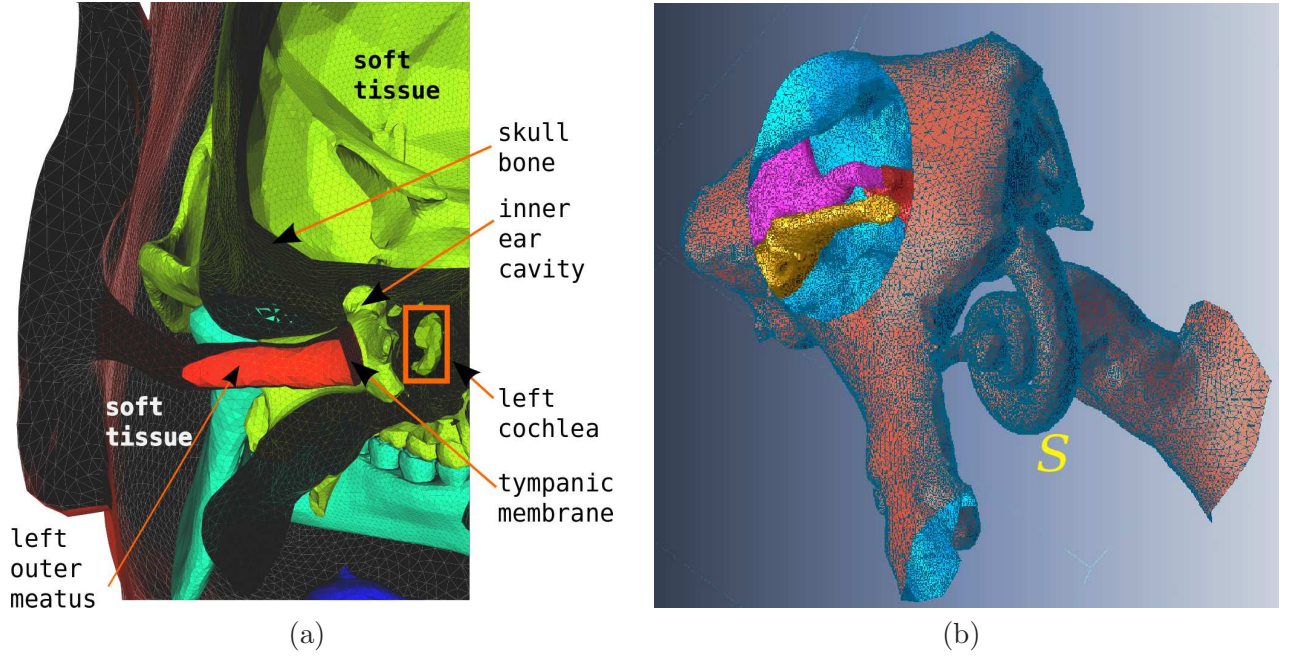


Figure 10: (a) A part of the discretized head geometry model in the vicinity of the left ear, shown as a coronal section seen from the back. The dark surfaces visible in the cross-section are interior sides of the boundaries of the bone and the outer boundary of the head (the skin). The space between the skin and skull, and the interior of the skull are filled with soft tissue. Since the clipping plane intersects the outer ear canal, its interior is partly exposed. (b) Part of the discretized geometry containing the left middle- and inner-ear cavity, viewed from below. The surface of the cochlear cavity is marked with S .

The results are shown in Fig. 11. It can be seen that the reduction of the flux due to the presence of the skull is not large, of the order of 40 %, and can be plausibly attributed to an additional reflection of the sound wave from the interfaces between the skull and soft tissues.

Results for the analogous model *with* the outer ear canals are shown in Fig. 11(II). Again, the flux densities in the the three models are not strongly affected by the presence of the skull. In particular, the persistent resonant structure suggests that it is due rather to the shape of the head itself than to the presence of the skull.

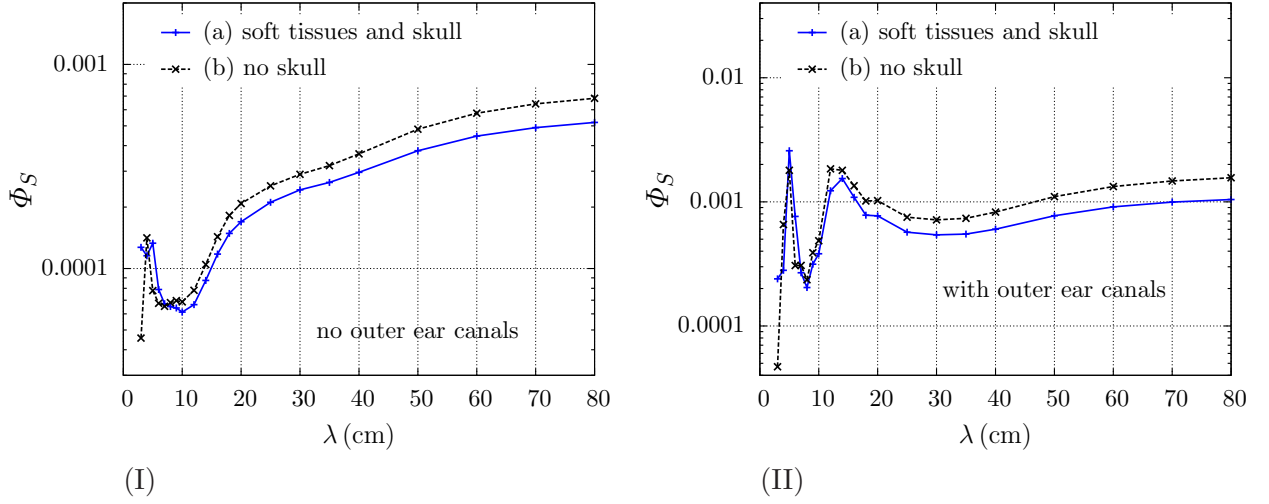


Figure 11: The average relative energy flux density through the the cochlear cavity as a function of the wavelength, for the model without the skull (b), compared to the result for the reference model (a) with the skull. Plots (I) and (II) correspond to head surface models *without* and *with* the outer ear canals.

The above comparisons of the absolute energy flux densities might seem to suggest the skull does not play an important role in sound conduction. However, a more careful examination of the *spatial distribution* and *orientation* of the energy flow shows this is not the case:

As an example of such an analysis, we plot in Figs. 12 flux distributions on the middle- and inner-ear cavity at the wavelength 12 cm (in the resonance region), for the model with (a) and without (b) the skull, but in the presence of the outer ear canals. We find that the direction of the energy flow in these models is *almost exactly reversed*. This phenomenon (which is, in fact, observed for most of the considered wavelengths) has to be attributed to interactions (perhaps reflections) involving the skull bones.

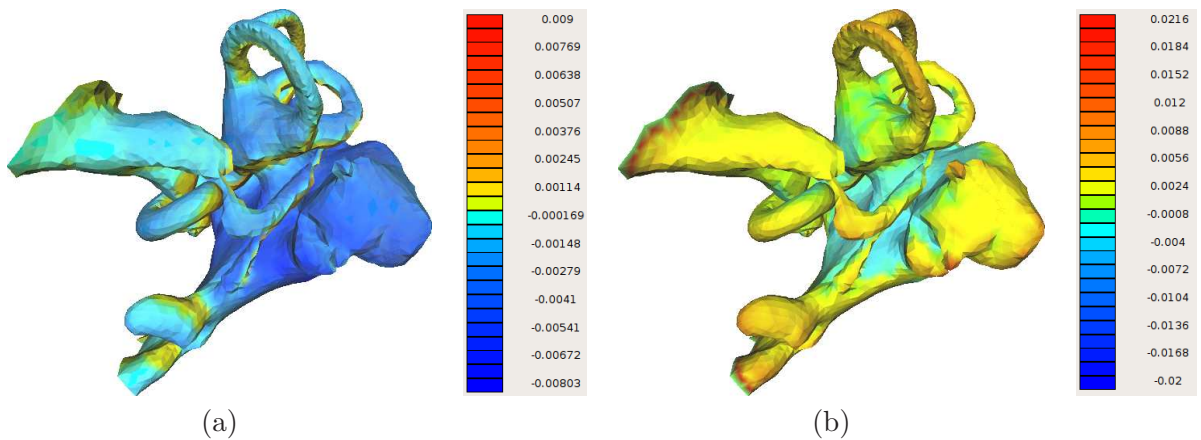


Figure 12: Energy flux density distributions on the left middle- and inner-ear cavity for wavelength 12 cm computed for the full model (a) and for the model without the skull (b). The cavity surface is viewed from the top; the canal directed to the left and up is the inner meatus.

5.3.5 Summary of simulation results

In summary:

- We were able to establish a general picture of energy flow inside the head model and identify the main non-air conduction mechanisms (in particular, transmission through and reflection from high-contrast interfaces, as well as resonances in air cavities).
- We found that the *overall magnitude of the energy flux* reaching the inner ear is relatively insensitive (within a factor \times to the details of the geometry and even the presence or absence of the skull (hence, sound conduction through soft tissues is also significant).
- However, the more detailed *energy flux distribution* and even the flux orientation proved to be highly sensitive to the shape of the interfaces and to the difference of material properties between the bone and the soft tissues. For instance, the presence of the skull bones may *reverse* the direction of energy flux near the middle ear. Such effects may be of importance in a more detailed analysis of the physiological effects of the energy delivered to the inner ear.
- We established the frequency dependence of the energy reaching the inner ear through the tissues. We found that at higher frequencies (few centimeter wavelengths in air) a large part of that energy emanates from the outer ear canal, which supports a resonant standing wave. However, at lower frequencies, the energy arriving at the inner ear is dominated by transmission through a large area of the head surface.
- The last result suggests that the higher frequency noise components may be significantly reduced by blocking the ear canals, but lower frequencies can only be suppressed by protecting the entire surface of the head.

6 Open problems requiring possible future research

Although we believe we achieved a substantial degree of understanding of the sound propagation mechanisms in the human head, we also encountered challenges requiring further investigation and offering, potentially, interesting and useful results. We list some of them:

- The role of large cavities in the head (in particular, the nasal cavity) should be investigated more thoroughly. Simulations should include possible shape variations (hence possibly different resonant behavior) and should establish the significance of the cavities' communication with the outer atmosphere.
- The skull bones are known to contain a multitude of small air cavities effectively forming a porous bone structure; their presence may significantly affect wave scattering. Because of their complexity and the lack of a reliable geometry model, the small cavities were not included in our simulations. It might be possible to take them into account by means of evaluating effective medium parameters, which would then probably exhibit substantial dispersion.

- The brain tissue is known to exhibit significant viscosity. Its effects in energy dissipation should be investigated.
- We found that although the overall magnitude of the tissue-conducted energy reaching the inner ear is relatively stable, the details of its spatial distribution strongly depend on the head geometry. It would be of interest to investigate more thoroughly these effects and their possible physiological role.
- In our simulations we found that high-contrast material layers (such as skull bones in air) reflect most of the acoustic energy and transmit very little, *even* if they are *thin* compared to the wavelength. This behavior suggests possible efficient noise protection devices based on high-contrast layered structures. A detailed investigation conducted with the developed simulation tools may prove to be of significant interest and usefulness.

Appendices

A Details of the formulation

We provide here the main elements of the theory and some details of implementation of our solver for elastodynamics problems. More information on the formulation of the acoustic integral-equations and their implementation in our current solver are given in the draft of a paper contained in Appendix B.

A.1 Formulation of elastodynamics integral equations and algorithm development

In this Section we provide details on the elasto-dynamics integral equations for multi-domain problems we constructed and partially implemented. We start with the Lamé equation for the displacement in elastic medium subject to an external plane wave excitation $\mathbf{F}(\mathbf{r})$. The displacement $\mathbf{u}(\mathbf{r})$ satisfies the equations

$$\{(\lambda + \mu) \nabla_{\mathbf{r}} \otimes \nabla_{\mathbf{r}} + \mu \nabla_{\mathbf{r}}^2 + \rho \omega^2\} \mathbf{u}(\mathbf{r}) = \mathbf{F}(\mathbf{r}), \quad (\text{A.1})$$

where λ and μ are the (position dependent) Lamé parameters, ρ is the medium density and ω is the incident wave frequency.

The homogeneous medium Green function of the Lamé equation is the second rank symmetric tensor

$$G(\mathbf{R}) = \frac{1}{\mu} g_S(R) \hat{I} + \frac{1}{\mu k_S^2} \nabla_{\mathbf{R}} \otimes \nabla_{\mathbf{R}} [g_S(R) - g_C(R)], \quad (\text{A.2})$$

where

$$\begin{aligned} g_C(R) &= \frac{e^{ik_C R}}{4\pi R}, \\ g_S(R) &= \frac{e^{ik_S R}}{4\pi R}, \\ \mathbf{R} &= \mathbf{x} - \mathbf{y}. \end{aligned} \quad (\text{A.3})$$

The two wave-numbers,

$$k_C = \frac{\omega}{c_C}, \quad k_S = \frac{\omega}{c_S}, \quad (\text{A.4})$$

are related to the longitudinal (compressional) and transverse (shear) wave speeds,

$$c_C = \sqrt{\frac{\lambda + 2\mu}{\rho}}, \quad c_S = \sqrt{\frac{\mu}{\rho}}. \quad (\text{A.5})$$

We consider a single material region Ω bounded by $\partial\Omega$. By assuming that, inside Ω , the displacement $\mathbf{u}(\mathbf{x})$ satisfies the Lamé equation (C.14), we may construct the following *integral*

representation for the displacement field, which allows us to find its value at any point \mathbf{x} in Ω in terms of an integral of two fields, $\mathbf{u}(\mathbf{x})$ and $\mathbf{t}(\mathbf{x})$, on the region boundary:

$$\mathbf{u}(\mathbf{x}) = \int_{\partial\Omega} d^2y [\mathbf{u}(\mathbf{y}) \cdot \Gamma(\mathbf{x}, \mathbf{y}) + \mathbf{t}(\mathbf{y}) \cdot G(\mathbf{x} - \mathbf{y})] . \quad (\text{A.6})$$

The symbols appearing in the integrand of the above integral representation are as follows:

- $\mathbf{u}(\mathbf{y})$ is the displacement vector field,
- $\mathbf{t}(\mathbf{y})$ is the traction vector field related to the stress tensor $\hat{\tau}(\mathbf{y})$ as follows:

$$\begin{aligned} \mathbf{t}(\mathbf{y}) &= \mathbf{n}(\mathbf{y}) \cdot \hat{\tau}(\mathbf{y}) , \\ \hat{\tau}(\mathbf{y}) &= \lambda \hat{I} \nabla_{\mathbf{y}} \cdot \mathbf{u}(\mathbf{y}) + \mu [\nabla_{\mathbf{y}} \otimes \mathbf{u}(\mathbf{y}) + \mathbf{u}(\mathbf{y}) \otimes \nabla_{\mathbf{y}}] , \\ \mathbf{t}(\mathbf{y}) &= \lambda \mathbf{n}(\mathbf{y}) [\nabla_{\mathbf{y}} \cdot \mathbf{u}(\mathbf{y})] + \mu \{ [\mathbf{n}(\mathbf{y}) \cdot \nabla_{\mathbf{y}}] \mathbf{u}(\mathbf{y}) + \nabla_{\mathbf{y}} [\mathbf{n}(\mathbf{y}) \cdot \mathbf{u}(\mathbf{y})] \} , \\ \hat{\tau}_{ij}(\mathbf{y}) &= C_{ijkm} \partial_k u_m(\mathbf{y}) , \\ C_{ijkl} &= \lambda \delta_{ij} \delta_{kl} + \mu (\delta_{ik} \delta_{jl} + \delta_{il} \delta_{jk}) , \end{aligned} \quad (\text{A.7})$$

- $G(\mathbf{x} - \mathbf{y})$ is a second rank symmetric tensor, the Green function of the Lamé equation given by (C.2),
- $\Gamma(\mathbf{x}, \mathbf{y})$ is a second rank non-symmetric tensor, related to the third rank stress tensor Green function $\Sigma(\mathbf{x})$ (symmetric in its first two indices)

$$\begin{aligned} \Gamma(\mathbf{x}, \mathbf{y}) &= \mathbf{n}(\mathbf{y}) \cdot \Sigma(\mathbf{R}) , \\ \Gamma_{ij}(\mathbf{x}, \mathbf{y}) &= \frac{\partial}{\partial y_q} G_{ip}(\mathbf{x} - \mathbf{y}) C_{jkpq} n_k(\mathbf{y}) = \{ \mathbf{n}(\mathbf{y}) \cdot \Sigma(\mathbf{x} - \mathbf{y}) \}_{ij} , \\ \Gamma_{jk}(\mathbf{x} - \mathbf{y}) &= n_i(\mathbf{y}) C_{ijml} \partial_m G_{lk}(\mathbf{R}) , \\ [\Sigma(\mathbf{R})]_{ijk} &= \lambda \delta_{ij} \partial_m G_{mk}(\mathbf{R}) + \mu [\partial_i G_{jk}(\mathbf{R}) + \partial_j G_{ik}(\mathbf{R})] = C_{ijml} \partial_m G_{lk}(\mathbf{R}) , \\ \Gamma_{jk}(\mathbf{x}, \mathbf{y}) &= n_i(\mathbf{y}) \Sigma_{ijk}(\mathbf{R}) , \\ \Phi_{jk}(\mathbf{x}, \mathbf{y}) &= \Sigma_{ijk}(\mathbf{R}) n_i(\mathbf{x}) , \\ \Sigma(\mathbf{R}) &= -\Sigma(-\mathbf{R}) . \end{aligned} \quad (\text{A.8})$$

The tensor Green functions $G(\mathbf{R})$ and $\Sigma(\mathbf{R})$ satisfy the following equations:

$$\begin{aligned} [(\lambda + \mu) \nabla_{\mathbf{R}} \otimes \nabla_{\mathbf{R}} + \mu \nabla_{\mathbf{R}}^2 + \rho \omega^2] G(\mathbf{R}) &= -\delta(\mathbf{R}) \hat{I} , \\ \nabla_{\mathbf{R}} \cdot \Sigma(\mathbf{R}) + \rho \omega^2 G(\mathbf{R}) &= -\delta(\mathbf{R}) \hat{I} , \\ \Sigma(\mathbf{R}) \cdot \nabla_{\mathbf{R}} + \rho \omega^2 G(\mathbf{R}) - \lambda (\nabla_{\mathbf{R}} \cdot -\nabla_{\mathbf{R}} \otimes) \nabla_{\mathbf{R}} \cdot G(\mathbf{R}) &= -\delta(\mathbf{R}) \hat{I} , \\ \partial_i [C_{ijkl} \partial_k G_{lm}(\mathbf{R})] + \rho \omega^2 G_{jm}(\mathbf{R}) &= -\delta_{jm} \delta(\mathbf{R}) , \\ \partial_i [\Sigma_{ijm}(\mathbf{R})] + \rho \omega^2 G_{jm}(\mathbf{R}) &= -\delta_{jm} \delta(\mathbf{R}) , \\ \nabla_{\mathbf{R}} \cdot G(\mathbf{R}) &= \frac{k_C^2}{\rho \omega^2} \nabla_{\mathbf{R}} g_C(R) , \end{aligned} \quad (\text{A.9})$$

while $\hat{\tau}(\mathbf{x})$ satisfies the equation

$$\begin{aligned} \nabla_{\mathbf{r}} \cdot \hat{\tau}(\mathbf{r}) + \rho \omega^2 \mathbf{u}(\mathbf{r}) &= 0 , \\ \frac{1}{2}[\nabla_{\mathbf{r}} \otimes \mathbf{u}(\mathbf{r}) + \mathbf{u}(\mathbf{r}) \otimes \nabla_{\mathbf{r}}] - D_{ijkl} \hat{\tau}_{kl}(\mathbf{r}) &= 0 , \end{aligned} \quad (\text{A.10})$$

with

$$\begin{aligned} C_{ijkl} &= \lambda \delta_{ij} \delta_{kl} + \mu (\delta_{ik} \delta_{jl} + \delta_{il} \delta_{jk}) , \\ C_{ijkl} &= C_{jikl} = C_{ijlk} = C_{klij} . \end{aligned} \quad (\text{A.11})$$

is the fourth-rank elastic stiffness tensor and

$$D_{ijkl} = \frac{1}{4\mu} \left[(\delta_{ik} \delta_{jl} + \delta_{il} \delta_{jk}) - \frac{2\lambda}{3\lambda + 2\mu} \delta_{ij} \delta_{kl} \right] . \quad (\text{A.12})$$

An additional useful relation is

$$C_{ijkl} \partial_k u_l(\mathbf{x}) \partial_i G_{jm}(\mathbf{R}) - C_{ijkl} \partial_i u_j(\mathbf{x}) \partial_k G_{lm}(\mathbf{R}) = 0 . \quad (\text{A.13})$$

A.2 Construction of coupled surface integral equations for displacement and surface-traction fields in piecewise homogeneous media

Surface integral equations or boundary integral equations (BIEs) are applicable to piecewise homogeneous materials, and provide solutions for the displacement and traction fields defined on interfaces S_{mn} separating different material regions Ω_m (Fig. 13). One of these regions, Ω_0 , is the unbounded background medium (air). Fields in the individual regions are described in terms of the appropriate Green functions for elastic materials. The displacement and traction fields are assumed to be continuous across the interfaces (i.e., to satisfy transmission boundary conditions).

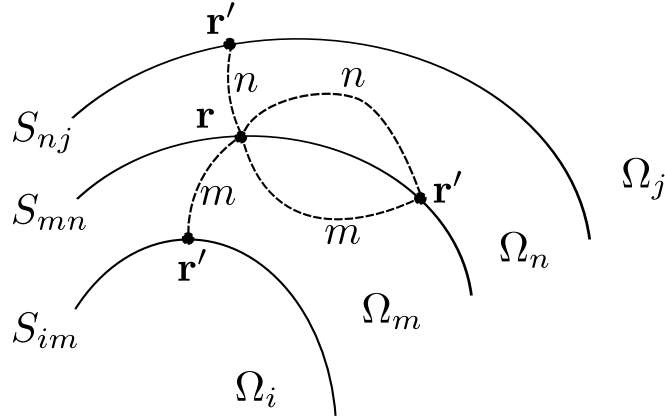


Figure 13: A schematic representation of regions Ω and interfaces S appearing in surface integral equations .

As an example, we give below explicit expressions for two alternative systems of surface integral equations describing for the above transmission problem. Such systems can be then obtained in the following three steps:

- (a) using a conventional representation theorem (found, e.g., in Ref. [4]) for each material region Ω for the displacement field in this region written in terms of the surface integrals over $\partial\Omega$ with displacement and traction fields, $\mathbf{u}(\mathbf{r})$ and $\mathbf{t}(\mathbf{r}) = \mathbf{n}(\mathbf{r}) \cdot \hat{\tau}(\mathbf{r})$, playing the role of surface sources,

$$\mathbf{u}(\mathbf{x}) = \int_{\partial\Omega} d^2y [\Gamma_m^T(\mathbf{x}, \mathbf{y}) \cdot \mathbf{u}(\mathbf{y}) + G_m^T(\mathbf{x}, \mathbf{y}) \cdot \mathbf{t}(\mathbf{y})] ; \quad (\text{A.14})$$

- (b) imposing continuity boundary conditions on the $\mathbf{u}(\mathbf{r})$ and $\mathbf{t}(\mathbf{r})$ values on each interface (oriented surface) S_{mn} separating the regions Ω_m (on the negative side of the interface) and Ω_n (on its positive side),

$$\mathbf{u}_m(\mathbf{r}) = \mathbf{u}_n(\mathbf{r}) , \quad (\text{A.15a})$$

$$\mathbf{t}_m(\mathbf{r}) = \mathbf{t}_n(\mathbf{r}) ; \quad (\text{A.15b})$$

and

- (c) writing two suitable equations following from the boundary conditions for each interface S_{mn} .

The choice of the integral equations is not unique. It is possible to form several different sets of integral equations by taking different linear combinations of equations representing the boundary conditions (A.15). While all such integral equations are theoretically equivalent, they tend to differ in terms of accuracy, computational resources needed, and solution convergence. We considered two representative choices marked below as (i) and (ii) and, after examining them, we decided to choose the second, non-conventional, integral equation set.

The set (i) of integral equations are obtained by imposing, on each interface S_{mn} , the transmission conditions on the displacements only (Eq. (A.15b)), but expressing them by means of the two representation formulae, Eq. (A.14) and its counterpart for the other region, Ω_n , adjacent to the interface. The resulting system of six equations for six unknown components of $\mathbf{u}(\mathbf{x})$ and $\mathbf{t}(\mathbf{x})$ is

$$\begin{aligned} & \frac{1}{2} \mathbf{u}(\mathbf{x}) + \int_{S_{mn}} d^2y [\Gamma_m^T(\mathbf{x}, \mathbf{y}) \cdot \mathbf{u}(\mathbf{y}) + G_m^T(\mathbf{x}, \mathbf{y}) \cdot \mathbf{t}(\mathbf{y})] \\ & - \sum_{\substack{S_{im} \in \partial\Omega_m \\ i \neq n}} \int_{S_{im}} d^2y [\Gamma_m^T(\mathbf{x}, \mathbf{y}) \cdot \mathbf{u}(\mathbf{y}) + G_m^T(\mathbf{x}, \mathbf{y}) \cdot \mathbf{t}(\mathbf{y})] = \delta_{m0} \mathbf{u}^{\text{in}}(\mathbf{x}) \quad \text{for } \mathbf{x} \in S_{mn} \text{ (i-a) ,} \end{aligned} \quad (\text{A.16a})$$

$$\begin{aligned} & \frac{1}{2} \mathbf{u}(\mathbf{x}) - \int_{S_{mn}} d^2y [\Gamma_n^T(\mathbf{x}, \mathbf{y}) \cdot \mathbf{u}(\mathbf{y}) + G_n^T(\mathbf{x}, \mathbf{y}) \cdot \mathbf{t}(\mathbf{y})] \\ & + \sum_{\substack{S_{nj} \in \partial\Omega_n \\ j \neq m}} \int_{S_{nj}} d^2y [\Gamma_n^T(\mathbf{x}, \mathbf{y}) \cdot \mathbf{u}(\mathbf{y}) + G_n^T(\mathbf{x}, \mathbf{y}) \cdot \mathbf{t}(\mathbf{y})] = \delta_{n0} \mathbf{u}^{\text{in}}(\mathbf{x}) \quad \text{for } \mathbf{x} \in S_{mn} \text{ (i-b) .} \end{aligned} \quad (\text{A.16b})$$

With reference to Fig. 13, the first of the above integral equations represents contributions to the displacement field \mathbf{u} on the interface S_{mn} due to the displacement and traction fields \mathbf{u} and \mathbf{t} on the same interface (the first integral) and on remaining interfaces, S_{im} , forming boundaries of the region Ω_m with other regions Ω_i , $i \neq n$; and similarly for the second equation, which represents contributions of the boundaries of the region Ω_n . The r.h.s.s of the above equations are the incident fields due to distant sources in the region Ω_0 , hence the delta-functions δ_{m0} and δ_{n0} .

We obtain the second, alternative, set (ii) of the integral equations by imposing the boundary conditions (A.15) on *both* the displacement and traction fields. We again express the displacements \mathbf{u} by means of the representation formula (A.14) and its Ω_n counterpart. For the traction fields \mathbf{t} we use the same representation formulae to which we apply the traction field operator $\mathbf{n}(\mathbf{x}) \cdot \hat{\tau}[\mathbf{u}(\mathbf{x})]$. The resulting system (ii) of six equations for six unknown components of $\mathbf{u}(\mathbf{x})$ and $\mathbf{t}(\mathbf{x})$ is now

$$\begin{aligned}
& \int_{S_{mn}} d^2y \{ [\Gamma_m^T(\mathbf{x}, \mathbf{y}) + \Gamma_n^T(\mathbf{x}, \mathbf{y})] \cdot \mathbf{u}(\mathbf{y}) + [G_m^T(\mathbf{x}, \mathbf{y}) + G_n^T(\mathbf{x}, \mathbf{y})] \cdot \mathbf{t}(\mathbf{y}) \} \\
& - \sum_{\substack{S_{im} \in \partial\Omega_m \\ i \neq n}} \int_{S_{im}} d^2y \{ \Gamma_m^T(\mathbf{x}, \mathbf{y}) \cdot \mathbf{u}(\mathbf{y}) + G_m^T(\mathbf{x}, \mathbf{y}) \cdot \mathbf{t}(\mathbf{y}) \} \\
& - \sum_{\substack{S_{nj} \in \partial\Omega_n \\ j \neq m}} \int_{S_{nj}} d^2y \{ \Gamma_n^T(\mathbf{x}, \mathbf{y}) \cdot \mathbf{u}(\mathbf{y}) + G_n^T(\mathbf{x}, \mathbf{y}) \cdot \mathbf{t}(\mathbf{y}) \} \\
& = [\delta_{m0} - \delta_{n0}] \mathbf{u}^{\text{in}}(\mathbf{x}) \quad \text{for } \mathbf{x} \in S_{mn} \text{ (ii-a) ,} \\
\end{aligned} \tag{A.17a}$$

$$\begin{aligned}
& \int_{S_{mn}} d^2y \{ [W_m^T(\mathbf{x}, \mathbf{y}) + W_n^T(\mathbf{x}, \mathbf{y})] \cdot \mathbf{u}(\mathbf{y}) + [\Phi^T(\mathbf{x}, \mathbf{y}) + \Phi_n^T(\mathbf{x}, \mathbf{y})] \cdot \mathbf{t}(\mathbf{y}) \} \\
& - \sum_{\substack{S_{im} \in \partial\Omega_m \\ i \neq n}} \int_{S_{im}} d^2y \{ W_m^T(\mathbf{x}, \mathbf{y}) \cdot \mathbf{u}(\mathbf{y}) + \Phi_m^T(\mathbf{x}, \mathbf{y}) \cdot \mathbf{t}(\mathbf{y}) \} \\
& - \sum_{\substack{S_{nj} \in \partial\Omega_n \\ j \neq m}} \int_{S_{nj}} d^2y \{ W_n^T(\mathbf{x}, \mathbf{y}) \cdot \mathbf{u}(\mathbf{y}) + \Phi_n^T(\mathbf{x}, \mathbf{y}) \cdot \mathbf{t}(\mathbf{y}) \} \\
& = [\delta_{m0} - \delta_{n0}] \mathbf{t}^{\text{in}}(\mathbf{x}) \quad \text{for } \mathbf{x} \in S_{mn} \text{ (ii-b) ,} \\
\end{aligned} \tag{A.17b}$$

where, in the second equation, the boundary-operator kernels are defined by

$$\begin{aligned}
W(\mathbf{x}, \mathbf{y}) \cdot \mathbf{u}(\mathbf{y}) &= \mathbf{n}(\mathbf{x}) \cdot \hat{\tau}[\Gamma(\mathbf{x}, \mathbf{y}) \cdot \mathbf{u}(\mathbf{y})] , \\
\Phi(\mathbf{x}, \mathbf{y}) \cdot \mathbf{t}(\mathbf{y}) &= \mathbf{n}(\mathbf{x}) \cdot \hat{\tau}[G(\mathbf{x}, \mathbf{y}) \cdot \mathbf{t}(\mathbf{y})] .
\end{aligned} \tag{A.18}$$

As before, the operators with indices m and n describe propagation of the displacement and

stress fields in the regions Ω_m and Ω_n . The details of the construction and regularization of the kernels G_i, Γ_i, W_i , and Φ_i are described in a paper we are preparing for publication in JASA.

The main advantage of the set (ii) of the integral equations is that it results in higher solution accuracy at material discontinuities; it is achieved through explicit imposition of boundary conditions on the displacement *and* the traction fields, rather than by means of the weaker integral relations used in the formulation (i). We also find that the second choice, (ii), yields a better solution convergence in high contrast problems. Theoretical aspects of the differences between the two above-mentioned choices, (i) and (ii), will be more fully investigated in the near future.

A.3 Matrix compression

The underlying element of our approach is the Fast Fourier Transform (FFT)-based AIM matrix compression method, initially developed in the context of electromagnetics for solving large-scale problems, and described in detail in Ref. [5]. Adaptation of this formulation to large-scale acoustic problems [1, 2] was the initial step of our effort.

The main reason for choosing the FFT-based compression method, rather than other compression techniques, is that it provides superior efficiency in the treatment of both volumetric and surface integral equations, particularly for sub-wavelength problems (geometrical elements used in objects' discretizations – triangular facets and tetrahedrons – are much smaller than the wavelength). We note that sub-wavelength geometry regions constitute dominant portion of anatomically realistic head geometry models.

B Draft of the paper

“Integral-equation solver for investigation of acoustic energy flow in the human head”

E. Bleszynski, M. Bleszynski, and T. Jaroszewicz
Monopole Research, Thousand Oaks, CA 91360

Abstract

We describe selected aspects of the development and applications of integral equation based solver designed for large scale numerical simulation of interaction of sound waves with complex heterogeneous media. A particular application we are concerned with is modeling of the propagation of the waves inside the human head subject to a pressure wave in the surrounding air; the goal of this investigation is to estimate the amount of energy transferred to the inner ear by air- and bone-conduction mechanisms. The considered problem is characterized by a high density contrast (biological tissues vs. air), which causes the dominant part of the incident energy to be reflected, and makes the computation of the penetrating energy flux rather nontrivial. In our previous work we developed and employed a computational model based on volumetric integral-equations of acoustic/elasticity, with the object modeled by means of a tetrahedral mesh. Since in this formulation the equations were only providing the pressure (or displacement) distribution, computation of the energy flux required numerical (finite-difference) evaluation of the normal derivative of the pressure (or the traction), which we did not find sufficiently reliable, especially in the geometrically complex region of the model near the inner ear. The present formulation is based on surface integral equations, which provide simultaneously solutions for the pressure and its normal derivative (or for the displacement and the traction). The equations are discretized in terms of piecewise-constant and piecewise-linear basis functions supported on facets of a triangulated surface model representing the human head including the skull, the soft tissues, and the geometrical details of the middle and inner ear. The resulting stiffness matrix is compressed by means of the Fast Fourier Transform (FFT)-based algorithm, implemented in distributed-memory parallel processing environment, which allows handling of problems involving several million unknowns. Particular attention was paid to the appropriate choice of the compression parameters in the practically available anatomical models characterized by large differences of the mesh densities. We also present results employing several alternative integral-equation formulations of the multi-region transmission problem, giving rise to either first- or second-kind equations, with different conditioning properties. In this context we analyzed some pertinent preconditioning techniques, including a Calderón-type preconditioner for the first-kind and an additive-type preconditioner for the second-kind equations in the high-contrast problems.

B.1 Introduction

The purpose of this work is to analyze some aspects of wave propagation and the resulting energy flow in a human head subject to an incident acoustic wave propagating in the surrounding air. This analysis is carried with the goal of estimating the amounts of energy reaching the inner ear, due to various sound wave conduction mechanisms. In the following we briefly discuss difficulties arising in this investigation and the solutions implemented in our work.

Mechanisms of energy transport in the human head. It is known that the normal airborne mechanism of acoustic energy transfer to the cochlea – through the outer auditory canal, the tympanic membrane, and the middle-ear system of ossicles – is not the only one in operation. Alternative energy flow paths, in particular due to bone conduction, are being utilized in, e.g., in hearing-enhancement devices. The same mechanisms, however, can also transfer to the inner ear the energy due to an intense noise; since those pathways circumvent the usual airborne sound transmission channel, they may potentially cause inner ear damage in spite of application of conventional protective devices, such as ear plugs.

Significance of high medium contrasts in evaluation of energy transfer. A characteristic feature of the considered problem of acoustic wave propagation is a very high density contrast (density ratio of the order of 1000) between the biological tissues and the surrounding air; at the same time, the refractive indices of those media differ by only a modest factor of at most 5. The high density contrast causes a large impedance mismatch and greatly reduces the energy transfer through the air-tissue interface. This circumstance is the reason why the ear structure of animals living in the atmosphere evolved to form an exceedingly sensitive impedance-matching mechanism consisting of the tympanic membrane and the middle-ear system.

In this context, we note that the area of acoustics and elasticity we are concerned with – high-density objects subject to waves incident from the surrounding low-density medium – has been relatively little explored. For instance,

- Marine applications involve interaction of waves in water with denser materials (metallic objects, rock), but the density contrast is much lower than in our case; e.g., steel-to-water density ratio is about 8.
- In geophysical (seismic) applications the object of interest (the Earth) is surrounded by air, but wave propagation through the atmosphere is not being considered at all.
- Mechanical engineering problems often involve interaction of vibrating structures with air; however, it is the vibrating structure (e.g., a body of a vehicle) which is the source of sound waves, and the effect of the acoustic waves on that structure is negligible.
- Finally, relatively little theoretical work has been done on transmission problems involving high-contrast media.

Computational aspects. In view of the high density contrasts and the the resulting impedance mismatch, reliable computation of the amount of energy reaching the inner ear becomes a *highly demanding task*. This energy is relatively small and its value depends on the energy flux through the high-contrast air-tissue interface (including effects of many air cavities present in the head). The energy flux, in turn, is proportional to the product of two physical quantities on the outer side of the interface: the pressure p and its normal derivative $\partial p/\partial n$ (the latter quantity is, essentially, the normal component of the velocity of the medium). Because of the large density contrast, the problem of the tissue-air interface is nearly that of the hard surface: the value of p on the surface is roughly of the same magnitude as the pressure in the surrounding air, but the normal derivative $\partial p/\partial n$ is much smaller than in the surrounding

space, and its evaluation is not entirely straightforward. In addition, $\partial p / \partial n$ has to be known to a sufficient accuracy, since the relative energy flux value is linear in that quantity and the same is true for the error in the energy flux.

Past and present approaches. In our previous analysis [1, 2] we developed and implemented an approach based on a *volumetric* integral equation for an inhomogeneous material. Because of the high-contrast nature of the considered problems, that approach required, effectively, introducing *surface* distributions of the pressure and velocity fields associated with high-contrast interfaces.

In this work we extended the surface-related elements of our previous approach to a full surface-equation formulation for a problem involving multiple piecewise-homogeneous material regions *and* high-contrast interfaces. An additional motivation for this development was availability of detailed *surface* geometry data for the middle and inner ear structures: While moderate-resolution voxel-type data are readily accessible for entire human bodies (e.g., [6]), this is not the case for the more detailed skull and inner ear regions. Furthermore, a practical obstacle in utilizing voxel data is the necessity of “segmentation”, i.e., identification of tissue types – a difficult and time-consuming process that can be only partly automated. At the same time, more precise middle- and inner-ear data based on micro-magnetic-resonance imaging are typically available in the form of reconstructed interfaces between tissues.

Further, having implemented both volume and surface solution methods, we now envisage a comprehensive approach combining them into a full solvers based on a system of mutually coupled equations. It could be, in particular, applied to models consisting of both volumetric regions (with a relatively “coarse” discretization of one or few millimeters) and of detailed interfaces discretized with sub-millimeter resolution. In fact, in the surface geometries we have been using in the computations reported here, triangle sizes span two order of magnitude, from about 5 mm to 0.05 mm = 50 μ m.

Contents of the paper. The paper is organized as follows: In Section B.2 we present an integral-equation formulation applicable to two types of multi-domain problems which involve either a collection of piecewise homogeneous material domains or a collection of both piecewise homogeneous and inhomogeneous domains. In Section B.3 we discuss some aspects of discretization of the equations, in particular in the presence of junctions of several interfaces. We also describe some basic elements of the FFT-based matrix compression and matrix-vector product acceleration, which allow us to solve large scale problems. In Section B.5 we present results of representative numerical simulations for a geometry consisting of a human head containing a detailed geometry representation of the outer, middle, and inner ear. Results of such simulations may provide an insight into physics of sound wave propagation and energy flow to cochlea cavity obtained with nontrivial geometries of a realistic human head model and demonstrate the present capabilities of our solver.

B.2 Integral equations for the multi-region transmission problem in acoustics

Simulating sound propagation in an anatomically realistic model of the human head requires modeling of topologically complex structure of material regions and interfaces. The driving

physical mechanism controlling the energy flow through the model is the variation of densities between the material regions (modeled as homogeneous domains). Therefore, in order to obtain a reliable prediction for the energy transfer across the interfaces it is necessary to accurately discretize the pressure and its normal derivative on complicated surface geometries. The surfaces may be nested inside one another, a number of surfaces may be enclosed in another one, and several surfaces may form a “junction”, i.e., share a common boundary line or a boundary point (such structures are sometimes referred to as “triple-points” or “multiple points” [7]). Some of that complexity of the set of surfaces may also be introduced for convenience of geometry modeling (e.g., a complex surface may be built of a number of simpler patches).

A representative geometry structure of our interest is depicted schematically in Fig. 56. It involves a number of soft tissues, brain, and the skull with air cavities. The interfaces between various materials form a number of junctions, which, in this case, are common boundaries of triplets of interfaces.

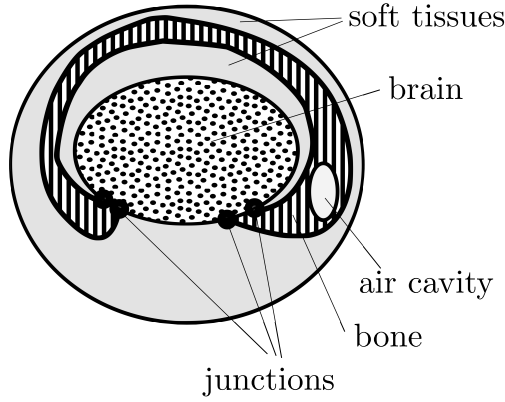


Figure 14: A simplified schematics of the topological structure of regions and interfaces in head model.

Since we are primarily interested in computing the energy flow, it is convenient to use as the unknowns the fields appearing in the expression for the energy flux (Eq. (B.4)): the pressure p and its normal derivative $\partial_n p$ (which we call, for simplicity, the velocity field). We obtain the surface integral equations in the following steps:

- We write the representation formulae for the *pressure fields* p on boundaries of material region Ω_m , in terms of the values of p and $\partial_n p$ on the same region boundaries.
- Write the representation formulae for the *velocity field* $\partial_n p$ of the boundaries $\partial\Omega_m$, again in terms of the boundary values of p and $\partial_n p$. This representation formula is obtained by taking the normal derivative of the previous formula.
- We impose boundary conditions (Eq. (B.1)) on the boundaries (i.e., region-region interfaces). These conditions relate both field p and $\partial_n p$ being represented by the integrals of the representation formulae and the quantities appearing in the integrands.

- We form appropriate linear combinations of the representation formulae. Here we may choose to use representation formulae for both p and $\partial_n p$, and obtain in this way first-kind (elliptic) equations; or we may utilize only the representation formulae for the pressure and obtain second-kind equations. In both cases the unknowns in the equations are the quantities appearing in the integrands of the representation formulae, i.e., the boundary values of p and $\partial_n p$.

B.2.1 Differential equations of acoustics and boundary conditions

In this section we briefly summarize here the differential equations governing acoustic fields, which will be used to obtain the integral equations described in Section B.2. We consider a bounded spatial domain Ω filled with a material characterized by (generally) position-dependent density and compressibility $\rho(\mathbf{r})$ and $\kappa(\mathbf{r})$. The surrounding unbounded “outer region” Ω_0 is assumed to be homogeneous and described by the “background” parameters ρ_0 and κ_0 . Correspondingly, in a time-harmonic problem with frequency ω the wave number in the background medium is $k_0 := \sqrt{\rho_0 \kappa_0} \omega$. The Euler equation for the pressure field $p(\mathbf{r})$ (known, in this form, as the Bergmann equation [8, 4]) is

$$\frac{\rho(\mathbf{r})}{\rho_0} \nabla \cdot \left(\frac{\rho_0}{\rho(\mathbf{r})} \nabla p(\mathbf{r}) \right) + k_0^2 \frac{\rho(\mathbf{r}) \kappa(\mathbf{r})}{\rho_0 \kappa_0} p(\mathbf{r}) = 0. \quad (\text{B.1})$$

Equation (B.1) for an inhomogeneous object can be solved as the volumetric Lippmann-Schwinger integral equation. We followed this venue in our previous work [1, 2], where we developed efficient numerical techniques for handling of situations relevant in the considered applications, i.e., discontinuous material parameters [9] and high-contrast interfaces.

The general result following from our previous investigations was that the energy flow through the object was essentially smooth even in inhomogeneous regions, as long as the material density was varying in a range typical of biological tissues (about a factor of two); however, the energy flux through high-contrast interfaces was strongly dependent on the *shape* and *geometrical details of the interface*.

Since the behavior of the energy flux is of main interest in the present application, we concentrate here on a *surface* form of the integral equations, assuming the object is modeled as a piecewise-homogeneous structure, such that in each homogeneous sub-region Ω_m described by the parameters (ρ_m, κ_m) the pressure field p_m satisfies the Helmholtz equation

$$(\nabla^2 + k_m^2) p(\mathbf{r}) = 0 \quad \text{for } \mathbf{r} \in \Omega_m. \quad (\text{B.2})$$

with the wave number $k_m := \sqrt{\rho_m \kappa_m} \omega$. The original equation (B.1) implies then the *transmission boundary conditions* on the interfaces of regions,

$$p(\mathbf{r}) \quad \text{and} \quad \frac{\rho_0}{\rho(\mathbf{r})} \frac{\partial p(\mathbf{r})}{\partial n(\mathbf{r})} := \frac{\rho_0}{\rho(\mathbf{r})} \mathbf{n}(\mathbf{r}) \cdot \nabla p(\mathbf{r}) \quad \text{continuous across the interface ;} \quad (\text{B.3})$$

here and below \mathbf{n} is the unit normal to the interface, and normal derivatives are denoted with ∂_n .

B.2.2 Surface integral equations for $p(\mathbf{r})$ and $\partial p(\mathbf{r})/\partial n(\mathbf{r})$ for a single material body

In this Section we present a brief derivation of the surface integral equations for a problem involving a single material region. The two unknown functions appearing in such integral equations are chosen to be as pressure $p(\mathbf{r})$ and the normal derivative of pressure defined on material interfaces.

We recount here the known basic forms of the surface integral equations for the transmission problem involving only a single body occupying a domain Ω_m (Fig. 15).

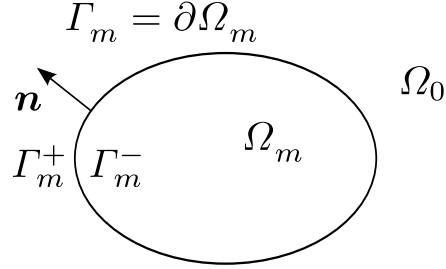


Figure 15: The simplest transmission problem with a single material region Ω_m . The boundary Γ_m is *oriented* according to the direction of the normal, and Γ_m^\pm are its “positive” and “negative” sides.

While there is some freedom in choosing the unknown quantities in integral-equation formulations, we opted for equations obtained by means of a *direct method*, in which the unknowns are the values of the physical quantities – the pressure and its normal derivative (i.e., velocity) on the surfaces. An advantage of such a form of integral equations is that the unknown fields appear directly in the expression for the density of the energy flux through a surface,

$$F(\mathbf{r}) := -\frac{\rho_0}{k_0 \rho} \text{Im} \{ p^*(\mathbf{r}) \partial_n p(\mathbf{r}) \} ; \quad (\text{B.4})$$

this quantity is normalized to be unity for a unit-amplitude plane pressure wave incident normally on the surface, and, in view of the boundary conditions (B.2), is continuous across the interfaces.

It is convenient to use in this formulation not directly the normal derivatives of the pressure field, but rather those derivatives divided by the density of the medium. More precisely, for a region Ω_m and its boundary $\partial\Omega_m$, we to define the boundary fields

$$q(\mathbf{r}) := \frac{\rho_0}{\rho_m} \frac{\partial p(\mathbf{r})}{\partial n(\mathbf{r})} \quad (\text{B.5})$$

for \mathbf{r} approaching the boundary from inside Ω_m . According to the boundary conditions (B.3), those fields are simply continuous across the interfaces. As a result, the energy flux density (B.4) through any interface can be expressed in terms of fields p and q as

$$F(\mathbf{r}) := -\frac{\lambda}{2\pi} \text{Im} \{ p^*(\mathbf{r}) q(\mathbf{r}) \} , \quad (\text{B.6})$$

where $\lambda := 2\pi/k_0$ is the wavelength in the background medium.

Our equations are obtained by means of the “direct method”, i.e., from the representation formulae (essentially Green’s second identities) applied to boundary values of the fields in all material regions. Such a formula for a field p satisfying Eq.(B.2) in a region Ω_m is

$$\begin{aligned} & \int_{\partial\Omega_m} d^2r' \left[\frac{\partial g_m(\mathbf{r} - \mathbf{r}')}{\partial n(\mathbf{r}')} p(\mathbf{r}') - \frac{\rho_m}{\rho_0} g_m(\mathbf{r} - \mathbf{r}') q(\mathbf{r}') \right] \\ & \equiv \int_{\partial\Omega_m} d^2r' [\partial'_n g_m(\mathbf{r} - \mathbf{r}') p(\mathbf{r}') - \hat{g}_m(\mathbf{r} - \mathbf{r}') q(\mathbf{r}')] = \begin{cases} -p(\mathbf{r}) & \text{for } \mathbf{r} \in \Omega_m, \\ 0 & \text{for } \mathbf{r} \notin \Omega_m, \end{cases} \end{aligned} \quad (\text{B.7})$$

where the derivatives are taken along the normal *exterior* to Ω_m (as in Fig. 15), p and q in the integrand are the boundary values of the fields, and

$$g_m(\mathbf{r}) = \frac{e^{ik_m r}}{4\pi r} \quad (\text{B.8})$$

is the Green function of the Helmholtz equation in the region Ω .

While the formula (B.7) holds in the entire space, integral equations relate boundary values of the fields. They can be expressed in terms of the single- and double-layer boundary operators, belonging to the standard set of operators:

$$(V_m \phi)(\mathbf{r}) := \frac{\rho_m}{\rho_0} \int_{\Gamma_m} d^2r' g_m(\mathbf{r} - \mathbf{r}') \phi(\mathbf{r}') \quad (\text{single-layer}), \quad (\text{B.9a})$$

$$(K_m \phi)(\mathbf{r}) := \int_{\Gamma_m} d^2r' \frac{\partial g_m(\mathbf{r} - \mathbf{r}')}{\partial n(\mathbf{r}')} \phi(\mathbf{r}') \quad (\text{double-layer}), \quad (\text{B.9b})$$

$$(K'_m \phi)(\mathbf{r}) := \int_{\Gamma_m} d^2r' \frac{\partial g_m(\mathbf{r} - \mathbf{r}')}{\partial n(\mathbf{r})} \phi(\mathbf{r}') \quad (\text{adjoint double-layer}), \quad (\text{B.9c})$$

$$(W_m \phi)(\mathbf{r}) := -\frac{\rho_0}{\rho_m} \frac{\partial}{\partial n(\mathbf{r})} \int_{\Gamma_m} d^2r' \frac{\partial g_m(\mathbf{r} - \mathbf{r}')}{\partial n(\mathbf{r}')} \phi(\mathbf{r}') \quad (\text{hyper-singular}) \quad (\text{B.9d})$$

(our definition does not include the factor “2” appearing in some references (e.g., in [10]).

[we do not enter into a rigorous discussion of the conditions under which the representation formulae are valid, including the question of the functional spaces of the sources and fields – this is a complex subject; we only mention that most of the results in the following hold not only for smooth surfaces, but also for Lipschitz-continuous surfaces, hence, in particular, for polyhedral domain boundaries commonly assumed in practical applications

In the notation of Fig. 15, the boundary values of the integrals in the representation formula (B.7) are now

$$\int_{\Gamma_m} d^2r' \partial'_n g_m(\mathbf{r} - \mathbf{r}') p(\mathbf{r}') = (K_m p)(\mathbf{r}) \pm \frac{1}{2} p(\mathbf{r}) \quad \text{for } \mathbf{r} \rightarrow \Gamma_m^\pm \quad (\text{B.10a})$$

and

$$\int_{\Gamma_m} d^2r' g_m(\mathbf{r} - \mathbf{r}') q(\mathbf{r}') = (V_m p)(\mathbf{r}) \quad \text{for } \mathbf{r} \rightarrow \Gamma_m^\pm. \quad (\text{B.10b})$$

Hence, for the observation point approaching the boundary from either side, the representation formula (B.7) yields the relation

$$\frac{1}{2} p = -K_m p + V_m q . \quad (\text{B.11})$$

By multiplying the above equality by ρ_0/ρ_m , taking its normal derivative, and using $K'_m = (\rho_0/\rho_m) \partial_n V_m$ and $W'_m = -(\rho_0/\rho_m) \partial_n K_m$, we find another relation,

$$\frac{1}{2} q = W_m p + K'_m q . \quad (\text{B.12})$$

Analogous relations are obtained for the exterior region Ω_0 , where the representation formula includes also the incident fields (asymptotic field values on the “boundary” of Ω_0 at infinity). The resulting set of four relations is then

$$W_0 p + \left(\frac{1}{2} I + K'_0\right) q = q^{(\text{inc})} , \quad (\text{B.13a})$$

$$\left(\frac{1}{2} I - K_0\right) p + V_0 q = p^{(\text{inc})} , \quad (\text{B.13b})$$

$$-W_m p + \left(\frac{1}{2} I - K'_m\right) q = 0 , \quad (\text{B.13c})$$

$$\left(\frac{1}{2} I + K_m\right) p - V_m q = 0 . \quad (\text{B.13d})$$

By taking the difference of (B.13a) and (B.13c), and the difference of (B.13d) and (B.13b), one obtains the manifestly symmetric first-kind system of equations

$$\begin{bmatrix} W_0 + W_m & K'_0 + K'_m \\ K_0 + K_m & -V_0 - V_m \end{bmatrix} \begin{bmatrix} p \\ q \end{bmatrix} = \begin{bmatrix} q^{(\text{inc})} \\ -p^{(\text{inc})} \end{bmatrix} , \quad (\text{B.14})$$

which can be proven to be strongly elliptic [11]. Similarly, by taking just equations (B.13b) and (B.13d), one finds the “simple equations” for the transmission problem [12, 13, 14, 15],

$$\begin{bmatrix} \frac{1}{2} I - K_0 & V_0 \\ \frac{1}{2} I + K_m & -V_m \end{bmatrix} \begin{bmatrix} p \\ q \end{bmatrix} = \begin{bmatrix} p^{(\text{inc})} \\ 0 \end{bmatrix} . \quad (\text{B.15})$$

Further, taking the sum and the difference of the above equations, results in the set of equations

$$\begin{bmatrix} I - K_0 + K_m & V_0 - V_m \\ -K_0 - K_m & V_0 + V_m \end{bmatrix} \begin{bmatrix} p \\ q \end{bmatrix} = \begin{bmatrix} p^{(\text{inc})} \\ 0 \end{bmatrix} , \quad (\text{B.16})$$

which, due to the appearance of the identity operator in one of the diagonal blocks, can be considered a second-kind system.

B.2.3 Surface integral equations for $p(\mathbf{r})$ and $\partial p(\mathbf{r})/\partial n(\mathbf{r})$ for multiple regions and interfaces

In this Section we present a brief derivation of the surface integral equation formulation for problems involving multiple material regions. The two unknown functions appearing in such integral equations are chosen to be the pressure $p(\mathbf{r})$ and its normal derivative, both defined on defined on material interfaces.

Although we have obtained such equation in both first- and second-kind formulations, we discuss here, for definiteness, the system of *second-kind* integral equations – a generalization of the system of equations (B.16).

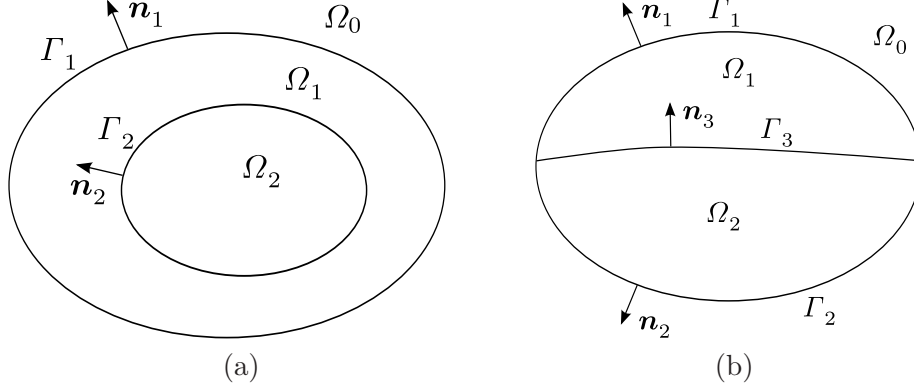


Figure 16: Examples of simplest multi-region geometries: nested regions (a) and adjacent regions with a triple-interface junction (b).

In a multi-region transmission problem we consider regions Ω_m and *oriented* interfaces Γ_i with normals pointing from their negative to the positive sides. We introduce “orientation factors” $\sigma_{im} = \pm 1$, defined such that

$$\sigma_{im} = \begin{cases} +1 & \text{if } \Omega_m \text{ is adjacent to the positive side of } \Gamma_i, \\ -1 & \text{if } \Omega_m \text{ is adjacent to the negative side of } \Gamma_i, \\ 0 & \text{otherwise.} \end{cases} \quad (\text{B.17})$$

In this notation, the relations (B.13b) and (B.13d) generalize to

$$\sum_j \left(\frac{1}{2} \delta_{ij} p_j - \sigma_{jm} K_m p_j + \sigma_{jm} V_m q_j \right) = \delta_{m0} p_i^{(\text{inc})} \quad (\text{B.18})$$

for any interface Γ_i belonging to the boundary $\partial\Omega_m$, and for any orientations of interfaces. By considering the other region adjacent to Γ_i , say Ω_n , we obtain the analogous relation

$$\sum_k \left(\frac{1}{2} \delta_{ik} p_k - \sigma_{kn} K_n p_k + \sigma_{kn} V_n q_k \right) = \delta_{n0} p_i^{(\text{inc})}, \quad (\text{B.19})$$

where the sum is taken over interfaces Γ_k forming the boundary of Ω_n (Fig. 54).

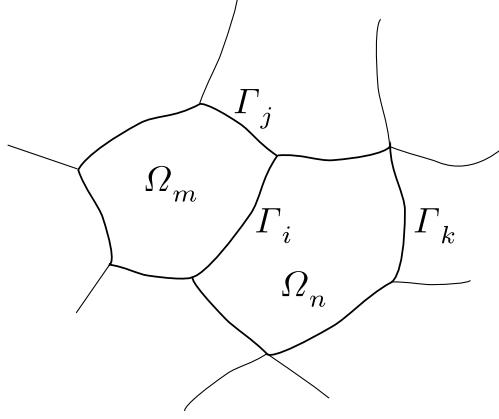


Figure 17: An interface Γ_i and the two adjacent regions with their boundaries.

In the matrix form, the system (B.18) and (B.19) can be represented as

$$\begin{aligned} & \begin{bmatrix} \frac{1}{2}I - \sigma_{im}K_m & \sigma_{im}V_m \\ \frac{1}{2}I - \sigma_{in}K_n & \sigma_{in}V_n \end{bmatrix} \begin{bmatrix} p_i \\ q_i \end{bmatrix} \\ & + \sum_{j \neq i} \begin{bmatrix} -\sigma_{jm}K_m & \sigma_{jm}V_m \\ 0 & 0 \end{bmatrix} \begin{bmatrix} p_j \\ q_j \end{bmatrix} + \sum_{k \neq i} \begin{bmatrix} 0 & 0 \\ -\sigma_{kn}K_n & \sigma_{kn}V_n \end{bmatrix} \begin{bmatrix} p_k \\ q_k \end{bmatrix} = \begin{bmatrix} \delta_{m0}p_i^{(\text{inc})} \\ \delta_{n0}p_i^{(\text{inc})} \end{bmatrix}. \end{aligned} \quad (\text{B.20})$$

By taking the sum of the first and second rows of these equations and the sum of the rows multiplied by σ_{im} and σ_{in} , and by rearranging the terms, we obtain, for each interface Γ_i , a system of equations of the form

$$\sum_j A_{ij} \begin{bmatrix} p_j \\ q_j \end{bmatrix} = \begin{bmatrix} \sigma_{i0}^2 p_i^{(\text{inc})} \\ \sigma_{i0} p_i^{(\text{inc})} \end{bmatrix}, \quad (\text{B.21})$$

where the blocks of operators are given by

$$A_{ij} = \delta_{ij} \begin{bmatrix} I & 0 \\ 0 & 0 \end{bmatrix} + \sum_m \begin{bmatrix} -\sigma_{jm}K_m & \sigma_{jm}V_m \\ -\sigma_{im}\sigma_{jm}K_m & \sigma_{im}\sigma_{jm}V_m \end{bmatrix}, \quad (\text{B.22})$$

where the sum runs over all regions Ω_m shared by both the interfaces Γ_i and Γ_j . In the case of a single material domain, the system (B.21) reduces to the sum-and-difference equations (B.16).

B.2.4 Scaling of matrix blocks for high-contrast problems

In high density-contrast problems equations (B.16) and their multi-region generalization (B.21) exhibit unfavorable conditioning properties: Since the single-layer operators V_m (Eq. (B.9a))

are proportional to the factors $\rho_m/\rho_0 \gg 1$ (for $m \neq 0$), the operators V_m dominate V_0 (wherever the latter appear) and all blocks involving single-layer operators are proportional to large density ratios. For instance, at low frequencies, the block of operators in the system (B.16) becomes

$$\begin{bmatrix} I - K_0 + K_m & V_0 - V_m \\ -K_0 - K_m & V_0 + V_m \end{bmatrix} \approx \begin{bmatrix} I & -V_m \\ -2K_0 & V_m \end{bmatrix}; \quad (\text{B.23})$$

we used here the fact that, for an object much smaller than the wavelength, there is little difference between the operators K_0 and K_m (provided the refraction indices of the media are similar, which we always assume). Hence, for a high density contrast, there is an imbalance between the operator blocks and the condition number of the system increases by a factor of order ρ_m/ρ_0 .

A simple way of improving the conditioning of the system is to multiply all the matrix blocks involving the single-layer operators by a small factor ξ of order ρ_0/ρ_m , solve the modified system, and finally multiply the q blocks of the solution by the same factor ξ . For instance, after solving the rescaled system (B.16),

$$\begin{bmatrix} I - K_0 + K_m & \xi(V_0 - V_m) \\ -K_0 - K_m & \xi(V_0 + V_m) \end{bmatrix} \begin{bmatrix} p \\ \hat{q} \end{bmatrix} = \begin{bmatrix} p^{(\text{inc})} \\ 0 \end{bmatrix}, \quad (\text{B.24})$$

the actual solution is obtained as $q = \xi \hat{q}$.

As we discuss in Section B.5.1, the above preconditioning procedure improves very significantly the convergence of the iterative solution. More importantly, for low frequencies and larger contrasts ($\rho_m/\rho_0 \gtrsim 100$), preconditioning is necessary in order to obtain the correct solution of the system, unless one is prepared to carry out a large number of iterations to reach relative residual values of order 10^{-6} or so; and even in that case the quality of the solution is questionable.

B.2.5 Coupled volume and surface equations for partly inhomogeneous objects

We present here a formulation of a system of integral equations describing an object consisting of both homogeneous and inhomogeneous regions; this type of a problem is illustrated with two examples:

A homogeneous inclusion in an inhomogeneous object. We consider an *inhomogeneous* region Ω embedded in background-space region Ω_0 and containing a *homogeneous* inclusion Ω_m (Fig. 18).

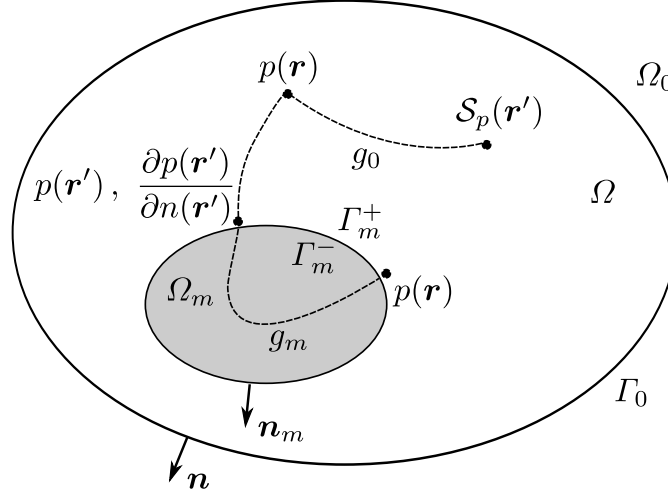


Figure 18: An inhomogeneous region Ω with a homogeneous inclusion Ω_m . Symbols Γ_0^\pm and Γ_m^\pm in the text refer to positive and negative sides of the interfaces, according to the directions of the normals.

In the region $\mathbb{R}^3 \setminus \overline{\Omega_m}$ the Euler equation satisfied by the pressure p can be written in an equivalent form

$$\begin{aligned} & (\nabla^2 + k_0^2) p(\mathbf{r}) - k_0^2 \left(1 - \frac{\kappa(\mathbf{r})}{\kappa_0}\right) p(\mathbf{r}) - \nabla \cdot \left[\left(1 - \frac{\rho_0}{\rho(\mathbf{r})}\right) \nabla p(\mathbf{r}) \right] \\ & =: (\nabla^2 + k_0^2) p(\mathbf{r}) + \mathcal{S}_p(\mathbf{r}) = 0 \end{aligned} \quad (\text{B.25})$$

where the source term \mathcal{S}_p is a functional of p (dependent on p and ∇p).

It follows from Eq. (B.25) that the pressure field satisfies the representation formula

$$\begin{aligned} & \int_{\Gamma_0^-} d^2 r' \left[\frac{\partial g_0(\mathbf{r} - \mathbf{r}')}{\partial n(\mathbf{r}')} p(\mathbf{r}') - g_0(\mathbf{r} - \mathbf{r}') \frac{\partial p(\mathbf{r}')}{\partial n(\mathbf{r}')} \right] \\ & - \int_{\Gamma_m^+} d^2 r' \left[\frac{\partial g_0(\mathbf{r} - \mathbf{r}')}{\partial n(\mathbf{r}')} p(\mathbf{r}') - g_0(\mathbf{r} - \mathbf{r}') \frac{\partial p(\mathbf{r}')}{\partial n(\mathbf{r}')} \right] - \int_{\Omega} d^3 r' g_0(\mathbf{r} - \mathbf{r}') \mathcal{S}_p(\mathbf{r}') \quad (\text{B.26}) \\ & = \begin{cases} 0 & \text{for } \mathbf{r} \notin \overline{\Omega}, \\ -p(\mathbf{r}) & \text{for } \mathbf{r} \in \Omega. \end{cases} \end{aligned}$$

The two surface integrals in the above equation are due to the outer and inner parts of the boundary of Ω , $\partial\Omega = \Gamma_0 \cup \Gamma_m$ (Fig. 18). The derivatives are taken, respectively, along the normals exterior to the domains Ω and Ω_m , as also shown in Fig. 18. The field and field derivative are the limiting values reached when approaching the boundaries from the interior of the domain Ω .

In order to obtain the L-S equation in Ω we also consider the scattered field, satisfying the representation formula

$$\int_{\Gamma_0^+ \cup \Gamma_R^-} d^2 r' \left[\frac{\partial g_0(\mathbf{r} - \mathbf{r}')}{\partial n(\mathbf{r}')} p^{(\text{sc})}(\mathbf{r}') - g_0(\mathbf{r} - \mathbf{r}') \frac{\partial p^{(\text{sc})}(\mathbf{r}')}{\partial n(\mathbf{r}')} \right] = \begin{cases} p^{(\text{sc})}(\mathbf{r}) & \text{for } \mathbf{r} \in \Omega_0, \\ 0 & \text{for } \mathbf{r} \notin \overline{\Omega}_0. \end{cases} \quad (\text{B.27})$$

The normal direction in Eq. (B.27) is the same as in (B.26), i.e., exterior to the domain Ω (as shown in Fig. 18) and the fields in the integral are taken on the “interior” side of the boundary of Ω_0 bounded by a large sphere of radius R , $\partial\Omega_{0,R} = \Gamma_0 \cup \Gamma_R$. The Sommerfeld radiation condition implies that the contribution to the integral from Γ_R can be dropped.

Similarly, the solution $p(\mathbf{r})$ of the Helmholtz equation (B.2) satisfies the representation formula

$$\int_{\Gamma_m^-} d^2 r' \left[\frac{\partial g_m(\mathbf{r} - \mathbf{r}')}{\partial n(\mathbf{r}')} p(\mathbf{r}') - g_m(\mathbf{r} - \mathbf{r}') \frac{\partial p(\mathbf{r}')}{\partial n(\mathbf{r}')} \right] = \begin{cases} 0 & \text{for } \mathbf{r} \notin \overline{\Omega}_m, \\ -p(\mathbf{r}) & \text{for } \mathbf{r} \in \Omega_m, \end{cases} \quad (\text{B.28})$$

with the normal \mathbf{n}_m shown in Fig. 18 and with the Green’s function in the region Ω_m ,

$$g_m(\mathbf{r}) = \frac{e^{ik_m r}}{4\pi r}. \quad (\text{B.29})$$

The representation formula (B.28) can be obtained in the same way as (B.26) in the absence of the source term \mathcal{S} . Further, by using the boundary conditions (B.1) to relate the values and gradients of p taken on the two sides of the boundary Γ_m , we can rewrite the representation formula (B.28) as

$$\int_{\Gamma_m^+} d^2 r' \left[\frac{\partial g_m(\mathbf{r} - \mathbf{r}')}{\partial n(\mathbf{r}')} p(\mathbf{r}') - g_m(\mathbf{r} - \mathbf{r}') \frac{\rho_m}{\rho(\mathbf{r}')} \frac{\partial p(\mathbf{r}')}{\partial n(\mathbf{r}')} \right] = \begin{cases} 0 & \text{for } \mathbf{r} \notin \overline{\Omega}_m, \\ -p(\mathbf{r}) & \text{for } \mathbf{r} \in \Omega_m, \end{cases} \quad (\text{B.30})$$

where $\rho(\mathbf{r}')$, $p(\mathbf{r}')$, and $\partial_n p(\mathbf{r}')$ are the limiting values of these functions for $\Omega \ni \mathbf{r}' \rightarrow \Gamma_m$.

By considering $\mathbf{r} \in \Omega$, taking the difference of Eqs. (B.26) and (B.27), and using the relation $p - p^{(\text{sc})} = p^{(\text{inc})}$ we obtain

$$\begin{aligned} & - \int_{\Gamma_m^+} d^2 r' \left[\frac{\partial g_0(\mathbf{r} - \mathbf{r}')}{\partial n(\mathbf{r}')} p(\mathbf{r}') - g_0(\mathbf{r} - \mathbf{r}') \frac{\partial p(\mathbf{r}')}{\partial n(\mathbf{r}')} \right] - \int_{\Omega} d^3 r' g_0(\mathbf{r} - \mathbf{r}') \mathcal{S}_p(\mathbf{r}') \\ & + \int_{\Gamma_0^-} d^2 r' \left[\frac{\partial g_0(\mathbf{r} - \mathbf{r}')}{\partial n(\mathbf{r}')} p(\mathbf{r}') - g_0(\mathbf{r} - \mathbf{r}') \frac{\partial p(\mathbf{r}')}{\partial n(\mathbf{r}')} \right] \\ & - \int_{\Gamma_0^+} d^2 r' \left[\frac{\partial g_0(\mathbf{r} - \mathbf{r}')}{\partial n(\mathbf{r}')} p^{(\text{sc})}(\mathbf{r}') - g_0(\mathbf{r} - \mathbf{r}') \frac{\partial p^{(\text{sc})}(\mathbf{r}')}{\partial n(\mathbf{r}')} \right] = -p(\mathbf{r}) \quad \text{for } \mathbf{r} \in \Omega. \end{aligned} \quad (\text{B.31})$$

By using again in the last integral $p^{(\text{sc})} = p - p^{(\text{inc})}$ we find

$$\begin{aligned}
& - \int_{\Gamma_m^+} d^2 r' \left[\frac{\partial g_0(\mathbf{r} - \mathbf{r}')}{\partial n(\mathbf{r}')} p(\mathbf{r}') - g_0(\mathbf{r} - \mathbf{r}') \frac{\partial p(\mathbf{r}')}{\partial n(\mathbf{r}')} \right] - \int_{\Omega} d^3 r' g_0(\mathbf{r} - \mathbf{r}') \mathcal{S}_p(\mathbf{r}') \\
& + \left\{ \int_{\Gamma_0^-} - \int_{\Gamma_0^+} \right\} d^2 r' \left[\frac{\partial g_0(\mathbf{r} - \mathbf{r}')}{\partial n(\mathbf{r}')} p(\mathbf{r}') - g_0(\mathbf{r} - \mathbf{r}') \frac{\partial p(\mathbf{r}')}{\partial n(\mathbf{r}')} \right] \\
& + \int_{\Gamma_0^+} d^2 r' \left[\frac{\partial g_0(\mathbf{r} - \mathbf{r}')}{\partial n(\mathbf{r}')} p^{(\text{inc})}(\mathbf{r}') - g_0(\mathbf{r} - \mathbf{r}') \frac{\partial p^{(\text{inc})}(\mathbf{r}')}{\partial n(\mathbf{r}')} \right] = -p(\mathbf{r}) \quad \text{for } \mathbf{r} \in \Omega .
\end{aligned} \tag{B.32}$$

But the last integral in this expression is, by the Green's second identity, simply $-p^{(\text{inc})}(\mathbf{r})$. In the previous difference of integrals the terms proportional to p cancel, because p is continuous across Γ_0 . However, if ρ is discontinuous across the boundary, $\partial p / \partial n$ is discontinuous as well. The boundary condition (B.3) yields then

$$\begin{aligned}
& - \int_{\Gamma_m^+} d^2 r' \left[\frac{\partial g_0(\mathbf{r} - \mathbf{r}')}{\partial n(\mathbf{r}')} p(\mathbf{r}') - g_0(\mathbf{r} - \mathbf{r}') \frac{\partial p(\mathbf{r}')}{\partial n(\mathbf{r}')} \right] - \int_{\Omega} d^3 r' g_0(\mathbf{r} - \mathbf{r}') \mathcal{S}_p(\mathbf{r}') \\
& - \int_{\Gamma_0^-} d^2 r' g_0(\mathbf{r} - \mathbf{r}') \left(1 - \frac{\rho_0}{\rho(\mathbf{r}')} \right) \frac{\partial p(\mathbf{r}')}{\partial n(\mathbf{r}')} - p^{(\text{inc})}(\mathbf{r}) = -p(\mathbf{r}) \quad \text{for } \mathbf{r} \in \Omega .
\end{aligned} \tag{B.33}$$

The above expression, with the source density \mathcal{S}_p given by Eq. (B.25), constitutes the volumetric equation in the desired system. The surface equation is simply the representation formula (B.30) with the point \mathbf{r} approaching the positive side of Γ_m . Thus, finally, the set of coupled volume and surface equations is

$$\begin{aligned}
& p^{(\text{inc})}(\mathbf{r}) = p(\mathbf{r}) \\
& + \int_{\Omega} d^3 r' g_0(\mathbf{r} - \mathbf{r}') \left\{ k_0^2 \left(1 - \frac{\kappa(\mathbf{r}')}{\kappa_0} \right) p(\mathbf{r}') + \nabla_{\mathbf{r}'} \cdot \left[\left(1 - \frac{\rho_0}{\rho(\mathbf{r}')} \right) \nabla_{\mathbf{r}'} p(\mathbf{r}') \right] \right\} \\
& - \int_{\Gamma_0^-} d^2 r' g_0(\mathbf{r} - \mathbf{r}') \left(1 - \frac{\rho_0}{\rho(\mathbf{r}')} \right) \frac{\partial p(\mathbf{r}')}{\partial n(\mathbf{r}')} \\
& - \int_{\Gamma_m^+} d^2 r' \left[\frac{\partial g_0(\mathbf{r} - \mathbf{r}')}{\partial n(\mathbf{r}')} p(\mathbf{r}') - g_0(\mathbf{r} - \mathbf{r}') \frac{\partial p(\mathbf{r}')}{\partial n(\mathbf{r}')} \right] \quad \text{for } \mathbf{r} \in \overline{\Omega}
\end{aligned} \tag{B.34a}$$

and

$$\int_{\Gamma_m^+} d^2 r' \left[\frac{\partial g_m(\mathbf{r} - \mathbf{r}')}{\partial n(\mathbf{r}')} p(\mathbf{r}') - g_m(\mathbf{r} - \mathbf{r}') \frac{\rho_m}{\rho(\mathbf{r}')} \frac{\partial p(\mathbf{r}')}{\partial n(\mathbf{r}')} \right] = 0 \quad \text{for } \mathbf{r} \in \Gamma_m^+ . \tag{B.34b}$$

In Eq. (B.34a) we marked explicitly that it holds not only inside the domain Ω but, by continuity, also on its boundary.

Adjacent homogeneous and inhomogeneous regions. As another example we consider adjacent inhomogeneous and homogeneous regions Ω and Ω_m , both embedded in background-space region Ω_0 and containing (Fig. 19).

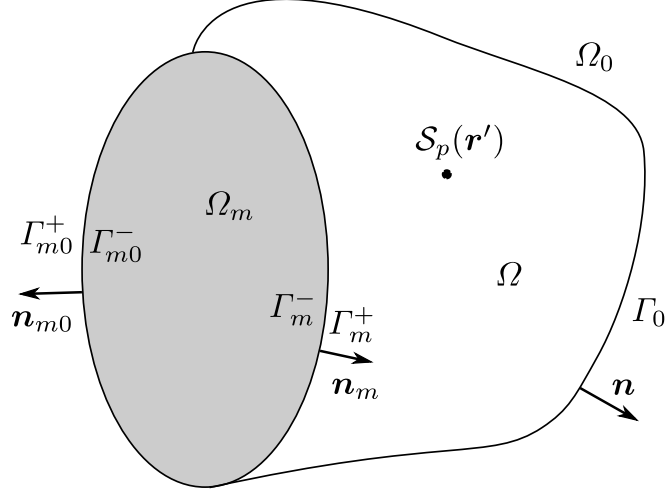


Figure 19: A homogeneous region Ω_m adjacent to an inhomogeneous region Ω . Γ_m and Γ_{m0} denote two parts of the boundary of Ω_m .

The representation formula (B.26) remains in this case unchanged, provided Γ_m^+ is the interface of Ω and Ω_m . On the other hand, the analogue of the formula (B.27) for the scattered field contains an additional contribution from the interface between the regions Ω_0 and Ω_m ,

$$\int_{\Gamma_0^+ \cup \Gamma_{m0}^+} d^2 r' \left[\frac{\partial g_0(\mathbf{r} - \mathbf{r}')}{\partial n(\mathbf{r}')} p^{(\text{sc})}(\mathbf{r}') - g_0(\mathbf{r} - \mathbf{r}') \frac{\partial p^{(\text{sc})}(\mathbf{r}')}{\partial n(\mathbf{r}')} \right] = \begin{cases} p^{(\text{sc})}(\mathbf{r}) & \text{for } \mathbf{r} \in \Omega_0, \\ 0 & \text{for } \mathbf{r} \notin \overline{\Omega_0}, \end{cases} \quad (\text{B.35})$$

where we dropped the vanishing contribution from Γ_R^- . By taking again the difference of Eqs. (B.26) and (B.35) for a point $\mathbf{r} \in \Omega$ and by using $p^{(\text{sc})} = p - p^{(\text{inc})}$ we obtain

$$\begin{aligned} & - \int_{\Gamma_m^+ \cup \Gamma_{m0}^+} d^2 r' \left[\frac{\partial g_0(\mathbf{r} - \mathbf{r}')}{\partial n(\mathbf{r}')} p(\mathbf{r}') - g_0(\mathbf{r} - \mathbf{r}') \frac{\partial p(\mathbf{r}')}{\partial n(\mathbf{r}')} \right] - \int_{\Omega} d^3 r' g_0(\mathbf{r} - \mathbf{r}') \mathcal{S}_p(\mathbf{r}') \\ & + \left\{ \int_{\Gamma_0^-} - \int_{\Gamma_0^+} \right\} d^2 r' \left[\frac{\partial g_0(\mathbf{r} - \mathbf{r}')}{\partial n(\mathbf{r}')} p(\mathbf{r}') - g_0(\mathbf{r} - \mathbf{r}') \frac{\partial p(\mathbf{r}')}{\partial n(\mathbf{r}')} \right] \\ & + \int_{\Gamma_0^+} d^2 r' \left[\frac{\partial g_0(\mathbf{r} - \mathbf{r}')}{\partial n(\mathbf{r}')} p^{(\text{inc})}(\mathbf{r}') - g_0(\mathbf{r} - \mathbf{r}') \frac{\partial p^{(\text{inc})}(\mathbf{r}')}{\partial n(\mathbf{r}')} \right] = -p(\mathbf{r}) \quad \text{for } \mathbf{r} \in \Omega. \end{aligned} \quad (\text{B.36})$$

which differs from Eq. (B.32) only by the additional contribution from the interface Γ_{m0}^+ . The remaining steps in the derivation are as before, and the final set of coupled volume and surface

equations becomes

$$\begin{aligned}
p^{(\text{inc})}(\mathbf{r}) &= p(\mathbf{r}) \\
&+ \int_{\Omega} d^3 r' g_0(\mathbf{r} - \mathbf{r}') \left\{ k_0^2 \left(1 - \frac{\kappa(\mathbf{r}')}{\kappa_0} \right) p(\mathbf{r}') + \nabla_{\mathbf{r}'} \cdot \left[\left(1 - \frac{\rho_0}{\rho(\mathbf{r}')}\right) \nabla_{\mathbf{r}'} p(\mathbf{r}') \right] \right\} \\
&- \int_{\Gamma_0^-} d^2 r' g_0(\mathbf{r} - \mathbf{r}') \left(1 - \frac{\rho_0}{\rho(\mathbf{r}')}\right) \frac{\partial p(\mathbf{r}')}{\partial n(\mathbf{r}')} \\
&- \int_{\Gamma_m^+ \cup \Gamma_{m0}^+} d^2 r' \left[\frac{\partial g_0(\mathbf{r} - \mathbf{r}')}{\partial n(\mathbf{r}')} p(\mathbf{r}') - g_0(\mathbf{r} - \mathbf{r}') \frac{\partial p(\mathbf{r}')}{\partial n(\mathbf{r}')} \right] \quad \text{for } \mathbf{r} \in \overline{\Omega} \quad (\text{B.37a})
\end{aligned}$$

and

$$\int_{\Gamma_m^+ \cup \Gamma_{m0}^+} d^2 r' \left[\frac{\partial g_m(\mathbf{r} - \mathbf{r}')}{\partial n(\mathbf{r}')} p(\mathbf{r}') - g_m(\mathbf{r} - \mathbf{r}') \frac{\rho_m}{\rho(\mathbf{r}')} \frac{\partial p(\mathbf{r}')}{\partial n(\mathbf{r}')} \right] = 0 \quad \text{for } \mathbf{r} \in \Gamma_m^+ \cup \Gamma_{m0}^+, \quad (\text{B.37b})$$

where the surface equation (B.37b) is simply the representation formula for the region Ω_m involving the entire boundary of that region.

Discretization. For concreteness we consider here the geometry of Fig. 18 and write the resulting system of equations (B.34) as

$$\begin{aligned}
p(\mathbf{r}) - (\mathcal{U} p_{\Omega})(\mathbf{r}) \\
- (\mathcal{K}_0 p_{\Gamma_m^+})(\mathbf{r}) + (\mathcal{V}_0 \partial_n p_{\Gamma_m^+})(\mathbf{r}) &= p^{(\text{inc})}(\mathbf{r}) \quad \text{for } \mathbf{r} \in \overline{\Omega}, \quad (\text{B.38a})
\end{aligned}$$

$$\left(\left(\frac{1}{2} I + K_m \right) p_{\Gamma_m^+} \right)(\mathbf{r}) - \left(\widehat{V}_m \frac{\rho_m}{\rho} \partial_n p_{\Gamma_m^+} \right)(\mathbf{r}) = 0 \quad \text{for } \mathbf{r} \in \Gamma_m. \quad (\text{B.38b})$$

Here in Eq. (B.37a) the operator \mathcal{U} is a generalization of the volumetric “Newton potential”,

$$(\mathcal{U} p_{\Omega})(\mathbf{r}) := \int_{\Omega} d^3 r' g_0(\mathbf{r} - \mathbf{r}') \mathcal{S}_p(\mathbf{r}'), \quad (\text{B.39})$$

expressed in terms of the source density (as defined by Eq. (B.25)); \mathcal{V}_0 is the single-layer *potential*

$$(\mathcal{V}_0 \phi_{\Gamma})(\mathbf{r}) := \int_{\Gamma} d^2 r' g_0(\mathbf{r} - \mathbf{r}') \phi(\mathbf{r}'), \quad (\text{B.40})$$

due to the source ϕ on an interface Γ , and \mathcal{K}_0 is the analogous double-layer potential, both defined at all points of the domain Ω . The operators K_m and \widehat{V}_m in Eq. (B.37b) are the usual double- and single-layer boundary operators, the latter *not* including the density factor present in the definition (B.9a). For simplicity, we assumed here material properties are smooth on the boundary Γ_0 , which allows us to omit the contribution of this surface to the volumetric equation (the third line of Eq. B.34a). The presence of absence of such contributions (related to discontinuities of the material parameters [9, 1, 2]) is a problem belonging to the purely volumetric formulation, unrelated to the coupling of volume and surface equations.

With Γ_m^+ denoted simply by Γ , the unknown fields appearing in Eqs. (B.38) are the volume pressure p_{Ω} , surface pressure p_{Γ} , and its normal derivative $\partial_n p_{\Gamma}$. For simplicity of notation,

we assume now that p_Ω is expanded in constant trial functions φ_t supported on tetrahedra t of Ω , while the p_Γ and p_Γ are represented in terms of constant functions ϕ_f supported on facets f of Γ . Accordingly, we denote the vector containing the unknown expansion coefficients as consisting of three blocks, $[p_t \ p_f \ \partial_n p_f]^\top$.

In devising the testing procedure, we recall that Eq. (B.38a) holds not only in the region Ω , but also on its boundary Γ . Therefore, that equation should be projected on both volume and surface testing functions, for which we again assume the functions φ_t and ϕ_f . Then, when projected on the latter functions, the potential operators \mathcal{K}_0 and \mathcal{V}_0 become the *boundary* operators K_0 and \widehat{V}_0 , and in this way one recovers the full set of surface equations. The resulting discretized equations take then the schematic form

$$\begin{bmatrix} (I - \mathcal{U})_{tt} & -(\mathcal{K}_0)_{tf} & (\mathcal{V}_0)_{tf} \\ (I - \mathcal{U})_{ft} & (\frac{1}{2}I - K_0)_{ff} & (\widehat{V}_0)_{ff} \\ 0 & (\frac{1}{2}I + K_m)_{ff} & -(\rho/\rho_m \widehat{V}_m)_{ff} \end{bmatrix} \begin{bmatrix} p_t \\ p_f \\ \partial_n p_f \end{bmatrix} = \begin{bmatrix} p_t^{(\text{inc})} \\ p_f^{(\text{inc})} \\ 0 \end{bmatrix}, \quad (\text{B.41})$$

with a square coefficient matrix.

In the absence of the homogeneous region Ω_m the system (B.41) reduces trivially to the purely volumetric L-S equation. It is also easy to show that, when region Ω becomes the background space, Eqs. (B.41) reduce to the usual surface equations (B.15) for the transmission problem, which can be then recast into the sum-and-difference form (B.16). In general, the system (B.41) can be similarly rearranged by taking the sum and the difference of the second and third equation. It is also evident that other than constant basis functions can be used in the discretization.

B.3 Implementation

In this Section we describe some features of the current implementation of the solver, in particular discretization of the integral equations for multiple material regions and compression of the resulting coefficient matrix.

B.3.1 Aspects of the discretization

Choice of trial and testing functions. The approach often used in discretizing transmission problems (involving single- and double-layer operators, and possibly hyper-singular operators) is to discretize the pressure and velocity fields p and q with piecewise constant and piecewise linear functions, respectively. This choice is motivated by the mapping properties of the operators [11] appearing in Eqs. (B.14) and (B.16): the operators K are of order 0, while V 's and W 's have orders -1 and $+1$.

From the point of view of the smoothing and differentiating properties of the operators, a possible drawback of a linear interpolation for q is that it enforces continuity even at sharp edges of the surface, where q is expected to be discontinuous. However, in anatomical models we are working with the surfaces tend to be relatively smooth, linear interpolation for both p and q appears to be advantageous. In fact, in our code we have implemented linear-functions discretization for p and both constant- and linear-functions discretizations for q and our experience has shown that, overall, *linear node-based functions* are preferable. With this choice, sharp edges and junctions of the surfaces can be handled by simply relaxing continuity constraints on the velocity field, i.e., by introducing independent variables on edges of separate surfaces.

As to the choice of testing functions, most engineering applications use collocation, in order to minimize the cost of the stiffness matrix construction (as discussed, e.g., in [16]). In our implementation we opted for a *Galerkin method* with the same spaces of testing and trial functions; its higher computational cost is offset by matrix compression which requires only computation of a highly sparse matrix representing couplings of nearby elements.

Treatment of junctions of surfaces. We first describe our treatment of junctions of tree interfaces in the context of the previously discussed system of a single body partitioned into two adjacent regions, shown in Fig. 16(b).

In this case the non-vanishing orientation parameters can be written as

$$\sigma_{11} = -1, \quad \sigma_{10} = +1, \tag{B.42a}$$

$$\sigma_{22} = -1, \quad \sigma_{20} = +1, \tag{B.42b}$$

$$\sigma_{32} = -1, \quad \sigma_{31} = +1. \tag{B.42c}$$

The final matrix of operators is, therefore,

$$A = \left[\begin{array}{cc|cc|cc} I - K_0 + K_1 & \widehat{V}_0 - \widehat{V}_1 & -K_0 & \widehat{V}_0 & -K_1 & \widehat{V}_1 \\ -K_0 - K_1 & \widehat{V}_0 + \widehat{V}_1 & -K_0 & \widehat{V}_0 & K_1 & -\widehat{V}_1 \\ \hline -K_0 & \widehat{V}_0 & I - K_0 + K_2 & \widehat{V}_0 - \widehat{V}_2 & K_2 & -\widehat{V}_2 \\ -K_0 & \widehat{V}_0 & -K_0 - K_2 & \widehat{V}_0 + \widehat{V}_2 & -K_2 & \widehat{V}_2 \\ \hline K_1 & -\widehat{V}_1 & K_2 & -\widehat{V}_2 & I - K_1 + K_2 & \widehat{V}_1 - \widehat{V}_2 \\ K_1 & -\widehat{V}_1 & -K_2 & \widehat{V}_2 & -K_1 - K_2 & \widehat{V}_1 + \widehat{V}_2 \end{array} \right] \quad (\text{B.43})$$

and the full system of equations takes the form

$$A \begin{bmatrix} p_1 \\ \widehat{q}_1 \\ \hline p_2 \\ \widehat{q}_2 \\ \hline p_3 \\ \widehat{q}_3 \end{bmatrix} = \begin{bmatrix} p_1^{(\text{inc})} \\ p_1^{(\text{inc})} \\ \hline p_2^{(\text{inc})} \\ p_2^{(\text{inc})} \\ \hline 0 \\ 0 \end{bmatrix} . \quad (\text{B.44})$$

According to the continuity criteria imposed on the solutions, we discretize the system (B.44) in terms of the total of seven sets of “composite basis functions” (CBFs), by expanding the unknown fields in trial basis functions as

$$p(\mathbf{r}) = \sum_{v1} p_{v1} \Phi_{v1}(\mathbf{r}) + \sum_{v2} p_{v2} \Phi_{v2}(\mathbf{r}) + \sum_{v3} p_{v3} \Phi_{v3}(\mathbf{r}) + \sum_{vJ} p_{vJ} \Upsilon_{vJ}(\mathbf{r}) \quad (\text{B.45a})$$

and

$$q(\mathbf{r}) = \sum_{V1} q_{V1} \Psi_{V1}(\mathbf{r}) + \sum_{V2} q_{V2} \Psi_{V2}(\mathbf{r}) + \sum_{V3} q_{V3} \Psi_{V3}(\mathbf{r}) . \quad (\text{B.45b})$$

All the basis functions are linear functions associated with vertices (nodes) of the surface mesh: Φ_{vi} are supported on sets of facets sharing *interior* vertices of an interface Γ_i , Ψ_{vi} are supported on sets of facets sharing *all* vertices (including boundary ones) of the interface, and Υ_{vJ} are associated with vertices of a junction J , i.e., with common vertices of several (here three) interfaces.

Assuming the same as above set of testing functions, we arrive at the discretized system described by the square matrix which can be represented as

$$M = \begin{bmatrix} M_{v1v1} & M_{v1V1} & M_{v1v2} & M_{v1V2} & M_{v1v3} & M_{v1V3} & M_{v1vJ} \\ M_{V1v1} & M_{V1V1} & M_{V1v2} & M_{V1V2} & M_{V1v3} & M_{V1V3} & M_{V1vJ} \\ M_{v2v1} & M_{v2V1} & M_{v2v2} & M_{v2V2} & M_{v2v3} & M_{v2V3} & M_{v2vJ} \\ M_{V2v1} & M_{V2V1} & M_{V2v2} & M_{V2V2} & M_{V2v3} & M_{V2V3} & M_{V2vJ} \\ M_{v3v1} & M_{v3V1} & M_{v3v2} & M_{v3V2} & M_{v3v3} & M_{v3V3} & M_{v3vJ} \\ M_{V3v1} & M_{V3V1} & M_{V3v2} & M_{V3V2} & M_{V3v3} & M_{V3V3} & M_{V3vJ} \\ M_{vJv1} & M_{vJV1} & M_{vJv2} & M_{vJV2} & M_{vJv3} & M_{vJV3} & M_{vJvJ} \end{bmatrix}. \quad (\text{B.46})$$

Here the 2×2 blocks involving the “ordinary” basis functions Φ and Ψ (associated with single interfaces) can be easily constructed from the operator matrix representation (B.43). For instance,

$$\begin{bmatrix} M_{v2v2} & M_{v2V2} \\ M_{V2v2} & M_{V2V2} \end{bmatrix} = \begin{bmatrix} (I - K_0 + K_2)_{v2v2} & (\hat{V}_0 - \hat{V}_2)_{v2V2} \\ (-K_0 - K_2)_{V2v2} & (\hat{V}_0 + \hat{V}_2)_{V2V2} \end{bmatrix} \quad (\text{B.47})$$

and

$$\begin{bmatrix} M_{v2v3} & M_{v2V3} \\ M_{V2v3} & M_{V2V3} \end{bmatrix} = \begin{bmatrix} (K_2)_{v2v3} & (-\hat{V}_2)_{v2V3} \\ (-K_2)_{V2v3} & (\hat{V}_2)_{V2V3} \end{bmatrix}, \quad (\text{B.48})$$

etc.

The blocks in the last row and the last column, involving the junction basis functions, have a more complex structure. To exhibit them explicitly, we have to represent the basis functions Υ_{vJ} (still schematically) as

$$\Upsilon_{vJ} = \Upsilon_{vJ1} + \Upsilon_{vJ2} + \Upsilon_{vJ3}, \quad (\text{B.49})$$

where Υ_{vJi} is supported on facets belonging to the interface Γ_i .

Suppose then we want to find the formula for the block M_{vJvJ} . We go back to the expression (B.22) and take its $(1, 1)$ block involving matrix elements between basis functions representing the pressure, i.e., $\delta_{ij} I + \sum_m (-\sigma_{jm} K_m)$, and obtain

$$\begin{aligned} & \sum_{i=1}^3 \sum_{j=1}^3 (\Upsilon_{vJi}, (\delta_{ij} I - \sum_m \sigma_{jm} K_m) \Upsilon_{vJj}) \\ &= \sum_{i=1}^3 (\Upsilon_{vJi}, I \Upsilon_{vJi}) - \sum_{i=1}^3 \sum_{j=1}^3 \sum_m \sigma_{jm} (\Upsilon_{vJi}, K_m \Upsilon_{vJj}). \end{aligned} \quad (\text{B.50})$$

This expression is still schematic, as it represents an entire matrix block. To be more specific, we may consider the matrix element between the basis functions $\Upsilon_{vJi\alpha}$ and $\Upsilon_{vJj\beta}$, where α and β label vertices on the junction (Fig. 20).

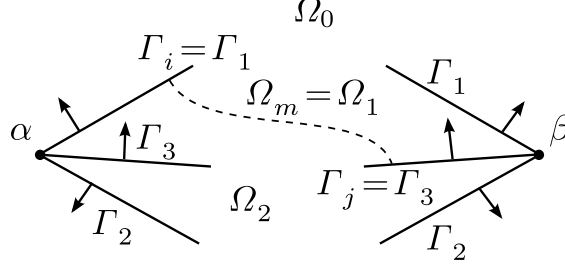


Figure 20: One of contributions to a matrix element between two junction-type basis functions associated with vertices α and β . The arrows indicate orientations of interfaces and the dashed line shows the coupling of the facets $f_i \subset \Gamma_i$ and $f_j \subset \Gamma_j$ through the operator K_1 in the region Ω_1 .

The contribution indicated in this Figure is the second term in the last expression of Eq. (B.50) with $i = 1$, $j = 3$, and $m = 1$, i.e., a coupling of facets f_1 and f_3 on interfaces Γ_1 and Γ_3 through the region Ω_1 .

In the actual implementation in the code, the junction-junction matrix elements such as given by Eq. (B.50) are evaluated together with all other matrix elements between ordinary basis functions. In fact, the considered facets f_1 and f_3 are also members of ordinary basis functions Φ_{v1} and Φ_{v3} supported on the interfaces Γ_1 and Γ_3 , and the contributions to various basis functions are being evaluated simultaneously.

More specifically, our matrix fill algorithm involves an outer loop through pairs of interfaces Γ_i and Γ_j and an inner loop through pairs of facets $f_i \subset \Gamma_i$ and $f_j \subset \Gamma_j$. In the latter loop all matrix elements between “primary” basis functions supported on f_i and f_j are computed (there are $3 \cdot 3 = 9$ such matrix elements, since each triangular facet supports three different linear basis functions associated with three vertices of the triangle); then, contributions of facet-facet matrix elements are being added to all relevant matrix elements between the “composite” basis functions, *including* junction-type functions. In other words, the formula (B.50) is not implemented literally as the sum indicated there, but rather by evaluating that expression “inside-out”: we first compute the matrix elements $(\Upsilon_{vJi\alpha}, K_m \Upsilon_{vJj\beta})$ for all regions Ω_m and for all pairs of “primary” basis functions labeled by interfaces Γ_i and Γ_j , facets f_i and f_j , and vertices α and β , and then add their contributions to the matrix elements in all blocks in (B.46).

B.3.2 Matrix compression and fast matrix-vector multiplication

In the approach we describe here, we utilize the FFT-based AIM compression technique [5] initially developed in the context of electromagnetics and adapted to acoustics [1]. Such a matrix compression was developed in order to enable solving large linear sets of equations with dense matrices utilizing storage and execution times characteristic of problems involving sparse linear systems. (The physical idea behind the compression methods is that interactions at large distances require less resolution than interactions at small distances. As the result, the computational complexity and memory requirements of the compression methods scale approximately linearly with the number of unknowns N .)

In order to explain the structure of this algorithm on a simple example, let us suppose we are evaluating the far-field contribution p' to the pressure, generated by the double-layer

operator K acting on the input pressure field. We assume the input pressure has the expansion

$$p(\mathbf{r}) = \sum_{\alpha} p_{\alpha} \Upsilon_{\alpha}(\mathbf{r}) \equiv \sum_{\alpha} p_{\alpha} \sum_i \Upsilon_{\alpha}^i(\mathbf{r}) . \quad (\text{B.51})$$

Here α s are the unknown numbers and the index i labels interfaces Γ_i supporting the composite basis functions (CBFs) Υ_{α}^i . Hence, in general, the sum

$$\Upsilon_{\alpha}(\mathbf{r}) := \sum_i \Upsilon_{\alpha}^i(\mathbf{r}) \quad (\text{B.52})$$

constitutes a junction-type basis function supported on several interfaces; a particular case are “ordinary” basis functions associated with single geometry components.

We are evaluating projections of $K p$ on the same set of basis functions, i.e.,

$$p'_{\alpha} := (\Upsilon_{\alpha}, K p) . \quad (\text{B.53})$$

For the purpose of evaluating the far field, the basis functions Υ_{α} are approximated by distributions of sources on nodes of a Cartesian grid,

$$\Upsilon_{\alpha}^i(\mathbf{r}) \approx \sum_{\mathbf{u}} \Lambda_{\alpha \mathbf{u}}^i \delta^3(\mathbf{r} - \mathbf{u}) . \quad (\text{B.54})$$

With the operator kernel $K(\mathbf{r}, \mathbf{r}') = \partial g(\mathbf{r} - \mathbf{r}') / \partial n(\mathbf{r}')$, the result of the operator acting on the field is

$$(K p)(\mathbf{r}) = \sum_{\beta} p_{\beta} \int d^3 r' \frac{\partial g(\mathbf{r} - \mathbf{r}')}{\partial n(\mathbf{r}')} \Upsilon_{\beta}(\mathbf{r}') \equiv \sum_{\beta} p_{\beta} \int d^3 r' g(\mathbf{r} - \mathbf{r}') \frac{\partial}{\partial n(\mathbf{r}')} \Upsilon_{\beta}(\mathbf{r}') , \quad (\text{B.55})$$

where the Green function g is taken with the parameters of the region through which the points \mathbf{r} and \mathbf{r}' communicate.

Suppose first the equations involve only a single operator \mathcal{K} of the form such as one of the blocks of (B.22). In this case, the far-field computation procedure is as follows:

We assume that the source x is represented in terms of the trial basis functions Υ^x

$$x^l(\mathbf{r}) = \sum_{\beta} x_{\beta} \Upsilon_{\beta}^{x^l}(\mathbf{r}) \equiv \sum_{\beta} x_{\beta}^l \sum_j \Upsilon_{\beta}^{x^l j}(\mathbf{r}) . \quad (\text{B.56})$$

Here α s are the unknown numbers and the index i labels interfaces Γ_i supporting the composite basis functions (CBFs) Υ_{α}^i . We then consider the field $y = \mathcal{K} x$ created by an operator \mathcal{K} acting on the sources, projected on the testing basis functions $\Upsilon_{\alpha}^{y^i}$,

$$y_{\alpha} := (\Upsilon_{\alpha}^y, \mathcal{K} x) . \quad (\text{B.57})$$

The operator is assumed to be of the form

$$\mathcal{K} = D_y g D_x , \quad (\text{B.58})$$

where g is the Green function of the region in which the operator acts, and D_y and D_x are differential operators (e.g., normal derivatives) acting at the field and sources points, hence the field projections can be, after integrating by parts, represented as

$$y_\alpha^k = \sum_\beta \int d^2 r_1 \int d^2 r_2 D_y \Upsilon_\alpha^{y k}(\mathbf{r}_1) g(\mathbf{r}_1 - \mathbf{r}_2) D_x \Upsilon_\beta^{x l}(\mathbf{r}_2) x_\beta^l . \quad (\text{B.59})$$

At large distance between the field (observation) and the source points the (derivatives of) the basis functions appearing in Eq. (B.59) can be approximated, for each interface Γ_i , by distributions of sources on nodes of a Cartesian grid,

$$D_y \Upsilon_\alpha^{y k i}(\mathbf{r}) \approx \sum_{\mathbf{u}} \Lambda(D_y \Upsilon_\alpha^{y k i})_{\mathbf{u}} \delta^3(\mathbf{r} - \mathbf{u}) , \quad D_x \Upsilon_\alpha^{x l i}(\mathbf{r}) \approx \sum_{\mathbf{v}} \Lambda(D_x \Upsilon_\alpha^{x l i})_{\mathbf{v}} \delta^3(\mathbf{r} - \mathbf{v}) . \quad (\text{B.60})$$

The basis function is then approximated as

$$\phi_f(\mathbf{r}) \simeq \sum_{\mathbf{q} \in \mathcal{C}} \Lambda_{f, \mathbf{q}} \delta^3(\mathbf{r} - \mathbf{q}) , \quad (\text{B.61})$$

One of possible expressions for the far-field contribution to the coefficient matrix results from substituting the expansions of auxiliary basis function given in terms of monopole sources is

$$A_{f_1, f_2}^{\text{Far}} = \sum_{\mathbf{q}_1 \in \mathcal{C}} \sum_{\mathbf{q}_2 \in \mathcal{C}} \Lambda_{f_1, \mathbf{q}_1} g_0(\mathbf{q}_1 - \mathbf{q}_2) \Lambda_{f_2, \mathbf{q}_2}^n . \quad (\text{B.62})$$

In the case of the general integral-equation problem involving a *matrix* of operators and the corresponding vectors of solution and r.h.s. functions, as exemplified by Eq. (B.44), the far-field contribution to a matrix block acting on a source vector x has the form

$$\begin{aligned} y_\alpha^k &= \sum_m \sum_i \sum_{\mathbf{u}, \mathbf{v}} \sum_j \sum_{l \beta} \Lambda(D_y \Upsilon_\alpha^{y k i})_{\mathbf{u}} \sigma_{i m}^\eta g_m(\mathbf{u} - \mathbf{v}) \sigma_{j m}^\xi \Lambda(D_x \Upsilon_\beta^{x l j})_{\mathbf{v}} x_\beta^l \\ &\equiv \sum_m \sum_{i \mathbf{u}} \Lambda(D_y \Upsilon_\alpha^{y k i})_{\mathbf{u}} \sigma_{i m}^\eta \sum_{\mathbf{v}} g_m(\mathbf{u} - \mathbf{v}) \underbrace{\sum_{j l \beta} \sigma_{j m}^\xi \Lambda(D_x \Upsilon_\beta^{x l j})_{\mathbf{v}} x_\beta^l}_{X_{\mathbf{v}}^m} \\ &\equiv \sum_m \sum_{i \mathbf{u}} \Lambda(D_y \Upsilon_\alpha^{y k i})_{\mathbf{u}} \sigma_{i m}^\eta \underbrace{\sum_{\mathbf{v}} g_m(\mathbf{u} - \mathbf{v}) X_{\mathbf{v}}^m}_{Y_{\mathbf{u}}^m} \\ &\equiv \sum_m \sum_{i \mathbf{u}} \Lambda(D_y \Upsilon_\alpha^{y k i})_{\mathbf{u}} \sigma_{i m}^\eta Y_{\mathbf{u}}^m . \end{aligned} \quad (\text{B.63})$$

The formula (B.63) is implemented as an outer loop through regions Ω_m , containing nested loops through the indices (j, β) , \mathbf{v} , and (i, \mathbf{u}) . The first inner (j, β) -loop evaluates the “Cartesian vector” $X_{\mathbf{v}}^m$, i.e., the equivalent-source representation, in the region Ω_m , of the input MoM vector of coefficients x_β . The \mathbf{v} -loop is implemented in terms of FFTs: the Cartesian source vector $X_{\mathbf{v}}^m$ is transformed to the Fourier space, multiplied by the Fourier transform of the Green function g_m , and transformed back to form the Cartesian field vector $Y_{\mathbf{u}}^m$. In the (i, \mathbf{u}) -loop that vector is converted to the output MoM representation of the vector y . All the above operations are performed for all regions Ω_m (the outer loop) and the contributions to the far output field are being added.

B.3.3 Parallelization

In view of the relatively large scale of the problems we are solving – a reasonably realistic geometry requires at least several hundred thousand unknowns – not only matrix compression, but also parallelization of the solver becomes a necessity.

In our previously developed volumetric solver [2, 1] we have implemented a distributed-memory message-passing (MPI) parallelization in conjunction with the FFT-based matrix compression. It involved partition of the object geometry into multiple slice-type segments and assigning each of the slices (together with its two or more nearest neighbors) to individual processors. Each processor was using its “main” slice and its neighbors to construct a geometry of a size sufficient to evaluate all the *near-field* couplings of the main slice elements with the remainder of the object. The far-field couplings were handled by means of the matrix compression and fast matrix-vector multiplication scheme, which also required each processor to store and handle only quantities dependent on its local geometry and only the corresponding segment (slice) of the global Cartesian grid.

One of the main reasons that distributed-memory approach has been effective was that the geometry was *volumetric* and relatively *uniformly discretized*. These circumstances contributed to a reasonable work load balancing, while the regular structure of the geometry partition allowed a fairly simple communication scheme in exchanging data between the processors and their memories.

In contrast, our present solver has to be able to handle *surface* models with fine geometry details and widely varying discretization scales. In fact, in our models the triangle sizes span two order of magnitude, from about 5 mm in smooth geometry regions to $0.05\text{ mm} = 50\text{ }\mu\text{m}$ in the middle and inner ear details. As a result, balancing the computational load by means of geometry partition becomes increasingly difficult. Even if the numbers of geometry elements (triangles, vertices) or unknowns were approximately equalized between the processors, the numbers of their near-field couplings (and thus matrix elements) would still vary in a wide range, typically from few tens to several thousand.

In this situation we opted, at least as an interim solution, for implementing a shared-memory parallelization, especially in view of the presently available computational hardware. Current desktop or even laptop systems provide relatively large amounts of RAM storage (tens of gigabytes) accessed by several processors. Higher numbers of processors, along with larger storage, are available on supercomputer architectures, typically allowing both message-passing and shared memory access.

Our experience has shown that the shared memory (OpenMP) parallelization of the present solver is entirely feasible and efficient. In the following we describe parallelization of the main operations in the solver, in the order of decreasing computational cost:

1. In our nonuniform discretization problems the most computationally intensive solution stage is the “far-field subtraction” in stiffness matrix construction. This operation (an essential part of the AIM algorithm) handles the precomputed near-field matrix and subtracts from them the corresponding far-field elements. Although the near-field is globally sparse, its parts associated with finely discretized geometry regions may be quite “dense”, i.e., matrix rows may contain several thousand nonzero elements. The main computational cost is, therefore, evaluation of the far field (expressed in terms of the equivalent-source coefficients and the Green function tabulated at nodes of the

Cartesian grid) for each of the near-field matrix elements. At the same time, however, this operation is performed independently for each matrix element, hence the resulting loop can be immediately distributed among the threads. As a result, a nearly perfect parallel speedup can be achieved.

2. The next most computationally expensive task is the evaluation of the near-field stiffness matrix itself, chronologically preceding the previously described subtraction step. It consists of two stages:

- (a) Computation of the sparsity pattern of the matrix, based on the near-field range. In this stage we generate a special structure (not yet the stiffness matrix itself) storing information on the elements to be included in the matrix. Depending on the type of basis functions (e.g., those associated with facets or with vertices), the sparsity pattern stores, for each facet or vertex, the list of near facets or vertices. The relevant geometry elements (facets or vertices) are here first distributed among geometry buckets, each assigned to one and only one bucket. Then a double loop through pairs of nonempty and sufficiently near buckets is executed and, within those loops, loops through pairs of geometry elements in the buckets. In the latter loops the distance the elements is checked and, if it does not exceed the near-field range, the appropriate element is stored in the sparsity pattern.

Since the geometry elements are exclusively assigned to buckets, the outermost loop through the buckets can be split into threads without causing storage conflicts: each row of the sparsity pattern is then handled by only one thread. This scheme results, therefore, in a speedup nearly equal the number of threads.

- (b) Filling the determined structure of the sparse matrix. This task is more difficult to parallelize,¹ since the outer loops run through facets and facet-facet contributions to vertex-vertex matrix elements are being gradually added (this scheme is most efficient from the point of view of the total number of operations). Now, since different pairs of facets contribute to the same vertex-vertex matrix element, different threads may simultaneously try to write to the same storage location – although probability of such an event decreases with the problem size. In order to prevent such storage conflicts, we currently use the OpenMP locking function around the critical operation of adding/storing contributions to the output matrix elements. This solution, however, is not fully satisfactory, as impairs the effectiveness of parallelization. A better scheme (in the process of implementation) is similar to that used in constructing the sparsity pattern. The outer loops are taken through another set of buckets, now defined as containing sets of facets, but based on exclusive partition of vertices. This arrangement results in some redundancy: some facet-facet matrix elements are being computed several times, but only for facets near the boundaries of buckets. However, because of the exclusive assignment of vertices, it guarantees the absence of simultaneous store operations by different threads.

Finally, the matrix-vector multiplication also involves two main operations:

¹ For basis functions associated with vertices; for basis functions supported on facets parallelization is trivial.

- (a) Computation of the near-field component of the matrix-vector product. Parallelization of this task depends on whether the near-field matrix (stored in the sparse row form) is symmetric or not. In the latter case (which arises in most types of equations we are solving) parallelization is straightforward: the outer loop can be taken to run through the matrix rows, i.e., the storage indices of the output vector. Therefore, if this loop is split among the threads, each output address is handled by one thread only.

There is no such simple solution in the case when the matrix is symmetric and only its independent (say, upper-triangular) part is stored. It seems that in this situation the optimal algorithm is to compute and store an additional list of matrix element numbers, organized by columns rather than by rows. This scheme allows computing the entire matrix-vector product in a loop through the output vector indices and, at the same time, increases the matrix size only by 1/3, rather than doubling it, as would be the case if the symmetric matrix were trivially stored as a nonsymmetric one.

- (b) Computation of the far-field contribution to the matrix-vector product. In this operation the main computational cost is the three-dimensional fast Fourier transform (FFT) performed on the sources or fields defined on the Cartesian grid covering the object. That FFT is implemented as a set of iterated one-dimensional transform taken in each of the three directions. The steps in the loops in which that transform is executed can be simply split among the threads without causing any conflicts.

B.4 Some qualitative features of energy flow through high-contrast interfaces

Before discussing examples of computation, we give a short qualitative discussion of the expected behavior of the energy flow in our problems.

We first give a very elementary account of the acoustic reflection and transmission properties in wave propagation through a half-space and through finite-thickness layers. We consider a one-dimensional problem of a layer of thickness a , filled with a material of density ρ and a refraction coefficient n , surrounded by a background medium of density ρ_0 and a unit refraction coefficient. The layer is subject to a plane wave propagating in the direction normal to the its boundaries with the wave number k (in the background medium). The reflection and transmission coefficients (for the *pressure* field) are then

$$\mathcal{R}_a = \frac{(1 - \zeta^2) \sin(nka)}{(1 + \zeta^2) \sin(nka) + 2i\zeta \cos(nka)} \quad (\text{B.64a})$$

and

$$\mathcal{T}_a = \frac{2i\zeta}{(1 + \zeta^2) \sin(nka) + 2i\zeta \cos(nka)} e^{-ika}, \quad (\text{B.64b})$$

where

$$\zeta := \frac{n\rho_0}{\rho} \quad (\text{B.65})$$

is the acoustic impedance of the considered material.

For a “thin” layer, in the sense $\zeta \ll nka \ll 1$, the above expressions can be approximated by

$$\mathcal{R}_a = 1 + \mathcal{O}((nka)^2, \zeta^2, \zeta/(nka)) , \quad \mathcal{T}_a = 2i \frac{\zeta}{nka} [1 + \mathcal{O}((nka)^2, \zeta^2, \zeta/(nka))] , \quad (\text{B.66})$$

while for a large layer thickness (more precisely, for $\text{Im } nka \gg 1$, allowing a complex n),

$$\mathcal{R}_a \asymp \frac{1 - \zeta}{1 + \zeta} , \quad \mathcal{T}_a \asymp \frac{4\zeta}{(1 + \zeta)^2} e^{i(n-1)ka} . \quad (\text{B.67})$$

For comparison, for a semi-infinite half-space filled with the same considered material, the reflection and transmission coefficients are

$$\mathcal{R} = \frac{1 - \zeta}{1 + \zeta} , \quad \mathcal{T} = \frac{2}{1 + \zeta} . \quad (\text{B.68})$$

of the pressure wave *entering* the medium, is *not* small.

The relative energy flux densities (Eqs. (B.4) or (B.6)) for the finite-thickness-layer and half-space problems are, respectively,

$$F_a = 1 - |\mathcal{R}_a|^2 \equiv |\mathcal{T}_a|^2 = \begin{cases} \left| \frac{2\zeta}{nka} \right|^2 & (\text{“thin” layer}) , \\ \left| \frac{4\zeta}{(1 + \zeta)^2} \right|^2 & (\text{“thick” layer}) \end{cases} \quad (\text{B.69a})$$

and

$$F = 1 - |\mathcal{R}|^2 \equiv \text{Re } \zeta |\mathcal{T}|^2 = \frac{4 \text{Re } \zeta}{|1 + \zeta|^2} . \quad (\text{B.69b})$$

Hence, the energy flux F_a through the “thick” layer is (at least for real ζ) the *square* of the flux F entering a half-space medium – due to the fact that the wave is being reflected on *two* high-contrast interfaces.

B.5 Examples of energy flow computations

In this Section we discuss applications of the solver in modeling acoustic energy flow through the human head and its transfer to the cochlea.

The most complete geometry model used consists of:

- (1) the outer surface of the skin surrounding the skull and containing
- (2) the outer ear represented by its exterior surface,
- (3) the surface of the auditory canal,
- (4) the tympanic membrane modeled as a finite-thickness surface;
- (5) the middle ear, consisting of the system of ossicles and supporting structures;
- (6) the skull, described by external surfaces of the bones constituting the skull and including

- (7) a set of surfaces representing the inner ear cavity (boundaries of the cochlea, the vestibule, and the semi-circular canals).

In order to assess the relative importance of various mechanisms of the energy transfer, we also discuss results of computations with modified or simplified models. In all geometry models we assume typical approximate values of the relative densities and the refractive indices, $\rho/\rho_0 = 1000$ and $n = 0.2$ for the soft tissues, and $\rho/\rho_0 = 2000$ and $n = 0.4$ for the bone. The model is being subject to a pressure plane wave of unit amplitude, incident from the left side of the head. The wavelengths λ given in the following are always the wavelengths in the air.

We first briefly characterize the models, and summarize the obtained results:

- (A): A model of a homogeneous human head, filled with soft tissue. The computations in this case illustrate the significance of the scaling of the operator matrix and vector blocks in solving high-contrast transmission problems (Section B.2.4). We find that, in the absence of rescaling, although the residual in the iterative solution decays approximately exponentially, the slope is much smaller (in our examples 3 to 7 times, depending on the frequency) than the slope in the solution of rescaled equations. Furthermore, the solution of the non-rescaled equations converges to the correct solution only when very small residual values (10^{-5} down to 10^{-7}) are reached,² and even then the resulting field distributions exhibit speckle-type fluctuations.
- (B): A model of an isolated skull, surrounded by air. The computations, involving a rather complex skull structure, show the role of bone thickness in controlling the amount of the energy transmitted through *two* high-contrast interfaces, air-to-bone and bone-to-air. We also compare, for relatively low frequencies (wavelength $\lambda = 1$ m) solutions of the transmission problem to the solutions of the hard-surface (Neumann) and the soft-surface (Dirichlet) problems; these problems serve as a verification of the soundness of our solution procedures. We find, in agreement with intuitive expectations, that the pressure in the Neumann problem tends to concentrate inside the skull cavity – in analogy to the expected behavior of the temperature distribution in the equivalent heat-conduction problem. On the other hand, the distribution of the velocity field in the Dirichlet problem is concentrated on protruding elements of the surface, in analogy to the charge distribution in the equivalent electrostatic problem.
- (C): A model of a skull surrounded and filled with homogeneous soft tissue, *with* or *without* the outer ear canal. Here we can establish some properties of energy flow in a more realistic model with a rather intricate skull geometry, which includes the middle- and inner-ear cavity, and in particular the cavity housing the cochlea. We stress, however, that in our model we *excluded* the impedance-matching mechanism of the middle ear; hence, the energy entering the outer ear canal can only propagate through the surrounding tissues, and *not* through the usual air-conduction pathway.

As a quantitative measure of the effect of the acoustic waves arriving at the inner ear through the head tissues, we compute the amount of energy *flowing through the cochlea*. More specifically, we evaluate the quantity Φ_S defined by Eq. (5.2) below as the average absolute value of the energy flux density through the surface of the cochlear cavity,

² Our computations are carried out in single precision.

relative to the energy flux density of the wave incident on the head. According to the estimate (B.69b) of the energy transmission through a high-contrast interface, the computed relative flux density is expected to be of the order of the ratio of the densities of the air and the tissues, i.e., $\sim 10^{-3}$.

The main results of the computations are that

- The relative energy flux density Φ_S is, as expected, of the order 10^{-3} for large wavelengths (λ larger than the head size) and, generally, decreases for smaller wavelengths.
- The presence of the outer ear canals increases the relative flux density by transporting the energy deeper inside the head. This enhancement is by about the factor of two at larger wavelengths ($\lambda > 30$ cm) and the factor of three for $10 \text{ cm} < \lambda < 30 \text{ cm}$. For wavelengths $\lambda < 30$ cm it exhibits a resonant behavior which, according to the computations with the this the next model (D) can be attributed to the outer ear canal.

(D): A model of homogeneous soft-tissue head, without the outer ear canals and *without* the skull, but including the *surface* of the middle- and inner-ear cavity surfaces. We carried out computations with this model in order to assess the significance of the sound transmission through the bone vs. that through the soft tissues. As before, we compute the average relative flux density Φ_S through the surface of the cochlear cavity. We find that for wavelengths $\lambda \gtrsim 10$ cm removing the skull from the head filled otherwise with soft tissue increases the flux by 10 % to 30 %. The results for smaller wavelengths indicate a resonant-type behavior similar to that seen in the absence of the skull and therefore attributable to the outer ear canal – the feature common to the two models.

B.5.1 Exterior head surface (A): rescaling in solution of high-contrast transmission problems

As an illustration of the conditioning problems encountered in high-contrast problems (Section B.2.3), we discuss computations for a model of a homogeneous human head, assumed to be filled with the soft tissue. The model discretization gives rise to $N = 58,062$ unknowns.

In the first set of computations we assume the wavelength $\lambda = 1$ m, corresponding to the frequency about 300 Hz. The resulting convergence histories for the original and rescaled sets of equations (Eqs. (B.16) and (B.24)) are shown in Fig. 21.

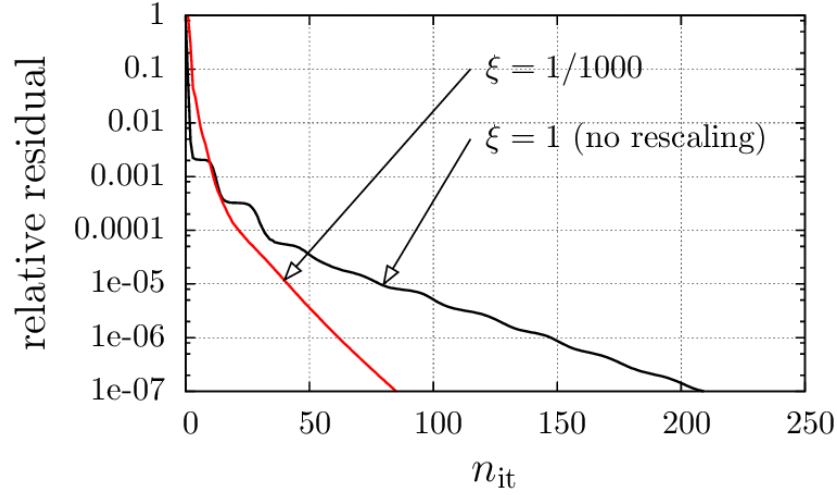


Figure 21: Convergence of the iterative solution to the transmission equations with the outer head surface, for $\lambda = 100$ cm and the tissue density $\rho_m/\rho_0 = 1000$: no rescaling ($\xi = 1$), and rescaling with the factor $\xi = 1/1000$.

Fig. 22 shows the energy flux distributions computed from solutions to the original and rescaled equations. Both solutions were obtained by iterating until the relative residual 10^{-7} was reached. At this very small residual value the energy fluxes are similar, but the distribution for the original equations exhibits distinct speckle-type irregularities. Further, the solution to the original equations approaches that for the rescaled equations *only* at this very low residual level, while the rescaled equations provide an accurate solution already for the relative residual of the order 10^{-3} .

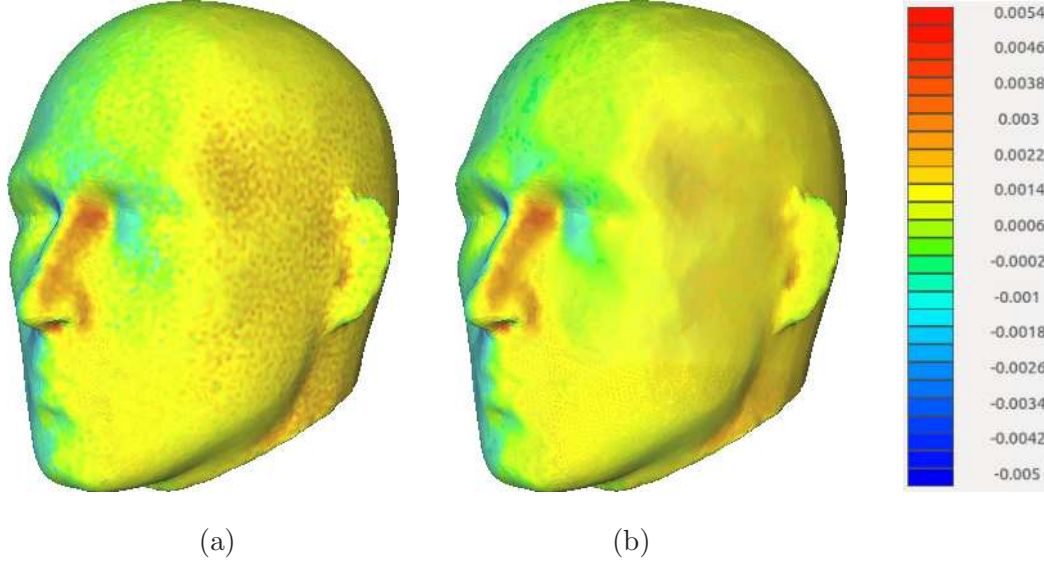


Figure 22: Distribution of the energy flux density in a model of a human head filled with a homogeneous tissue with $\rho_m/\rho_0 = 1000$ and $n_m = 0.2$, and for $\lambda = 100$ cm, obtained with solutions to the original (a) and rescaled (b) equations, both for the relative residual 10^{-7} .

We next consider a higher frequency, about 3 kHz, corresponding to the wavelength $\lambda = 10$ cm. In Fig. 23 we plot convergence histories for original and rescaled equations in this case. It is seen that convergence of the rescaled equations is fairly independent of variations – within a factor of about two – in the scaling parameter ξ .

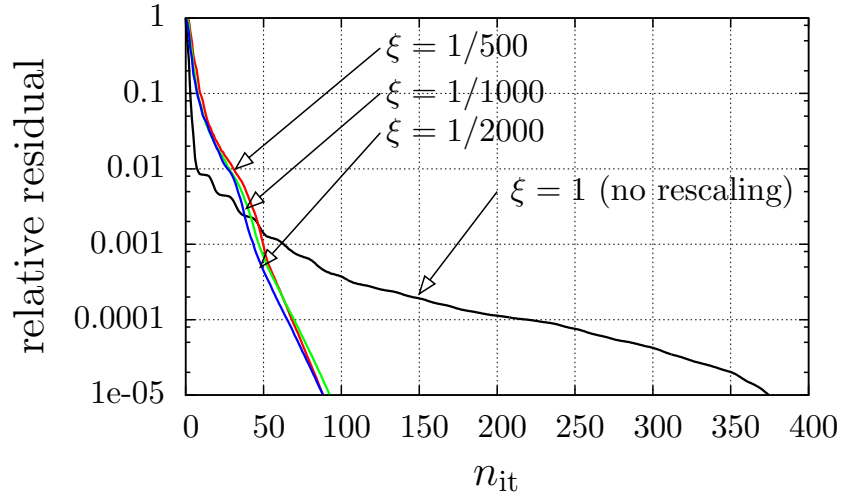


Figure 23: Convergence of the iterative solution to the transmission equations with the outer head surface, for $\lambda = 10$ cm and the tissue density $\rho_m/\rho_0 = 1000$: no rescaling ($\xi = 1$), and rescaling with factors $\xi = 1/500$, $\xi = 1/1000$, and $\xi = 1/2000$.

The energy flux distribution computed with rescaled equations is visualized in Fig. 24. In this case the solutions to the original equations are close to those shown in the Figures only provided the relative residual level $\sim 10^{-5}$ or better, while for the rescaled equations the relative residual level $\sim 10^{-3}$ is entirely adequate.

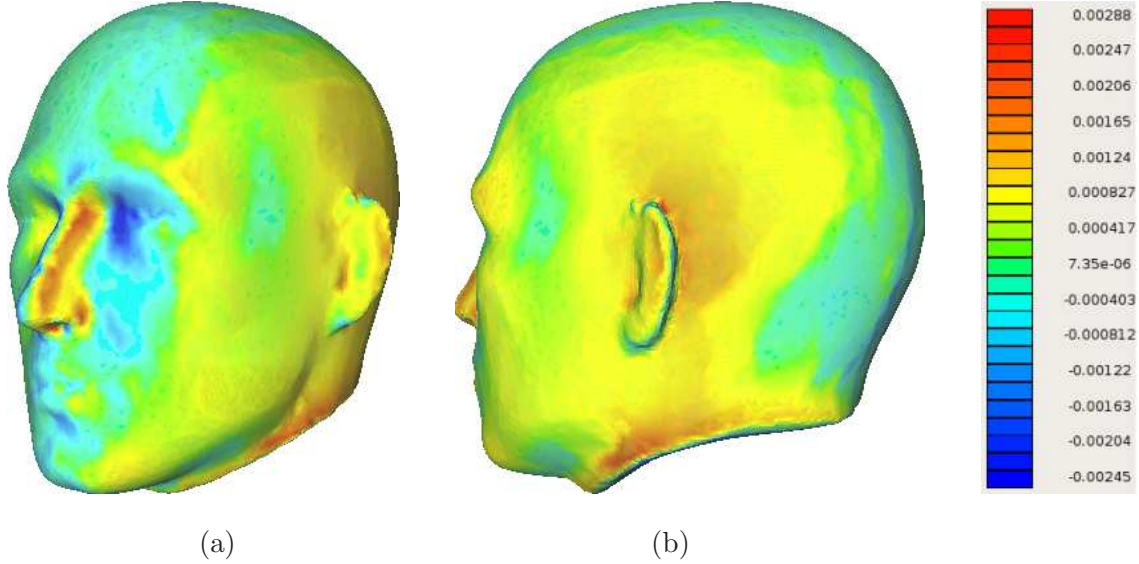


Figure 24: Distribution of the energy flux density in a model of a human head filled with a homogeneous tissue with $\rho_m/\rho_0 = 1000$ and $n_m = 0.2$, and for $\lambda = 10$ cm, seen from two points of view, (a) and (b).

For comparison, we plot in Fig. 25 the energy flux distribution for an even higher frequency ($\lambda = 5$ cm). It can be seen that it is more concentrated near the entrance to external ear canal, even though the ear canal itself is not modeled in the considered geometry; hence, the effect should be attributed to the shape of the auricle.

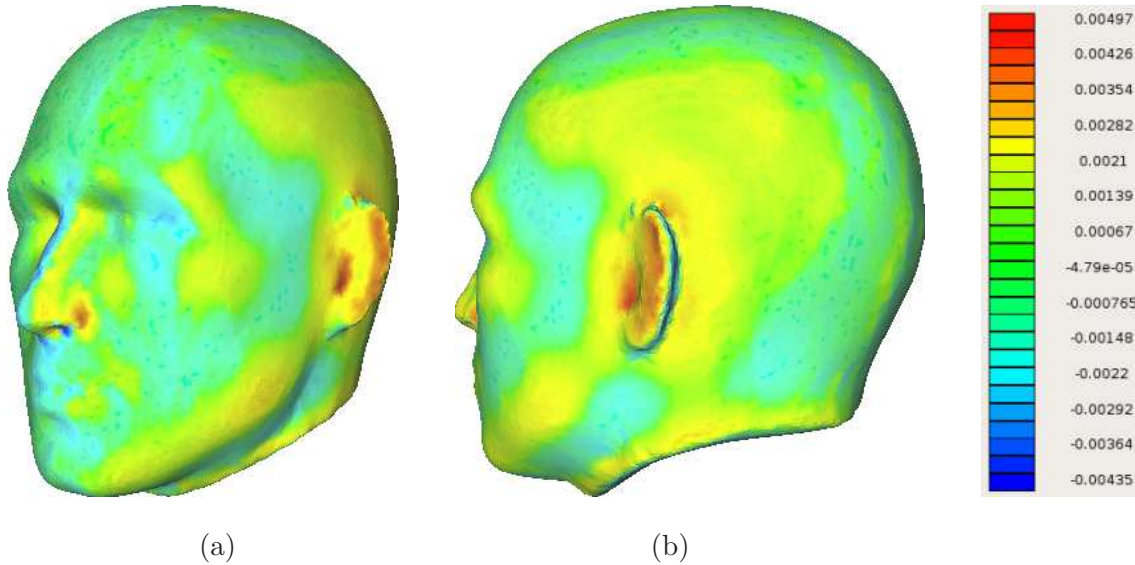


Figure 25: The same as Fig. 24, but for the frequency twice as high ($\lambda = 5$ cm).

B.5.2 Energy flow in model of a human skull (B)

Here we show results of computations for a model of an *empty* human skull. We do not consider this problem a realistic simulation of sound conduction in a human *head*, in which the skull is both surrounded by soft tissues and filled with them. This fact has been recognized long ago in the experimental work on bone conduction (e.g., [17, 18]); Nevertheless, it is of interest to analyze the energy flow in an isolated skull, to compare it with the behavior of a more complete model.

Our skull model is described by a triangular mesh with $N_v = 112,038$ vertices (hence the total number of unknowns is twice as large). The triangulation, shown in Fig. 26, is relatively uniform: the minimum, average, and maximum values of the edge length are 0.07 mm, 1.52 mm, and 4.62 mm.

Fig. 27 shows the distribution of the pressure field on the surface of the model, for wavelength $\lambda = 1$ m, corresponding roughly to the frequency 300 Hz.

As expected for a high-density material (nearly a hard surface), the pressure is of order unity. As also expected for a nearly hard surface, the velocity is much smaller (Fig. 28).

The velocity distribution is seen to be concentrated in the area of the temporal bone, simply because the bone is thinner in this region than elsewhere throughout the skull. The energy flux, shown in Fig. 29, is also small and concentrated in the same area as the velocity field; this is expected, since the distribution of pressure is quite uniform. The distributions of the flux density in Figs. 29(a) and Figs. 29(b) show that energy enters the bone from the outside and leaves through the inside surface.

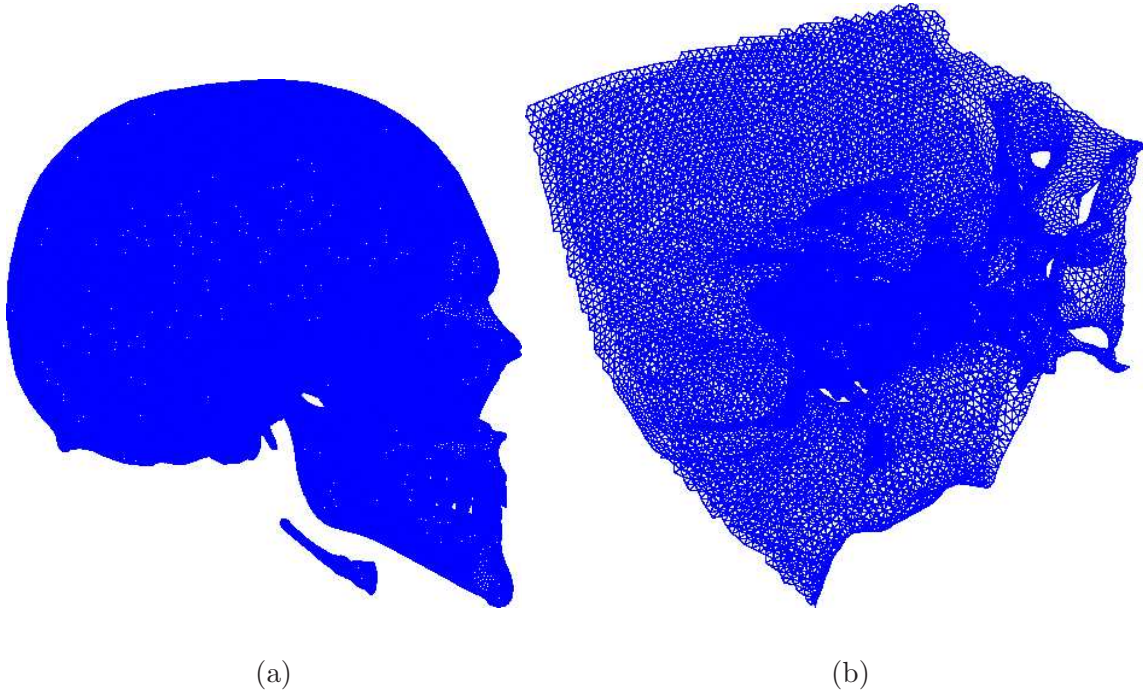


Figure 26: Triangulation of the left half of the skull model, as seen from the interior side (a), and a detail of the triangulation in the vicinity of the inner ear (b).

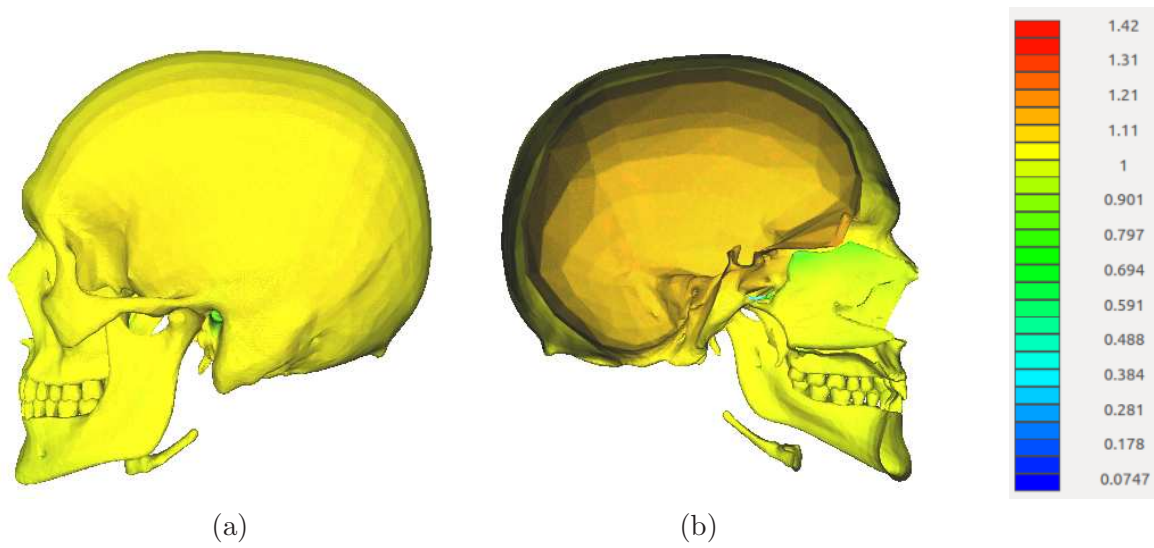


Figure 27: Distribution of the absolute value of the pressure field the exterior (a) and interior (b) surfaces of the left half of the skull.

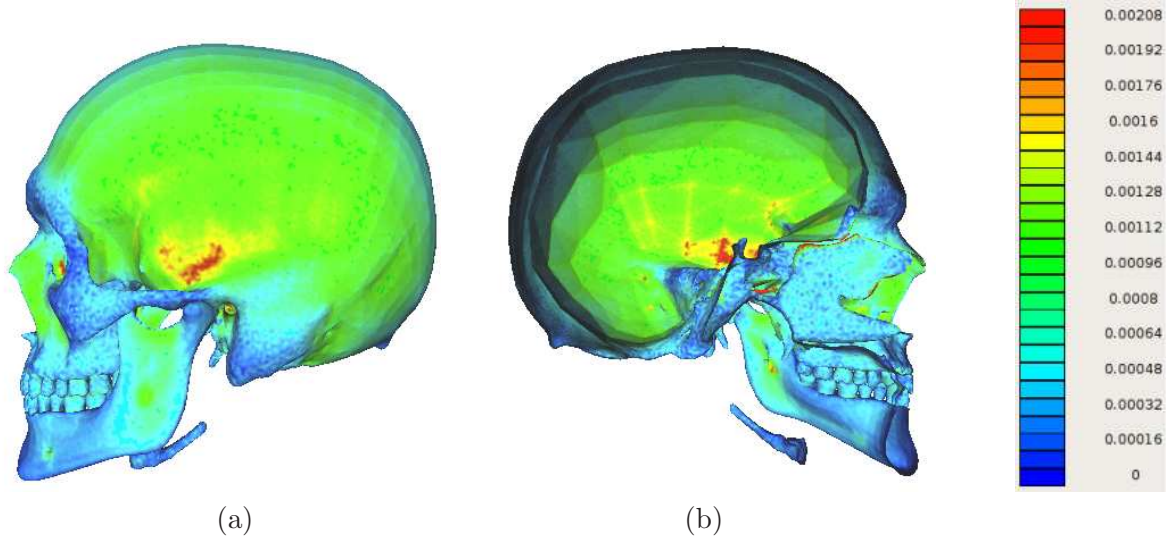


Figure 28: Distribution of the absolute value of the velocity field the exterior (a) and interior (b) surfaces of the skull.

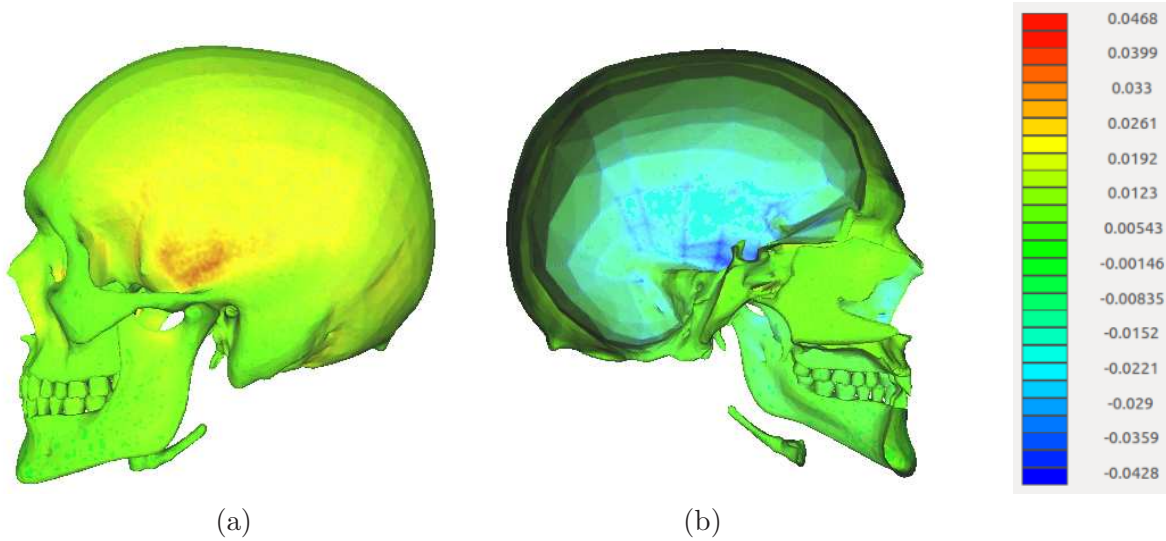


Figure 29: Distribution of the energy flux density on the exterior (a) and interior (b) surfaces of the skull. Positive/negative values indicate energy entering/leaving the bone.

For comparison with solution to the high-contrast transmission problem, we show in Fig. 30 the solution for the pressure field for the *hard-surface* (Neumann) problem. While the pressure on the outer surface (Fig. 30(a)) of the hard-surface skull is comparable to that in the transmission model, it is much (about 10 times) larger in the interior of the skull cavity (Fig. 30(b)).

This phenomenon can be intuitively understood by invoking the equivalence of the acoustic Neumann problem to the problem of steady-state heat transport in the presence of insulating boundaries, in which the pressure becomes the temperature, the Neumann boundary condition $\partial p/\partial n$ means zero energy flow through the boundary, and the incident plane wave plays the role of an external energy source. The “physical intuition” suggests then that the heat should be trapped in cavities.

The above comparison emphasizes the difference between the hard-surface problem and a transmission problem, even with a very large density contrast, hence small energy fluxes through the interfaces: even a small energy flow through the surfaces prevents its accumulation in a cavity.

As another comparison, Fig. 31 shows the distributions of the velocity field in the *soft-surface* (Dirichlet) problem. It is, of course, very different from the distribution in the transmission problem in Fig. 28, and (in agreement with the expected solution of the equivalent electrostatic problem) it exhibits maxima at pointed elements of the surface.

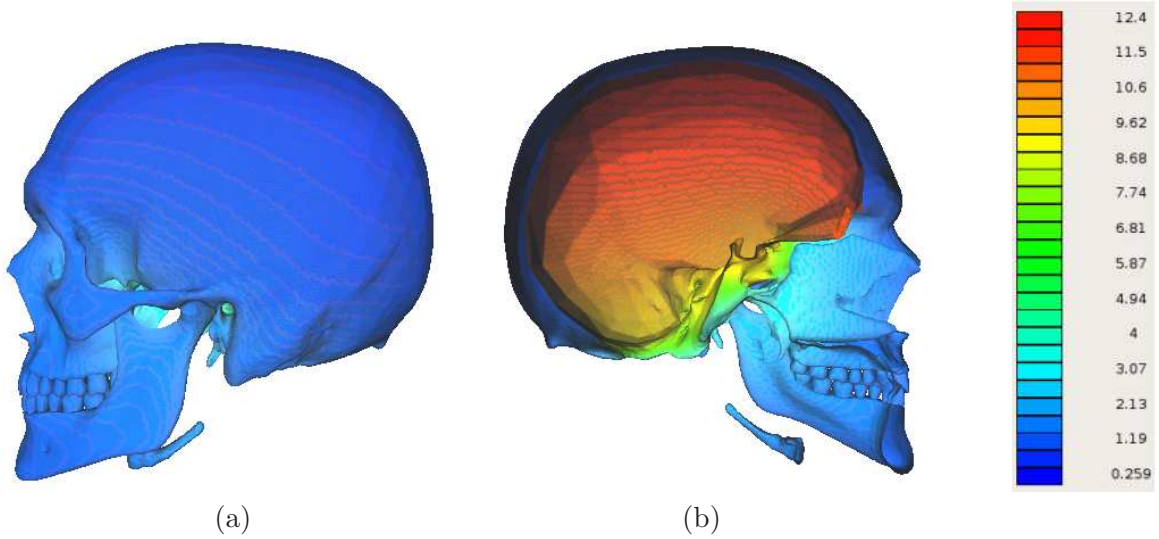


Figure 30: Distribution of the absolute value of the pressure field on the exterior (a) and interior (b) surfaces of the skull modeled as a hard surface (Neumann boundary conditions).

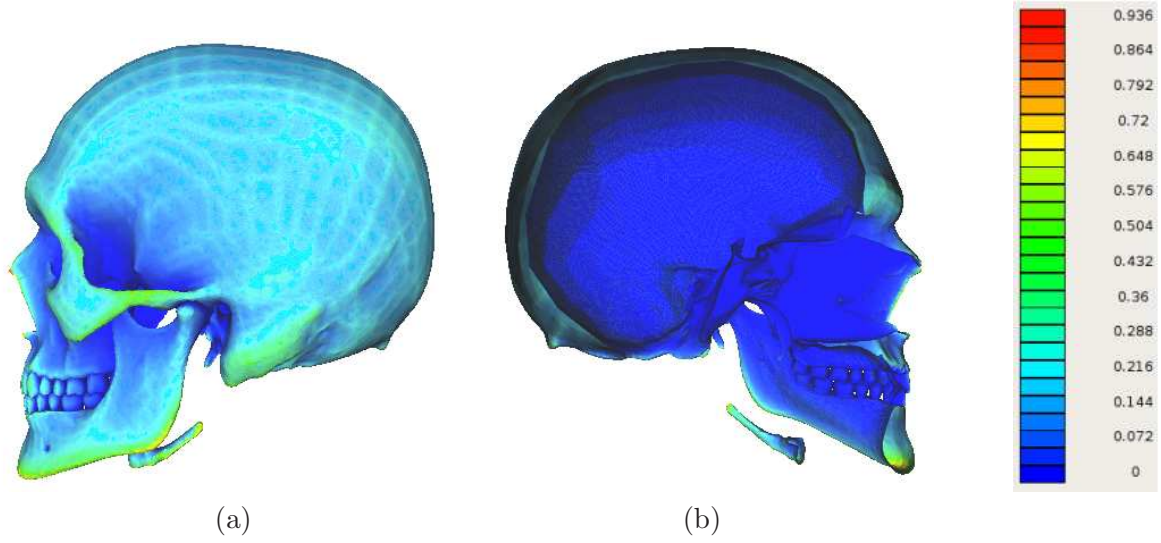


Figure 31: Distribution of the absolute value of the velocity field on the exterior (a) and interior (b) surfaces of the skull modeled as a soft surface (Dirichlet boundary conditions).

Finally, Fig. 32 displays some details of the energy flux distribution on surfaces in the area of the temporal bone. It can be seen here that the increased energy flow through the outer shell of the skull is related to the small bone thickness. One can also see the cochleas (as cavities in the bone). As indicated by the Figures 32, and in more detail in Fig. 33, the energy flow through the cochlea is directed from the inside to the outside of the skull.

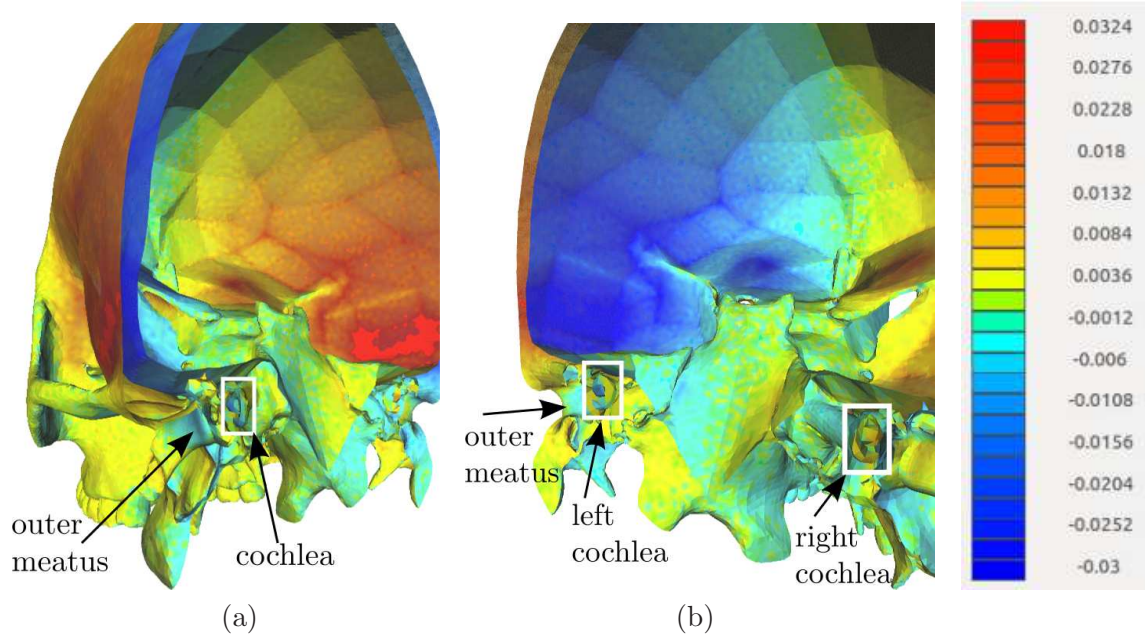


Figure 32: Distribution of the energy flux density in the area of the left temporal bone, seen from the back and outside (a) and inside (b) of the skull.

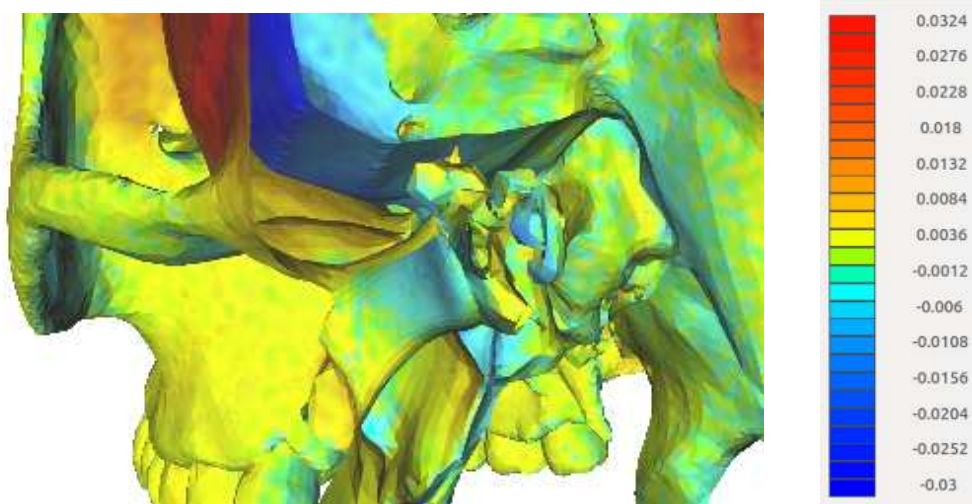


Figure 33: Distribution of the energy flux density in the area of the left temporal bone, including the outer auditory canal, and the middle and inner ear structures.

B.5.3 Energy flow in a model of a human head with skull and soft tissues (C)

We discuss here some results obtained with a model of a human head consisting of a skull embedded in undifferentiated soft tissues filling the outer “skin” boundary. In this model the head surface includes the outer ear canals terminated with a flat disc-shaped surfaces modeling, approximately, the tympanic membranes. A part of the model is visualized in Fig. 10(a). The triangulation used in the geometry results in about 260,000 unknowns. Most of the reported computations were done at the frequency of about 6 kHz, corresponding to the wavelength $\lambda = 5$ cm.

For comparison, we also carried out a number of computations with a head model *without* the outer ear canals. This model can be considered a realization of a *perfect ear-plug*, with which the outer auditory canal is effectively closed. We start with discussing results of computations with this model.

Head surface *without* the outer ear canal. The outer surface of the head is in this case described by the same model as in Figs. 21 and 23. Fig. 34 shows the resulting density of the energy flux through the surfaces of the model. The energy flux distribution on the exterior (skin) surface is nearly the same as in the model *without* the skull (Fig. 25(a)). A coronal cross-section through the model is shown in Fig. 25(b). The cross-section plane intersects the outer auditory meatus and the cochlea (a cavity in the skull bone). Further details of the vicinity of the left meatus and the cochlea are shown in Fig. 35, in which the range of the flux density has been reduced to $[-0.001, 0.001]$ (we recall these values are relative to the incident flux density). The boundary of the cochlea is visible near the right edge of Fig. 35(a), which presents the view from the back and the left of the head. Fig. 35(b) – the view from the right – shows positive values of the energy flux, approximately 0.0002, on the right boundary of the cochlea. Those values indicate that the energy flows from the cochlea (a cavity) *into* the bone. Similarly, the negative flux values on the opposite side of the cochlea show energy flowing *out* of the bone and into the cochlea. The overall energy flow through the cochlea is this from left to right.

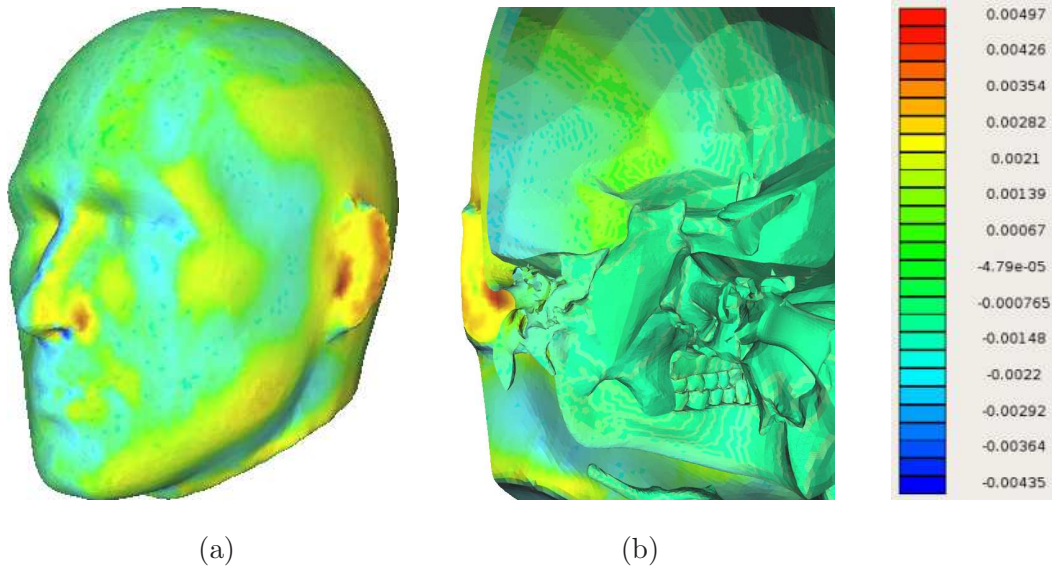


Figure 34: Distribution of the energy flux density in a model of head involving soft tissues and the skull: energy flux through the exterior surface (a) and through the interior interfaces (b). The latter shows a cross-section of the head, seen from the back and right side.

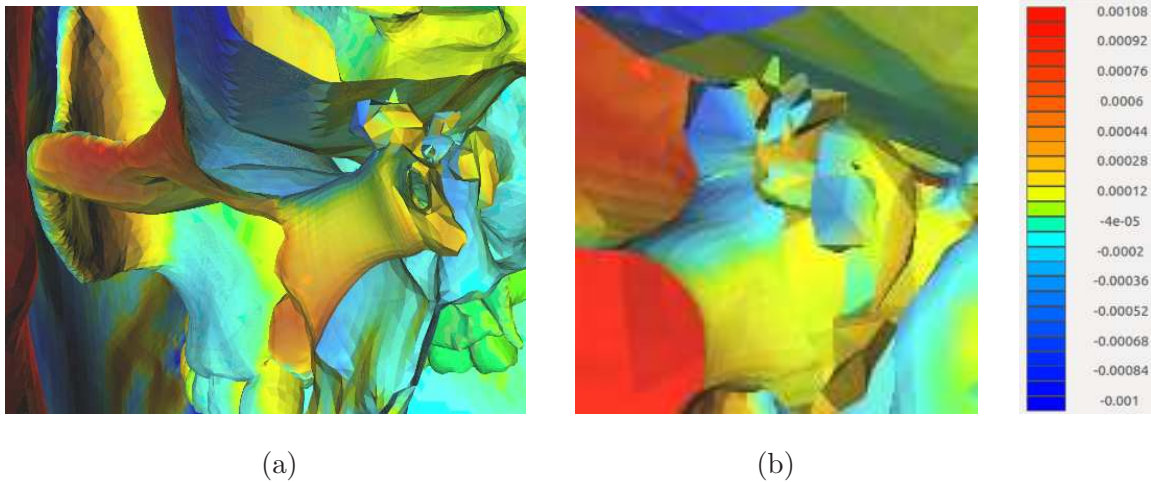


Figure 35: Details of the energy flux density distribution of Fig. 34.

Head surface *with* the outer ear canal. The following computation were carried out with the full head model, including the outer ear canal and, as before, the skull (Fig. 10(a)).

The significance of the outer auditory canal in air-conducted sound transmission is obvious. However, the results given below also indicate that the outer ear canal plays an important role in transporting the sound energy into the interior of the skull, and that a relatively large

amount of energy transmitted through the tissues emanates from the wall of the canal. Those phenomena are illustrated by the pressure, velocity, and energy flux distributions shown in Figures 36 and 37. The values of the energy fluxes are now significantly (by a factor of 10 or more) larger than in the previous model. An interesting feature is that in different parts of the canal the energy flows from the air into the tissue or in the opposite direction. Such pressure, velocity, and energy flux distributions are characteristic of a standing acoustic wave being formed in the ear canal [3]; consequently, these distributions change with the frequency (as confirmed by the computations).

The following Figures 36 and 37 show the distributions of the pressure and velocity fields, and the energy flux density in the region of the left temporal bone.

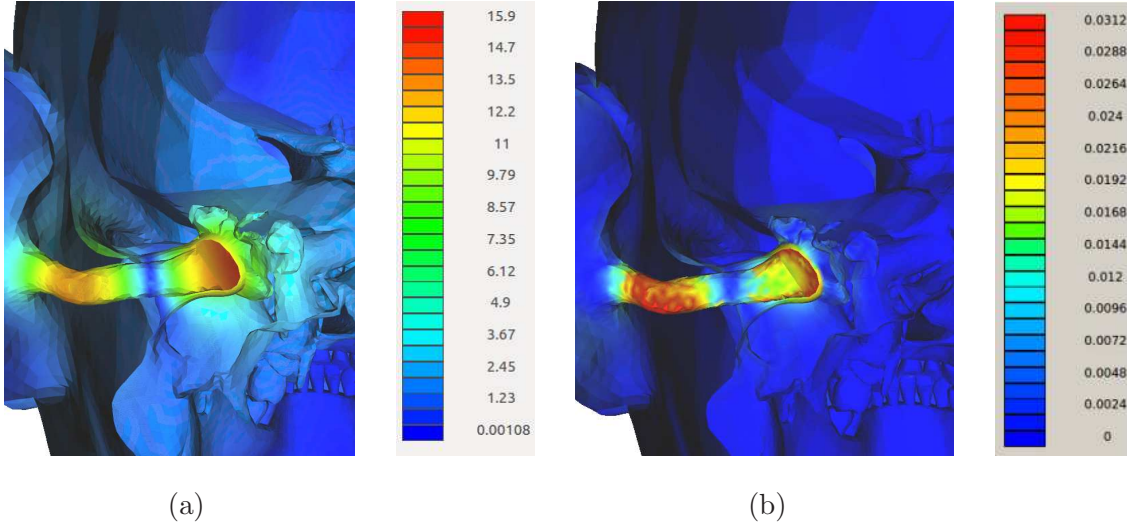


Figure 36: Distributions of the absolute value of the pressure (a) and velocity (b) fields, $|p(\mathbf{r})|$ and $|q(\mathbf{r})|$, on the material interfaces in the vicinity of the left temporal bone, for $\lambda = 5$ cm.

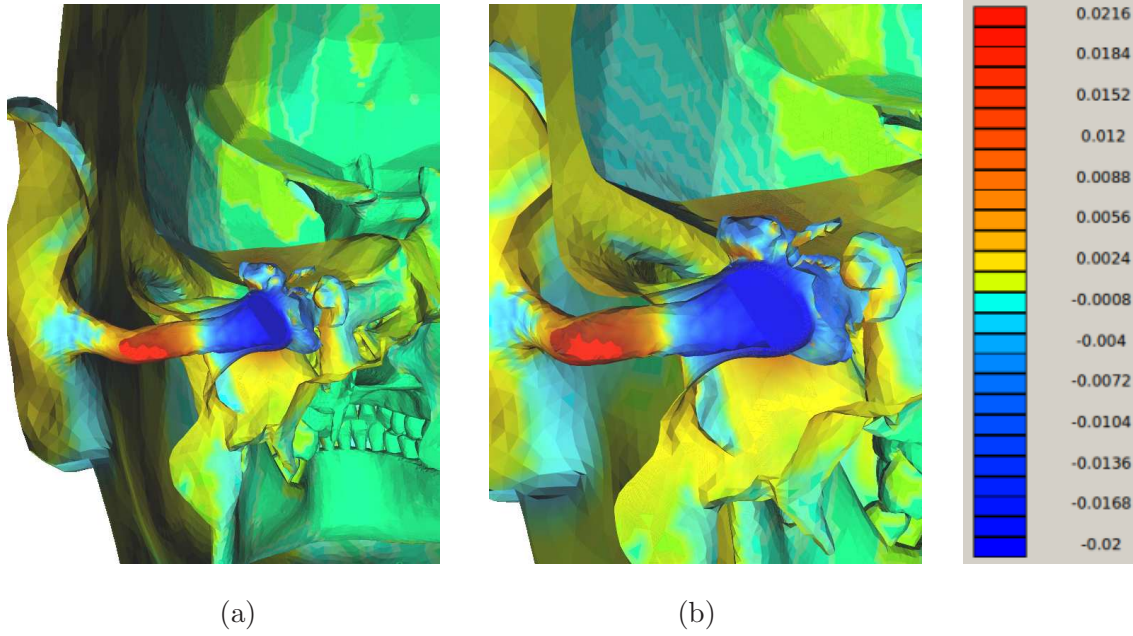


Figure 37: Distribution of the relative energy flux density, $F(\mathbf{r})$ of Eq. (B.6), on the interfaces in the vicinity of the left temporal bone, in a wider (a) and a smaller (b) regions, for $\lambda = 5$ cm.

Some features observed in the solution are as follows:

1. The outer auditory canal supports a standing wave with a node in pressure at about half-length of the canal (Fig. 36(a)). By examining the real and imaginary parts of the solution one can see that the pressure changes sign at that point.
2. The pressure p and the velocity field q (i.e., the velocity component *normal* to the walls of the canal, not the longitudinal velocity) has a more complex behavior and is not simply related by a proportionality constant (interface impedance).
3. As a consequence, the direction of the energy flow through the walls of the outer auditory canal changes sign along its length.

As the wavelength increases, the behavior of the pressure and velocity inside the outer auditory canal has no longer a wave character. Nevertheless, the fields and the energy flux are still largely concentrated inside the canal. The behavior of the resulting energy flux for $\lambda = 60$ cm is illustrated in Fig. 38.

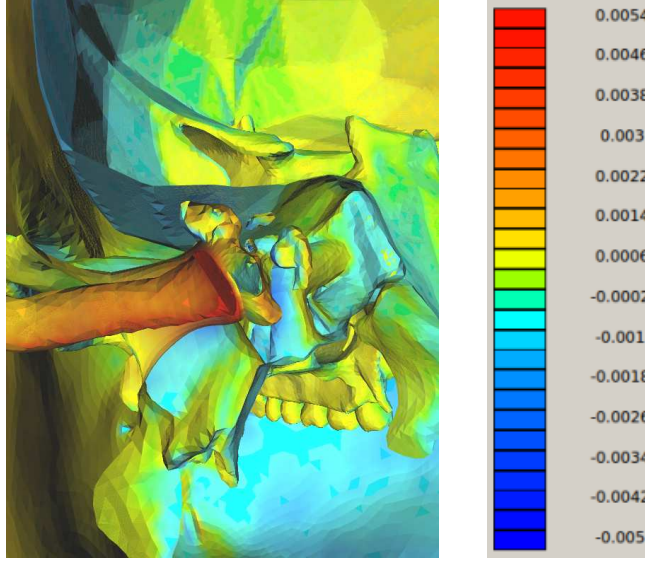


Figure 38: Distribution of the relative energy flux density $F(\mathbf{r})$ on the interfaces in the vicinity of the left temporal bone for $\lambda = 60$ cm.

Energy flow through the cochlea. Based on the solutions for the two head models, we compare now the amounts of energy flowing through the inner ear (more specifically, the surface of the cavity housing the cochlea). As a quantitative measure of that energy, we consider the integral of the *absolute value* of the average energy flux density over the surface S of the cochlear cavity,

$$\Phi_S := \frac{1}{|S|} \int_S d^2r |F(\mathbf{r})| , \quad (\text{B.70})$$

where $|S|$ is the area of the surface. (We recall that, since the energy is conserved the total energy flux through a closed surface is zero – a property satisfied also, to a good accuracy, by the numerical solution.)

In computing the flux density (5.2) we use the surface S shown in Fig. 39 or a similar one. The surface is *open*: one of its boundaries opens into the vestibule, and the other to canal containing the cochlear nerve (which then passes through the inner meatus); the solution for the pressure and velocity fields is, of course, always computed with closed surfaces separating various materials.

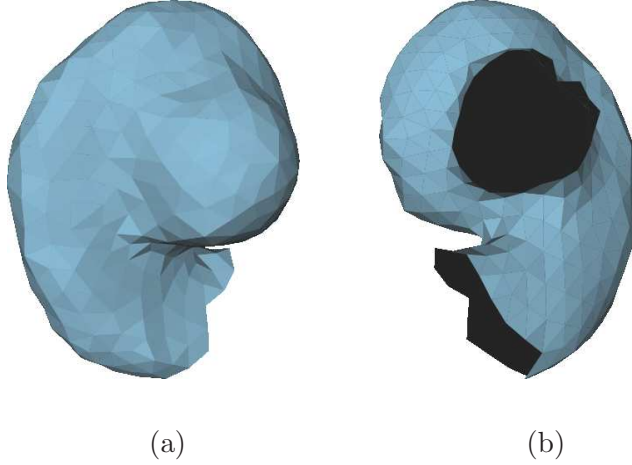


Figure 39: Discretized surface S of the skull cavity containing the left cochlea, used in the computing the energy flux Φ_S , seen from the front (a) and from the back (b) of the head. The average edge length in the discretization is about 1 mm. The dark interior of the surface is the *outer* side of the bone surface.

Fig. 40 shows the average relative energy flux (5.2) as a function of the wavelength of the incident wave. At larger wavelengths the presence of the outer auditory canal increases the energy flux by about a factor of two. At smaller wavelengths the effect is larger and exhibits a resonant behavior. The first, sharper, peak at $\lambda \approx 5$ cm is likely to be due to a resonance in the outer ear canal. The origin of the broader maximum at $\lambda \approx 15$ cm is less clear. One might speculate that it is related to vibrations of the entire skull or head; but, since it is absent in the model without the auditory canal, those vibrations would have to be excited specifically by the energy transported to the interior of the head.

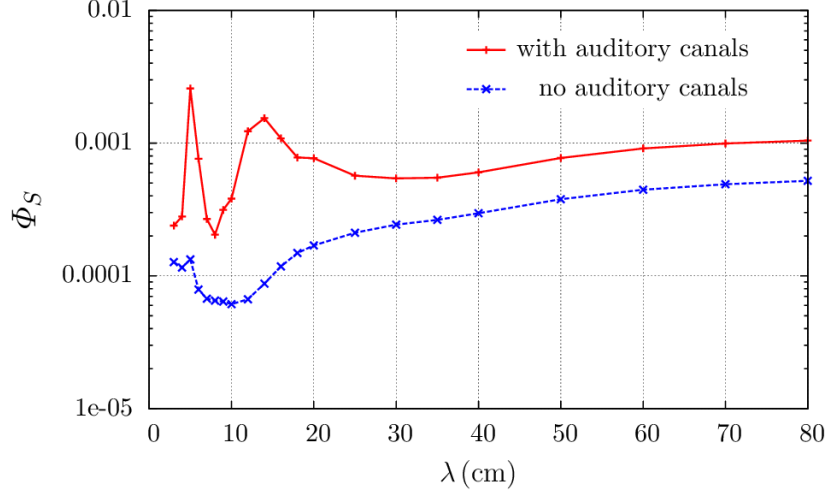


Figure 40: The average energy flux density through the surface of the cochlear cavity (relative to the incident wave flux density), as a function of the wavelength, for the model with the skull and soft tissues.

In order to assess the sensitivity of the energy flux Φ_S on the details of the inner ear, we carried out computations for three different geometries. The results, for the model of the head with the ear canals, shown in Fig. 41, indicate that the differences are minor.

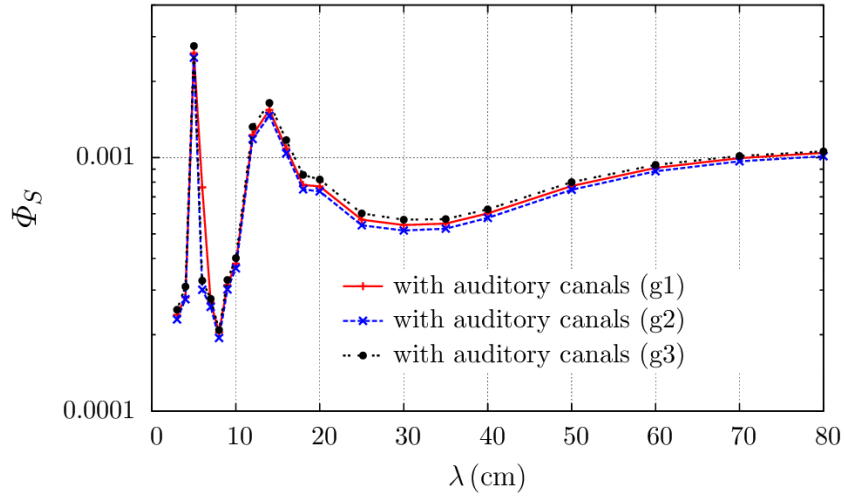


Figure 41: The average energy flux density through the surface of the cochlear cavity (relative to the incident wave flux density), as a function of the wavelength, for the model with the skull and soft tissues and three geometries (g1, g2, g3) of the inner ear cavity.

In order to correlate the observed resonant-type of the energy flux with the spatial flux distribution, we plot in Fig. 42 the flux density on the surface of the cochlear cavity, for a set of selected frequencies. The plots represents the left cochlea, subject to a sound wave incident on

the left ear, and seen from the front of the head. The positive and negative flux values indicate the energy flowing into and out of the bone surrounding the cochlea. Hence, for example, the distribution at $\lambda = 3$ cm indicates that the energy flows from the right to the left, i.e., from the outside to the inside of the head. However, the energy flow changes its direction *twice*, between the wavelengths 3 cm and 4 cm, and again between 12 cm and 14 cm.

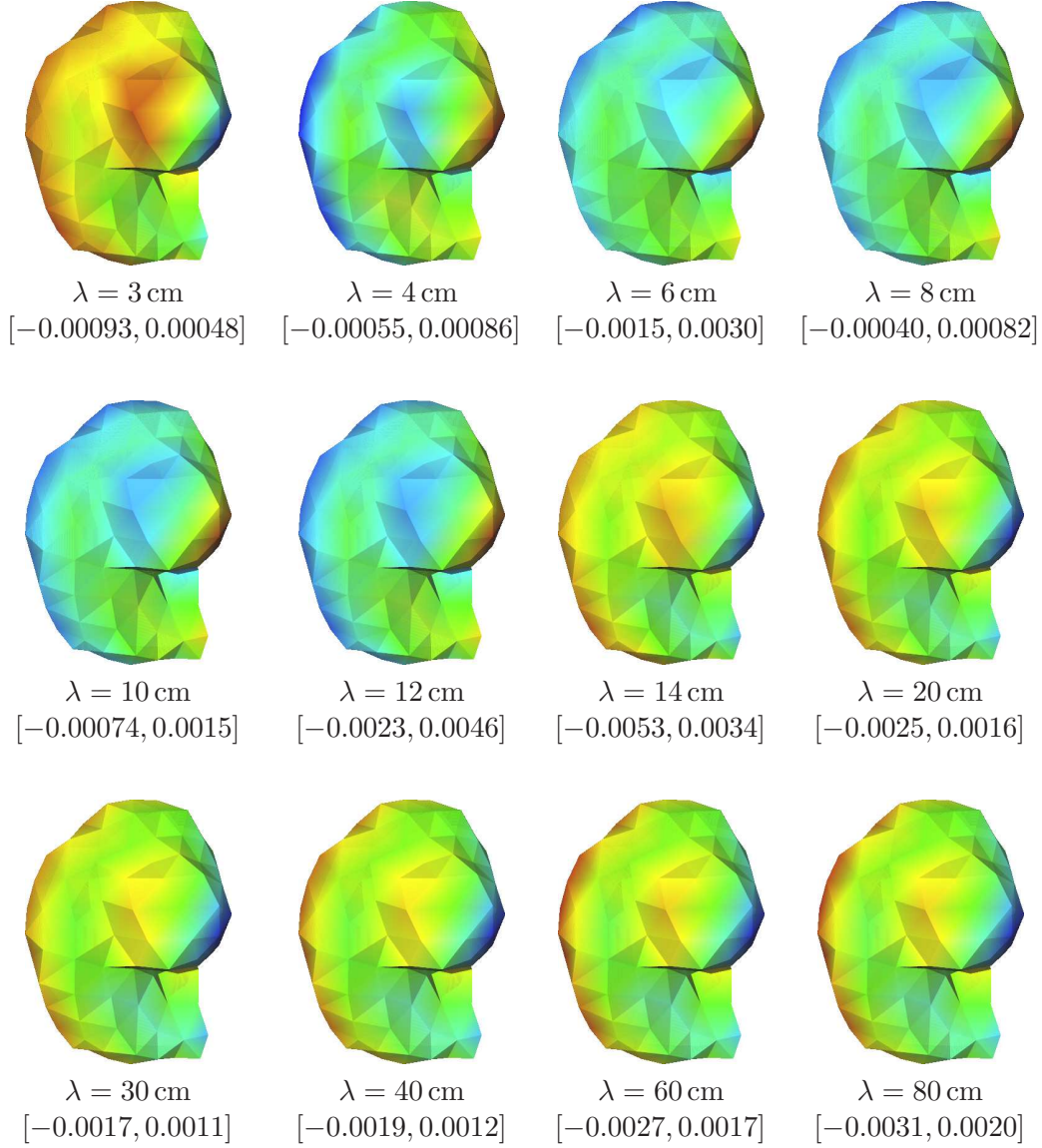


Figure 42: Distributions of the energy flux density on the surface of the left cochlear cavity (geometry g1) seen from the front, for a model of a head *with* the outer ear canals, and for the indicated wavelengths λ . Ranges of variation of the relative flux density $F(\mathbf{r})$ are shown in the square brackets.

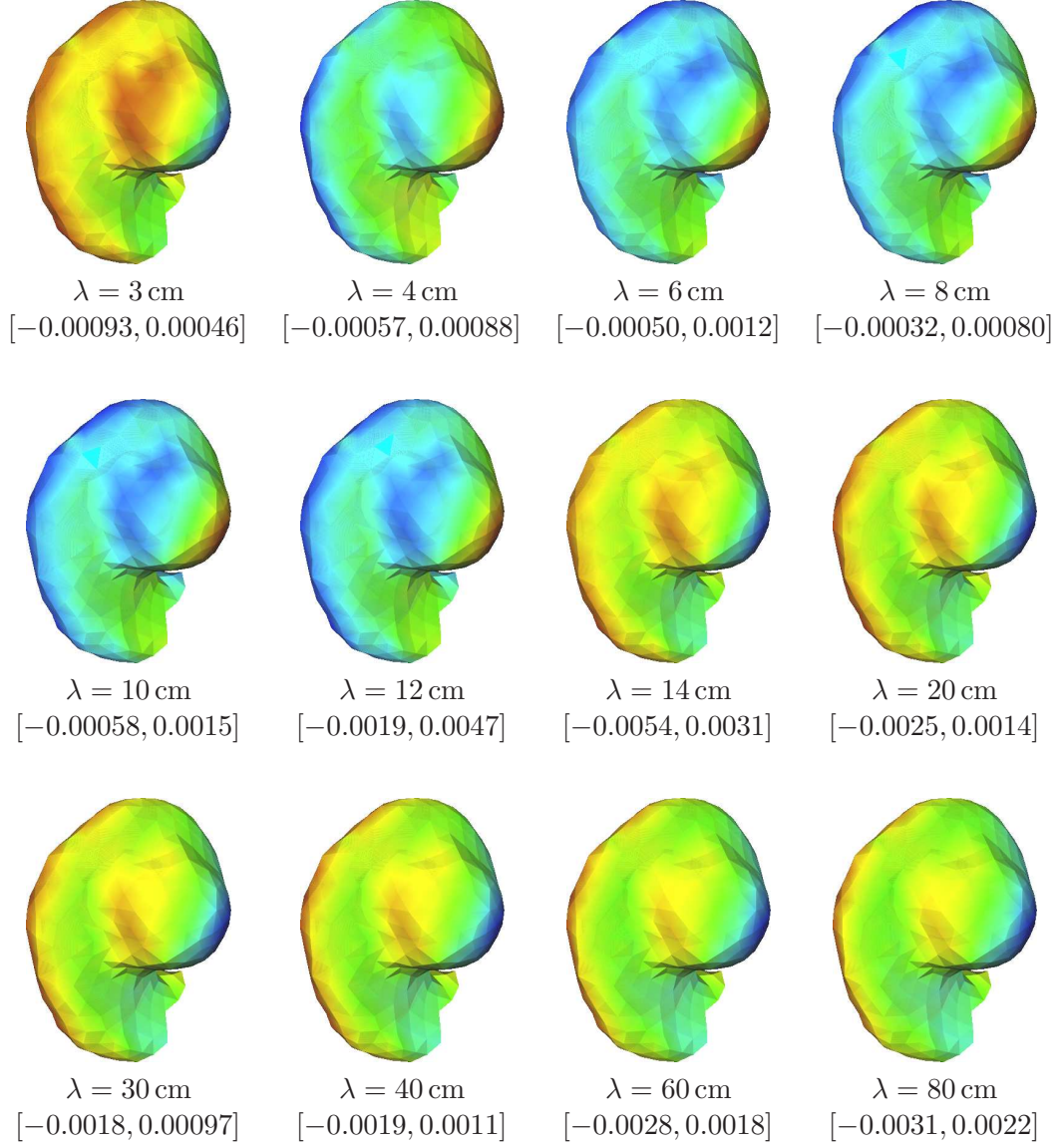


Figure 43: The same as Fig. 42, but for a more detailed model of the inner ear cavity (geometry g2), without the skull and *with* the outer ear canals, filled with the tissue of density $\rho/\rho_0 = 1000$. Discretization of the cochlear cavity is somewhat different than in the previous computation.

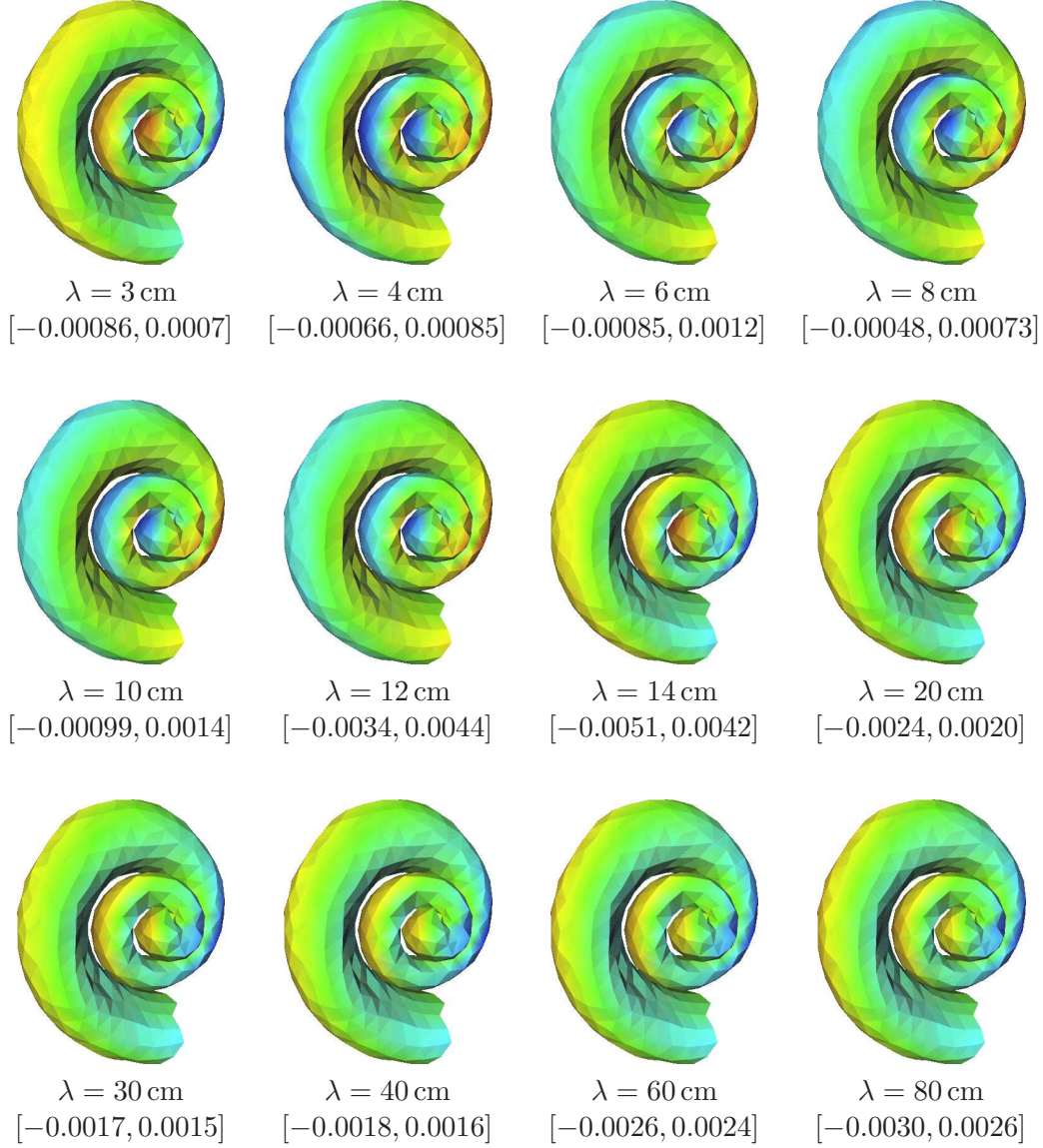


Figure 44: The same as Fig. 42, but for an even more detailed model of the inner ear cavity (geometry g_3), without the skull and *with* the outer ear canals, filled with the tissue of density $\rho/\rho_0 = 1000$. Discretization of the cochlear cavity is somewhat different than in the previous computation.

By looking at the flux distributions on the inner ear cavity and the outer ear canal we can verify that the sudden changes in the direction of the energy flow are due to changes of the field distributions in the outer ear canal near resonances seen in Figs. 40 and 41. As an example, we plot in Figs. 45 flux distributions on the middle- and inner-ear cavity for wavelengths 12 cm (a) and 14 cm (b).

The above observations are supported by the fact that in the model *without* the outer

auditory canals, and thus in the absence of noticeable resonances, the energy flow is, at all the considered wavelengths, directed from the outside to the inside of the skull.

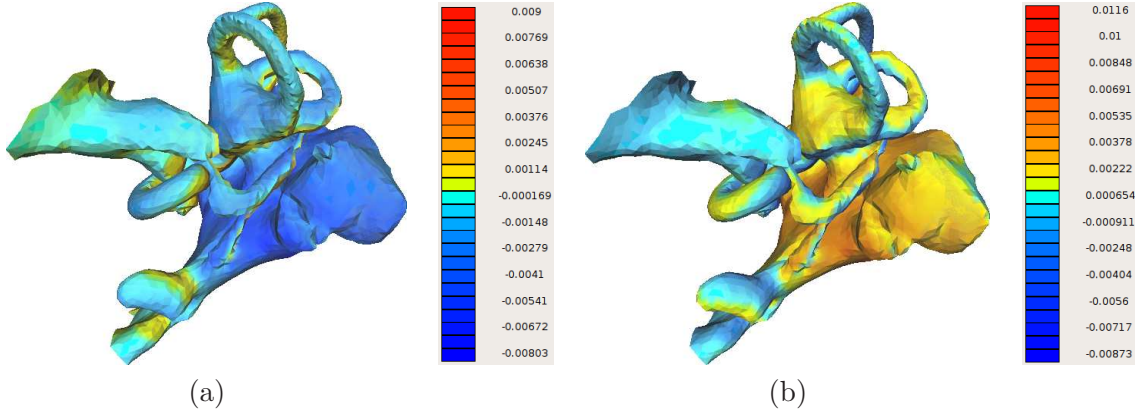


Figure 45: Energy flux density distributions on the left middle- and inner-ear cavity for wavelengths 12 cm (a) and 14 cm (b), seen from the top. The canal directed to the left and up is the inner meatus.

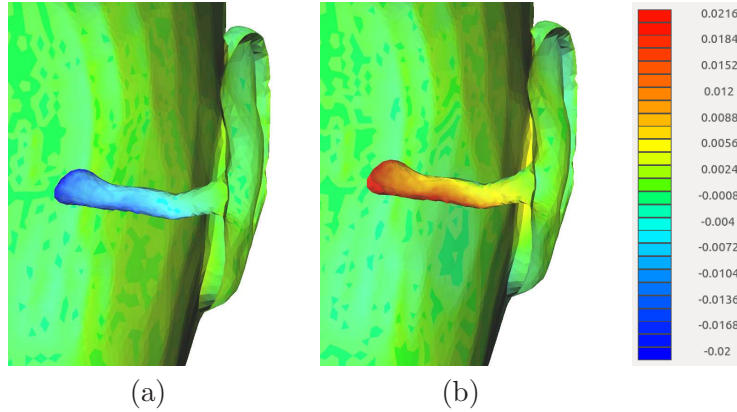


Figure 46: Energy flux density distributions on the left outer ear canal for wavelengths 12 cm (a) and 14 cm (b), seen from the front.

B.5.4 The role of acoustic bone conduction: energy flow in the *absence* of a skull (D)

In order to assess the significance of bone conduction vs. soft-tissue conduction, we also computed the amount of energy flowing through the cochlea in a model of the human head filled entirely with a *homogeneous* material, *without* the skull structure. In this comparison we

considered two models of the outer head surface: without outer ear canals (i.e., with “perfect ear-plugs”) and with ear canals.

Head surface *without* outer ear canals. We consider here two cases: the head filled with the soft tissue ($\rho/\rho_0 = 1000$, $n = 0.2$) and the bone ($\rho/\rho_0 = 2000$, $n = 0.4$). We then solve the resulting transmission problems with the outer head surface (the “skin”) and a part of the middle- and inner-ear cavity, including the cochlear cavity. Finally, we compute the average energy fluxes (5.2) through the same part S of the cochlea cavity surface as used before (Fig. 39). The results are shown in Fig. 47, together with the previous plot of Fig. 40 for the model without the outer ear canal, but *with* the skull.

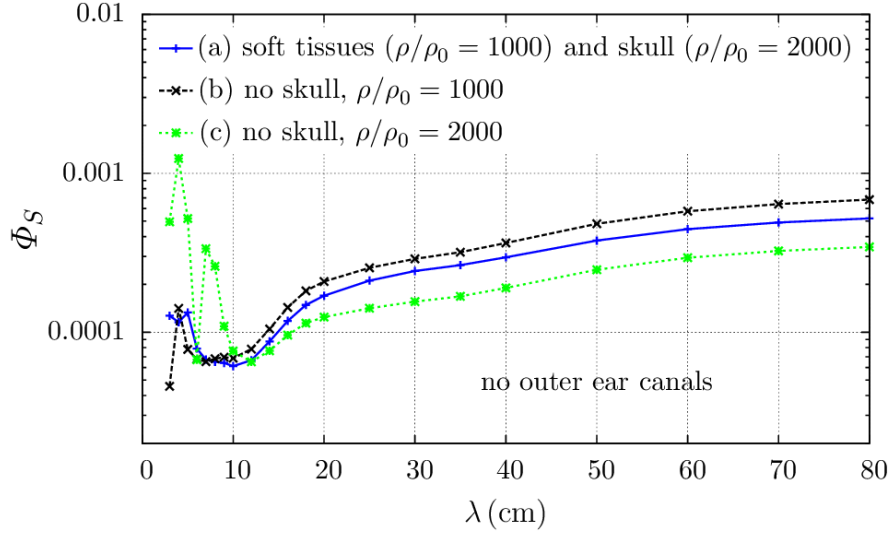


Figure 47: The average relative energy flux density through the the cochlear cavity as a function of the wavelength, for the model without the skull and two tissue densities ((b) and (c)), compared to the result for the reference model (a) with the skull. In this model the head surface model has *no outer ear canals*.

The relations between the fluxes for larger wavelengths can be plausibly explained:

- Comparison of the models (a) and (b) indicates that the presence of the higher-density skull in the soft tissue may reduce the energy flux due to its transmission through additional interfaces.
- Reduction of the flux in the model (c) compared to (b) (by about a factor of two) may be simply attributed to the higher density contrast in (c).

On the other hand, we find it difficult to explain in an intuitive way the behavior of the energy flux for wavelengths $\lambda \lesssim 10$ cm, especially for the higher-density model. As an example, we computed distributions of the pressure and velocity fields, as well as the energy flux density on the surface of the head model (c), for two wavelengths, $\lambda = 6$ cm and $\lambda = 7$ cm, for which the average flux densities Φ_S (Fig. 47) are about $6.5 \cdot 10^{-5}$ and $3.5 \cdot 10^{-4}$. The pressures for

the two wavelengths are quite similar, but the velocities for $\lambda = 7$ cm are significantly larger on most of the head surface than for $\lambda = 6$ cm. As a result, the flux density for $\lambda = 6$ cm is more concentrated near the center of the outer ear, but for $\lambda = 7$ cm it is more spread over the head surface and overall larger. This fact appears to indicate that the larger value of the flux Φ_S for $\lambda = 7$ cm is due to energy penetrating through a large area of the head surface, rather than through the vicinity of the ear.

At the same time, the wavelength-dependence of the flux for the model (b) – with the density $\rho/\rho_0 = 1000$ – is much more smooth, due to a more smooth dependence of the velocity field, but we cannot offer an explanation of that fact. Generally, we find that, as expected for the large-contrast problems, the behavior of the pressure distribution is nearly independent of the density and relatively weakly dependent on the wavelength; however, the velocity-field distribution, and thus the energy flux, vary with both the wavelength and the density in ways difficult to predict.

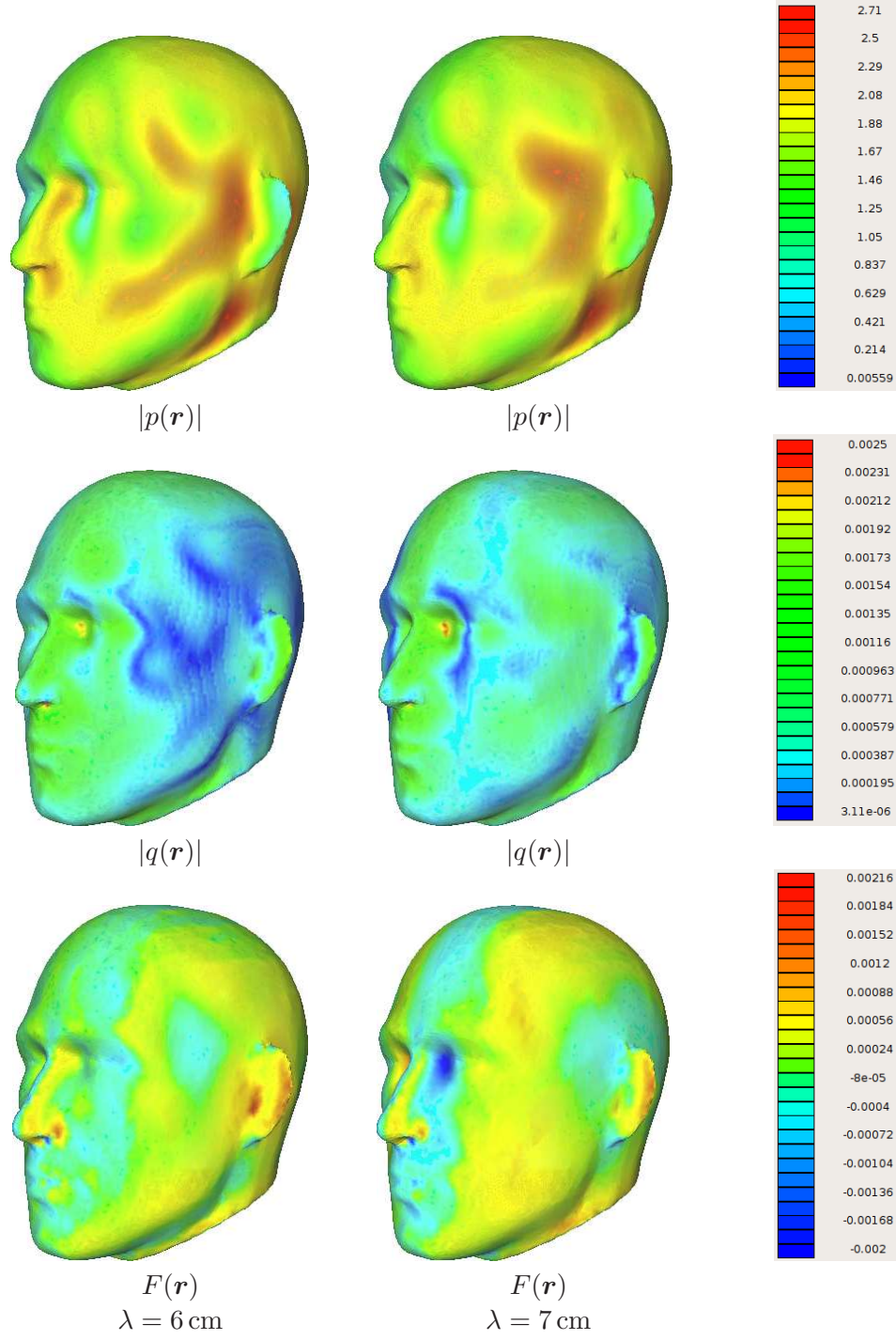


Figure 48: Distributions of the pressure and velocity fields, and of the energy flux density on the outer surface of head for $\lambda = 6$ cm (left column) and $\lambda = 7$ cm (right column), for the model without the skull and with $\rho/\rho_0 = 2000$, $n = 0.4$.

While the above discussion pertains to the energy flux on the outer surface of the head, the energy flux distributions on the cochlear cavity for several wavelengths and for the two considered materials are shown in Figs. 49 and 50. The distributions for the two materials are similar and show that, except for the first entries, the energy flux grows monotonically with the wavelength and becomes more uniform. We recall that the Figures represents the left cochlea, subject to a sound wave incident on the left ear, and seen from the front of the head. The positive and negative flux values indicate the energy flowing into and out of the bone surrounding the cochlea cavity; hence, the energy flux distributions show that the energy is flowing *from the inside to the outside of the head* – a phenomenon observed also, for some wavelengths, in the full model with the skull (Fig. 42). Again, this behavior appears to be difficult to explain intuitively without performing the actual computation.

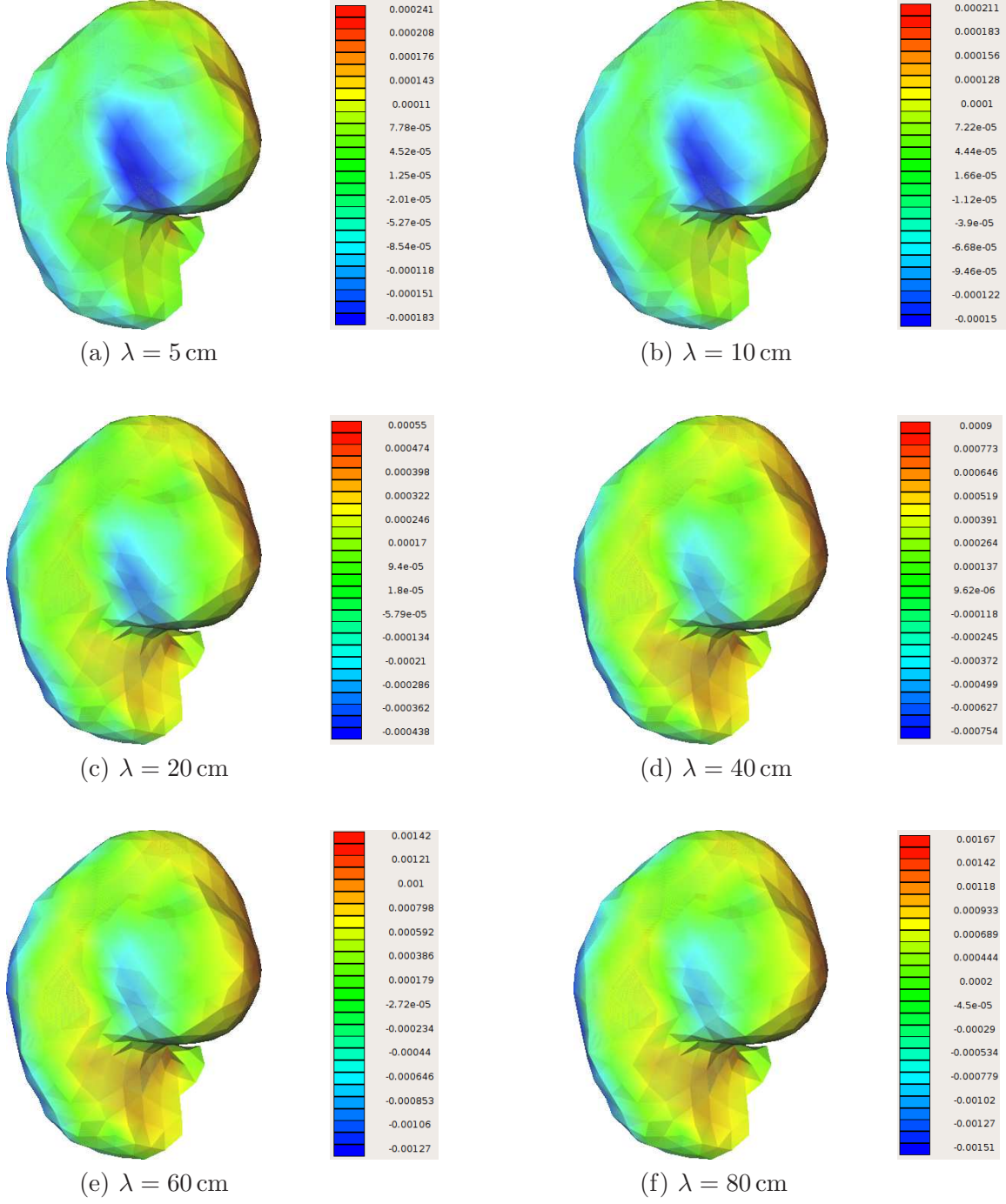


Figure 49: Distributions of the energy flux density on the surface of the left cochlea cavity, seen from the front, for a model of a head *without* the skull and with the tissue density $\rho/\rho_0 = 1000$. The distributions are shown in varying scales for a number of wavelengths, from $\lambda = 5$ cm to $\lambda = 80$ cm.

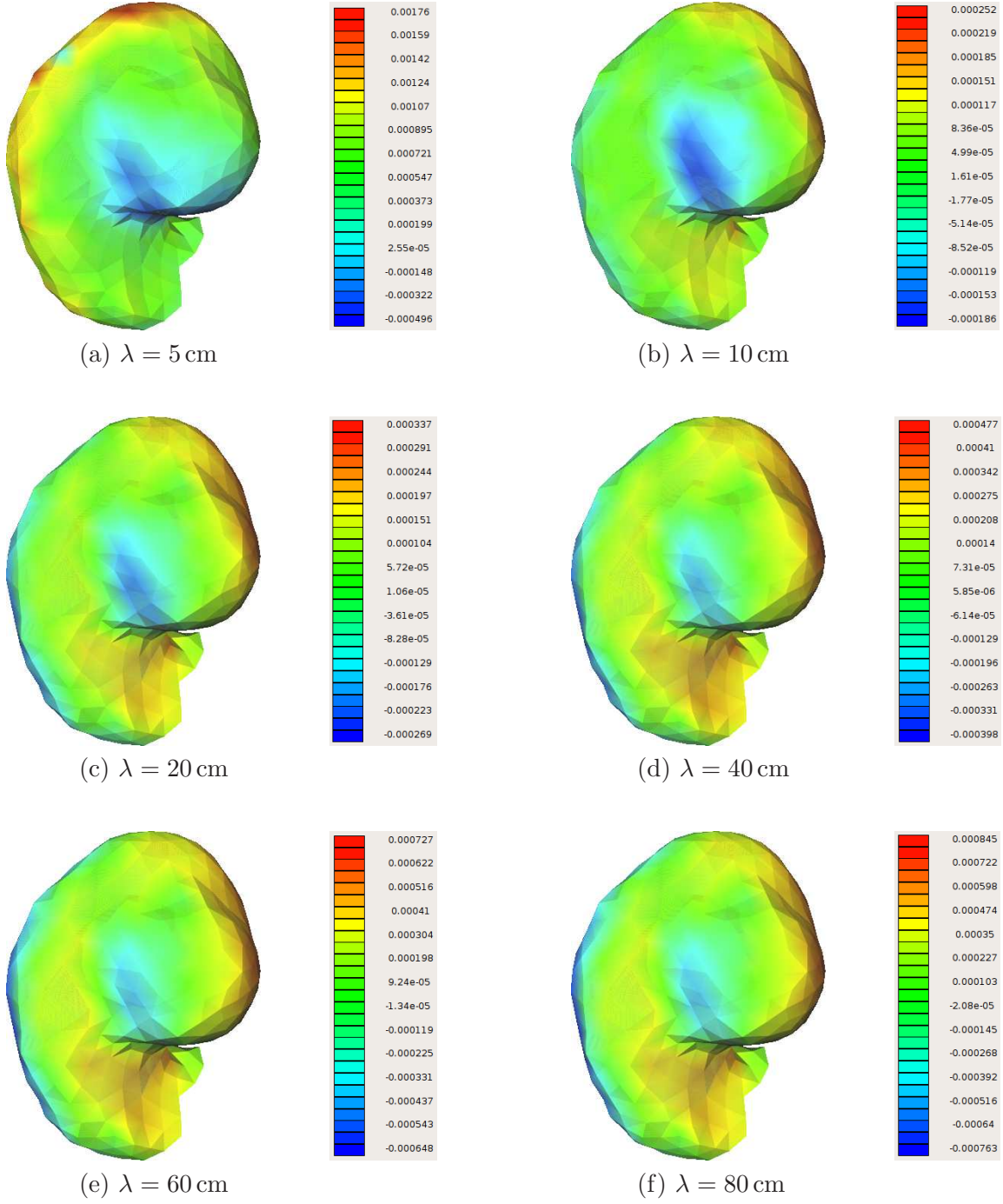


Figure 50: The same as Fig. 49, but for a the tissue density $\rho/\rho_0 = 2000$. The distributions are shown in varying scales.

Head surface *with* outer ear canals. In this problem we also consider the reference full head model with the soft tissue and the bone (a), and compare it with skull-less heads filled with either of the two materials (models (b) and (c)). The results for the average energy flux density on the cochlear cavity are shown in Fig. 51.

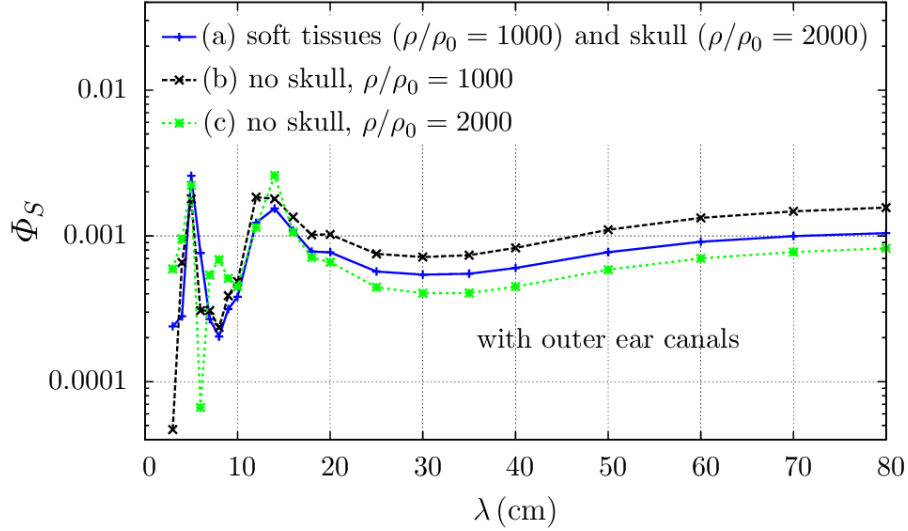


Figure 51: The average relative energy flux density through the the cochlear cavity as a function of the wavelength, for the model without the skull and two tissue densities ((b) and (c)), compared to the result for the reference model (a) with the skull. Here the head surface model contains outer ear canals.

Again, for $\lambda \gtrsim 10$ cm the flux densities in the the three models differ by less than about 30 % and the relations between them can be explained as in the previous problem. For smaller wavelengths we observe a close agreement of the models (a) and (b), but the model (c) continues to exhibit more resonance-type structure.

Now, since the skull-less model (at least for the density $\rho/\rho_0 = 1000$) yields a flux density behavior closely similar to the model with the skull, it is also of interest to analyze the flux density distribution on the cochlear cavity – as shown, for the full model, in Fig. 42. The results for the present model (with a somewhat different cavity discretization) are visualized in Fig. 52.

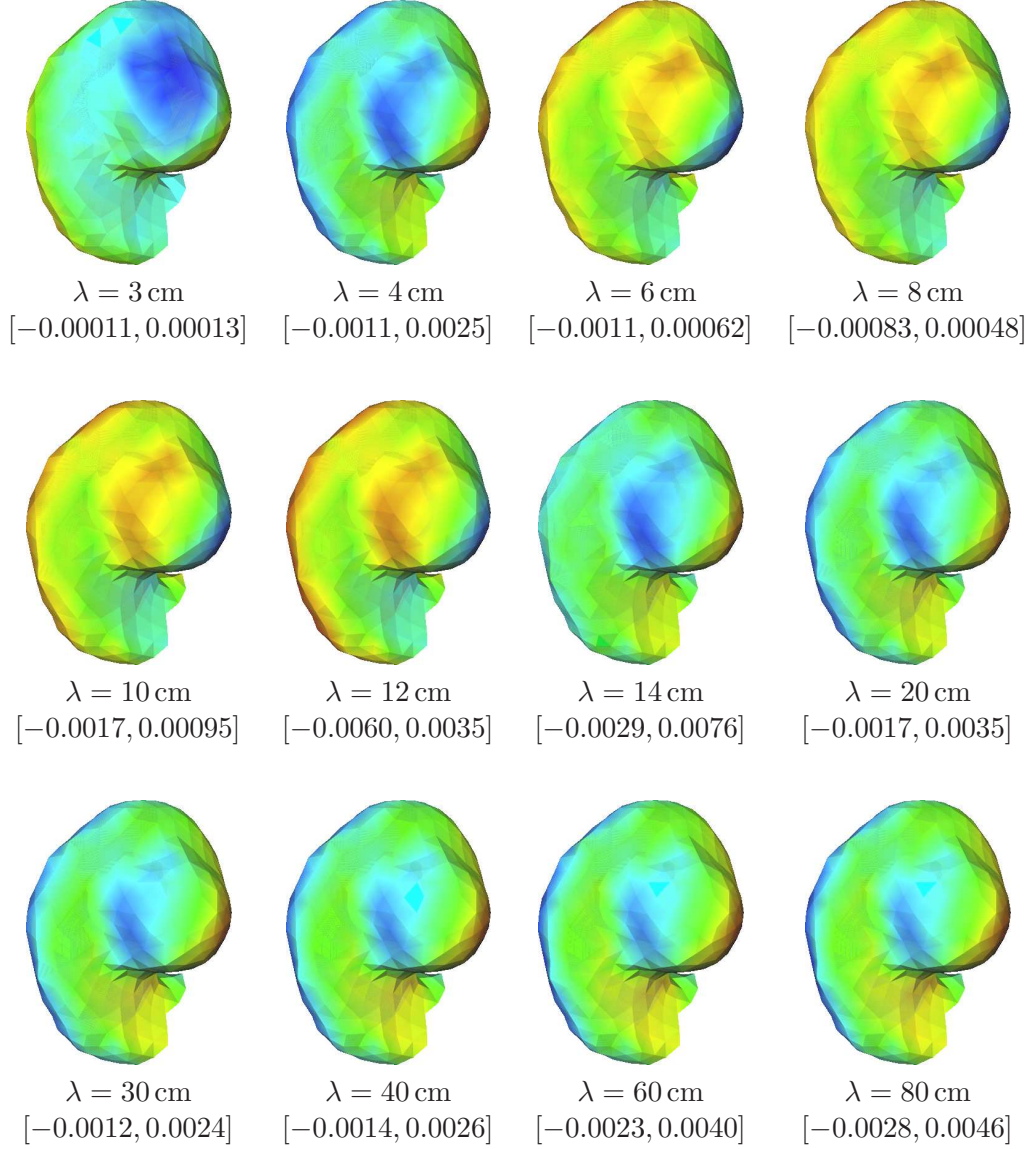


Figure 52: The counterpart of Fig. 42, now for a head model without the skull and *with* the outer ear canals, filled with the tissue of density $\rho/\rho_0 = 1000$. Discretization of the cochlear cavity is somewhat different than in the previous computation.

We observe a remarkable correlation between the distributions in Figs. 42 and 52. In both cases the energy flux through the cochlea changes direction in the resonance region. Interestingly, however, the directions of the energy flow in the two models are almost exactly *opposite* throughout the entire wavelength range! On the basis of this comparison we conjecture that

- The resonant behavior of the flux at smaller wavelengths is independent of the presence of the skull, and is thus due to the outer ear canals.

- The overall magnitude of the energy flux inside the model is primarily controlled by the outer model surface and is fairly independent of the skull.
- The skull, however, affects the local distribution of the flux, possibly through reflections from the interfaces between the bone and the soft tissue.

B.5.5 Summary of the results on energy flow

The main findings of our analysis on energy flow through the human head can be summarized as follows:

1. Transmission problems involving multi-region systems of the types listed above can be accurately solved by means of either first- or second-kind equations. Expectedly, second-kind equations have a certain advantage in terms of better conditioning and thus a smaller number of iterations in the solution.
2. Solution for the pressure on the exterior air-tissue interface is insensitive to the interior regions of the model. Actually, the pressure on that surface can be well approximated by the solution of a simpler hard-surface scattering (Neumann) problem.
3. The value of the normal derivative of the pressure on the exterior surface depends primarily on the density of the tissue adjacent of the surface, but it is also more sensitive to the materials and the geometry of the interior of the model.
4. We have observed some interesting features of the distributions of the pressure and its normal-derivative on the exterior high-contrast interface, and the corresponding features of the energy flux through the surface. As we discuss below, our problem of a high-contrast interface involves features of both the hard-surface (Neumann boundary condition) and soft-surface (Dirichlet boundary condition) problems.
 - (a) The pressure p tends to be concentrated in depressions and indentations of the surface, in particular in canals penetrating inside the object (including the outer auditory meatus). Intuitively, this behavior is expected by analogy with the temperature distribution in heat transport in the presence of an insulating boundary – formally, a problem identical to acoustic scattering off a hard (Neumann condition) surface.
 - (b) At the same time, the normal derivative of the pressure, $\partial p / \partial n$, tends to concentrate at protruding elements of the surface. Again, this behavior can be intuitively understood by analogy with the distribution of the charge density distribution on the surface of a conductor, described by the Laplace equation with the Dirichlet boundary conditions.
5. We found that the distributions of p and $\partial p / \partial n$ depend in very different ways on the surface geometry, hence the behavior of the their product (i.e., the energy flux) may be highly nontrivial and difficult to predict without an actual computation. In particular, the behavior of the energy flux in the vicinity of the outer ear canal suggests that a significant part of the non-airborne sound transmission may come from this area.

6. The comparison of the results of models with and without outer ear canals (with the latter model representing effects of “perfect ear-plugs”) shows that at relatively high frequencies (the wavelengths $\lesssim 15$ cm) a large part of the non-air-borne energy transfer to the inner ear is due to the resonant behavior of the wave in the outer ear canals. This contribution to the energy flux can be significantly reduced by blocking the ear canals. However, as the frequency decreases, the contribution of the energy penetrating through the surfaces of the head and the skull becomes dominant; and this energy-transfer mechanism can only be suppressed by protecting the entire surface of the head.

References

- [1] E. Bleszynski, M. Bleszynski, and T. Jaroszewicz, “Fast volumetric integral solver for acoustic wave propagation through inhomogeneous media,” *J. Acoust. Soc. Am.*, vol. 124, pp. 396–408, 2008.
- [2] —, “Fast volumetric integral-equation solver for high-contrast acoustics,” *J. Acoust. Soc. Am.*, vol. 124, pp. 3684–3693, 2008.
- [3] B. W. Lawton and M. R. Stinson, “Standing wave patterns in the human ear canal used for estimation of acoustic energy reflectance at the eardrum,” *The Journal of the Acoustical Society of America*, vol. 79, pp. 1003–1009, 1986.
- [4] P. M. Morse and K. U. Ingard, *Theoretical Acoustics*. New York: McGraw-Hill, 1968.
- [5] E. Bleszynski, M. Bleszynski, and T. Jaroszewicz, “AIM: Adaptive Integral Method for solving large-scale electromagnetic scattering and radiation problems,” *Radio Science*, vol. 31, pp. 1225–1251, 1996.
- [6] M. J. Ackerman, “The Visible Human project,” *J. Biocomm.*, vol. 18, 1991. [Online]. Available: <http://www.nlm.nih.gov>
- [7] M. Bonnet, S. Chaillat, and J.-F. Semblat, “Multi-level fast multipole BEM for 3-D elastodynamics,” *Recent advances in boundary element methods*, pp. 15–27, 2009.
- [8] P. G. Bergmann, “The wave equation in a medium with a variable index of refraction,” *J. Acoust. Soc. Am.*, vol. 17, pp. 329–333, 1946.
- [9] P. A. Martin, “Acoustic scattering by inhomogeneous obstacles,” *SIAM J. Appl. Math.*, vol. 64, pp. 297–308, 2003.
- [10] D. Colton and R. Kress, *Integral Equation Methods in Scattering Theory*. John Wiley & Sons, 1983.
- [11] M. Costabel and E. P. Stephan, “Integral equations for transmission problems in linear elasticity,” *J. Integral Equations and Applications*, vol. 2, pp. 211–222, 1990.
- [12] R. Kittappa and R. E. Kleinman, “Acoustic scattering by penetrable homogeneous objects,” *J. Math. Phys.*, vol. 16, pp. 421–432, 1975.
- [13] M. Costabel and E. P. Stephan, “A direct boundary integral equation method for transmission problems,” *J. Math. Anal. Appl.*, vol. 106, pp. 367–413, 1985.
- [14] R. E. Kleinman and P. A. Martin, “On single integral equations for the transmission problem of acoustics,” *SIAM J. Appl. Math.*, vol. 48, pp. 307–325, 1988.
- [15] P. A. Martin, “Identification of irregular frequencies in simple direct integral-equation methods for scattering by homogeneous inclusions,” *Wave Motion*, vol. 13, pp. 185–192, 1991.

- [16] H. Andrä, “Einführung in moderne Galerkin-Randelementmethoden mit einer Anwendung aus dem Maschinenbau,” *Forschung im Ingenieurwesen*, vol. 65, no. 2, pp. 58–90, 1999.
- [17] B. Håkansson and S. Stenfelt, “Vibration characteristics of bone conducted sound *in vitro*,” *J. Acoust. Soc. Am.*, vol. 107, pp. 422–431, 2000.
- [18] B. Håkansson, A. Brandt, P. Carlsson, and A. Tjellström, “Resonance frequencies of the human skull *in vivo*,” *J. Acoust. Soc. Am.*, vol. 95, pp. 1474–1481, 1994.

C Draft of the paper

“Formulation and Applications of the First and the Second Kind Elastodynamics Integral Equations in Simulation of Elastic Wave propagation in Human Head (part 1)”

E. Bleszynski, M. Bleszynski, and T. Jaroszewicz
Monopole Research, Thousand Oaks, CA 91360

Abstract

We present formulation and selective applications of the boundary integral method formulation in elastodynamics applicable to a general multi-domain object composed of piecewise homogeneous material regions characterized by distinct Lamé material parameters. The most exterior region may have exclusive acoustic properties.

The constructed integral equation solver offers a versatile numerical simulation framework providing high accuracy, ease of treating high-contrast interfaces and material properties, essential in modeling intricate geometrical structures with complex biological material properties present in the area of human middle and inner ear.

C.1 Introduction

We present elements of the formulation and implementation of the elastodynamics integral equation solver applicable to a general problem involving an object composed of a number of domains characterized by different Lamé material parameters. The resulting formulation consists of a coupled set of surface integral equations, for two unknown surface vector fields: displacement $\mathbf{u}(\mathbf{r})$, and the traction $\mathbf{t}(\mathbf{r})$ fields. The discrete representation of the integral equations is constructed by expanding the displacement \mathbf{u} and traction \mathbf{t} fields on material interfaces in terms of piecewise linear basis functions supported on sets of triangular facets sharing a common vertex. We have constructed two different versions of integral equations: (a) in the first-kind form and (b) in the second-kind form, for the displacement and traction fields expanded in terms of the linear node-based basis functions. We constructed explicit, numerically stable expressions for Galerkin matrix elements, of all pertinent kernels appearing in both types of integral equations for solid-solid, fluid-solid, and fluid-fluid material interfaces.

In order to be able to handle the large scale realistic numerical simulations we interfaced the solver with a suitable FFT-based matrix compression algorithm which reduces the numerical complexity of the iterative solution to $N \log N$. The choice of the compression method is motivated by its efficiency in treatment of subwavelength problems present at frequencies associated with typical external acoustic excitation. The parallelization scheme for the matrix-compressed version of the elastodynamics integral equations has been developed as well.

C.2 Lamé differential equations

We start with the Lamé equation for the displacement in elastic medium characterized by Lamé coefficients λ and μ . The displacement $\mathbf{u}(\mathbf{r})$ and the stress tensor $\hat{\tau}(\mathbf{r})$

$$\hat{\tau}(\mathbf{r}, \omega) = \lambda \hat{I} \nabla_{\mathbf{r}} \cdot \mathbf{u}(\mathbf{r}) + \mu [\nabla_{\mathbf{r}} \otimes \mathbf{u}(\mathbf{r}, \omega) + \mathbf{u}(\mathbf{r}, \omega) \otimes \nabla_{\mathbf{r}}]$$

satisfy the following equations

$$\begin{aligned} \{(\lambda + \mu)\nabla_{\mathbf{x}} \otimes \nabla_{\mathbf{x}} + \mu\nabla_{\mathbf{x}}^2 + \rho\omega^2\}\mathbf{u}(\mathbf{x}, \omega) &= \rho(\mathbf{x})\mathbf{F}(\mathbf{x}, \omega), \\ \nabla_{\mathbf{x}} \cdot \hat{\tau}(\mathbf{x}, \omega) + \rho(\mathbf{x})\omega^2\mathbf{u}(\mathbf{x}, \omega) &= -\rho(\mathbf{x})\mathbf{F}(\mathbf{x}, \omega), \end{aligned} \quad (\text{C.1})$$

The Green function of the Lamé equation is the second rank symmetric tensor

$$\begin{aligned} \hat{G}(\mathbf{R}) &= C(R)\hat{I} + \nabla_{\mathbf{R}} \otimes \nabla_{\mathbf{R}}D(R) \\ C(R) &= \frac{1}{\mu}g_S(R), \\ D(R) &= \frac{1}{\mu k_S^2}[g_S(R) - g_C(R)], \end{aligned} \quad (\text{C.2})$$

with

$$\begin{aligned} \mathbf{R} &= \mathbf{x} - \mathbf{y}. \\ g_C(R) &= \frac{e^{ik_C R}}{4\pi R}, \\ g_S(R) &= \frac{e^{ik_S R}}{4\pi R}, \\ \nabla_{\mathbf{R}}^2 g_C(R) &= -k_C^2 g_C(R) - \delta(\mathbf{R}), \\ \nabla_{\mathbf{R}}^2 g_S(R) &= -k_S^2 g_S(R) - \delta(\mathbf{R}), \\ \nabla_{\mathbf{R}}^2 D(R) &= \frac{1}{\mu k_S^2}[k_C^2 g_C(R) - k_S^2 g_S(R)], \\ \frac{1}{\rho\omega^2}k_C^2 g_C(R) &= \frac{k_C^2}{k_S^2}C(R) - k_C^2 D(R), \\ \nabla_{\mathbf{R}} \cdot \hat{G}(\mathbf{R}) &= \frac{k_C^2}{\mu k_S^2}\nabla_{\mathbf{R}} g_C(R) = \frac{1}{\lambda + 2\mu}\nabla_{\mathbf{R}} g_C(R), \end{aligned} \quad (\text{C.3})$$

We define the stress tensor

$$\begin{aligned} \hat{\tau}(\mathbf{y}) &= \lambda \hat{I} \nabla_{\mathbf{y}} \cdot \mathbf{u}(\mathbf{y}) + \mu[\nabla_{\mathbf{y}} \otimes \mathbf{u}(\mathbf{y}) + \mathbf{u}(\mathbf{y}) \otimes \nabla_{\mathbf{y}}], \\ \hat{\tau}_{ij}(\mathbf{y}) &= C_{ijkm}\partial_k u_m(\mathbf{y}), \\ C_{ijkl} &= \lambda\delta_{ij}\delta_{kl} + \mu(\delta_{ik}\delta_{jl} + \delta_{il}\delta_{jk}), \end{aligned} \quad (\text{C.4})$$

The two wave-numbers,

$$k_C = \frac{\omega}{c_C}, \quad k_S = \frac{\omega}{c_S}, \quad (\text{C.5})$$

are related to the longitudinal (compressional) and transverse (shear) wave speeds as follows

$$c_C = \sqrt{\frac{\lambda + 2\mu}{\rho}}, \quad c_S = \sqrt{\frac{\mu}{\rho}}. \quad (\text{C.6})$$

$$\begin{aligned}
\hat{\Gamma}(\mathbf{x}, \mathbf{y}) &= \hat{\mathbf{n}}(\mathbf{y}) \cdot \hat{\Sigma}(\mathbf{R}), \\
\Gamma_{ij}(\mathbf{x}, \mathbf{y}) &= \frac{\partial}{\partial y_q} G_{ip}(\mathbf{x} - \mathbf{y}) C_{j k p q} n_k(\mathbf{y}) = \{\hat{\mathbf{n}}(\mathbf{y}) \cdot \hat{\Sigma}(\mathbf{x} - \mathbf{y})\}_{ij} = n_i(\mathbf{y}) C_{ij m l} \partial_m G_{l k}(\mathbf{R}), \\
\hat{\Sigma}(\mathbf{R}) &= \lambda \hat{\mathbf{I}} \nabla \cdot \hat{\mathbf{G}}(\mathbf{R}) + \mu \nabla \otimes \hat{\mathbf{G}}(\mathbf{R}) + \mu \hat{\mathbf{G}}(\mathbf{R}) \otimes \nabla, \\
[\hat{\Sigma}(\mathbf{R})]_{ijk} &= \lambda \delta_{ij} \partial_m G_{mk}(\mathbf{R}) + \mu [\partial_i G_{jk}(\mathbf{R}) + \partial_j G_{ik}(\mathbf{R})] = C_{ij m l} \partial_m G_{l k}(\mathbf{R}), \\
\Gamma_{jk}(\mathbf{x}, \mathbf{y}) &= n_i(\mathbf{y}) \Sigma_{ijk}, \\
\Phi_{jk}(\mathbf{x}, \mathbf{y}) &= \Sigma_{ijk} n_i(\mathbf{x}) \\
\hat{\Sigma}(\mathbf{R}) &= -\hat{\Sigma}(-\mathbf{R}).
\end{aligned} \tag{C.7}$$

The Green tensor functions $\hat{\mathbf{G}}(\mathbf{R})$ and $\hat{\Sigma}(\mathbf{R})$ satisfy the following equations

$$\begin{aligned}
[(\lambda + \mu) \nabla_{\mathbf{R}} \otimes \nabla_{\mathbf{R}} + \mu \nabla_{\mathbf{R}}^2 + \rho \omega^2] \hat{\mathbf{G}}(\mathbf{R}) &= -\delta(\mathbf{R}) \hat{\mathbf{I}}, \\
\nabla_{\mathbf{R}} \cdot \hat{\Sigma}(\mathbf{R}) + \rho \omega^2 \hat{\mathbf{G}}(\mathbf{R}) &= -\delta(\mathbf{R}) \hat{\mathbf{I}}, \\
\hat{\Sigma}(\mathbf{R}) \cdot \nabla_{\mathbf{R}} + \rho \omega^2 \hat{\mathbf{G}}(\mathbf{R}) - \lambda (\nabla_{\mathbf{R}} \cdot -\nabla_{\mathbf{R}} \otimes) \nabla_{\mathbf{R}} \cdot \hat{\mathbf{G}}(\mathbf{R}) &= -\delta(\mathbf{R}) \hat{\mathbf{I}}, \\
\partial_i [C_{ijkl} \partial_k \hat{G}_{lm}(\mathbf{R})] + \rho \omega^2 \hat{G}_{jm}(\mathbf{R}) &= -\delta_{jm} \delta(\mathbf{R}), \\
\partial_i [\hat{\Sigma}_{ijm}(\mathbf{R})] + \rho \omega^2 \hat{G}_{jm}(\mathbf{R}) &= -\delta_{jm} \delta(\mathbf{R}), \\
\nabla_{\mathbf{R}} \cdot \hat{\mathbf{G}}(\mathbf{R}) &= \frac{1}{\lambda + 2\mu} \nabla_{\mathbf{R}} g_C(\mathbf{R}),
\end{aligned} \tag{C.8}$$

while $\hat{\tau}(\mathbf{x})$ satisfies the following equation

$$\begin{aligned}
\rho(\mathbf{r}) \omega^2 \mathbf{u}(\mathbf{r}) &= 0, \\
\frac{1}{2} [\nabla_{\mathbf{r}} \otimes \mathbf{u}(\mathbf{r}) + \mathbf{u}(\mathbf{r}) \otimes \nabla_{\mathbf{r}}] - \hat{\tau}_{kl}(\mathbf{r}) &= 0,
\end{aligned} \tag{C.9}$$

where

$$\begin{aligned}
C_{ijkl} &= \lambda \delta_{ij} \delta_{kl} + \mu (\delta_{ik} \delta_{jl} + \delta_{il} \delta_{jk}) \\
D_{ijkl} &= \frac{1}{4\mu} \left[(\delta_{ik} \delta_{jl} + \delta_{il} \delta_{jk}) - \frac{2\lambda}{3\lambda + 2\mu} \delta_{ij} \delta_{kl} \right] = \\
&= \frac{1}{4\mu} \left[\frac{1}{\mu} C_{ijkl} - \frac{\lambda}{\mu} \delta_{ij} \delta_{kl} - \frac{2\lambda}{3\lambda + 2\mu} \delta_{ij} \delta_{kl} \right] = \\
C_{ijkl} &= C_{jikl} = C_{ijlk} = C_{klij}.
\end{aligned} \tag{C.10}$$

is the 4-th rank elastic stiffness tensor. A useful relation is

$$C_{ijkl} \partial_k u_l(\mathbf{x}) \partial_i G_{jm}(\mathbf{R}) - C_{ijkl} \partial_i u_j(\mathbf{x}) \partial_k G_{lm}(\mathbf{R}) = 0. \tag{C.11}$$

C.3 Representation formulae in elastodynamics

C.3.1 Representation formulae for the displacement field

We consider a single region Ω bounded by $\partial\Omega$ containing homogeneous material with Lamé parameters λ and μ (see Fig. 53). By assuming that, inside Ω the displacement $\mathbf{u}(\mathbf{x})$ satisfies the Lamé equation (C.14)

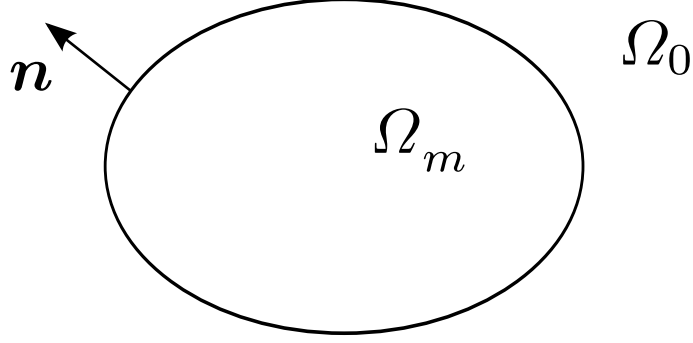


Figure 53: A region $\Omega \equiv \Omega_m$ separated by $\partial\Omega$ in Ω_0 used in the derivation of the integral representation for \mathbf{u} .

The integral representations for the displacement and traction fields inside and a region Ω can be derived by applying the of Gauss divergence formula to the equations satisfied by the Green tensor functions $\hat{G}(\mathbf{R})$ and $\hat{\Sigma}(\mathbf{R})$ for a single frequency ω :

$$\begin{aligned}\nabla_{\mathbf{y}} \cdot \hat{\tau}(\mathbf{y}) + \rho\omega^2 \mathbf{u}(\mathbf{y}) &= -\rho(\mathbf{y})\mathbf{F}(\mathbf{y}), \\ \nabla_{\mathbf{y}} \cdot \hat{\Sigma}(\mathbf{y}, \mathbf{x}) + \rho\omega^2 \hat{G}(\mathbf{y}, \mathbf{x}) &= -\delta(\mathbf{y} - \mathbf{x})\hat{I},\end{aligned}\tag{C.12}$$

By multiplying the first of the above equations by $\hat{G}(\mathbf{x}, \mathbf{y})$ from the right side and by multiplying the second by $\mathbf{u}(\mathbf{x})$ from the left side and by subtracting them we obtain

$$[\nabla_{\mathbf{y}} \cdot \hat{\tau}(\mathbf{y})] \cdot \hat{G}(\mathbf{y}, \mathbf{x}) - \mathbf{u}(\mathbf{y}) \cdot [\nabla_{\mathbf{y}} \cdot \hat{\Sigma}(\mathbf{y}, \mathbf{x})] = \mathbf{u}(\mathbf{y})\delta(\mathbf{y} - \mathbf{x}) - \rho(\mathbf{y})[\mathbf{F}(\mathbf{y}) \cdot \hat{G}(\mathbf{y}, \mathbf{x})], \tag{C.13}$$

But

$$\begin{aligned}\nabla_{\mathbf{y}} \cdot \{\hat{\tau}(\mathbf{y}) \cdot \hat{G}(\mathbf{y}, \mathbf{x})\} - \mathbf{u}(\mathbf{y}) \cdot \hat{\Sigma}(\mathbf{y}, \mathbf{x})] &= [\nabla_{\mathbf{y}} \cdot \hat{\tau}(\mathbf{y})] \cdot \hat{G}(\mathbf{y}, \mathbf{x}) - \mathbf{u}(\mathbf{y}) \cdot [\nabla_{\mathbf{y}} \cdot \hat{\Sigma}(\mathbf{y}, \mathbf{x})] + \\ &+ [\hat{\tau}(\mathbf{y})] \cdot \cdot [\nabla_{\mathbf{y}} \otimes \hat{G}(\mathbf{y}, \mathbf{x})] - [\nabla_{\mathbf{y}} \otimes \mathbf{u}(\mathbf{y})] \cdot \cdot [\hat{\Sigma}(\mathbf{y}, \mathbf{x})]\end{aligned}\tag{C.14}$$

where $\cdot \cdot$ denotes contraction in the first two indices,

Also,

$$\begin{aligned}\hat{\Sigma}(\mathbf{x} - \mathbf{y}) &= -\hat{\Sigma}(\mathbf{y} - \mathbf{x}), \\ \hat{G}(\mathbf{x}, \mathbf{y}) &= \hat{G}(\mathbf{y}, \mathbf{x}), \\ \nabla_{\mathbf{y}} \cdot \hat{G}(\mathbf{y}, \mathbf{x}) &= -\nabla_{\mathbf{x}} \cdot \hat{G}(\mathbf{y}, \mathbf{x}),\end{aligned}\tag{C.15}$$

and

$$[\nabla_{\mathbf{y}} \otimes \mathbf{u}(\mathbf{y})] \cdot \cdot [\hat{\Sigma}(\mathbf{y}, \mathbf{x}, \omega)] - [\hat{\tau}(\mathbf{y})] \cdot \cdot [\nabla_{\mathbf{y}} \otimes \hat{G}(\mathbf{y}, \mathbf{x})] = 0 \tag{C.16}$$

Let us verify the above identity in the indicial notation

$$\begin{aligned}\frac{\partial u_j}{\partial y_i} \hat{\Sigma}_{ijk}(\mathbf{y}, \mathbf{x}) - \hat{\tau}_{ij}(\mathbf{y}) \frac{\partial \hat{G}_{jk}(\mathbf{y}, \mathbf{x})}{\partial y_i} &= \frac{\partial u_j}{\partial y_i} C_{ijmn} \frac{\partial \hat{G}_{nk}(\mathbf{y}, \mathbf{x})}{\partial y_m} - C_{ijmn} \frac{\partial u_n}{\partial y_m} \frac{\partial \hat{G}_{jk}(\mathbf{y}, \mathbf{x})}{\partial y_i} = \\ &= \frac{\partial u_n}{\partial y_m} C_{mni j} \frac{\partial \hat{G}_{jk}(\mathbf{y}, \mathbf{x})}{\partial y_i} - C_{ijmn} \frac{\partial u_n}{\partial y_m} \frac{\partial \hat{G}_{jk}(\mathbf{y}, \mathbf{x})}{\partial y_i} = 0\end{aligned}\tag{C.17}$$

We may now rewrite (C.14) as follows

$$= \nabla_{\mathbf{y}} \cdot \{\hat{\tau}(\mathbf{y}) \cdot \hat{G}(\mathbf{x}, \mathbf{y}) + \mathbf{u}(\mathbf{y}) \cdot \hat{\Sigma}(\mathbf{x}, \mathbf{y})\} = \mathbf{u}(\mathbf{y})\delta(\mathbf{x} - \mathbf{y}) - \rho(\mathbf{y})[\mathbf{F}(\mathbf{y}) \cdot \hat{G}(\mathbf{x}, \mathbf{y})], \quad (\text{C.18})$$

By taking the volume integral of the above equation we obtain and by applying the Gauss divergence formula we may convert left side to the surface integral

$$\begin{aligned} & \int_{\Omega} dV \nabla_{\mathbf{y}} \cdot \{\hat{\tau}(\mathbf{y}) \cdot \hat{G}(\mathbf{x}, \mathbf{y}) + \mathbf{u}(\mathbf{y}) \cdot \hat{\Sigma}(\mathbf{x}, \mathbf{y})\} = \\ &= \int_{\partial\Omega} dS_{\mathbf{y}} \{[\hat{\mathbf{n}}(\mathbf{y}) \cdot \hat{\tau}(\mathbf{y})] \cdot \hat{G}(\mathbf{x}, \mathbf{y}) + [\mathbf{u}(\mathbf{y}) \cdot \hat{\mathbf{n}}(\mathbf{y}) \cdot \hat{\Sigma}(\mathbf{x}, \mathbf{y})]\} = \\ &= \int_{\partial\Omega} dS_{\mathbf{y}} \{\mathbf{t}(\mathbf{y}) \cdot \hat{G}(\mathbf{x}, \mathbf{y}) + \mathbf{u}(\mathbf{y}) \cdot \hat{I}(\mathbf{x}, \mathbf{y})\} \end{aligned} \quad (\text{C.19})$$

We obtain the integral representation for the displacement field for a region Ω bounded by $\partial\Omega$ which allows to find the value of the displacement field at any point \mathbf{x} in Ω in terms of the integral of 2 fields $\mathbf{u}(\mathbf{x})$ and $\mathbf{t}(\mathbf{x})$ on the region boundary for $\mathbf{u}(\mathbf{x})$

$$\begin{aligned} \int_{\partial\Omega} dS_{\mathbf{y}} [\mathbf{t}(\mathbf{y}) \cdot \hat{G}(\mathbf{x}, \mathbf{y}) + \mathbf{u}(\mathbf{y}) \cdot \hat{I}(\mathbf{x}, \mathbf{y})] &= \begin{cases} \mathbf{u}(\mathbf{x}) & \text{for } \mathbf{x} \notin \Omega, \\ \mathbf{0} & \text{for } \mathbf{x} \in \Omega. \end{cases} \\ \mathbf{t}(\mathbf{y}) &= \hat{\mathbf{n}}(\mathbf{y}) \cdot \hat{\tau}(\mathbf{y}), \\ \hat{I}(\mathbf{x}, \mathbf{y}) &= \hat{\mathbf{n}}(\mathbf{y}) \cdot \hat{\Sigma}(\mathbf{x}, \mathbf{y}), \end{aligned} \quad (\text{C.20})$$

The symbols appearing in the integrand of the above integral representations are as follows

- $\mathbf{u}(\mathbf{y})$ is the displacement vector field
- $\mathbf{t}(\mathbf{y})$ is the traction vector field related to the stress tensor $\hat{\tau}(\mathbf{y})$ as follows

$$\begin{aligned} \mathbf{t}(\mathbf{y}) &= \hat{\mathbf{n}}(\mathbf{y}) \cdot \hat{\tau}(\mathbf{y}) = \\ &= \lambda \hat{\mathbf{n}}(\mathbf{y})[\nabla_{\mathbf{y}} \cdot \mathbf{u}(\mathbf{y})] + \mu\{[\hat{\mathbf{n}}(\mathbf{y}) \cdot \nabla_{\mathbf{y}}]\mathbf{u}(\mathbf{y}) + \nabla_{\mathbf{y}}[\hat{\mathbf{n}}(\mathbf{y}) \cdot \mathbf{u}(\mathbf{y})]\}, \end{aligned} \quad (\text{C.21})$$

- $\hat{G}(\mathbf{x} - \mathbf{y})$ is a second rank symmetric tensor, the Green function of the Lamé equation given by (C.2)
- $\hat{I}(\mathbf{x}, \mathbf{y})$ is a second rank non-symmetric tensor, related to
- $\hat{\Sigma}(\mathbf{x})$, a third rank stress tensor (symmetric in first 2 indices)

C.3.2 Representation formulae for the traction field

In this section we construct the representation formulas for the traction field which we will use in the context of first kind of integral equation formulation. We consider a single region Ω bounded by $\partial\Omega$ By assuming that, inside Ω the displacement $\mathbf{u}(\mathbf{x})$ satisfies the Lamé

equation (C.14) we may construct the **integral representations for the traction fields** inside and a region Ω . We obtain the integral representation for the displacement field for a region Ω bounded by $\partial\Omega$ which allows to find the value of the displacement field at any point \mathbf{x} in Ω in terms of the integral of 2 fields $\mathbf{u}(\mathbf{x})$ and $\mathbf{t}(\mathbf{x})$ on the region boundary

$$\int_{\partial\Omega} dS_{\mathbf{y}} [\mathbf{t}(\mathbf{y}) \cdot \hat{\Phi}(\mathbf{x}, \mathbf{y}) + \mathbf{u}(\mathbf{y}) \cdot \hat{W}(\mathbf{x}, \mathbf{y})] = \begin{cases} \mathbf{t}(\mathbf{x}) & \text{for } \mathbf{x} \notin \Omega, \\ \mathbf{0} & \text{for } \mathbf{x} \in \Omega^+. \end{cases} \quad (\text{C.22})$$

$$\mathbf{t}(\mathbf{y}) = \hat{\mathbf{n}}(\mathbf{y}) \cdot \hat{\tau}(\mathbf{y}),$$

$$\hat{F}(\mathbf{x}, \mathbf{y}) = \hat{\mathbf{n}}(\mathbf{y}) \cdot \hat{\Sigma}(\mathbf{x}, \mathbf{y}),$$

where Ω^+ denotes the position located just above the surface Ω .

In order to construct the above **integral representation for the traction field** outside region Ω bounded by $\partial\Omega$ we applying the traction field operator to the integral representation for displacement $\mathbf{u}(\mathbf{x})$

$$\begin{aligned} \hat{\tau}[\mathbf{u}(\mathbf{x})] &= \lambda \hat{F}[\nabla_{\mathbf{x}} \cdot \mathbf{u}(\mathbf{x})] + \mu [\nabla_{\mathbf{x}} \otimes \mathbf{u}(\mathbf{x}) + \mathbf{u}(\mathbf{x}) \otimes \nabla_{\mathbf{x}}] = \\ &= \hat{\tau} \left\{ \int_{\partial\Omega} dS_{\mathbf{y}} [\mathbf{u}(\mathbf{y}) \cdot \hat{F}(\mathbf{x}, \mathbf{y}) + \mathbf{t}(\mathbf{y}) \cdot \hat{G}(\mathbf{x}, \mathbf{y})] \right\} \\ &= \int_{\partial\Omega} dS_{\mathbf{y}} [\hat{\tau}[\mathbf{u}(\mathbf{y}) \cdot \hat{F}(\mathbf{x}, \mathbf{y})] + \hat{\tau}[\mathbf{t}(\mathbf{y}) \cdot \hat{G}(\mathbf{x}, \mathbf{y})]] \\ \hat{\tau}[\mathbf{u}(\mathbf{y}) \cdot \hat{F}(\mathbf{x}, \mathbf{y})] &= \lambda \hat{F} \nabla_{\mathbf{x}} \cdot [\mathbf{u}(\mathbf{y}) \cdot \hat{F}(\mathbf{x}, \mathbf{y})] + \mu \nabla_{\mathbf{x}} \otimes [\mathbf{u}(\mathbf{y}) \cdot \hat{F}(\mathbf{x}, \mathbf{y})] + \mu [\mathbf{u}(\mathbf{y}) \cdot \hat{F}(\mathbf{x}, \mathbf{y})] \otimes \nabla_{\mathbf{x}} \\ \hat{\tau}[\mathbf{t}(\mathbf{y}) \cdot \hat{G}(\mathbf{x}, \mathbf{y})] &= \lambda \hat{F} \nabla_{\mathbf{x}} \cdot [\mathbf{t}(\mathbf{y}) \cdot \hat{G}(\mathbf{x}, \mathbf{y})] + \mu \nabla_{\mathbf{x}} \otimes [\mathbf{t}(\mathbf{y}) \cdot \hat{G}(\mathbf{x}, \mathbf{y})] + \mu [\mathbf{t}(\mathbf{y}) \cdot \hat{G}(\mathbf{x}, \mathbf{y})] \otimes \nabla_{\mathbf{x}} \end{aligned} \quad (\text{C.23})$$

The contributions to traction field components associated with the last 2 terms of (C.57) are

$$\begin{aligned} \hat{\mathbf{n}}(\mathbf{x}) \cdot \hat{\tau}[\mathbf{u}(\mathbf{y}) \cdot \hat{F}(\mathbf{x}, \mathbf{y})] &= \mathbf{u}(\mathbf{y}) \cdot \hat{W}(\mathbf{x}, \mathbf{y}) = \\ &= \lambda \hat{\mathbf{n}}(\mathbf{x}) \{ \nabla_{\mathbf{x}} \cdot [\mathbf{u}(\mathbf{y}) \cdot \hat{F}(\mathbf{x}, \mathbf{y})] \} + \mu [\hat{\mathbf{n}}(\mathbf{x}) \cdot \nabla_{\mathbf{x}}] [\mathbf{u}(\mathbf{y}) \cdot \hat{F}(\mathbf{x}, \mathbf{y})] + \mu \nabla_{\mathbf{x}} \{ \mathbf{u}(\mathbf{x}) \cdot \hat{F}(\mathbf{x}, \mathbf{y}) \cdot \hat{\mathbf{n}}(\mathbf{y}) \} \\ \hat{\mathbf{n}}(\mathbf{x}) \cdot \hat{\tau}[\mathbf{t}(\mathbf{y}) \cdot \hat{G}(\mathbf{x}, \mathbf{y})] &= \mathbf{t}(\mathbf{y}) \cdot \hat{\Phi}(\mathbf{x}, \mathbf{y}) = \\ &= \lambda \hat{\mathbf{n}}(\mathbf{x}) \{ \nabla_{\mathbf{x}} \cdot [\mathbf{t}(\mathbf{y}) \cdot \hat{G}(\mathbf{x}, \mathbf{y})] \} + \mu [\hat{\mathbf{n}}(\mathbf{x}) \cdot \nabla_{\mathbf{x}}] [\mathbf{t}(\mathbf{y}) \cdot \hat{G}(\mathbf{x}, \mathbf{y})] + \mu \nabla_{\mathbf{x}} \{ \hat{\mathbf{n}}(\mathbf{x}) \cdot \hat{G}(\mathbf{x}, \mathbf{y}) \cdot \mathbf{t}(\mathbf{y}) \} = \\ &= \mathbf{t}(\mathbf{y}) \cdot \{ \lambda [\nabla_{\mathbf{x}} \cdot \hat{G}(\mathbf{x}, \mathbf{y})] \otimes \hat{\mathbf{n}}(\mathbf{x}) + \mu [\hat{\mathbf{n}}(\mathbf{x}) \cdot \nabla_{\mathbf{x}}] \hat{G}(\mathbf{x}, \mathbf{y}) + \mu [\hat{\mathbf{n}}(\mathbf{x}) \cdot \hat{G}(\mathbf{x}, \mathbf{y})] \otimes \nabla_{\mathbf{x}} \} \end{aligned} \quad (\text{C.24})$$

The above equations can be used to identify the Green function operators $\hat{W}(\mathbf{x}, \mathbf{y})$ and $\hat{\Phi}(\mathbf{x}, \mathbf{y})$

$$\begin{aligned} \hat{W}(\mathbf{x}, \mathbf{y}) &= \lambda [\hat{F}(\mathbf{x}, \mathbf{y}) \cdot \nabla_{\mathbf{x}}] \otimes \hat{\mathbf{n}}_a + \mu [\hat{\mathbf{n}}_a \cdot \nabla_{\mathbf{x}}] \hat{F}(\mathbf{x}, \mathbf{y}) + \mu [\hat{F}(\mathbf{x}, \mathbf{y}) \cdot \hat{\mathbf{n}}_a] \otimes \nabla_{\mathbf{x}} \\ \hat{\Phi}(\mathbf{x}, \mathbf{y}) &= \lambda [\nabla_{\mathbf{x}} \cdot \hat{G}(\mathbf{x}, \mathbf{y})] \otimes \hat{\mathbf{n}}(\mathbf{x}) + \mu [\hat{\mathbf{n}}(\mathbf{x}) \cdot \nabla_{\mathbf{x}}] \hat{G}(\mathbf{x}, \mathbf{y}) + \mu [\hat{\mathbf{n}}(\mathbf{x}) \cdot \hat{G}(\mathbf{x}, \mathbf{y})] \otimes \nabla_{\mathbf{x}} \end{aligned} \quad (\text{C.25})$$

and their matrix elements.

We may deduce the form of $\hat{W}(\mathbf{x}, \mathbf{y})$ from as follows:

$$\begin{aligned}
\hat{W}(\mathbf{x}, \mathbf{y}) = & \lambda[\hat{I}(\mathbf{x}, \mathbf{y}) \cdot \nabla_{\mathbf{x}}] \otimes \hat{\mathbf{n}}_a + \mu(\hat{\mathbf{n}}_a \cdot \nabla_{\mathbf{x}})\hat{I}(\mathbf{x}, \mathbf{y}) + \mu[\hat{I}(\mathbf{x}, \mathbf{y}) \cdot \hat{\mathbf{n}}_a] \otimes \nabla_{\mathbf{x}} = \\
& - \frac{\lambda k_C^2}{\lambda + 2\mu} \hat{\mathbf{n}}_b \otimes \hat{\mathbf{n}}_a g_C(R) + \frac{2\lambda\mu}{\lambda + 2\mu} \{ (\hat{\mathbf{n}}_b \cdot \nabla_{\mathbf{x}}) \nabla_{\mathbf{x}} \otimes \hat{\mathbf{n}}_a + (\hat{\mathbf{n}}_a \cdot \nabla_{\mathbf{x}}) \hat{\mathbf{n}}_b \otimes \nabla_{\mathbf{x}} \} g_C(R) + \\
& + \mu^2 \{ (\hat{\mathbf{n}}_a \cdot \nabla_{\mathbf{x}}) (\hat{\mathbf{n}}_b \cdot \nabla_{\mathbf{x}}) \hat{G}(\mathbf{x}, \mathbf{y}) + (\hat{\mathbf{n}}_a \cdot \nabla_{\mathbf{x}}) \nabla_{\mathbf{x}} \otimes [\hat{\mathbf{n}}_b \cdot \hat{G}(\mathbf{x}, \mathbf{y})] + \\
& + (\hat{\mathbf{n}}_b \cdot \nabla_{\mathbf{x}}) [\hat{\mathbf{n}}_a \cdot \hat{G}(\mathbf{x}, \mathbf{y})] \otimes \nabla_{\mathbf{x}} + [\hat{\mathbf{n}}_b \cdot \hat{G}(\mathbf{x}, \mathbf{y}) \cdot \hat{\mathbf{n}}_a] \nabla_{\mathbf{x}} \otimes \nabla_{\mathbf{x}} \}
\end{aligned} \tag{C.26}$$

C.3.3 The acoustics limit

As a check of the representation formulae and the Green functions in elastodynamics, we consider in the following their acoustics limit, $\mu \rightarrow 0$.

The Green functions in the acoustics limit. In the acoustics limit the Fourier transform of \hat{G} becomes

$$\begin{aligned}
\tilde{G}_{ij} &= \frac{1}{\mu} (\delta_{ij} - \frac{q_i q_j}{k_S^2}) \frac{1}{q^2 - k_S^2} + \frac{1}{\mu k_S^2} \frac{q_i q_j}{q^2 - k_C^2} \\
\tilde{G}_{ij}(\mu \rightarrow 0) &= -\frac{1}{\lambda k_C^2} (\delta_{ij} - \frac{q_i q_j}{q^2 - k_C^2}) \\
\tilde{\Sigma}(\mathbf{R})_{ijk}(\mu \rightarrow 0) &= \delta_{ij} \frac{q_k}{q^2 - k_C^2} \\
\hat{G}(\mathbf{R})_{\mu=0} &= -\frac{1}{\lambda k_C^2} [\hat{I} \delta^3(\mathbf{R}) + \nabla_{\mathbf{R}} \otimes \nabla_{\mathbf{R}} g_C(R)], \\
\hat{\Sigma}(\mathbf{R}) &= \lambda \hat{I} \nabla_{\mathbf{R}} \cdot \hat{G}(\mathbf{R}) = \hat{I} \nabla_{\mathbf{R}} g_C(R), \\
\hat{I}(\mathbf{R}) &= \hat{\mathbf{n}}(\mathbf{y}) \otimes \nabla_{\mathbf{R}} g_C(\mathbf{R}), \\
\hat{\Phi}(\mathbf{R}) &= \nabla_{\mathbf{R}} g_C(R) \otimes \hat{\mathbf{n}}(\mathbf{x}), \\
\hat{W}(\mathbf{x}, \mathbf{y}) &= -\lambda k_C^2 \hat{\mathbf{n}}_b \otimes \hat{\mathbf{n}}_a g_C(R).
\end{aligned} \tag{C.27}$$

Representation formulae in the acoustics limit. We consider a single region Ω bounded by $\partial\Omega$. By assuming that, inside Ω the displacement $\mathbf{u}(\mathbf{x})$ satisfies the Lamé equation (C.14) we may construct the following **integral representations for the displacement and traction fields** in a region Ω bounded by $\partial\Omega$ which allows to find the value of the displacement field at any point \mathbf{x} in Ω in terms of the integral of 2 fields $\mathbf{u}(\cdot)$ and $\mathbf{t}(\mathbf{x})$ on the region boundary

$$\mathbf{u}(\mathbf{x}) = \int_{\partial\Omega} dS_{\mathbf{y}} [\mathbf{u}(\mathbf{y}) \cdot \hat{I}(\mathbf{x}, \mathbf{y}) + \mathbf{t}(\mathbf{y}) \cdot \hat{G}(\mathbf{x}, \mathbf{y})] \tag{C.29}$$

$$\mathbf{t}(\mathbf{x}) = \int_{\partial\Omega} dS_{\mathbf{y}} [\mathbf{u}(\mathbf{y}) \cdot \hat{W}(\mathbf{x}, \mathbf{y}) + \mathbf{t}(\mathbf{y}) \cdot \hat{\Phi}(\mathbf{x}, \mathbf{y})] \tag{C.30}$$

Since the operators appearing in the integral equations are obtained as boundary limits of the expressions for the fields, the “contact” $\delta(\mathbf{R})$ terms do not contribute to the expressions for the operators. After discarding such terms, we obtain

$$\begin{aligned}
\hat{G}(\mathbf{x}, \mathbf{y})_{\mu=0} &= -\frac{1}{\lambda k_C^2} [\nabla_{\mathbf{R}} \otimes \nabla_{\mathbf{R}} g_C(R)], \\
\hat{\Gamma}(\mathbf{x}, \mathbf{y})_{\mu=0} &= \hat{\mathbf{n}}(\mathbf{y}) \otimes \nabla_{\mathbf{R}} g_C(R), \\
\hat{\Phi}(\mathbf{x}, \mathbf{y})_{\mu=0} &= \nabla_{\mathbf{R}} g_C(R) \otimes \hat{\mathbf{n}}(\mathbf{x}), \\
\hat{W}(\mathbf{x}, \mathbf{y})_{\mu=0} &= -\lambda k_C^2 \hat{\mathbf{n}}(\mathbf{y}) \otimes \hat{\mathbf{n}}(\mathbf{x}) g_C(R), \\
(\mathbf{b} \hat{G} \mathbf{a})_{\mu=0} &= -\frac{1}{\lambda k_C^2} (\nabla_{\mathbf{R}} \cdot \mathbf{b}) (\nabla_{\mathbf{R}} \cdot \mathbf{a}) g_C(R), \\
(\mathbf{b} \hat{\Gamma} \mathbf{a})_{\mu=0} &= (\mathbf{b} \cdot \hat{\mathbf{n}}_b) (\mathbf{a} \cdot \nabla_{\mathbf{R}}) g_C(R), \\
(\mathbf{b} \hat{\Phi} \mathbf{a})_{\mu=0} &= (\mathbf{a} \cdot \hat{\mathbf{n}}_a) (\mathbf{b} \cdot \nabla_{\mathbf{R}}) g_C(R), \\
(\mathbf{b} \hat{W} \mathbf{a})_{\mu=0} &= -\lambda k_C^2 (\hat{\mathbf{n}}_b \cdot \mathbf{b}) (\hat{\mathbf{n}}_a \cdot \mathbf{a}) g_C(R)
\end{aligned} \tag{C.31}$$

C.4 Construction of coupled surface integral equations for piecewise homogeneous media for displacement and surface traction fields

Surface integral equations – or boundary integral equations, BIEs – are applicable to piecewise homogeneous materials, and provide solutions for the displacement and traction fields defined on interfaces separating different material regions. Fields in the individual regions are described in terms of the appropriate Green functions for elastic materials.

C.4.1 Structure of a system of regions and the resultant integral equations

As an example, we give below explicit expressions for a system of surface integral equations describing a set of homogeneous regions Ω_m separated by interfaces;

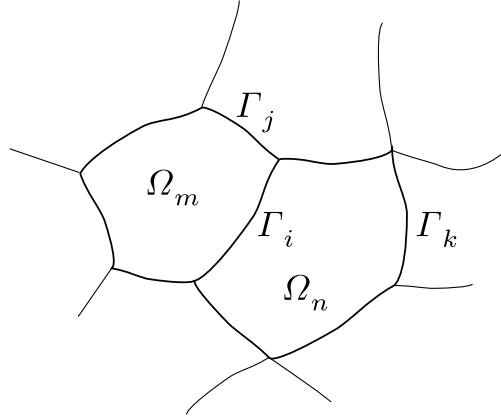


Figure 54: A schematic representation of regions Ω and interfaces S appearing in surface integral equations .

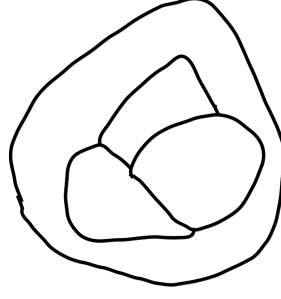


Figure 55: A simplified schematics of the topological structure of regions and interfaces .

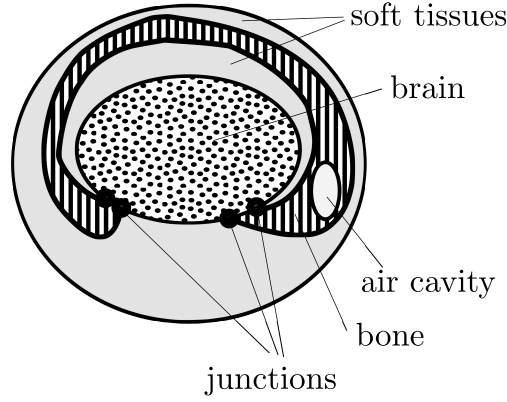


Figure 56: A simplified schematics of the topological structure of regions and interfaces in head model.

One of these regions, Ω_0 , is the unbounded background medium (air). The displacement and traction fields are assumed to be continuous across the interfaces.

The resulting system of integral equations is then obtained in the following three steps

- (a) using a conventional representation theorem (found e.g. in Morse and Feshbach) for each material region Ω for the displacement field in this region written in terms of the surface integrals over $\partial\Omega$ with “surface sources” displacements and traction fields

$$\mathbf{u}(\mathbf{x}) = + \int_{\partial\Omega} dS_{\mathbf{y}} [\mathbf{u}(\mathbf{y}) \cdot \hat{\Gamma}_m(\mathbf{x}, \mathbf{y}) + \mathbf{t}(\mathbf{y}) \cdot \hat{G}_m(\mathbf{x}, \mathbf{y}),]$$

for the displacement $\mathbf{u}(\mathbf{r})$ and the traction $\mathbf{t}(\mathbf{r}) = \hat{\mathbf{n}}(\mathbf{r}) \cdot \hat{\boldsymbol{\tau}}(\mathbf{r})$ fields

- (b) imposing boundary conditions on the continuity of $\mathbf{u}(\mathbf{r})$ and of $\mathbf{t}(\mathbf{r})$ on each interface (oriented surface) S_{mn} separating the regions two equations per interface (oriented

surface) S_{mn} separating the regions Ω_m (on the negative side of the interface) and Ω_n (on its positive side),

$$\begin{aligned}\mathbf{u}_m(\mathbf{r}) &= \mathbf{u}_n(\mathbf{r}), \\ \mathbf{t}_m(\mathbf{r}) &= \mathbf{t}_n(\mathbf{r}).\end{aligned}\tag{C.32}$$

- (c) by writing two suitable equations following from the boundary conditions for each interface S_{mn} .

C.4.2 Boundary conditions

If the n -th interface is an interface between

- two elastic media (1) and (2),
- two viscous fluids, or,
- a viscous fluid (1) and an elastic medium (2),

we impose the following boundary conditions (six in general)

- equality of the three components of the displacement field on both sides of the interface,

$$\mathbf{u}^{(1)}(\mathbf{r}) = \mathbf{u}^{(2)}(\mathbf{r}),\tag{C.33}$$

- equality of the three components of the traction field on both sides of the interface,

$$\tilde{T}^{(1)}\mathbf{u}^{(1)}(\mathbf{r}) = \tilde{T}^{(2)}\mathbf{u}^{(2)}(\mathbf{r}).\tag{C.34}$$

On the interface between **non-viscous fluid and the elastic medium** we impose the following reduced number of boundary conditions (four in general):

- equality of the normal component of the displacement field on both sides of the interface,

$$\hat{\mathbf{n}}^{(1)}(\mathbf{r}) \cdot \mathbf{u}^{(1)}(\mathbf{r}) = \hat{\mathbf{n}}^{(1)}(\mathbf{r}) \cdot \mathbf{u}^{(2)}(\mathbf{r}),\tag{C.35}$$

- equality of the normal component of the traction field on both sides of the interface.

$$\hat{\mathbf{n}}^{(1)}(\mathbf{r}) \cdot \mathbf{t}^{(1)}(\mathbf{r}) = \hat{\mathbf{n}}^{(1)}(\mathbf{r}) \cdot \mathbf{t}^{(2)}(\mathbf{r}),\tag{C.36}$$

- vanishing tangential components of the traction field

$$\hat{\mathbf{n}}^{(1)}(\mathbf{r}) \times [\hat{\mathbf{n}}^{(1)}(\mathbf{r}) \times \mathbf{t}^{(1)}(\mathbf{r})] = \hat{\mathbf{n}}^{(2)}(\mathbf{r}) \times [\hat{\mathbf{n}}^{(2)}(\mathbf{r}) \times \mathbf{t}^{(2)}(\mathbf{r})] = 0,\tag{C.37}$$

on both sides of the interface

Finally on the interface between **two non-viscous fluids** we impose the following reduced number of boundary conditions (four in general):

- equality of the normal component of the displacement field on both sides of the interface,

$$\hat{\mathbf{n}}^{(1)}(\mathbf{r}) \cdot \mathbf{u}^{(1)}(\mathbf{r}) = \hat{\mathbf{n}}^{(1)}(\mathbf{r}) \cdot \mathbf{u}^{(2)}(\mathbf{r}), \quad (\text{C.38})$$

- equality of the normal component of the traction field on both sides of the interface.

$$\hat{\mathbf{n}}^{(1)}(\mathbf{r}) \cdot \mathbf{t}^{(1)}(\mathbf{r}) = \hat{\mathbf{n}}^{(1)}(\mathbf{r}) \cdot \mathbf{t}^{(2)}(\mathbf{r}), \quad (\text{C.39})$$

- vanishing tangential components of the traction field

$$\hat{\mathbf{n}}^{(1)}(\mathbf{r}) \times [\hat{\mathbf{n}}^{(1)}(\mathbf{r}) \times \mathbf{t}^{(1)}(\mathbf{r})] = \hat{\mathbf{n}}^{(2)}(\mathbf{r}) \times [\hat{\mathbf{n}}^{(2)}(\mathbf{r}) \times \mathbf{t}^{(2)}(\mathbf{r})] = 0, \quad (\text{C.40})$$

on both sides of the interface

C.4.3 Choice of the integral equation formulation

The choice of the integral equations is not unique. It is possible to write several different set of integral equations by taking different linear combinations of equations representing boundary condition for continuity of displacement and and traction fields across material interfaces. While all such integral equations are theoretically equivalent, they tend to differ in terms of accuracy, computational resources needed and solution convergence

We considered the two integral representations for the displacement and of the traction fields

$$\begin{aligned} \mathbf{u}(\mathbf{x}) &= \int_{\partial\Omega} dS_{\mathbf{y}} [\mathbf{u}(\mathbf{y}) \cdot \hat{\Gamma}(\mathbf{x}, \mathbf{y}) + \mathbf{t}(\mathbf{y}) \cdot \hat{G}(\mathbf{x}, \mathbf{y})] \\ \mathbf{t}(\mathbf{x}) &= \int_{\partial\Omega} dS_{\mathbf{y}} [\mathbf{u}(\mathbf{y}) \cdot \hat{W}(\mathbf{x}, \mathbf{y}) + \mathbf{t}(\mathbf{y}) \cdot \hat{\Phi}(\mathbf{x}, \mathbf{y})] \end{aligned} \quad (\text{C.41})$$

C.4.4 Construction of the second-kind integral equations system

On the interface S_{mn} we write 6 equations for 6 unknowns $\mathbf{u}(\mathbf{x}), \mathbf{t}(\mathbf{x})$

$$\begin{aligned} \lim_{\mathbf{x} \in \partial\Omega_m} u(\mathbf{x}) &\text{ in region } \Omega_m \\ \lim_{\mathbf{x} \in \partial\Omega_n} u(\mathbf{x}) &\text{ in region } \Omega_n \end{aligned}$$

The resulting **second kind pair surface integral equations** for \mathbf{u} and \mathbf{t} for the **interface separating two regions** Ω_m and Ω_n is

$$\begin{aligned}
& \frac{1}{2} \mathbf{u}(\mathbf{x}) + \int_{S_{mn}} dS_{\mathbf{y}} [\mathbf{u}(\mathbf{y}) \cdot \hat{F}_m(\mathbf{x}, \mathbf{y}) + \mathbf{t}(\mathbf{y}) \cdot \hat{G}_m(\mathbf{x}, \mathbf{y})] \\
& - \sum_{\substack{S_{im} \in \partial\Omega_m \\ i \neq n}} \int dS_{\mathbf{y}} [\mathbf{u}(\mathbf{y}) \cdot \hat{F}_m(\mathbf{x}, \mathbf{y}) + \mathbf{t}(\mathbf{y}) \cdot \hat{G}_m(\mathbf{x}, \mathbf{y})] = \delta_{m0} \mathbf{u}^{\text{in}}(\mathbf{x}) \\
& \frac{1}{2} \mathbf{u}(\mathbf{x}) - \int_{S_{mn}} dS_{\mathbf{y}} [\mathbf{u}(\mathbf{y}) \cdot \hat{F}_n(\mathbf{x}, \mathbf{y}) + \mathbf{t}(\mathbf{y}) \cdot \hat{G}_n(\mathbf{x}, \mathbf{y})] \\
& + \sum_{\substack{S_{nj} \in \partial\Omega_n \\ j \neq m}} - \int_{S_{nj}} dS_{\mathbf{y}} [\mathbf{u}(\mathbf{y}) \cdot \hat{F}_n(\mathbf{x}, \mathbf{y}) + \mathbf{t}(\mathbf{y}) \cdot \hat{G}_n(\mathbf{x}, \mathbf{y})] = \delta_{n0} \mathbf{u}^{\text{in}}(\mathbf{x}) \quad \text{for } \mathbf{x} \in S_{mn} .
\end{aligned} \tag{C.42}$$

C.4.5 Construction of the first-kind integral equations

The resulting **first kind pair surface integral equations for \mathbf{u} and \mathbf{t}**

On the interface S_{mn} we write 6 equations for 6 unknowns $\mathbf{u}(\mathbf{x}), \mathbf{t}(\mathbf{x})$

$$\begin{aligned}
\mathbf{u}_m(\mathbf{x}) &= \mathbf{u}_n(\mathbf{x}) \quad \text{for } \mathbf{x} \text{ on interface } S_{mn} \\
\mathbf{t}_m(\mathbf{x}) &= \mathbf{t}_n(\mathbf{x}) \quad \text{for } \mathbf{x} \text{ on interface } S_{mn}
\end{aligned}$$

The equations of our interest can be obtained in the following way:

By taking the difference of the equations (C.45) we obtain the first equation of the second set

$$\begin{aligned}
& \int_{S_{mn}} dS_{\mathbf{y}} \{ \mathbf{u}(\mathbf{y}) \cdot [\hat{F}_m(\mathbf{x}, \mathbf{y}) + \hat{F}_n(\mathbf{x}, \mathbf{y})] + \mathbf{t}(\mathbf{y}) \cdot [\hat{G}_m(\mathbf{x}, \mathbf{y}) + \hat{G}_n(\mathbf{x}, \mathbf{y})] \} \\
& - \sum_{\substack{S_{im} \in \partial\Omega_m \\ i \neq n}} \int dS_{\mathbf{y}} \{ \mathbf{u}(\mathbf{y}) \cdot [\hat{F}_m(\mathbf{x}, \mathbf{y}) + \hat{F}_n(\mathbf{x}, \mathbf{y})] + \mathbf{t}(\mathbf{y}) \cdot [\hat{G}_m(\mathbf{x}, \mathbf{y}) + \hat{G}_n(\mathbf{x}, \mathbf{y})] \} = \\
& = [\delta_{m0} - \delta_{n0}] \mathbf{u}^{\text{in}}(\mathbf{x})
\end{aligned} \tag{C.43}$$

By applying the traction filed operator $\hat{\mathbf{n}}(\mathbf{x}) \cdot [\tau(\mathbf{u}(\mathbf{x}))]$ to both sides of the above equation

(C.44) we obtain the second equation of the second set

$$\begin{aligned}
& \int_{S_{mn}} dS_{\mathbf{y}} \{ \mathbf{u}(\mathbf{y}) \cdot [\hat{W}_m(\mathbf{x}, \mathbf{y}) + \hat{W}_n(\mathbf{x}, \mathbf{y})] + \mathbf{t}(\mathbf{y}) \cdot [\hat{\Phi}_m(\mathbf{x}, \mathbf{y}) + \hat{\Phi}_n(\mathbf{x}, \mathbf{y})] \} \\
& - \sum_{\substack{S_{im} \in \partial \Omega_m \\ i \neq n}} \int_{S_{im}} dS_{\mathbf{y}} \{ \mathbf{u}(\mathbf{y}) \cdot [\hat{W}_m(\mathbf{x}, \mathbf{y}) + \hat{W}_n(\mathbf{x}, \mathbf{y})] + \mathbf{t}(\mathbf{y}) \cdot [\hat{\Phi}_m(\mathbf{x}, \mathbf{y}) + \hat{\Phi}_n(\mathbf{x}, \mathbf{y})] \} \\
& = [\delta_{m0} - \delta_{n0}] \mathbf{t}^{\text{in}}(\mathbf{x})
\end{aligned} \tag{C.44}$$

The resulting **first kind pair surface integral equations for \mathbf{u} and \mathbf{t} for the interface separating two regions Ω_m and Ω_n** is

$$\begin{aligned}
& \frac{1}{2} \mathbf{u}(\mathbf{x}) + \int_{S_{mn}} dS_{\mathbf{y}} [\mathbf{u}(\mathbf{y}) \cdot \hat{\Gamma}_m(\mathbf{x}, \mathbf{y}) + \mathbf{t}(\mathbf{y}) \cdot \hat{G}_m(\mathbf{x}, \mathbf{y})] \\
& - \sum_{\substack{S_{im} \in \partial \Omega_m \\ i \neq n}} \int_{S_{im}} dS_{\mathbf{y}} [\mathbf{u}(\mathbf{y}) \cdot \hat{\Gamma}_m(\mathbf{x}, \mathbf{y}) + \mathbf{t}(\mathbf{y}) \cdot \hat{G}_m(\mathbf{x}, \mathbf{y})] = \delta_{m0} \mathbf{u}^{\text{in}}(\mathbf{x}) \\
& \frac{1}{2} \mathbf{t}(\mathbf{x}) - \int_{S_{mn}} dS_{\mathbf{y}} [\mathbf{u}(\mathbf{y}) \cdot \hat{W}_n(\mathbf{x}, \mathbf{y}) + \mathbf{t}(\mathbf{y}) \cdot \hat{\Phi}_n(\mathbf{x}, \mathbf{y})] \\
& + \sum_{\substack{S_{nj} \in \partial \Omega_n \\ j \neq m}} \int_{S_{nj}} dS_{\mathbf{y}} [\mathbf{u}(\mathbf{y}) \cdot \hat{W}_n(\mathbf{x}, \mathbf{y}) + \mathbf{t}(\mathbf{y}) \cdot \hat{\Phi}_n(\mathbf{x}, \mathbf{y})] = \delta_{n0} \mathbf{t}^{\text{in}}(\mathbf{x}) \quad \text{for } \mathbf{x} \in S_{mn} .
\end{aligned} \tag{C.45}$$

With reference to Fig. 55, the first of the above integral equations represents contributions to the displacement field \mathbf{u} on the interface S_{mn} due to the displacement and traction fields \mathbf{u} and \mathbf{t} on the same interface (the first integral) and on other interfaces, S_{im} , forming boundaries of the region Ω_m with other regions Ω_i , $i \neq n$.

The integrals involve Green functions

$$\hat{G}_i, \hat{\Gamma}_i, \hat{W}_i, \text{ and } \hat{\Phi}_i, \quad i = 1, \dots, N$$

describing propagation of the displacement and stress fields in the region Ω_j .

Similarly, the second of the above integral equations represents contributions to the field \mathbf{u} on the interface S_{mn} due to the fields on the boundaries of the other region, Ω_n , adjacent to the interface. The r.h.s of the above equations are the incident fields due to distant sources in the region Ω_0 (hence the delta-functions δ_{m0} and δ_{n0}).

The details of the construction and regularization of $\hat{G}_i, \hat{\Gamma}_i, \hat{\Omega}_i$, and $\hat{\Phi}_i$ are described in the subsequent section.

We discuss here briefly the form of the surface boundary equations and their discretization, which is now being implemented in our solver.

C.5 Basis functions and discretization of surface integral equations

In order to solve the surface integral equations numerically, it is necessary to make assumptions on the discretization of the solution, i.e., on the trial basis functions, and on the test basis functions.

In our implementation we use a discretization uniquely determined by our choice of discretization in the surface integral equations. We also use, similarly to the volumetric problem, the Galerkin discretization, i.e., identical trial and testing basis functions.

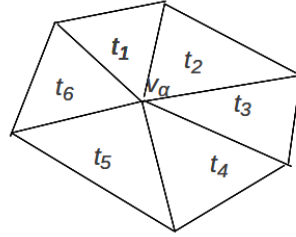


Figure 57: A set of six triangles sharing a common vertex v_α supporting the node based basis function

In the surface problems we assume the displacement field is expanded in piecewise linear basis functions supported on sets of triangles. The resulting surface basis functions are piecewise linear vector basis functions describing the components of the displacement field \mathbf{u} . By symmetry between the displacement and traction fields in the integral equations, we assume analogous linear basis functions for the components of \mathbf{t} .

According to the above criteria, we specify the basis functions as follows:

For each vertex \mathbf{v}_α of the surface mesh we define three vector basis functions, denoted $\boldsymbol{\psi}_\alpha(\mathbf{r})$, representing displacements in the x , y , and z directions. Correspondingly, the index α refers to the vertex and the direction, $\alpha = (\mathbf{v}_\alpha, m)$, $m = 1, 2, 3$ (or $m = x, y, z$).

Each such function, $\boldsymbol{\psi}_\alpha(\mathbf{r})$, is associated with a vertex \mathbf{v}_α and supported on a set of triangles (facets) f_α sharing that vertex. We parameterize the basis function as

$$\boldsymbol{\psi}_\alpha(\mathbf{r}) \equiv \boldsymbol{\psi}_{\mathbf{v}_\alpha, m}(\mathbf{r}) = \mathbf{e}_m \phi_{\mathbf{v}_\alpha}(\mathbf{r}) , \quad (\text{C.46})$$

where \mathbf{e}_m is the unit vector along the m -th axis, and $\phi_{\mathbf{v}_\alpha}$ is a scalar basis function defined by

$$\phi_\alpha(\mathbf{x}) \equiv \phi_{\mathbf{v}_\alpha}(\mathbf{x}) = \sum_{f_\alpha \in \mathcal{F}_\alpha} \phi_{\mathbf{v}_\alpha, f_\alpha}(\mathbf{x}) , \quad (\text{C.47})$$

where the sum is taken over the set \mathcal{F}_α of all facets f_α sharing the vertex \mathbf{v}_α . Further, each of the linear functions $\phi_{\mathbf{v}_\alpha, f_\alpha}(\mathbf{x})$, supported on the facet f_α , is uniquely defined by setting

its value to unity at $\mathbf{r} = \mathbf{v}_\alpha$ and to zero at the remaining vertices of the facet. An explicit expression is

$$\phi_{\mathbf{v}_\alpha, f_\alpha}(\mathbf{x}) = \left[1 - \frac{1}{h_{\mathbf{v}_\alpha, f_\alpha}} \hat{\mathbf{n}}_{\mathbf{v}_\alpha, f_\alpha} \cdot (\mathbf{x} - \mathbf{v}_\alpha) \right] \chi_{f_\alpha}(\mathbf{x}), \quad (\text{C.48})$$

where $\chi_{f_\alpha}(\mathbf{x})$ is the characteristic function of the facet f_α , $\hat{\mathbf{n}}_{\mathbf{v}_\alpha, f_\alpha}$ is the unit outer normal to the facet edge opposite the vertex \mathbf{v}_α , and $h_{\mathbf{v}_\alpha, f_\alpha}$ is the facet height relative to that edge. Components of the basis function ψ_α are then

$$\psi_\alpha^i(\mathbf{r}) \equiv \psi_{\mathbf{v}_\alpha, m}^i(\mathbf{r}) = \delta_{mi} \phi_{\mathbf{v}_\alpha}(\mathbf{r}). \quad (\text{C.49})$$

In order to simplify the notation in the following we will use a simplified notation

$$\begin{aligned} \psi_\alpha^i(\mathbf{x}) &\equiv \psi_{\mathbf{v}_\alpha, m}^i(\mathbf{x}) = \delta_{mi} \phi_{\mathbf{v}_\alpha}(\mathbf{x}) \equiv \phi_a(\mathbf{x}) \chi_a(\mathbf{x}), \\ a &\equiv \mathbf{v}_\alpha, m \end{aligned} \quad (\text{C.50})$$

We represent the linear basis functions components associated with one triangle a or b as follows:

$$\begin{aligned} \Psi_a(\mathbf{x}) &= \mathbf{a} \phi_a(\mathbf{x}), \\ \Psi_b(\mathbf{x}) &= \mathbf{b} \phi_b(\mathbf{x}), \\ \phi_a(\mathbf{x}) &= \xi_a \chi_a(\mathbf{x}) = \left[1 - \frac{\hat{\mathbf{h}}_a \cdot (\mathbf{x} - \mathbf{v}_a)}{h_a} \right] \chi_a(\mathbf{x}), \\ \phi_b(\mathbf{x}) &= \xi_b \chi_b(\mathbf{x}) = \left[1 - \frac{\hat{\mathbf{h}}_b \cdot (\mathbf{x} - \mathbf{v}_b)}{h_b} \right] \chi_b(\mathbf{x}). \end{aligned} \quad (\text{C.51})$$

As follows from the construction, the scalar and vectorial basis functions (C.47) and (C.46) are two-dimensional analogues (actually, restrictions) of the piecewise linear basis functions supported on tetrahedra and used in our previously developed volumetric formulation. The advantage of this discretization scheme is that the solutions of the surface and volumetric equations can be directly compared with one another.

Let $\psi_\alpha(\mathbf{r})$ and $\psi_\beta(\mathbf{r})$ be the two vector basis functions associated with nodes v_α and v_β ,

$$\begin{aligned} \psi_\alpha(\mathbf{r}) &= \boldsymbol{\alpha} \phi_{v_\alpha}(\mathbf{r}), \\ \psi_\beta(\mathbf{r}') &= \boldsymbol{\beta} \phi_{v_\beta}(\mathbf{r}'). \\ \boldsymbol{\alpha} &= \begin{bmatrix} \alpha_x \\ \alpha_y \\ \alpha_z \end{bmatrix} \\ \boldsymbol{\beta} &= \begin{bmatrix} \beta_x \\ \beta_y \\ \beta_z \end{bmatrix} \end{aligned} \quad (\text{C.52})$$

C.5.1 Matrix elements of the integral equation kernels appearing in representation formulas for the displacement and traction fields

The explicit forms of the matrix elements of $\hat{G}(\mathbf{x}, \mathbf{y})$, $\hat{\Gamma}(\mathbf{x}, \mathbf{y})$, $\hat{\Phi}(\mathbf{x}, \mathbf{y})$, and $\hat{W}(\mathbf{x}, \mathbf{y})$ sandwiched between single triangle contributions to the linear basis functions $\Psi_a(\mathbf{x})$ and $\Psi_b(\mathbf{y})$ are : associated with triangles a and b

$$\begin{aligned}\Psi_a(\mathbf{x}) &= \mathbf{a}\phi_a(\mathbf{x}), \\ \Psi_b(\mathbf{x}) &= \mathbf{b}\phi_b(\mathbf{x}), \\ \phi_a(\mathbf{x}) &= \xi_a\chi_a(\mathbf{x}) = [1 - \frac{\hat{\mathbf{h}}_a \cdot (\mathbf{x} - \mathbf{v}_a)}{h_a}]\chi_a(\mathbf{x}), \\ \phi_b(\mathbf{x}) &= \xi_b\chi_b(\mathbf{x}) = [1 - \frac{\hat{\mathbf{h}}_b \cdot (\mathbf{x} - \mathbf{v}_b)}{h_b}]\chi_b(\mathbf{x}).\end{aligned}\tag{C.53}$$

are

$$\begin{aligned}[\Psi_b(\mathbf{y}) \cdot \hat{G}(\mathbf{x}, \mathbf{y}) \cdot \Psi_a(\mathbf{x})] &\equiv \phi_b(\mathbf{y})\phi_a(\mathbf{x})[\mathbf{b} \cdot \hat{G}(\mathbf{x}, \mathbf{y}) \cdot \mathbf{a}] \\ [\Psi_b(\mathbf{y}) \cdot \hat{\Gamma}(\mathbf{x}, \mathbf{y}) \cdot \Psi_a(\mathbf{x})] &\equiv \phi_b(\mathbf{y})\phi_a(\mathbf{x})[\mathbf{b} \cdot \hat{\Gamma}(\mathbf{x}, \mathbf{y}) \cdot \mathbf{a}] \\ [\Psi_b(\mathbf{y}) \cdot \hat{\Phi}(\mathbf{x}, \mathbf{y}) \cdot \Psi_a(\mathbf{x})] &\equiv \phi_b(\mathbf{y})\phi_a(\mathbf{x})[\mathbf{b} \cdot \hat{\Phi}(\mathbf{x}, \mathbf{y}) \cdot \mathbf{a}] \\ [\Psi_b(\mathbf{y}) \cdot \hat{W}(\mathbf{x}, \mathbf{y}) \cdot \Psi_a(\mathbf{x})] &\equiv \phi_b(\mathbf{y})\phi_a(\mathbf{x})[\mathbf{b} \cdot \hat{W}(\mathbf{x}, \mathbf{y}) \cdot \mathbf{a}],\end{aligned}\tag{C.54}$$

with

$$\begin{aligned}[\mathbf{b} \cdot \hat{\Gamma} \cdot \mathbf{a}] &= \lambda(\mathbf{b} \cdot \hat{\mathbf{n}}_b)(\mathbf{a} \cdot \hat{G} \cdot \nabla_x) + \mu(\hat{\mathbf{n}}_b \cdot \nabla_x)(\mathbf{a} \cdot \hat{G} \cdot \mathbf{b}) + \mu(\mathbf{b} \cdot \nabla_x)(\mathbf{a} \cdot \hat{G} \cdot \hat{\mathbf{n}}_b) \\ [\mathbf{b} \cdot \hat{\Phi} \cdot \mathbf{a}] &= \lambda(\hat{\mathbf{n}}_a \cdot \mathbf{a})(\hat{\mathbf{b}} \cdot \hat{G} \cdot \nabla_x) + \mu(\hat{\mathbf{n}}_a \cdot \nabla_R)(\mathbf{a} \cdot \hat{G} \cdot \mathbf{b}) + \mu(\mathbf{a} \cdot \nabla_R)(\hat{\mathbf{n}}_a \cdot \hat{G} \cdot \mathbf{b}) \\ [\mathbf{b} \cdot \hat{W} \cdot \mathbf{a}] &= \lambda[\mathbf{b} \cdot \hat{\Gamma} \cdot \nabla_x](\mathbf{a} \cdot \hat{\mathbf{n}}_a) + \mu(\hat{\mathbf{n}}_a \cdot \nabla_x)(\mathbf{b} \cdot \hat{\Gamma} \cdot \mathbf{a}) + \mu(\mathbf{a} \cdot \nabla_x)(\mathbf{b} \cdot \hat{\Gamma} \cdot \hat{\mathbf{n}}_a) \\ &= -\frac{\lambda^2 k_C^2}{\lambda + 2\mu}(\mathbf{a} \cdot \hat{\mathbf{n}}_a)(\mathbf{b} \cdot \hat{\mathbf{n}}_b)g_C(R) + \\ &\quad + \frac{2\lambda\mu}{\lambda + 2\mu}[(\hat{\mathbf{n}}_a \cdot \mathbf{a})(\hat{\mathbf{n}}_b \cdot \nabla_x)(\mathbf{b} \cdot \nabla_x) + (\hat{\mathbf{n}}_b \cdot \mathbf{b})(\hat{\mathbf{n}}_a \cdot \nabla_x)(\mathbf{a} \cdot \nabla_x)]g_C(R) + \\ &\quad + \mu^2\{(\hat{\mathbf{n}}_a \cdot \nabla_x)(\hat{\mathbf{n}}_b \cdot \nabla_x)[\mathbf{b} \cdot \hat{G}(\mathbf{x}, \mathbf{y}) \cdot \mathbf{a}] + (\hat{\mathbf{n}}_a \cdot \nabla_x)(\mathbf{b} \cdot \nabla_x)[\hat{\mathbf{n}}_b \cdot \hat{G}(\mathbf{x}, \mathbf{y}) \cdot \mathbf{a}] + \\ &\quad + (\mathbf{a} \cdot \nabla_x)(\hat{\mathbf{n}}_b \cdot \nabla_x)[\mathbf{b} \cdot \hat{G}(\mathbf{x}, \mathbf{y}) \cdot \hat{\mathbf{n}}_a] + (\mathbf{a} \cdot \nabla_x)(\mathbf{b} \cdot \nabla_x)[\hat{\mathbf{n}}_b \cdot \hat{G}(\mathbf{x}, \mathbf{y}) \cdot \hat{\mathbf{n}}_a]\}\end{aligned}\tag{C.55}$$

By substituting explicit expressions for \hat{G} in terms of g_S and g_C we obtain

$$\begin{aligned}
(\mathbf{b}\hat{G}\mathbf{a}) &= (\mathbf{a} \cdot \mathbf{b}) \frac{g_S(R)}{\mu} + (\mathbf{a} \cdot \nabla_{\mathbf{R}})(\mathbf{b} \cdot \nabla_{\mathbf{R}}) \frac{g_S(R) - g_C(R)}{\mu k_S^2}, \\
(\mathbf{b}\hat{\Gamma}\mathbf{a}) &= \frac{\lambda}{\lambda + 2\mu} (\hat{\mathbf{n}}_b \cdot \mathbf{b})(\mathbf{a} \cdot \nabla_{\mathbf{R}})g_C(R) + \{(\mathbf{a} \cdot \mathbf{b})(\hat{\mathbf{n}}_b \cdot \nabla_{\mathbf{R}}) + (\hat{\mathbf{n}}_b \cdot \mathbf{a})(\mathbf{b} \cdot \nabla_{\mathbf{R}})\}g_S(R) + \\
&\quad + \frac{2}{k_S^2} (\mathbf{a} \cdot \nabla_{\mathbf{R}})(\mathbf{b} \cdot \nabla_{\mathbf{R}})(\hat{\mathbf{n}}_b \cdot \nabla_{\mathbf{R}})[g_S(R) - g_C(R)], \\
(\mathbf{b}\hat{\Phi}\mathbf{a}) &= \frac{\lambda}{\lambda + 2\mu} (\hat{\mathbf{n}}_a \cdot \mathbf{a})(\hat{\mathbf{b}} \cdot \nabla_{\mathbf{R}})g_C(R) + \{(\mathbf{a} \cdot \mathbf{b})(\hat{\mathbf{n}}_a \cdot \nabla_{\mathbf{R}}) + (\hat{\mathbf{n}}_a \cdot \mathbf{b})(\mathbf{a} \cdot \nabla_{\mathbf{R}})\}g_S(R) + \\
&\quad + \frac{2}{k_S^2} (\mathbf{a} \cdot \nabla_{\mathbf{R}})(\mathbf{b} \cdot \nabla_{\mathbf{R}})(\hat{\mathbf{n}}_a \cdot \nabla_{\mathbf{R}})[g_S(R) - g_C(R)], \\
(\mathbf{b} \cdot \hat{W} \cdot \mathbf{a}) &= -\frac{\lambda^2 k_C^2}{\lambda + 2\mu} (\mathbf{a} \cdot \hat{\mathbf{n}}_a)(\mathbf{b} \cdot \hat{\mathbf{n}}_b)g_C(R) + \\
&\quad + \frac{2\lambda\mu}{\lambda + 2\mu} [(\hat{\mathbf{n}}_a \cdot \mathbf{a})(\hat{\mathbf{n}}_b \cdot \nabla_{\mathbf{x}})(\mathbf{b} \cdot \nabla_{\mathbf{x}}) + (\hat{\mathbf{n}}_b \cdot \mathbf{b})(\hat{\mathbf{n}}_a \cdot \nabla_{\mathbf{x}})(\mathbf{a} \cdot \nabla_{\mathbf{x}})]g_C(R) + \\
&\quad + \mu \{(\mathbf{a} \cdot \mathbf{b})(\hat{\mathbf{n}}_a \cdot \nabla_{\mathbf{x}})(\hat{\mathbf{n}}_b \cdot \nabla_{\mathbf{x}}) + (\hat{\mathbf{n}}_b \cdot \mathbf{a})(\hat{\mathbf{n}}_a \cdot \nabla_{\mathbf{x}})(\mathbf{b} \cdot \nabla_{\mathbf{x}}) + \\
&\quad + (\hat{\mathbf{n}}_a \cdot \mathbf{b})(\mathbf{a} \cdot \nabla_{\mathbf{x}})(\hat{\mathbf{n}}_b \cdot \nabla_{\mathbf{x}}) + (\hat{\mathbf{n}}_a \cdot \hat{\mathbf{n}}_b)(\mathbf{a} \cdot \nabla_{\mathbf{x}})(\mathbf{b} \cdot \nabla_{\mathbf{x}})\}g_S(R) + \\
&\quad + \frac{4\mu}{k_S^2} (\hat{\mathbf{n}}_a \cdot \nabla_{\mathbf{x}})(\hat{\mathbf{n}}_b \cdot \nabla_{\mathbf{x}})(\mathbf{a} \cdot \nabla_{\mathbf{x}})(\mathbf{b} \cdot \nabla_{\mathbf{x}})[g_S(R) - g_C(R)].
\end{aligned} \tag{C.56}$$

C.5.2 Construction of the integral representation and matrix elements for the traction field

We consider the second choices of coupled integral equations for a multi-region problem. An apparent advantage of this formulation is that it enforces boundary conditions on each interface in a stronger way than the first set.

In order to construct the **integral representation for the traction field** in a region Ω bounded by $\partial\Omega$ we applying the traction field operator yo the integral representation for displacement $\mathbf{u}(\mathbf{x})$

$$\begin{aligned}
\hat{\tau}[\mathbf{u}(\mathbf{x})] &= \lambda \hat{I}[\nabla_{\mathbf{x}} \cdot \mathbf{u}(\mathbf{x})] + \mu [\nabla_{\mathbf{x}} \otimes \mathbf{u}(\mathbf{x}) + \mathbf{u}(\mathbf{x}) \otimes \nabla_{\mathbf{x}}] = \\
&= \hat{\tau} \left\{ \int_{\partial\Omega} dS_{\mathbf{y}} [\mathbf{u}(\mathbf{y}) \cdot \hat{\Gamma}(\mathbf{x}, \mathbf{y}) + \mathbf{t}(\mathbf{y}) \cdot \hat{G}(\mathbf{x}, \mathbf{y})] \right\} \\
&= \int_{\partial\Omega} dS_{\mathbf{y}} [\hat{\tau}[\mathbf{u}(\mathbf{y}) \cdot \hat{\Gamma}(\mathbf{x}, \mathbf{y})] + \hat{\tau}[\mathbf{t}(\mathbf{y}) \cdot \hat{G}(\mathbf{x}, \mathbf{y})]] \\
\hat{\tau}[\mathbf{u}(\mathbf{y}) \cdot \hat{\Gamma}(\mathbf{x}, \mathbf{y})] &= \lambda \hat{I} \nabla_{\mathbf{x}} \cdot [\mathbf{u}(\mathbf{y}) \cdot \hat{\Gamma}(\mathbf{x}, \mathbf{y})] + \mu \nabla_{\mathbf{x}} \otimes [\mathbf{u}(\mathbf{y}) \cdot \hat{\Gamma}(\mathbf{x}, \mathbf{y})] + \mu [\mathbf{u}(\mathbf{y}) \cdot \hat{\Gamma}(\mathbf{x}, \mathbf{y})] \otimes \nabla_{\mathbf{x}} \\
\hat{\tau}[\mathbf{t}(\mathbf{y}) \cdot \hat{G}(\mathbf{x}, \mathbf{y})] &= \lambda \hat{I} \nabla_{\mathbf{x}} \cdot [\mathbf{t}(\mathbf{y}) \cdot \hat{G}(\mathbf{x}, \mathbf{y})] + \mu \nabla_{\mathbf{x}} \otimes [\mathbf{t}(\mathbf{y}) \cdot \hat{G}(\mathbf{x}, \mathbf{y})] + \mu [\mathbf{t}(\mathbf{y}) \cdot \hat{G}(\mathbf{x}, \mathbf{y})] \otimes \nabla_{\mathbf{x}}
\end{aligned} \tag{C.57}$$

The contributions to traction field components associated with the last 2 terms of (C.57) are

$$\begin{aligned}
\hat{\mathbf{n}}(\mathbf{x}) \cdot \hat{\tau}[\mathbf{u}(\mathbf{y}) \cdot \hat{\Gamma}(\mathbf{x}, \mathbf{y})] &= \mathbf{u}(\mathbf{y}) \cdot \hat{W}(\mathbf{x}, \mathbf{y}) = \\
&= \lambda \hat{\mathbf{n}}(\mathbf{x}) \{ \nabla_{\mathbf{x}} \cdot [\mathbf{u}(\mathbf{y}) \cdot \hat{\Gamma}(\mathbf{x}, \mathbf{y})] \} + \mu [\hat{\mathbf{n}}(\mathbf{x}) \cdot \nabla_{\mathbf{x}}] [\mathbf{u}(\mathbf{y}) \cdot \hat{\Gamma}(\mathbf{x}, \mathbf{y})] + \mu \nabla_{\mathbf{x}} \{ \mathbf{u}(\mathbf{x}) \cdot \hat{\Gamma}(\mathbf{x}, \mathbf{y}) \cdot \hat{\mathbf{n}}(\mathbf{y}) \} \\
\hat{\mathbf{n}}(\mathbf{x}) \cdot \hat{\tau}[\mathbf{t}(\mathbf{y}) \cdot \hat{G}(\mathbf{x}, \mathbf{y})] &= \mathbf{t}(\mathbf{y}) \cdot \hat{\Phi}(\mathbf{x}, \mathbf{y}) = \\
&= \lambda \hat{\mathbf{n}}(\mathbf{x}) \{ \nabla_{\mathbf{x}} \cdot [\mathbf{t}(\mathbf{y}) \cdot \hat{G}(\mathbf{x}, \mathbf{y})] \} + \mu [\hat{\mathbf{n}}(\mathbf{x}) \cdot \nabla_{\mathbf{x}}] [\mathbf{t}(\mathbf{y}) \cdot \hat{G}(\mathbf{x}, \mathbf{y})] + \mu \nabla_{\mathbf{x}} \{ \hat{\mathbf{n}}(\mathbf{x}) \cdot \hat{G}(\mathbf{x}, \mathbf{y}) \cdot \mathbf{t}(\mathbf{y}) \} = \\
&= \mathbf{t}(\mathbf{y}) \cdot \{ \lambda [\nabla_{\mathbf{x}} \cdot \hat{G}(\mathbf{x}, \mathbf{y})] \otimes \hat{\mathbf{n}}(\mathbf{x}) + \mu [\hat{\mathbf{n}}(\mathbf{x}) \cdot \nabla_{\mathbf{x}}] \hat{G}(\mathbf{x}, \mathbf{y}) + \mu [\hat{\mathbf{n}}(\mathbf{x}) \cdot \hat{G}(\mathbf{x}, \mathbf{y})] \otimes \nabla_{\mathbf{x}} \}
\end{aligned} \tag{C.58}$$

The above equations can be used to identify the Green function operators $\hat{W}(\mathbf{x}, \mathbf{y})$ and $\hat{\Phi}(\mathbf{x}, \mathbf{y})$

$$\begin{aligned}
\hat{W}(\mathbf{x}, \mathbf{y}) &= \lambda [\hat{\Gamma}(\mathbf{x}, \mathbf{y}) \cdot \nabla_{\mathbf{x}}] \otimes \hat{\mathbf{n}}_a + \mu [\hat{\mathbf{n}}_a \cdot \nabla_{\mathbf{x}}] \hat{\Gamma}(\mathbf{x}, \mathbf{y}) + \mu [\hat{\Gamma}(\mathbf{x}, \mathbf{y}) \cdot \hat{\mathbf{n}}_a] \otimes \nabla_{\mathbf{x}} \\
\hat{\Phi}(\mathbf{x}, \mathbf{y}) &= \lambda [\nabla_{\mathbf{x}} \cdot \hat{G}(\mathbf{x}, \mathbf{y})] \otimes \hat{\mathbf{n}}(\mathbf{x}) + \mu [\hat{\mathbf{n}}(\mathbf{x}) \cdot \nabla_{\mathbf{x}}] \hat{G}(\mathbf{x}, \mathbf{y}) + \mu [\hat{\mathbf{n}}(\mathbf{x}) \cdot \hat{G}(\mathbf{x}, \mathbf{y})] \otimes \nabla_{\mathbf{x}}
\end{aligned} \tag{C.59}$$

and their matrix elements.

The explicit forms of the matrix elements of $\hat{W}(\mathbf{x}, \mathbf{y})$ and $\hat{\Phi}(\mathbf{x}, \mathbf{y})$ sandwiched between $\Psi_a(\mathbf{x})$ and $\Psi_b(\mathbf{y})$ are :

$$\begin{aligned}
[\Psi_b(\mathbf{y}) \cdot \hat{W}(\mathbf{x}, \mathbf{y}) \cdot \Psi_a(\mathbf{x})] &\equiv \phi_b(\mathbf{y}) \phi_a(\mathbf{x}) [\mathbf{b} \cdot \hat{W}(\mathbf{x}, \mathbf{y}) \cdot \mathbf{a}] \equiv \{ \hat{\mathbf{n}}(\mathbf{x}) \cdot \hat{\tau}[\Psi_b(\mathbf{y}) \cdot \hat{\Gamma}(\mathbf{x}, \mathbf{y})] \} \cdot \Psi_a(\mathbf{x}) = \\
&= \phi_a(\mathbf{x}) \phi_b(\mathbf{y}) \{ \lambda (\mathbf{a} \cdot \hat{\mathbf{n}}_a) \{ \nabla_{\mathbf{x}} \cdot [\mathbf{b} \cdot \hat{\Gamma}(\mathbf{x}, \mathbf{y})] \} + \\
&+ \mu [\hat{\mathbf{n}}_a \cdot \nabla_{\mathbf{x}}] \{ [\mathbf{b} \cdot \hat{\Gamma}(\mathbf{x}, \mathbf{y})] \cdot \mathbf{a} \} + \mu (\mathbf{a} \cdot \nabla_{\mathbf{x}}) \{ [\mathbf{b} \cdot \hat{\Gamma}(\mathbf{x}, \mathbf{y})] \cdot \hat{\mathbf{n}}_a \} \} \\
[\Psi_b(\mathbf{y}) \cdot \hat{\Phi}(\mathbf{x}, \mathbf{y}) \cdot \Psi_a(\mathbf{x})] &\equiv \phi_b(\mathbf{y}) \phi_a(\mathbf{x}) [\mathbf{b} \cdot \hat{\Phi}(\mathbf{x}, \mathbf{y}) \cdot \mathbf{a}] \equiv \{ \hat{\mathbf{n}}(\mathbf{x}) \cdot \hat{\tau}[\Psi_b(\mathbf{y}) \cdot \hat{G}(\mathbf{x}, \mathbf{y})] \} \cdot \Psi_a(\mathbf{x}) = \\
&= \phi_a(\mathbf{x}) \phi_b(\mathbf{y}) \{ \lambda (\mathbf{a} \cdot \hat{\mathbf{n}}_a) \{ \mathbf{b} \cdot [\nabla_{\mathbf{x}} \cdot \hat{G}(\mathbf{x}, \mathbf{y})] \} + \mu [\hat{\mathbf{n}}_a \cdot \nabla_{\mathbf{x}}] [\mathbf{a} \cdot \hat{G}(\mathbf{x}, \mathbf{y}) \cdot \mathbf{b}] + \\
&+ \mu (\mathbf{a} \cdot \nabla_{\mathbf{x}}) \{ \hat{\mathbf{n}}_a \cdot \hat{G}(\mathbf{x}, \mathbf{y}) \cdot \mathbf{b} \} \}
\end{aligned} \tag{C.60}$$

We may deduce the form of $\hat{W}(\mathbf{x}, \mathbf{y})$ from as follows:

$$\begin{aligned}
\hat{W}(\mathbf{x}, \mathbf{y}) &= \lambda [\hat{\Gamma}(\mathbf{x}, \mathbf{y}) \cdot \nabla_{\mathbf{x}}] \otimes \hat{\mathbf{n}}_a + \mu (\hat{\mathbf{n}}_a \cdot \nabla_{\mathbf{x}}) \hat{\Gamma}(\mathbf{x}, \mathbf{y}) + \mu [\hat{\Gamma}(\mathbf{x}, \mathbf{y}) \cdot \hat{\mathbf{n}}_a] \otimes \nabla_{\mathbf{x}} = \\
&- \frac{\lambda k_C^2}{\lambda + 2\mu} \hat{\mathbf{n}}_b \otimes \hat{\mathbf{n}}_a g_C(R) + \frac{2\lambda\mu}{\lambda + 2\mu} \{ (\hat{\mathbf{n}}_b \cdot \nabla_{\mathbf{x}}) \nabla_{\mathbf{x}} \otimes \hat{\mathbf{n}}_a + (\hat{\mathbf{n}}_a \cdot \nabla_{\mathbf{x}}) \hat{\mathbf{n}}_b \otimes \nabla_{\mathbf{x}} \} g_C(R) + \\
&+ \mu^2 \{ (\hat{\mathbf{n}}_a \cdot \nabla_{\mathbf{x}}) (\hat{\mathbf{n}}_b \cdot \nabla_{\mathbf{x}}) \hat{G}(\mathbf{x}, \mathbf{y}) + (\hat{\mathbf{n}}_a \cdot \nabla_{\mathbf{x}}) \nabla_{\mathbf{x}} \otimes [\hat{\mathbf{n}}_b \cdot \hat{G}(\mathbf{x}, \mathbf{y})] + \\
&+ (\hat{\mathbf{n}}_b \cdot \nabla_{\mathbf{x}}) [\hat{\mathbf{n}}_a \cdot \hat{G}(\mathbf{x}, \mathbf{y})] \otimes \nabla_{\mathbf{x}} + [\hat{\mathbf{n}}_b \cdot \hat{G}(\mathbf{x}, \mathbf{y}) \cdot \hat{\mathbf{n}}_a] \nabla_{\mathbf{x}} \otimes \nabla_{\mathbf{x}} \}
\end{aligned} \tag{C.61}$$

By using the following auxiliary expressions for terms appearing in the matrix elements

$$\begin{aligned}
\nabla_{\mathbf{x}} \cdot \hat{G}(\mathbf{x}, \mathbf{y}) &= \frac{1}{\lambda + 2\mu} \nabla_{\mathbf{x}} g_C(R), \\
\nabla_{\mathbf{x}} \cdot [\nabla_{\mathbf{x}} \cdot \hat{G}(\mathbf{x}, \mathbf{y})] &= [\nabla_{\mathbf{x}} \cdot \hat{G}(\mathbf{x}, \mathbf{y}) \cdot \nabla_{\mathbf{x}}] = -\frac{k_C^2}{\lambda + 2\mu} [g_C(R) + \delta(\mathbf{R})], \\
\nabla_{\mathbf{x}} \cdot [\hat{G}(\mathbf{x}, \mathbf{y}) \cdot \mathbf{b}] &= [\mathbf{b} \cdot \hat{G}(\mathbf{x}, \mathbf{y}) \cdot \nabla_{\mathbf{x}}] = \frac{1}{\lambda + 2\mu} (\mathbf{b} \cdot \nabla_{\mathbf{x}}) g_C(R),
\end{aligned} \tag{C.62}$$

we find the following formula for the matrix element of \hat{W}

$$\begin{aligned}
\mathbf{b} \cdot \hat{W}(\mathbf{x}, \mathbf{y}) \cdot \mathbf{a} &= \\
&= -\frac{\lambda^2 k_C^2}{\lambda + 2\mu} (\mathbf{a} \cdot \hat{\mathbf{n}}_a) (\mathbf{b} \cdot \hat{\mathbf{n}}_b) g_C(R) + \\
&+ \frac{2\lambda\mu}{\lambda + 2\mu} [(\hat{\mathbf{n}}_a \cdot \mathbf{a})(\hat{\mathbf{n}}_b \cdot \nabla_{\mathbf{x}})(\mathbf{b} \cdot \nabla_{\mathbf{x}}) + (\hat{\mathbf{n}}_b \cdot \mathbf{b})(\hat{\mathbf{n}}_a \cdot \nabla_{\mathbf{x}})(\mathbf{a} \cdot \nabla_{\mathbf{x}})] g_C(R) + \\
&+ \mu^2 \{ (\hat{\mathbf{n}}_a \cdot \nabla_{\mathbf{x}})(\hat{\mathbf{n}}_b \cdot \nabla_{\mathbf{x}}) [\mathbf{b} \cdot \hat{G}(\mathbf{x}, \mathbf{y}) \cdot \mathbf{a}] + (\hat{\mathbf{n}}_a \cdot \nabla_{\mathbf{x}})(\mathbf{b} \cdot \nabla_{\mathbf{x}}) [\hat{\mathbf{n}}_b \cdot \hat{G}(\mathbf{x}, \mathbf{y}) \cdot \mathbf{a}] + \\
&+ (\mathbf{a} \cdot \nabla_{\mathbf{x}})(\hat{\mathbf{n}}_b \cdot \nabla_{\mathbf{x}}) [\mathbf{b} \cdot \hat{G}(\mathbf{x}, \mathbf{y}) \cdot \hat{\mathbf{n}}_a] + (\mathbf{a} \cdot \nabla_{\mathbf{x}})(\mathbf{b} \cdot \nabla_{\mathbf{x}}) [\hat{\mathbf{n}}_b \cdot \hat{G}(\mathbf{x}, \mathbf{y}) \cdot \hat{\mathbf{n}}_a] \}
\end{aligned} \tag{C.63}$$

$$\begin{aligned}
\mathbf{b} \cdot \hat{W}(\mathbf{x}, \mathbf{y}) \cdot \mathbf{a} &= \\
&- \frac{\lambda^2 k_C^2}{\lambda + 2\mu} (\mathbf{a} \cdot \hat{\mathbf{n}}_a) (\mathbf{b} \cdot \hat{\mathbf{n}}_b) g_C(R) + \\
&+ \frac{2\lambda\mu}{\lambda + 2\mu} [(\hat{\mathbf{n}}_a \cdot \mathbf{a})(\hat{\mathbf{n}}_b \cdot \nabla_{\mathbf{x}})(\mathbf{b} \cdot \nabla_{\mathbf{x}}) + (\hat{\mathbf{n}}_b \cdot \mathbf{b})(\hat{\mathbf{n}}_a \cdot \nabla_{\mathbf{x}})(\mathbf{a} \cdot \nabla_{\mathbf{x}})] g_C(R) + \\
&+ \mu \{ (\mathbf{a} \cdot \mathbf{b})(\hat{\mathbf{n}}_a \cdot \nabla_{\mathbf{x}})(\hat{\mathbf{n}}_b \cdot \nabla_{\mathbf{x}}) + (\hat{\mathbf{n}}_b \cdot \mathbf{a})(\hat{\mathbf{n}}_a \cdot \nabla_{\mathbf{x}})(\mathbf{b} \cdot \nabla_{\mathbf{x}}) + \\
&+ (\hat{\mathbf{n}}_a \cdot \mathbf{b})(\mathbf{a} \cdot \nabla_{\mathbf{x}})(\hat{\mathbf{n}}_b \cdot \nabla_{\mathbf{x}}) + (\hat{\mathbf{n}}_a \cdot \hat{\mathbf{n}}_b)(\mathbf{a} \cdot \nabla_{\mathbf{x}})(\mathbf{b} \cdot \nabla_{\mathbf{x}}) \} g_S(R) + \\
&+ \frac{4\mu}{k_S^2} (\hat{\mathbf{n}}_a \cdot \nabla_{\mathbf{x}})(\hat{\mathbf{n}}_b \cdot \nabla_{\mathbf{x}})(\mathbf{a} \cdot \nabla_{\mathbf{x}})(\mathbf{b} \cdot \nabla_{\mathbf{x}}) [g_S(R) - g_C(R)].
\end{aligned} \tag{C.64}$$

C.5.3 Basic formulae needed for the evaluation of matrix elements of \hat{G} , \hat{I} , $\hat{\Phi}$, and \hat{W}

The kernels \hat{G} , \hat{I} , $\hat{\Phi}$, and \hat{W} need to be sandwiched between **the piecewise linear node basis function associated with a set of triangles sharing common vertices α and β .**

We consider a pair of triangles a and b with normal unit vectors $\hat{\mathbf{n}}_a$ and $\hat{\mathbf{n}}_b$. The normal vectors to the sides a and b are $\hat{\mathbf{h}}_a$ and $\hat{\mathbf{h}}_b$. We note that $\hat{\mathbf{n}}_a$ is perpendicular to the edge \mathbf{l}_a facing vertex a .

Let us represent the linear basis functions components associated with one triangle a or b as follows

$$\begin{aligned}
\boldsymbol{\Psi}_a(\mathbf{x}) &= \mathbf{a} \phi_a(\mathbf{x}), \\
\boldsymbol{\Psi}_b(\mathbf{x}) &= \mathbf{b} \phi_b(\mathbf{x}), \\
\phi_a(\mathbf{x}) &= \xi_a \chi_a(\mathbf{x}) = \left[1 - \frac{\hat{\mathbf{h}}_a \cdot (\mathbf{x} - \mathbf{v}_a)}{h_a} \right] \chi_a(\mathbf{x}), \\
\phi_b(\mathbf{x}) &= \xi_b \chi_b(\mathbf{x}) = \left[1 - \frac{\hat{\mathbf{h}}_b \cdot (\mathbf{x} - \mathbf{v}_b)}{h_b} \right] \chi_b(\mathbf{x}).
\end{aligned} \tag{C.65}$$

We may decompose both \mathbf{a} and \mathbf{b} into tangential and normal components to triangle faces

$$\begin{aligned}
\mathbf{a} &= (\hat{\mathbf{n}}_a \times \mathbf{a}) \times \hat{\mathbf{n}}_a + (\hat{\mathbf{n}}_a \cdot \mathbf{a}) \hat{\mathbf{n}}_a = \mathbf{a}_t + \mathbf{a}_n \\
\mathbf{b} &= (\hat{\mathbf{n}}_b \times \mathbf{b}) \times \hat{\mathbf{n}}_b + (\hat{\mathbf{n}}_b \cdot \mathbf{b}) \hat{\mathbf{n}}_b = \mathbf{b}_t + \mathbf{b}_n \\
\mathbf{a}_n &= (\hat{\mathbf{n}}_a \cdot \mathbf{a}) \hat{\mathbf{n}}_a \\
\mathbf{a}_t &= (\hat{\mathbf{n}}_a \times \mathbf{a}) \times \hat{\mathbf{n}}_a = a_t \hat{\mathbf{a}}_t \\
a_n &= (\hat{\mathbf{n}}_a \cdot \mathbf{a}) \\
a_t &= \sqrt{|\mathbf{a}|^2 - a_n^2}, \\
\mathbf{l}_a &= \hat{\mathbf{n}}_a \times \hat{\mathbf{h}}_a
\end{aligned} \tag{C.66}$$

Tangential derivatives of basis functions (we neglect the contributions associated with derivatives of the characteristic function χ_a)

$$\begin{aligned}
\{(\hat{\mathbf{n}}_a \times \nabla_{\mathbf{x}}) \times \hat{\mathbf{n}}_a\} \phi_a(\mathbf{x}) &= -2 \frac{\hat{\mathbf{h}}_a}{h_a} \chi_a(\mathbf{x}) \\
(\hat{\mathbf{n}}_a \times \nabla_{\mathbf{x}}) \phi_a(\mathbf{x}) &= -2 \frac{(\hat{\mathbf{n}}_a \times \hat{\mathbf{h}}_a)}{h_a} \chi_a(\mathbf{x}) = -2 \frac{\hat{\mathbf{l}}_a}{h_a} \chi_a(\mathbf{x}), \\
[\mathbf{a}_t \cdot \nabla_{\mathbf{x}}] \phi_a(\mathbf{x}) &= -2 a_t \frac{(\hat{\mathbf{a}}_t \cdot \hat{\mathbf{h}}_a)}{h_a} \chi_a(\mathbf{x})
\end{aligned} \tag{C.67}$$

$$\begin{aligned}
(\mathbf{a} \cdot \nabla_{\mathbf{R}})(\mathbf{b} \cdot \nabla_{\mathbf{R}}) &= (\mathbf{a}_n \cdot \nabla_{\mathbf{R}})(\mathbf{b}_n \cdot \nabla_{\mathbf{R}}) + (\mathbf{a}_t \cdot \nabla_{\mathbf{R}})(\mathbf{b}_n \cdot \nabla_{\mathbf{R}}) + \\
&\quad + (\mathbf{a}_n \cdot \nabla_{\mathbf{R}})(\mathbf{b}_t \cdot \nabla_{\mathbf{R}}) + (\mathbf{a}_t \cdot \nabla_{\mathbf{R}})(\mathbf{b}_t \cdot \nabla_{\mathbf{R}}) \\
(\mathbf{a}_n \cdot \nabla_{\mathbf{R}})(\mathbf{b}_n \cdot \nabla_{\mathbf{R}}) &= -(\mathbf{a}_n \times \nabla_{\mathbf{R}}) \cdot (\mathbf{b}_n \times \nabla_{\mathbf{R}}) + (\mathbf{a}_n \cdot \mathbf{b}_n) \nabla_{\mathbf{R}}^2
\end{aligned} \tag{C.68}$$

In the following we provide explicit expressions for matrix elements of the kernels \hat{G} , \hat{I} $\hat{\Phi}$ and \hat{W} .

Evaluation of matrix elements of \hat{G} .

$$\begin{aligned}
\int dS_{\mathbf{x}} dS_{\mathbf{y}} \Psi_a(\mathbf{x}) \hat{G}(\mathbf{x}, \mathbf{y}) \Psi_b(\mathbf{y}) &= \\
&= \frac{1}{\mu} \int_{T_a T_b} dS_{\mathbf{x}} dS_{\mathbf{y}} \phi_a(\mathbf{x}) \phi_b(\mathbf{y}) [(\mathbf{a} \cdot \mathbf{b}) g_S(R) + \frac{1}{k_S^2} (\mathbf{a} \cdot \nabla_{\mathbf{R}})(\mathbf{b} \cdot \nabla_{\mathbf{R}}) g_{SC}(R)]
\end{aligned} \tag{C.69}$$

$$\begin{aligned}
& \int_{T_a T_b} dS_{\mathbf{x}} dS_{\mathbf{y}} \phi_a(\mathbf{x}) \phi_b(\mathbf{y}) (\mathbf{a}_n \cdot \nabla_{\mathbf{R}}) (\mathbf{b}_t \cdot \nabla_{\mathbf{R}}) g_{SC}(R) = \frac{2(\mathbf{b}_t \cdot \mathbf{h}_b)}{h_b} \int dS_{\mathbf{x}} dS_{\mathbf{y}} \phi_a(\mathbf{x}) (\mathbf{a}_n \cdot \hat{\mathbf{R}}) g'_{SC}(R) \\
& \int_{T_a T_b} dS_{\mathbf{x}} dS_{\mathbf{y}} \phi_a(\mathbf{x}) \phi_b(\mathbf{y}) (\mathbf{a}_t \cdot \nabla_{\mathbf{R}}) (\mathbf{b}_n \cdot \nabla_{\mathbf{R}}) g_{SC}(R) = \frac{2(\mathbf{a}_t \cdot \mathbf{h}_a)}{h_a} \int dS_{\mathbf{x}} dS_{\mathbf{y}} \phi_b(\mathbf{y}) (\mathbf{b}_n \cdot \hat{\mathbf{R}}) g'_{SC}(R) \\
& \int_{T_a T_b} dS_{\mathbf{x}} dS_{\mathbf{y}} \phi_a(\mathbf{x}) \phi_b(\mathbf{y}) (\mathbf{a}_t \cdot \nabla_{\mathbf{R}}) (\mathbf{b}_t \cdot \nabla_{\mathbf{R}}) g_{SC}(R) = \frac{4(\mathbf{a}_t \cdot \hat{\mathbf{h}}_a)(\mathbf{b}_t \cdot \hat{\mathbf{h}}_b)}{h_a h_b} \int dS_{\mathbf{x}} dS_{\mathbf{y}} g_{SC}(R) \\
& \int_{T_a T_b} dS_{\mathbf{x}} dS_{\mathbf{y}} \phi_a(\mathbf{x}) \phi_b(\mathbf{y}) \{ (\mathbf{a}_n \cdot \nabla_{\mathbf{R}}) (\mathbf{b}_n \cdot \nabla_{\mathbf{R}}) g_{SC}(R) = \\
& = a_n b_n \int_{T_a T_b} dS_{\mathbf{x}} dS_{\mathbf{y}} \{ \phi_a(\mathbf{x}) \phi_b(\mathbf{y}) (\hat{\mathbf{n}}_a \cdot \hat{\mathbf{n}}_b) [k_S^2 g_S(R) - k_C^2 g_C(R)] - \frac{4(\hat{\mathbf{l}}_a \cdot \hat{\mathbf{l}}_b)}{h_a h_b} g_{SC}(R) \}
\end{aligned} \tag{C.70}$$

By collecting the above terms we obtain

$$\begin{aligned}
& \int_{T_a T_b} dS_{\mathbf{x}} dS_{\mathbf{y}} \phi_a(\mathbf{x}) g_{SC}(R) (\mathbf{a} \cdot \nabla_{\mathbf{R}}) (\mathbf{b} \cdot \nabla_{\mathbf{R}}) \phi_b(\mathbf{y}) = \\
& = a_n b_n (\hat{\mathbf{n}}_a \cdot \hat{\mathbf{n}}_b) \int_{T_a T_b} dS_{\mathbf{x}} dS_{\mathbf{y}} \phi_a(\mathbf{x}) \phi_b(\mathbf{y}) [k_S^2 g_S(R) - k_C^2 g_C(R)] + \\
& + \frac{2a_n (\hat{\mathbf{b}}_t \cdot \hat{\mathbf{h}}_b)}{h_a} \int_{T_a T_b} dS_{\mathbf{x}} dS_{\mathbf{y}} \phi_a(\mathbf{x}) (\hat{\mathbf{R}} \cdot \hat{\mathbf{n}}_a) g'_{SC}(R) + \\
& + \frac{2b_n (\mathbf{a}_t \cdot \hat{\mathbf{h}}_a)}{h_b} \int_{T_a T_b} dS_{\mathbf{x}} dS_{\mathbf{y}} \phi_b(\mathbf{y}) (\hat{\mathbf{R}} \cdot \hat{\mathbf{n}}_b) g'_{SC}(R) + \\
& + 4 \frac{(\mathbf{a} \cdot \hat{\mathbf{h}}_a)(\mathbf{b} \cdot \hat{\mathbf{h}}_b) - a_n b_n (\hat{\mathbf{l}}_a \cdot \hat{\mathbf{l}}_b)}{h_a h_b} \int_{T_a T_b} dS_{\mathbf{x}} dS_{\mathbf{y}} g_{SC}(R).
\end{aligned} \tag{C.71}$$

In deriving the above we used the following auxiliary relations

$$\hat{\mathbf{n}}_a \times \hat{\mathbf{h}}_a = \hat{\mathbf{l}}_a$$

For the linear basis function associated with node \mathbf{v}_b we have

$$\begin{aligned}
& \nabla_{\mathbf{x}} \psi_a(\mathbf{x}) = -\frac{\hat{\mathbf{h}}_a}{h_a} \\
& \int dS g_{SC}(R) \nabla_{\mathbf{x}} \phi_a(\mathbf{x}) = -\hat{\mathbf{h}}_a \int dS g_{SC}(R)
\end{aligned}$$

For the constant basis function associated with triangle T' and vertex \mathbf{v}_b we have

$$\nabla_{\mathbf{x}} \psi_a(\mathbf{x}) = -\sum_{b=1}^3 \hat{\mathbf{h}}_b \delta_b(\mathbf{r})$$

$$\int dS g_{SC}(R) [\nabla_{\mathbf{x}} \phi_a(\mathbf{x})] = -\hat{\mathbf{h}}_a \int_{\partial l_a} dS g_{SC}(R)$$

Complete matrix element of \hat{G} for the linear basis functions

$$\begin{aligned} \int_{T_a T_b} dS_{\mathbf{x}} dS_{\mathbf{y}} \Psi_b(\mathbf{y}) \hat{G}(\mathbf{R}) \Psi_a(\mathbf{x}) &= \frac{(\mathbf{a} \cdot \mathbf{b})}{\mu} I_1 + \frac{(\mathbf{a} \cdot \hat{\mathbf{n}}_a)(\mathbf{b} \cdot \hat{\mathbf{n}}_b)(\hat{\mathbf{n}}_a \cdot \hat{\mathbf{n}}_b)}{\mu k_S^2} I_2 + \\ &+ \frac{4[(\mathbf{b} \cdot \hat{\mathbf{h}}_b)(\mathbf{a} \cdot \hat{\mathbf{h}}_a) - (\mathbf{b} \cdot \hat{\mathbf{n}}_b)(\mathbf{a} \cdot \hat{\mathbf{n}}_a)(\hat{\mathbf{l}}_a \cdot \hat{\mathbf{l}}_b)]}{\mu k_S^2 h_a h_b} I_3 + \frac{2(\hat{\mathbf{h}}_b \cdot \mathbf{b})(\mathbf{a} \cdot \hat{\mathbf{n}}_a)}{\mu k_S^2 h_b} I_4 + \frac{2(\hat{\mathbf{h}}_a \cdot \mathbf{a})(\mathbf{b} \cdot \hat{\mathbf{n}}_b)}{\mu k_S^2 h_a} I_5, \end{aligned} \quad (\text{C.72})$$

where

$$\begin{aligned} I_1 &= \int_{T_a} dS_{\mathbf{x}} \int_{T_b} dS_{\mathbf{y}} \phi_a(\mathbf{x}) \phi_b(\mathbf{y}) g_S(R), \\ I_2 &= \int_{T_a} dS_{\mathbf{x}} \int_{T_b} dS_{\mathbf{y}} \phi_a(\mathbf{x}) \phi_b(\mathbf{y}) [k_S^2 g_S(R) - k_C^2 g_C(R)], \\ I_3 &= \int_{T_a} dS_{\mathbf{x}} \int_{T_b} dS_{\mathbf{y}} g_{SC}(R), \\ I_4 &= \int_{T_a} dS_{\mathbf{x}} \int_{T_b} dS_{\mathbf{y}} \phi_a(\mathbf{x}) (\hat{\mathbf{n}}_a \cdot \hat{\mathbf{R}}) g'_{SC}(R), \\ I_5 &= \int_{T_a} dS_{\mathbf{x}} \int_{T_b} dS_{\mathbf{y}} \phi_b(\mathbf{y}) (\hat{\mathbf{n}}_b \cdot \hat{\mathbf{R}}) g'_{SC}(R). \end{aligned} \quad (\text{C.73})$$

Evaluation of matrix elements of $\hat{\Gamma}$.

$$\int dS_{\mathbf{x}} dS_{\mathbf{y}} [\Psi_a(\mathbf{x}) \cdot \hat{\Gamma}(\mathbf{x}, \mathbf{y}) \cdot \Psi_b(\mathbf{y})] = \int dS_{\mathbf{x}} dS_{\mathbf{y}} \phi_a(\mathbf{x}) \phi_b(\mathbf{y}) [\mathbf{b} \hat{\Gamma} \mathbf{a}], \quad (\text{C.74})$$

where

$$\begin{aligned} (\mathbf{b} \hat{\Gamma} \mathbf{a}) &= \frac{\lambda}{\lambda + 2\mu} (\hat{\mathbf{n}}_b \cdot \mathbf{b})(\mathbf{a} \cdot \nabla_{\mathbf{R}}) g_C(R) + \{(\mathbf{a} \cdot \mathbf{b})(\hat{\mathbf{n}}_b \cdot \nabla_{\mathbf{R}}) + (\hat{\mathbf{n}}_b \cdot \mathbf{a})(\mathbf{b} \cdot \nabla_{\mathbf{R}})\} g_S(R) + \\ &+ \frac{2}{k_S^2} (\mathbf{a} \cdot \nabla_{\mathbf{R}})(\mathbf{b} \cdot \nabla_{\mathbf{R}})(\hat{\mathbf{n}}_b \cdot \nabla_{\mathbf{R}}) [g_S(R) - g_C(R)], \end{aligned} \quad (\text{C.75})$$

The operator $\hat{\Gamma}$ needs to be sandwiched between the piecewise linear basis function associated with vertex a of a triangle a and a piecewise constant function associated with triangle b :

We will use the following decompositions of the $\nabla_{\mathbf{R}}$ into its tangential and normal components

$$(\mathbf{a} \cdot \nabla_{\mathbf{R}}) = a_n (\hat{\mathbf{n}}_a \cdot \nabla_{\mathbf{R}}) + a_t (\hat{\mathbf{t}}_a \cdot \nabla_{\mathbf{R}}), \quad (\text{C.76})$$

Subsequently we evaluate the matrix elements

$$\begin{aligned}
\int dS_{\mathbf{x}} dS_{\mathbf{y}} \phi_a(\mathbf{x}) \phi_b(\mathbf{y}) (\hat{\mathbf{n}}_b \cdot \mathbf{b}) (\mathbf{a} \cdot \hat{\mathbf{R}}) g'_C(R) &= (\hat{\mathbf{n}}_b \cdot \mathbf{b}) [a_n G_1 + a_t (\hat{\mathbf{t}}_a \cdot \hat{\mathbf{h}}_a) G_2], \\
(\hat{\mathbf{n}}_b \cdot \mathbf{a}) \int dS_{\mathbf{x}} dS_{\mathbf{y}} \phi_a(\mathbf{x}) \phi_b(\mathbf{y}) (\mathbf{b} \cdot \nabla_{\mathbf{R}}) g_S(R) &= (\hat{\mathbf{n}}_b \cdot \mathbf{a}) + b_t (\hat{\mathbf{t}}_b \cdot \hat{\mathbf{h}}_b) G_4, \\
(\mathbf{a} \cdot \mathbf{b}) \int dS_{\mathbf{x}} dS_{\mathbf{y}} \phi_a(\mathbf{x}) \phi_b(\mathbf{y}) (\hat{\mathbf{n}}_b \cdot \nabla_{\mathbf{R}}) g_S(R) &= (\mathbf{a} \cdot \mathbf{b}) G_5,
\end{aligned} \tag{C.77}$$

The product of the three projections of the $\nabla_{\mathbf{R}}$ appearing in the matrix element of \hat{F} can be suitably written as

$$\begin{aligned}
(\hat{\mathbf{n}}_b \cdot \nabla)(\mathbf{b} \cdot \nabla)(\mathbf{a} \cdot \nabla) &= a_n b_n (\hat{\mathbf{n}}_a \cdot \nabla)(\hat{\mathbf{n}}_b \cdot \nabla)(\hat{\mathbf{n}}_b \cdot \nabla) + \\
&+ a_t b_t (\hat{\mathbf{n}}_b \cdot \nabla)(\hat{\mathbf{t}}_a \cdot \nabla)(\hat{\mathbf{t}}_b \cdot \nabla) + \\
&+ a_n b_t (\hat{\mathbf{n}}_b \cdot \nabla)(\hat{\mathbf{n}}_a \cdot \nabla)(\hat{\mathbf{t}}_b \cdot \nabla) + \\
&+ a_t b_n (\hat{\mathbf{n}}_b \cdot \nabla)(\hat{\mathbf{t}}_a \cdot \nabla)(\hat{\mathbf{n}}_b \cdot \nabla) = \\
&= a_n b_n (\hat{\mathbf{n}}_b \cdot \nabla) [(\hat{\mathbf{n}}_a \cdot \hat{\mathbf{n}}_b) \nabla^2 - (\hat{\mathbf{n}}_a \times \nabla) \cdot (\hat{\mathbf{n}}_b \times \nabla)] + \\
&+ a_t b_t (\hat{\mathbf{n}}_b \cdot \nabla)(\hat{\mathbf{t}}_a \cdot \nabla)(\hat{\mathbf{t}}_b \cdot \nabla) + \\
&+ a_n b_t (\hat{\mathbf{t}}_b \cdot \nabla) [(\hat{\mathbf{n}}_a \cdot \hat{\mathbf{n}}_b) \nabla^2 - (\hat{\mathbf{n}}_a \times \nabla) \cdot (\hat{\mathbf{n}}_b \times \nabla)] + \\
&+ a_t b_n (\hat{\mathbf{t}}_a \cdot \nabla) [(\hat{\mathbf{n}}_b \cdot \hat{\mathbf{n}}_b) \nabla^2 - (\hat{\mathbf{n}}_b \times \nabla) \cdot (\hat{\mathbf{n}}_b \times \nabla)]
\end{aligned} \tag{C.78}$$

When sandwiched between the basis functions in the matrix element integrals the above terms yield

$$\begin{aligned}
&\left\{ a_n b_n (\hat{\mathbf{n}}_a \cdot \hat{\mathbf{n}}_b) \phi_a(\mathbf{x}) \phi_b(\mathbf{y}) + \frac{-a_n b_n (\hat{\mathbf{l}}_a \cdot \hat{\mathbf{l}}_b) + a_t b_t (\hat{\mathbf{t}}_a \cdot \hat{\mathbf{h}}_a) (\hat{\mathbf{t}}_b \cdot \hat{\mathbf{h}}_b)}{h_a h_b} \right\} (\hat{\mathbf{n}}_b \cdot \nabla) [g_S(R) - g_C(R)] + \\
&+ \left[\frac{a_n b_t (\hat{\mathbf{n}}_a \cdot \hat{\mathbf{n}}_b) (\hat{\mathbf{t}}_b \cdot \hat{\mathbf{h}}_b)}{h_b} \phi_a(R) + \frac{a_t b_n (\hat{\mathbf{n}}_a \cdot \hat{\mathbf{n}}_b) (\hat{\mathbf{t}}_a \cdot \hat{\mathbf{h}}_a)}{h_a} \phi_b(R) \right] [k_S^2 g_S(R) - k_C^2 g_C(R)] + \\
&+ \frac{(\hat{\mathbf{n}}_a \cdot \hat{\mathbf{n}}_b) (\hat{\mathbf{l}}_a \cdot \hat{\mathbf{l}}_b)}{h_a h_b} [a_n b_t (\hat{\mathbf{t}}_b \cdot \hat{\mathbf{h}}_b) \phi_a(R) \delta(\mathbf{r}_b) + a_t b_n (\hat{\mathbf{t}}_a \cdot \hat{\mathbf{h}}_a) \phi_b(R) \delta(\mathbf{r}_a)] [g_S(R) - g_C(R)].
\end{aligned} \tag{C.79}$$

Now the integrals of the term appearing in the above formula

$$\begin{aligned}
&\int dS_{\mathbf{x}} dS_{\mathbf{y}} \phi_a(\mathbf{x}) \phi_b(\mathbf{y}) (\hat{\mathbf{n}}_b \cdot \nabla)(\mathbf{a} \cdot \nabla)(\mathbf{b} \cdot \nabla) [g_S(R) - g_C(R)] = \\
&= a_n b_n (\hat{\mathbf{n}}_a \cdot \hat{\mathbf{n}}_b) G_6 + 4 \frac{-a_n b_n (\hat{\mathbf{l}}_a \cdot \hat{\mathbf{l}}_b) + a_t b_t (\hat{\mathbf{t}}_a \cdot \hat{\mathbf{h}}_a) (\hat{\mathbf{t}}_b \cdot \hat{\mathbf{h}}_b)}{h_a h_b} G_7 + \\
&+ 2 \frac{a_n b_t (\hat{\mathbf{n}}_a \cdot \hat{\mathbf{n}}_b) (\hat{\mathbf{t}}_b \cdot \hat{\mathbf{h}}_b)}{h_b} G_8 + \frac{a_t b_n (\hat{\mathbf{n}}_a \cdot \hat{\mathbf{n}}_b) (\hat{\mathbf{t}}_a \cdot \hat{\mathbf{h}}_a)}{h_a} G_9 + \\
&+ 4 \frac{(\hat{\mathbf{n}}_a \cdot \hat{\mathbf{n}}_b) (\hat{\mathbf{l}}_a \cdot \hat{\mathbf{l}}_b)}{h_a h_b} [a_n b_t (\hat{\mathbf{t}}_b \cdot \hat{\mathbf{h}}_b) G_{10} + a_t b_n (\hat{\mathbf{t}}_a \cdot \hat{\mathbf{h}}_a) G_{11}].
\end{aligned} \tag{C.80}$$

Complete matrix element of \hat{I} for the linear basis functions

$$\begin{aligned}
& \int_{T_a T_b} dS_{\mathbf{x}} dS_{\mathbf{y}} \Psi_b(\mathbf{y}) \hat{I}(\mathbf{R}) \Psi_a(\mathbf{x}) = \\
& = \frac{\lambda}{\lambda + 2\mu} \{ (\hat{\mathbf{n}}_b \cdot \mathbf{b}) [a_n G_1 + a_t (\hat{\mathbf{t}}_a \cdot \hat{\mathbf{h}}_a) G_2] + (\hat{\mathbf{n}}_b \cdot \mathbf{a}) [b_n G_3 + b_t (\hat{\mathbf{t}}_b \cdot \hat{\mathbf{h}}_b) G_4] + (\mathbf{a} \cdot \mathbf{b}) G_5 \} + \\
& + \frac{2a_n b_n (\hat{\mathbf{n}}_a \cdot \hat{\mathbf{n}}_b)}{k_S^2} G_6 + \frac{8[-a_n b_n (\hat{\mathbf{l}}_a \cdot \hat{\mathbf{l}}_b) + a_t b_t (\hat{\mathbf{t}}_a \cdot \hat{\mathbf{h}}_a) (\hat{\mathbf{t}}_b \cdot \hat{\mathbf{h}}_b)]}{h_a h_b k_S^2} G_7 + \\
& + \frac{4a_n b_t (\hat{\mathbf{n}}_a \cdot \hat{\mathbf{n}}_b) (\hat{\mathbf{t}}_b \cdot \hat{\mathbf{h}}_b)}{h_b k_S^2} G_8 + \frac{4a_t b_n (\hat{\mathbf{n}}_a \cdot \hat{\mathbf{n}}_b) (\hat{\mathbf{t}}_a \cdot \hat{\mathbf{h}}_a)}{h_a k_S^2} G_9 + \\
& + \frac{8(\hat{\mathbf{n}}_a \cdot \hat{\mathbf{n}}_b) (\hat{\mathbf{l}}_a \cdot \hat{\mathbf{l}}_b)}{h_a h_b k_S^2} [a_n b_t (\hat{\mathbf{t}}_b \cdot \hat{\mathbf{h}}_b) G_{10} + a_t b_n (\hat{\mathbf{t}}_a \cdot \hat{\mathbf{h}}_a) G_{11}].
\end{aligned} \tag{C.81}$$

The evaluation of the above matrix elements reduces to the calculation of the following

basic integrals

$$\begin{aligned}
G_1 &= \int_{T_a} dS_{\mathbf{x}} \int_{T_b} dS_{\mathbf{y}} \phi_a(\mathbf{x}) \phi_b(\mathbf{y}) (\hat{\mathbf{n}}_a \cdot \hat{\mathbf{R}}) g'_C(R), \\
G_2 &= \int_{T_a} dS_{\mathbf{x}} \int_{T_b} dS_{\mathbf{y}} \phi_b(\mathbf{y}) g_C(R), \\
G_3 &= \int_{T_a} dS_{\mathbf{x}} \int_{T_b} dS_{\mathbf{y}} (\hat{\mathbf{n}}_a \cdot \hat{\mathbf{R}}) g'_S(R) = \\
G_4 &= \int_{T_a} dS_{\mathbf{x}} \int_{T_b} dS_{\mathbf{y}} g_S(R), \\
G_5 &= \int_{T_a} dS_{\mathbf{x}} \int_{T_b} dS_{\mathbf{y}} \phi_a(\mathbf{x}) \phi_b(\mathbf{y}) (\hat{\mathbf{n}}_b \cdot \hat{\mathbf{R}}) g'_S(R), \\
G_6 &= \int_{T_a} dS_{\mathbf{x}} \int_{T_b} dS_{\mathbf{y}} \phi_a(\mathbf{x}) \phi_b(\mathbf{y}) (\hat{\mathbf{n}}_b \cdot \hat{\mathbf{R}}) [k_S^2 g_S(R) - k_C^2 g_C(R)], \\
G_7 &= \int_{T_a} dS_{\mathbf{x}} \int_{T_b} dS_{\mathbf{y}} (\hat{\mathbf{n}}_b \cdot \hat{\mathbf{R}}) [k_S^2 g_S(R) - k_C^2 g_C(R)], \\
G_8 &= \int_{T_a} dS_{\mathbf{x}} \int_{T_b} dS_{\mathbf{y}} \phi_a(\mathbf{x}) [k_S^2 g_S(R) - k_C^2 g_C(R)], \\
G_9 &= \int_{T_a} dS_{\mathbf{x}} \int_{T_b} dl_{\mathbf{y}} \phi_b(\mathbf{x}) [k_S^2 g_S(R) - k_C^2 g_C(R)], \\
G_{10} &= \int_{T_a} dS_{\mathbf{x}} \int_{l_b} dl_{\mathbf{y}} \phi_a(\mathbf{x}) [g_S(R) - g_C(R)], \\
G_{11} &= \int_{l_a} dl_{\mathbf{x}} \int_{T_b} dS_{\mathbf{y}} \phi_b(\mathbf{x}) [g_S(R) - g_C(R)],
\end{aligned} \tag{C.82}$$

Evaluation of matrix elements of $\hat{\Phi}$. Matrix elements of $\hat{\Phi}$ Complete matrix element of $\hat{\Phi}$ for the linear basis functions

$$\int dS_{\mathbf{x}} dS_{\mathbf{y}} [\Psi_a(\mathbf{x}) \cdot \hat{\Phi}(\mathbf{x}, \mathbf{y}) \cdot \Psi_b(\mathbf{y})] = \int dS_{\mathbf{x}} dS_{\mathbf{y}} \phi_a(\mathbf{x}) \phi_b(\mathbf{y}) [\mathbf{b} \hat{\Phi} \mathbf{a}], \tag{C.83}$$

with

$$\begin{aligned}
(\mathbf{b} \hat{\Phi} \mathbf{a}) &= \frac{\lambda}{\lambda + 2\mu} (\hat{\mathbf{n}}_a \cdot \mathbf{a}) (\hat{\mathbf{b}} \cdot \nabla_{\mathbf{R}}) g_C(R) + \{(\mathbf{a} \cdot \mathbf{b}) (\hat{\mathbf{n}}_a \cdot \nabla_{\mathbf{R}}) + (\hat{\mathbf{n}}_a \cdot \mathbf{b}) (\mathbf{a} \cdot \nabla_{\mathbf{R}})\} g_S(R) + \\
&+ \frac{2}{k_S^2} (\mathbf{a} \cdot \nabla_{\mathbf{R}}) (\mathbf{b} \cdot \nabla_{\mathbf{R}}) (\hat{\mathbf{n}}_a \cdot \nabla_{\mathbf{R}}) [g_S(R) - g_C(R)],
\end{aligned} \tag{C.84}$$

can obtained by transposition i.e., the following replacement in the expression for matrix elements of \hat{I}

$$a \rightarrow b$$

$$\begin{aligned}
& \int_{T_a T_b} dS_{\mathbf{x}} dS_{\mathbf{y}} \boldsymbol{\Psi}_b(\mathbf{y}) \hat{\Phi}(\mathbf{x}, \mathbf{y} R) \boldsymbol{\Psi}_a(\mathbf{x}) = \\
& = \frac{\lambda}{\lambda + 2\mu} \{ (\hat{\mathbf{n}}_a \cdot \mathbf{a}) [b_n F_1 + b_t (\hat{\mathbf{t}}_b \cdot \hat{\mathbf{h}}_b) F_2] + (\hat{\mathbf{n}}_a \cdot \mathbf{b}) [a_n F_3 + a_t (\hat{\mathbf{t}}_b \cdot \hat{\mathbf{h}}_b) F_4] + (\mathbf{a} \cdot \mathbf{b}) F_5 \} + \\
& + \frac{2a_n b_n (\hat{\mathbf{n}}_a \cdot \hat{\mathbf{n}}_b)}{k_S^2} F_6 + \frac{8[-a_n b_n (\hat{\mathbf{l}}_a \cdot \hat{\mathbf{l}}_b) + a_t b_t (\hat{\mathbf{t}}_a \cdot \hat{\mathbf{h}}_a) (\hat{\mathbf{t}}_b \cdot \hat{\mathbf{h}}_b)]}{h_a h_b k_S^2} F_7 + \\
& + \frac{4a_n b_t (\hat{\mathbf{n}}_a \cdot \hat{\mathbf{n}}_b) (\hat{\mathbf{t}}_b \cdot \hat{\mathbf{h}}_b)}{h_b k_S^2} F_8 + \frac{4a_t b_n (\hat{\mathbf{n}}_a \cdot \hat{\mathbf{n}}_b) (\hat{\mathbf{t}}_a \cdot \hat{\mathbf{h}}_a)}{h_a k_S^2} F_9 + \\
& + \frac{8(\hat{\mathbf{n}}_a \cdot \hat{\mathbf{n}}_b) (\hat{\mathbf{l}}_a \cdot \hat{\mathbf{l}}_b)}{h_a h_b k_S^2} [a_n b_t (\hat{\mathbf{t}}_b \cdot \hat{\mathbf{h}}_b) F_{10} + a_t b_n (\hat{\mathbf{t}}_a \cdot \hat{\mathbf{h}}_a) F_{11}].
\end{aligned} \tag{C.85}$$

$$\begin{aligned}
F_1 &= \int_{T_a} dS_{\mathbf{x}} \int_{T_b} dS_{\mathbf{y}} \phi_a(\mathbf{x}) \phi_b(\mathbf{y}) (\hat{\mathbf{n}}_b \cdot \hat{\mathbf{R}}) g'_C(R), \\
F_2 &= \int_{T_a} dS_{\mathbf{x}} \int_{T_b} dS_{\mathbf{y}} \phi_a(\mathbf{x}) g_C(R), \\
F_3 &= \int_{T_a} dS_{\mathbf{x}} \int_{T_b} dS_{\mathbf{y}} (\hat{\mathbf{n}}_b \cdot \hat{\mathbf{R}}) g'_S(R) = \\
F_4 &= \int_{T_a} dS_{\mathbf{x}} \int_{T_b} dS_{\mathbf{y}} g_S(R), \\
F_5 &= \int_{T_a} dS_{\mathbf{x}} \int_{T_b} dS_{\mathbf{y}} \phi_a(\mathbf{x}) \phi_b(\mathbf{y}) (\hat{\mathbf{n}}_a \cdot \hat{\mathbf{R}}) g'_S(R), \\
F_6 &= \int_{T_a} dS_{\mathbf{x}} \int_{T_b} dS_{\mathbf{y}} \phi_a(\mathbf{x}) \phi_b(\mathbf{y}) (\hat{\mathbf{n}}_a \cdot \hat{\mathbf{R}}) [k_S^2 g_S(R) - k_C^2 g_C(R)], \\
F_7 &= \int_{T_a} dS_{\mathbf{x}} \int_{T_b} dS_{\mathbf{y}} (\hat{\mathbf{n}}_a \cdot \hat{\mathbf{R}}) [k_S^2 g_S(R) - k_C^2 g_C(R)], \\
F_8 &= \int_{T_a} dS_{\mathbf{x}} \int_{T_b} dS_{\mathbf{y}} \phi_b(\mathbf{y}) [k_S^2 g_S(R) - k_C^2 g_C(R)], \\
F_9 &= \int_{T_a} dS_{\mathbf{x}} \int_{T_b} dl_{\mathbf{y}} \phi_b(\mathbf{y}) [k_S^2 g_S(R) - k_C^2 g_C(R)], \\
F_{10} &= \int_{T_a} dS_{\mathbf{x}} \int_{l_b} dl_{\mathbf{y}} \phi_a(\mathbf{x}) [g_S(R) - g_C(R)], \\
F_{11} &= \int_{l_a} dl_{\mathbf{x}} \int_{T_b} dS_{\mathbf{y}} \phi_b(\mathbf{y}) [g_S(R) - g_C(R)],
\end{aligned} \tag{C.86}$$

Evaluation of matrix elements of \hat{W} . Complete matrix element of \hat{W} for the linear basis functions

$$\int dS_{\mathbf{x}} dS_{\mathbf{y}} [\Psi_a(\mathbf{x}) \cdot \hat{W}(\mathbf{x}, \mathbf{y}) \cdot \Psi_b(\mathbf{y})] = \int dS_{\mathbf{x}} dS_{\mathbf{y}} \phi_a(\mathbf{x}) \phi_b(\mathbf{y}) [\mathbf{b} \hat{W} \mathbf{a}], \tag{C.87}$$

with

$$\begin{aligned}
(\mathbf{b} \cdot \hat{W} \cdot \mathbf{a}) = & -\frac{\lambda^2 k_C^2}{\lambda + 2\mu} a_n b_n g_C(R) + \\
& + \frac{2\lambda\mu}{\lambda + 2\mu} [a_n(\hat{\mathbf{n}}_b \cdot \nabla_{\mathbf{x}})(\mathbf{b} \cdot \nabla_{\mathbf{x}}) + b_n(\hat{\mathbf{n}}_a \cdot \nabla_{\mathbf{x}})(\mathbf{a} \cdot \nabla_{\mathbf{x}})] g_C(R) + \\
& + \mu \{ (\mathbf{a} \cdot \mathbf{b})(\hat{\mathbf{n}}_a \cdot \nabla_{\mathbf{x}})(\hat{\mathbf{n}}_b \cdot \nabla_{\mathbf{x}}) + (\hat{\mathbf{n}}_b \cdot \mathbf{a})(\hat{\mathbf{n}}_a \cdot \nabla_{\mathbf{x}})(\mathbf{b} \cdot \nabla_{\mathbf{x}}) + \\
& + (\hat{\mathbf{n}}_a \cdot \mathbf{b})(\mathbf{a} \cdot \nabla_{\mathbf{x}})(\hat{\mathbf{n}}_b \cdot \nabla_{\mathbf{x}}) + (\hat{\mathbf{n}}_a \cdot \hat{\mathbf{n}}_b)(\mathbf{a} \cdot \nabla_{\mathbf{x}})(\mathbf{b} \cdot \nabla_{\mathbf{x}}) \} g_S(R) + \\
& + \frac{4\mu}{k_S^2} (\hat{\mathbf{n}}_a \cdot \nabla_{\mathbf{x}})(\hat{\mathbf{n}}_b \cdot \nabla_{\mathbf{x}})(\mathbf{a} \cdot \nabla_{\mathbf{x}})(\mathbf{b} \cdot \nabla_{\mathbf{x}}) [g_S(R) - g_C(R)].
\end{aligned} \tag{C.88}$$

We note that

$$\begin{aligned}
& a_n(\hat{\mathbf{n}}_b \cdot \nabla_{\mathbf{x}})(\mathbf{b} \cdot \nabla_{\mathbf{x}}) + b_n(\hat{\mathbf{n}}_a \cdot \nabla_{\mathbf{x}})(\mathbf{a} \cdot \nabla_{\mathbf{x}}) = \\
& a_n b_n [2\nabla_{\mathbf{x}}^2 - (\hat{\mathbf{n}}_b \times \nabla_{\mathbf{x}})^2 - (\hat{\mathbf{n}}_a \times \nabla_{\mathbf{x}})^2] + \\
& + a_n b_t(\hat{\mathbf{n}}_b \cdot \nabla_{\mathbf{x}})(\hat{\mathbf{t}}_b \cdot \nabla_{\mathbf{x}}) + a_t b_n(\hat{\mathbf{t}}_a \cdot \nabla_{\mathbf{x}})(\hat{\mathbf{n}}_a \cdot \nabla_{\mathbf{x}}),
\end{aligned} \tag{C.89}$$

Subsequently we evaluate the integrals

$$\begin{aligned}
& \int_{T_a T_b} dS_{\mathbf{x}} dS_{\mathbf{y}} \phi_a(\mathbf{x}) \phi_b(\mathbf{y}) [a_n(\hat{\mathbf{n}}_b \cdot \nabla_{\mathbf{x}})(\mathbf{b} \cdot \nabla_{\mathbf{x}}) + b_n(\hat{\mathbf{n}}_a \cdot \nabla_{\mathbf{x}})(\mathbf{a} \cdot \nabla_{\mathbf{x}})] g_C(R) = \\
& - 2k_C^2 a_n b_n W_2 - 4 \frac{a_n b_n}{h_a^2} W_3 - 4 \frac{a_n b_n}{h_b^2} W_4 - \frac{2a_n b_t(\hat{\mathbf{t}}_b \cdot \hat{\mathbf{h}}_b)}{h_b} W_5, - \frac{2a_t b_n(\hat{\mathbf{t}}_a \cdot \hat{\mathbf{h}}_a)}{h_a} W_6.
\end{aligned} \tag{C.90}$$

$$\begin{aligned}
& \{ (\mathbf{a} \cdot \mathbf{b})(\hat{\mathbf{n}}_a \cdot \nabla_{\mathbf{x}})(\hat{\mathbf{n}}_b \cdot \nabla_{\mathbf{x}}) + (\hat{\mathbf{n}}_b \cdot \mathbf{a})(\hat{\mathbf{n}}_a \cdot \nabla_{\mathbf{x}})(\mathbf{b} \cdot \nabla_{\mathbf{x}}) + \\
& + (\hat{\mathbf{n}}_a \cdot \mathbf{b})(\mathbf{a} \cdot \nabla_{\mathbf{x}})(\hat{\mathbf{n}}_b \cdot \nabla_{\mathbf{x}}) + (\hat{\mathbf{n}}_a \cdot \hat{\mathbf{n}}_b)(\mathbf{a} \cdot \nabla_{\mathbf{x}})(\mathbf{b} \cdot \nabla_{\mathbf{x}}) \} = \\
& \{ (\mathbf{a} \cdot \mathbf{b})(\hat{\mathbf{n}}_a \cdot \nabla_{\mathbf{x}})(\hat{\mathbf{n}}_a \cdot \nabla_{\mathbf{x}}) + b_n(\hat{\mathbf{n}}_b \cdot \mathbf{a})(\hat{\mathbf{n}}_a \cdot \nabla_{\mathbf{x}})(\hat{\mathbf{n}}_b \cdot \nabla_{\mathbf{x}}) + b_t(\hat{\mathbf{n}}_b \cdot \mathbf{a})(\hat{\mathbf{n}}_a \cdot \nabla_{\mathbf{x}})(\hat{\mathbf{t}}_b \cdot \nabla_{\mathbf{x}}) + \\
& + a_n(\hat{\mathbf{n}}_a \cdot \mathbf{b})(\hat{\mathbf{n}}_a \cdot \nabla_{\mathbf{x}})(\hat{\mathbf{n}}_b \cdot \nabla_{\mathbf{x}}) + a_t(\hat{\mathbf{n}}_a \cdot \mathbf{b})(\hat{\mathbf{t}}_a \cdot \nabla_{\mathbf{x}})(\hat{\mathbf{n}}_b \cdot \nabla_{\mathbf{x}}) + \\
& + a_n b_n(\hat{\mathbf{n}}_a \cdot \hat{\mathbf{n}}_b)(\hat{\mathbf{n}}_a \cdot \nabla_{\mathbf{x}})(\hat{\mathbf{n}}_b \cdot \nabla_{\mathbf{x}}) + a_n b_t(\hat{\mathbf{n}}_a \cdot \hat{\mathbf{n}}_b)(\hat{\mathbf{n}}_a \cdot \nabla_{\mathbf{x}})(\hat{\mathbf{t}}_b \cdot \nabla_{\mathbf{x}}) + \\
& + a_t b_n(\hat{\mathbf{n}}_a \cdot \hat{\mathbf{n}}_b)(\hat{\mathbf{t}}_a \cdot \nabla_{\mathbf{x}})(\hat{\mathbf{n}}_b \cdot \nabla_{\mathbf{x}}) + a_t b_t(\hat{\mathbf{n}}_a \cdot \hat{\mathbf{n}}_b)(\hat{\mathbf{t}}_a \cdot \nabla_{\mathbf{x}})(\hat{\mathbf{t}}_b \cdot \nabla_{\mathbf{x}}) \} = \\
& \{ (\mathbf{a} \cdot \mathbf{b}) + b_n(\hat{\mathbf{n}}_b \cdot \mathbf{a}) + a_n(\hat{\mathbf{n}}_b \cdot \mathbf{a}) + a_n b_n(\hat{\mathbf{n}}_a \cdot \hat{\mathbf{n}}_b) \} (\hat{\mathbf{n}}_a \cdot \nabla_{\mathbf{x}})(\hat{\mathbf{n}}_b \cdot \nabla_{\mathbf{x}}) + \\
& + \{ b_t(\hat{\mathbf{n}}_b \cdot \mathbf{a}) + a_n b_t(\hat{\mathbf{n}}_a \cdot \hat{\mathbf{n}}_b) \} (\hat{\mathbf{n}}_a \cdot \nabla_{\mathbf{x}})(\hat{\mathbf{t}}_b \cdot \nabla_{\mathbf{x}}) + \\
& + \{ a_t(\hat{\mathbf{n}}_a \cdot \mathbf{b}) + a_t b_n(\hat{\mathbf{n}}_a \cdot \hat{\mathbf{n}}_b) \} (\hat{\mathbf{t}}_a \cdot \nabla_{\mathbf{x}})(\hat{\mathbf{n}}_b \cdot \nabla_{\mathbf{x}}) + \\
& + \{ a_t b_t(\hat{\mathbf{n}}_a \cdot \hat{\mathbf{n}}_b) \} (\hat{\mathbf{t}}_a \cdot \nabla_{\mathbf{x}})(\hat{\mathbf{t}}_b \cdot \nabla_{\mathbf{x}}).
\end{aligned} \tag{C.91}$$

Finally

$$\begin{aligned}
& \{(\mathbf{a} \cdot \mathbf{b})(\hat{\mathbf{n}}_a \cdot \nabla_{\mathbf{x}})(\hat{\mathbf{n}}_b \cdot \nabla_{\mathbf{x}}) + (\hat{\mathbf{n}}_b \cdot \mathbf{a})(\hat{\mathbf{n}}_a \cdot \nabla_{\mathbf{x}})(\mathbf{b} \cdot \nabla_{\mathbf{x}}) + \\
& + (\hat{\mathbf{n}}_a \cdot \mathbf{b})(\mathbf{a} \cdot \nabla_{\mathbf{x}})(\hat{\mathbf{n}}_b \cdot \nabla_{\mathbf{x}}) + (\hat{\mathbf{n}}_a \cdot \hat{\mathbf{n}}_b)(\mathbf{a} \cdot \nabla_{\mathbf{x}})(\mathbf{b} \cdot \nabla_{\mathbf{x}})\} = \\
& = \{[(\mathbf{a} \cdot \mathbf{b}) + b_n(\hat{\mathbf{n}}_b \cdot \mathbf{a}) + a_n(\hat{\mathbf{n}}_b \cdot \mathbf{a}) + a_nb_n(\hat{\mathbf{n}}_a \cdot \hat{\mathbf{n}}_b)](\hat{\mathbf{n}}_a \cdot \hat{\mathbf{n}}_b)\}\nabla_{\mathbf{x}}^2 + \\
& \{[(\mathbf{a} \cdot \mathbf{b}) + b_n(\hat{\mathbf{n}}_b \cdot \mathbf{a}) + a_n(\hat{\mathbf{n}}_b \cdot \mathbf{a}) + a_nb_n(\hat{\mathbf{n}}_a \cdot \hat{\mathbf{n}}_b)](\hat{\mathbf{n}}_a \cdot \hat{\mathbf{n}}_b)\}(\hat{\mathbf{n}}_a \times \nabla_{\mathbf{x}}) \cdot (\hat{\mathbf{n}}_b \times \nabla_{\mathbf{x}}) + \quad (C.92) \\
& + \{b_t(\hat{\mathbf{n}}_b \cdot \mathbf{a}) + a_nb_t(\hat{\mathbf{n}}_a \cdot \hat{\mathbf{n}}_b)\}(\hat{\mathbf{n}}_a \cdot \nabla_{\mathbf{x}})(\hat{\mathbf{t}}_b \cdot \nabla_{\mathbf{x}}) + \\
& + \{a_t(\hat{\mathbf{n}}_a \cdot \mathbf{b}) + a_tb_n(\hat{\mathbf{n}}_a \cdot \hat{\mathbf{n}}_b)\}(\hat{\mathbf{t}}_a \cdot \nabla_{\mathbf{x}})(\hat{\mathbf{n}}_b \cdot \nabla_{\mathbf{x}}) + \\
& + \{a_tb_t(\hat{\mathbf{n}}_a \cdot \hat{\mathbf{n}}_b)\}(\hat{\mathbf{t}}_a \cdot \nabla_{\mathbf{x}})(\hat{\mathbf{t}}_b \cdot \nabla_{\mathbf{x}}).
\end{aligned}$$

$$\begin{aligned}
& \int_{T_a T_b} dS_{\mathbf{x}} dS_{\mathbf{y}} \phi_a(\mathbf{x}) \phi_b(\mathbf{y}) \{(\mathbf{a} \cdot \mathbf{b})(\hat{\mathbf{n}}_a \cdot \nabla_{\mathbf{x}})(\hat{\mathbf{n}}_b \cdot \nabla_{\mathbf{x}}) + (\hat{\mathbf{n}}_b \cdot \mathbf{a})(\hat{\mathbf{n}}_a \cdot \nabla_{\mathbf{x}})(\mathbf{b} \cdot \nabla_{\mathbf{x}}) + \\
& + (\hat{\mathbf{n}}_a \cdot \mathbf{b})(\mathbf{a} \cdot \nabla_{\mathbf{x}})(\hat{\mathbf{n}}_b \cdot \nabla_{\mathbf{x}}) + (\hat{\mathbf{n}}_a \cdot \hat{\mathbf{n}}_b)(\mathbf{a} \cdot \nabla_{\mathbf{x}})(\mathbf{b} \cdot \nabla_{\mathbf{x}})\} g_S(R) = \\
& \{[(\mathbf{a} \cdot \mathbf{b}) + b_n(\hat{\mathbf{n}}_b \cdot \mathbf{a}) + a_n(\hat{\mathbf{n}}_b \cdot \mathbf{a}) + a_nb_n(\hat{\mathbf{n}}_a \cdot \hat{\mathbf{n}}_b)](\hat{\mathbf{n}}_a \cdot \hat{\mathbf{n}}_b)\} [-k_S^2 W_7 - \frac{4\hat{\mathbf{h}}_a \cdot \hat{\mathbf{h}}_b}{h_a h_b} W_8] + \\
& + \frac{-2[b_t(\hat{\mathbf{n}}_b \cdot \mathbf{a}) + a_nb_t(\hat{\mathbf{n}}_a \cdot \hat{\mathbf{n}}_b)](\hat{\mathbf{t}}_b \cdot \hat{\mathbf{h}}_b)}{h_b} W_9 - \frac{2[a_t(\hat{\mathbf{n}}_a \cdot \mathbf{b}) + a_tb_n(\hat{\mathbf{n}}_a \cdot \hat{\mathbf{n}}_b)](\hat{\mathbf{t}}_a \cdot \hat{\mathbf{h}}_a)}{h_a} W_{10} + \\
& + \frac{4a_tb_t(\hat{\mathbf{n}}_a \cdot \hat{\mathbf{n}}_b)(\hat{\mathbf{t}}_a \cdot \hat{\mathbf{h}}_a)(\hat{\mathbf{t}}_b \cdot \hat{\mathbf{h}}_b)}{h_a h_b} W_8. \quad (C.93)
\end{aligned}$$

$$\begin{aligned}
& (\hat{\mathbf{n}}_a \cdot \nabla_{\mathbf{x}})(\hat{\mathbf{n}}_b \cdot \nabla_{\mathbf{x}})(\mathbf{a} \cdot \nabla_{\mathbf{x}})(\mathbf{b} \cdot \nabla_{\mathbf{x}})[g_S(R) - g_C(R)] = \\
& = -\phi_a(\mathbf{x}) \phi_b(\mathbf{y}) (\hat{\mathbf{n}}_a \cdot \hat{\mathbf{n}}_b)(\mathbf{a} \cdot \nabla_{\mathbf{x}})(\mathbf{b} \cdot \nabla_{\mathbf{x}})[k_S^2 g_S(R) - k_C^2 g_C(R)] + \\
& - \frac{4(\hat{\mathbf{l}}_a \cdot \hat{\mathbf{l}}_b)}{h_a h_b} (\mathbf{a} \cdot \nabla_{\mathbf{x}})(\mathbf{b} \cdot \nabla_{\mathbf{x}})[g_S(R) - g_C(R)]. \quad (C.94)
\end{aligned}$$

$$\begin{aligned}
& \int_{T_a T_b} dS_{\mathbf{x}} dS_{\mathbf{y}} \phi_a(\mathbf{x}) \phi_b(\mathbf{y}) (\mathbf{a} \cdot \nabla_{\mathbf{R}})(\mathbf{b} \cdot \nabla_{\mathbf{R}})[k_S^2 g_S(R) - k_C^2 g_C(R)] = \\
& = a_nb_n(\hat{\mathbf{n}}_a \cdot \hat{\mathbf{n}}_b)W_{11} + \frac{2a_n(\mathbf{b}_t \cdot \hat{\mathbf{h}}_b)}{h_a} W_{12} + \frac{2b_n(\mathbf{a}_t \cdot \hat{\mathbf{h}}_a)}{h_b} W_{13} + \\
& + \frac{4[(\mathbf{a} \cdot \hat{\mathbf{h}}_a)(\mathbf{b} \cdot \hat{\mathbf{h}}_b) - a_nb_n(\hat{\mathbf{l}}_a \cdot \hat{\mathbf{l}}_b)]}{h_a h_b} W_{14}. \quad (C.95)
\end{aligned}$$

$$\begin{aligned}
& \int_{T_a T_b} dS_{\mathbf{x}} dS_{\mathbf{y}} (\mathbf{a} \cdot \nabla_{\mathbf{R}})(\mathbf{b} \cdot \nabla_{\mathbf{R}})[g_S(R) - g_C(R)] = \\
& = a_nb_n(\hat{\mathbf{n}}_a \cdot \hat{\mathbf{n}}_b)W_{14} + 2a_n(\mathbf{b}_t \cdot \hat{\mathbf{h}}_b)W_{15} + 2b_n(\mathbf{a}_t \cdot \hat{\mathbf{h}}_a)W_{16} + \\
& + 4[(\mathbf{a} \cdot \hat{\mathbf{h}}_a)(\mathbf{b} \cdot \hat{\mathbf{h}}_b) - a_nb_n(\hat{\mathbf{l}}_a \cdot \hat{\mathbf{l}}_b)]W_{17}. \quad (C.96)
\end{aligned}$$

Final expression for matrix element of \hat{W}

$$\begin{aligned}
& \int_{T_a T_b} dS_{\mathbf{x}} dS_{\mathbf{y}} \phi_a(\mathbf{x}) \phi_b(\mathbf{y}) (\mathbf{b} \cdot \hat{W} \mathbf{a}) = \\
& = -\frac{\lambda k_C^2}{\lambda + 2\mu} W_2 + \\
& + \frac{2\lambda\mu}{\lambda + 2\mu} \left\{ -2k_C^2 a_n b_n W_2 - 4\frac{a_n b_n}{h_a^2} W_3 - 4\frac{a_n b_n}{h_b^2} W_4 - \frac{2a_n b_t (\hat{\mathbf{t}}_b \cdot \hat{\mathbf{h}}_b)}{h_b} W_5, -\frac{2a_t b_n (\hat{\mathbf{t}}_a \cdot \hat{\mathbf{h}}_a)}{h_a} W_6 \right\} + \\
& + \mu \left\{ [(\mathbf{a} \cdot \mathbf{b}) + b_n (\hat{\mathbf{n}}_b \cdot \mathbf{a}) + a_n (\hat{\mathbf{n}}_b \cdot \mathbf{a}) + a_n b_n (\hat{\mathbf{n}}_a \cdot \hat{\mathbf{n}}_b)] (\hat{\mathbf{n}}_a \cdot \hat{\mathbf{n}}_b) [-k_S^2 W_7 - \frac{4\hat{\mathbf{h}}_a \cdot \hat{\mathbf{h}}_b}{h_a h_b} W_8] + \right. \\
& + \frac{-2[b_t (\hat{\mathbf{n}}_b \cdot \mathbf{a}) + a_n b_t (\hat{\mathbf{n}}_a \cdot \hat{\mathbf{n}}_b)] (\hat{\mathbf{t}}_b \cdot \hat{\mathbf{h}}_b)}{h_b} W_9 - \frac{2[a_t (\hat{\mathbf{n}}_a \cdot \mathbf{b}) + a_t b_n (\hat{\mathbf{n}}_a \cdot \hat{\mathbf{n}}_b)] (\hat{\mathbf{t}}_a \cdot \hat{\mathbf{h}}_a)}{h_a} W_{10} + \\
& + \frac{4a_t b_t (\hat{\mathbf{n}}_a \cdot \hat{\mathbf{n}}_b) (\hat{\mathbf{t}}_a \cdot \hat{\mathbf{h}}_a) (\hat{\mathbf{t}}_b \cdot \hat{\mathbf{h}}_b)}{h_a h_b} W_8 \left. \right\} + \\
& - \frac{4\mu (\hat{\mathbf{n}}_a \cdot \hat{\mathbf{n}}_b)}{k_S^2} \left\{ a_n b_n (\hat{\mathbf{n}}_a \cdot \hat{\mathbf{n}}_b) W_{11} + \frac{2a_n (\mathbf{b}_t \cdot \hat{\mathbf{h}}_b)}{h_a} W_{12} + \frac{2b_n (\mathbf{a}_t \cdot \hat{\mathbf{h}}_a)}{h_b} W_{13} + \right. \\
& + \frac{4[(\mathbf{a} \cdot \hat{\mathbf{h}}_a) (\mathbf{b} \cdot \hat{\mathbf{h}}_b) - a_n b_n (\hat{\mathbf{l}}_a \cdot \hat{\mathbf{l}}_b)]}{h_a h_b} W_{14} \left. \right\} + \\
& - \frac{4(\hat{\mathbf{l}}_a \cdot \hat{\mathbf{l}}_b)}{h_a h_b} \left\{ a_n b_n (\hat{\mathbf{n}}_a \cdot \hat{\mathbf{n}}_b) W_{14} + \right. \\
& + 2a_n (\mathbf{b}_t \cdot \hat{\mathbf{h}}_b) W_{15} + 2b_n (\mathbf{a}_t \cdot \hat{\mathbf{h}}_a) W_{16} + 4[(\mathbf{a} \cdot \hat{\mathbf{h}}_a) (\mathbf{b} \cdot \hat{\mathbf{h}}_b) - a_n b_n (\hat{\mathbf{l}}_a \cdot \hat{\mathbf{l}}_b)] W_{17} \left. \right\}.
\end{aligned} \tag{C.97}$$

where

$$\begin{aligned}
W_2 &= \int_{T_a T_b} dS_{\mathbf{x}} dS_{\mathbf{y}} \phi_a(\mathbf{x}) \phi_b(\mathbf{y}) g_C(R), \\
W_3 &= \int_{l_a} dl_a \int_{T_b} dS_{\mathbf{y}} \phi_b(\mathbf{y}) g_C(R), \\
W_4 &= \int_{T_a} dS_{\mathbf{x}} \int_{l_b} dl_b \phi_a(\mathbf{x}) g_C(R) + \\
W_5 &= \int_{T_a T_b} dS_{\mathbf{x}} dS_{\mathbf{y}} \phi_a(\mathbf{x}) (\hat{\mathbf{n}}_b \cdot \nabla_{\mathbf{x}}) g_C(R), \\
W_6 &= \int_{T_a T_b} dS_{\mathbf{x}} dS_{\mathbf{y}} \phi_b(\mathbf{y}) (\hat{\mathbf{n}}_a \cdot \nabla_{\mathbf{x}}) g_C(R), \\
W_7 &= \int_{T_a T_b} dS_{\mathbf{x}} dS_{\mathbf{y}} \phi_a(\mathbf{x}) \phi_b(\mathbf{y}) g_S(R), \\
W_8 &= \int_{T_a T_b} dS_{\mathbf{x}} dS_{\mathbf{y}} g_S(R), \\
W_9 &= \int_{T_a T_b} dS_{\mathbf{x}} dS_{\mathbf{y}} \phi_a(\mathbf{x}) (\hat{\mathbf{n}}_b \cdot \nabla_{\mathbf{x}}) g_S(R), \\
W_{10} &= \int_{T_a T_b} dS_{\mathbf{x}} dS_{\mathbf{y}} \phi_b(\mathbf{y}) (\hat{\mathbf{n}}_a \cdot \nabla_{\mathbf{x}}) g_S(R), \\
W_{11} &= \int_{T_a T_b} dS_{\mathbf{x}} dS_{\mathbf{y}} \phi_a(\mathbf{x}) \phi_b(\mathbf{y}) [k_S^4 g_S(R) - k_C^4 g_C(R)], \\
W_{12} &= \int_{T_a T_b} dS_{\mathbf{x}} dS_{\mathbf{y}} \phi_a(\mathbf{x}) (\hat{\mathbf{R}} \cdot \hat{\mathbf{n}}_a) [k_S^2 g'_S(R) - k_C^2 g'_C(R)], \\
W_{13} &= \int_{T_a T_b} dS_{\mathbf{x}} dS_{\mathbf{y}} \phi_b(\mathbf{y}) (\hat{\mathbf{R}} \cdot \hat{\mathbf{n}}_b) [k_S^2 g'_S(R) - k_C^2 g'_C(R)], \\
W_{14} &= \int_{T_a T_b} dS_{\mathbf{x}} dS_{\mathbf{y}} [k_S^2 g_S(R) - k_C^2 g_C(R)], \\
W_{15} &= \int_{T_a} \int_{l_b} dS_{\mathbf{x}} dl_b (\hat{\mathbf{R}} \cdot \hat{\mathbf{n}}_a) [g'_S(R) - g'_C(R)], \\
W_{16} &= \int_{l_a} \int_{T_b} dl_a dS_{\mathbf{y}} (\hat{\mathbf{R}} \cdot \hat{\mathbf{n}}_b) [g'_S(R) - k_C^2 g'_C(R)], \\
W_{17} &= \int_{l_a l_b} dl_a dl_b [k_S^2 g_S(R) - k_C^2 g_C(R)].
\end{aligned} \tag{C.98}$$

C.5.4 Behavior of the kernels near the Green function singularity $R = 0$

We note that the displacement Green functions $\hat{G}(R)$ and the surface stress tensor Green function $\Gamma(\mathbf{r}, \mathbf{r}')$ appearing in the surface integral equation exhibit an important property in the limit $R \rightarrow 0$. Since the function

$$g_S(R) - g_C(R) = \frac{1}{4\pi} \left(\frac{e^{ik_S R} - 1}{R} - \frac{e^{ik_C R} - 1}{R} \right) \quad (\text{C.99})$$

is regular for $R \rightarrow 0$ (due to cancellation of the singularities in the two Green functions), the second terms of the Green functions $\hat{G}(R)$ and $\hat{\mathbf{n}} \cdot \Sigma(\mathbf{r}, \mathbf{r}')$ are also nonsingular, while, without the cancellation, they would have contained a $1/R^3$ singularity. The reduced degree of singularity is particularly important in the discretization of surface integral equations (Sec. C.4). Specifically we have for small R

$$[g_S(R) - g_C(R)] \rightarrow \frac{1}{4\pi} \{i(k_S - k_C) + \frac{1}{2}[(ik_S)^2 - (ik_C)^2]R + \dots\}$$

as well as

$$(\hat{\mathbf{n}} \cdot \nabla_{\mathbf{R}})[g_S(R) - g_C(R)] = (\hat{\mathbf{n}} \cdot \hat{\mathbf{R}}) \frac{1}{4\pi} \frac{d}{dR} [g_S(R) - g_C(R)] \rightarrow -\frac{1}{8\pi} (\hat{\mathbf{n}} \cdot \hat{\mathbf{R}}) [(k_S^2 - k_C^2) + \dots]$$

are finite at $R = 0$. This fact facilitates discretization of the integral equations and computation of the matrix elements.

References

- [1] E. Bleszynski, M. Bleszynski, and T. Jaroszewicz, “Fast volumetric integral solver for acoustic wave propagation through inhomogeneous media,” *J. Acoust. Soc. Am.*, vol. 124, pp. 396–408, 2008.
- [2] —, “Fast volumetric integral-equation solver for high-contrast acoustics,” *J. Acoust. Soc. Am.*, vol. 124, pp. 3684–3693, 2008.
- [3] B. W. Lawton and M. R. Stinson, “Standing wave patterns in the human ear canal used for estimation of acoustic energy reflectance at the eardrum,” *The Journal of the Acoustical Society of America*, vol. 79, pp. 1003–1009, 1986.
- [4] P. M. Morse and K. U. Ingard, *Theoretical Acoustics*. New York: McGraw-Hill, 1968.
- [5] E. Bleszynski, M. Bleszynski, and T. Jaroszewicz, “AIM: Adaptive Integral Method for solving large-scale electromagnetic scattering and radiation problems,” *Radio Science*, vol. 31, pp. 1225–1251, 1996.
- [6] M. J. Ackerman, “The Visible Human project,” *J. Biocomm.*, vol. 18, 1991. [Online]. Available: <http://www.nlm.nih.gov>
- [7] M. Bonnet, S. Chaillat, and J.-F. Semblat, “Multi-level fast multipole BEM for 3-D elastodynamics,” *Recent advances in boundary element methods*, pp. 15–27, 2009.
- [8] P. G. Bergmann, “The wave equation in a medium with a variable index of refraction,” *J. Acoust. Soc. Am.*, vol. 17, pp. 329–333, 1946.
- [9] P. A. Martin, “Acoustic scattering by inhomogeneous obstacles,” *SIAM J. Appl. Math.*, vol. 64, pp. 297–308, 2003.
- [10] D. Colton and R. Kress, *Integral Equation Methods in Scattering Theory*. John Wiley & Sons, 1983.
- [11] M. Costabel and E. P. Stephan, “Integral equations for transmission problems in linear elasticity,” *J. Integral Equations and Applications*, vol. 2, pp. 211–222, 1990.
- [12] R. Kittappa and R. E. Kleinman, “Acoustic scattering by penetrable homogeneous objects,” *J. Math. Phys.*, vol. 16, pp. 421–432, 1975.
- [13] M. Costabel and E. P. Stephan, “A direct boundary integral equation method for transmission problems,” *J. Math. Anal. Appl.*, vol. 106, pp. 367–413, 1985.
- [14] R. E. Kleinman and P. A. Martin, “On single integral equations for the transmission problem of acoustics,” *SIAM J. Appl. Math.*, vol. 48, pp. 307–325, 1988.
- [15] P. A. Martin, “Identification of irregular frequencies in simple direct integral-equation methods for scattering by homogeneous inclusions,” *Wave Motion*, vol. 13, pp. 185–192, 1991.

- [16] H. Andrä, “Einführung in moderne Galerkin-Randelementmethoden mit einer Anwendung aus dem Maschinenbau,” *Forschung im Ingenieurwesen*, vol. 65, no. 2, pp. 58–90, 1999.
- [17] B. Håkansson and S. Stenfelt, “Vibration characteristics of bone conducted sound *in vitro*,” *J. Acoust. Soc. Am.*, vol. 107, pp. 422–431, 2000.
- [18] B. Håkansson, A. Brandt, P. Carlsson, and A. Tjellström, “Resonance frequencies of the human skull *in vivo*,” *J. Acoust. Soc. Am.*, vol. 95, pp. 1474–1481, 1994.